Numerical Simulation of Debris Impact on Hydrokinetic Infrastructure

Akshay Basavaraj Bagi

A thesis
submitted in partial fulfillment of the
requirements for the degree of

Master of Science

University of Washington

2017

Committee:

Alberto Aliseda, Chair

James J. Riley

Dana Dabiri

Program Authorized to Offer Degree:
Mechanical Engineering

University of Washington

Abstract

Numerical Simulation of Debris Impact on Hydrokinetic Infrastructure

Akshay Basavaraj Bagi

Chair of the Supervisory Committee:
Associate Professor Alberto Aliseda
Mechanical Engineering Department

This thesis studies the impacts of river debris on a hydro-kinetic infrastructure (Research Debris Diversion Platform - RDDP) by coupling Computational Fluid Dynamics (CFD) and Discrete Element Method (DEM). Debris under study are wooden logs that have been cut off from the trees and are floating in the river. The fluid in the computational domain is water, so this study only deals with the motion of debris under water and not above it. The logs are injected at different times and from different locations. The impact forces on the RDDP and the logs are studied in these conditions. Further, the flow velocity and the lengths of the logs (maintaining the same volume) are also changed to study their effects on the forces. The objective is to get statistics of debris impact forces for a wide range of current velocity, debris size and location within the river cross section. This information can be used to improve the structural strength of the RDDP and also to understand the hydrokinetic effect of the RDDP.

TABLE OF CONTENTS

LIST OF FIGURES

LIST OF TABLES

ACKNOWLEDGMENTS

I am ever grateful to my advisor, Dr. Alberto Aliseda, who has been a great mentor, and someone I look up to. I have learned so much from him in my two years of study. I am also grateful to Dr. James Riley and Dr. Dana Dabiri for teaching me about fluid mechanics, fluid turbulence, and continuum mechanics. This knowledge has contributed considerable to my research. I am also grateful to them for agreeing to be on my committee. I would also like to thank Dr. Jeremy Kasper, Dr. Paul Duvoy and entire team at University of Alaska involved in this project for inviting me to collaborate and for providing all required information and materials. This work would not have been possible without the support of faculty and staff members of the University of Washington Mechanical Engineering Department. Last, I would like to thank my family and friends for all their support and encouragement.

DEDICATION

To my dear mother, father, and sister
for their constant support and encouragement,
and their sacrifices which helped me achieve my dream.

Chapter 1
INTRODUCTION

1.1 Renewable Energy

Current renewable energy technologies include wind energy, solar energy, hydrokinetic (marine and riverine) energy, geothermal energy, and others. Solar and wind energies have been used from millennia, and, in their current form have been developed into large scale commercial use in the last five decades. Hydrokinetic energy technologies are new and still require significant research to become established affordable resources. This thesis contributes to the engineering development of hydrokinetic energy for riverine applications.

1.2 River Energy

Run of the river energy technology uses hydrokinetic turbines to generate electricity using the kinetic energy of river waters. One of the main hurdles in the development of this technology is river debris. River debris can cause considerable damage to River Energy Converters (REC). The impact of debris and debris pile-up can both lead to a reduction in performance of the RECs or, worse, lead to failure of the structure rendering them useless for the production of electricity and incurring high maintenance costs. The debris pile-up on RECs reduces the flow leading to a reduction in the efficiency.

There are few options to solve this problem. RECs can be placed in areas where the probability of debris impact is low. This option would limit the number of possible sites to deploy RECs, reducing the economic viability of the technology. Another solution is to divert the debris away from the REC before impact. This can be done by placing a hydrokinetic structure upstream of the REC so that the debris impacts the structure and is diverted away from the REC. Using this method, the number of possible sites available for the deployment

of RECs is significantly increased. This thesis is focused on the effect of hydrokinetics in the design of such structures, studying the debris impact forces which can lead to failure of the structure. By obtaining statistics of debris impacts forces for a wide range of current velocity, debris size and location within the river cross section, the structural strength and hydrokinetic effect of the debris-diverter can be improved.

1.3 Context for this thesis

In the summer of 2010, Alaska Power and Telephone (AP&T) installed a 25 kW Encurrent Turbine in Eagle, Alaska, in Yukon River [18]. During the initial days, the turbine blades were damaged by debris impact. There was debris accumulation on the turbine and the efficiency was noted to be lower than expected. The power connection to the shore was also jeopardized due to submerged debris. They realized that the debris issue was the most important problem to be solved before deploying the hydrokinetic turbines in Alaskan rivers. The Alaska Power and Telephone (AP&T) company initiated a project with the Alaska Hydrokinetic Energy Research Center (AHERC) to examine ways to reduce the surface debris hazard. The AHERC studied the important factors affecting the debris impacts and methods to divert the debris.

Before looking at their study, it is important to understand what types of debris are likely to be found in rivers, and the current strategies to mitigate the risk of debris impact on RECs.

1.3.1 River Debris Characterization

Types of Debris

Debris can be classified into three main categories based on their size although the sizes exist in a continuum [18]. The first type is *small debris*, which includes small branches of trees, leaves, and refuse [18]. Next is *medium debris*, which includes larger branches of trees [18]. Large tree branches and entire trees can be categorized as *large debris* (Figure 1.1)[18]. The small debris can enter the river through wind events and seasonal changes. Medium debris

Figure 1.1: Large debris entering the flow due to bank erosion [18].

can enter through smaller tributaries, bank erosion or large debris breakdown, and through floods. Large debris are transported generally when there are floods and bank erosion. The vast majority of these debris generally floats on the river surface, but, it is possible there might be debris throughout the water column.

Impact Forces of Debris on Engineering Structures

Haehnel and Daly, in their study, found that the maximum impact force results when the log is oriented parallel to the flow and strikes with its end [10]. Least forces were registered for oblique impacts and it was found that the force increases as the angle increases [10].

Debris Accumulation

Geometry of the engineering structures plays an important role in debris accumulation. Apertures in the structures increase the probability of accumulation [15]. Skewed alignment of the structures results in greater chances of debris accumulation [15].

1.3.2 Existing Debris Mitigation Techniques

Techniques to protect the RECs from debris include either diverting or capturing debris well upstream of the REC or trapping debris at the device.

Treibholzfange Debris Detention/Debris Basin

The Treibholzfange debris detention device consists of circular posts driven into the riverbed upstream of the device [18]. The size of debris that can be captured is determined by the geometry of the posts and the distance between the posts. LainBach and Arzbach through their lab tests at the Technical University of Munich, determined that the best configuration of retaining debris while allowing the water and sediment to flow through is to orient the posts in a downstream pointing "V", and have the posts as a distance equal to (or less than) the minimum length of the debris to be captured [20]. There are some water separation and recirculation issues with this method.

Debris Deflectors

Debris deflectors can be thought of as a localized version of Treibholzfange posts. The design generally consists of a pair of vertical grids that form a "V" shape, with the apex pointing upstream, and are made of either wood or metal [18]. The deflectors are placed immediately upstream of the RECs. These do not require a river-wide structure and can deflect most of the debris; however, there is a good chance of debris accumulation.

Trash Racks

Trash racks are used upstream of the device to prevent impact by arresting debris. One issue with trash racks is debris accumulation. This greatly reduces the flow to the hydrokinetic devices. This problem is worsened in jungle environments. Placing the trash racks far upstream will let the flow recover but so will the debris. These issues have made this technique not a viable option for debris mitigation [18].

Furling

This technique involves lifting the device when debris is present in the flow. This method can only be used when the device is small and easy to lift. This process can be automated but no such technique is being pursued now as it requires close human supervision.

Blade Design

Turbine manufacturers are also looking at modifying blade designs in order to shed debris [18]. Some companies claim that swept blades are effective in shedding debris although quantitative evidence has not been presented. Companies are also thinking of using folding blades to reduce the impact of debris on the blades. This design concept is yet to be tested.

Manual Debris Removal

This is one of the most effective techniques for handling debris. Humans can observe debris and manually remove it before the impact with the turbines. The success of this technique depends on the monitor's ability to detect the debris and intercept it in time [18].

Debris Booms

Debris booms consist of floating deflector designed to divert surface debris (Figure 1.2). They are usually made of timber and are held in place by anchors or guides [1]. Debris booms are easy to install and provide safety against floating debris but do not divert submerged debris.

Figure 1.2: Debris boom on 5 kW Encurrent Turbine in Ruby, Alaska [18].

There is also the possibility of debris accumulation. (Figure 11 Tyler). The AP&T company considers the refinement of debris boom designs to be the best strategy to produce a viable solution to debris diversion [18].

Chapter 2

BACKGROUND

The Alaska Power and Telephone (AP&T) company initiated a project with the Alaska Hydrokinetic Energy Research Center (AHERC) to develop methods to avoid debris hazard [13]. The team at AHREC developed a Research Debris Diversion Platform (RDDP) to study the important factors involved in diverting debris around the RECs using the statistics of debris occurrence from its studies at AHERC's Tanana River Test Site at Nenana, Alaska. The RDDP consists of two steel pontoons joined in a wedge with its apex facing upstream (Figure 2.1). A vertical-axis freely rotating cylinder (1.1 m diameter) was placed at the leading edge of the wedge. The rotating cylinder initially had hinged vanes to help the rotation, but later was covered with plastic to reduce surface friction. The debris diverted by the RDDP follows a path along the edge of the wake produced by the RDDP.

Figure 2.1: The RDDP debris sweep (front cylinder) and pontoons with plastic sheet covering to reduce contact friction between the RDDP and debris. [13].

2.1 RDDP Design and Testing

2.1.1 RDDP design modifications

Several modifications were made to the initial design of the RDDP including covering the pontoon surface with low-friction, high-density plastic (Figure 2.1), and adding solid ballast at the back of the RDDP [14].

The team at the University of Alaska Fairbanks has conducted field tests of RDDP to determine its effectiveness to divert debris away from the protected zone and its effect on river turbulence [14]. The RDDP was moored to a buoy and the tether connecting the two ran parallel to the river surface. The mooring buoy helped in reorienting the debris lengthwise, parallel to the direction of the river current.

During the initial deployment of RDDP in high river stage conditions, the platform tended to float with its debris sweep pitched down (Figure 2.2). This was due to the force of water against the debris sweep and upwelling of water at the rear of the debris sweep. Ballast plates were installed on the inside surface at the rear of the pontoons (Figure 2.3). The necessary ballast was added, supplemented by filling the pontoon chambers with water.

The Alaska team conducted various field tests to determine the best opening angle between the RDDP pontoons. They conducted direct impact tests of the RDDP with the debris to determine the maximum impact forces on both the buoy and the RDDP, and to determine the most difficult conditions for clearing debris [14]. Debris of various cross sections up to 0.7 m and length up to 20 m were used for tests. Tree types included branches, logs, and twisted birch. The most efficient opening angle was found to be 39 degrees which could easily clear off such debris. Opening angles greater than this led to debris pinning against the pontoons and staying there for long times before clearing off.

The team also conducted long-term deployments and used real logs for testing. The logs were towed to a position downstream of the buoy and released to impact the front end of RDDP. As initially RDDP was covered with hinged vanes, these dug into the debris and the

Figure 2.2: RDDP nose pitched down due to high river velocity before installing the ballast plates[13].

Figure 2.3: RDDP Ballast plates [13].

debris sweep had to rotate far enough to clear the debris. Also, the inertia of the debris sweep was considerable as it was built to withstand large impact loads. This problem was avoided by covering the outer surface of the rotating cylinder with high-density low-friction plastic.

After determining the parameters affecting the RDDP performance, and finalizing the design of the RDDP, it was decided to conduct a numerical study to complement the field tests. This study was initiated to contribute to this research effort. Debris impact on a simplified design of the RDDP (Figure 2.4) is simulated using CD-Adapco's commercial computational fluid dynamics (CFD) software, STAR-CCM+. The debris sweep is fixed and does not rotate. The RDDP is 2/3rd submerged under water. As a simplification, this study only considers the dynamics of the logs and the river flow under the water surface. The flow under the RDDP and the logs under water are simulated via CFD, and Discrete Element Method (DEM), respectively. The logs are made up of multiple DEM particles. Only medium-sized debris are considered for this study. Since the logs are neutrally buoyant and the simulation only consider the part that is fully immersed in water, the logs are modeled as submerged half-cylinders, that slide under the free-slip water surface, as shown in Figure 2.5.

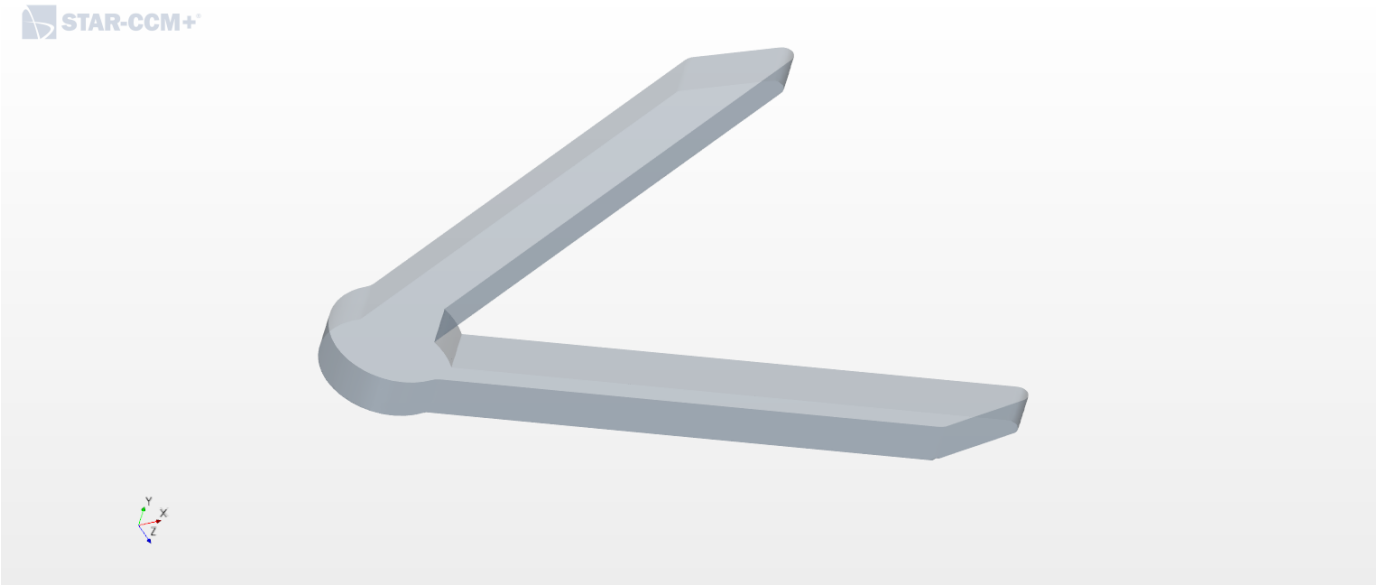

Figure 2.4: Simplified model of the RDDP for numerical study.

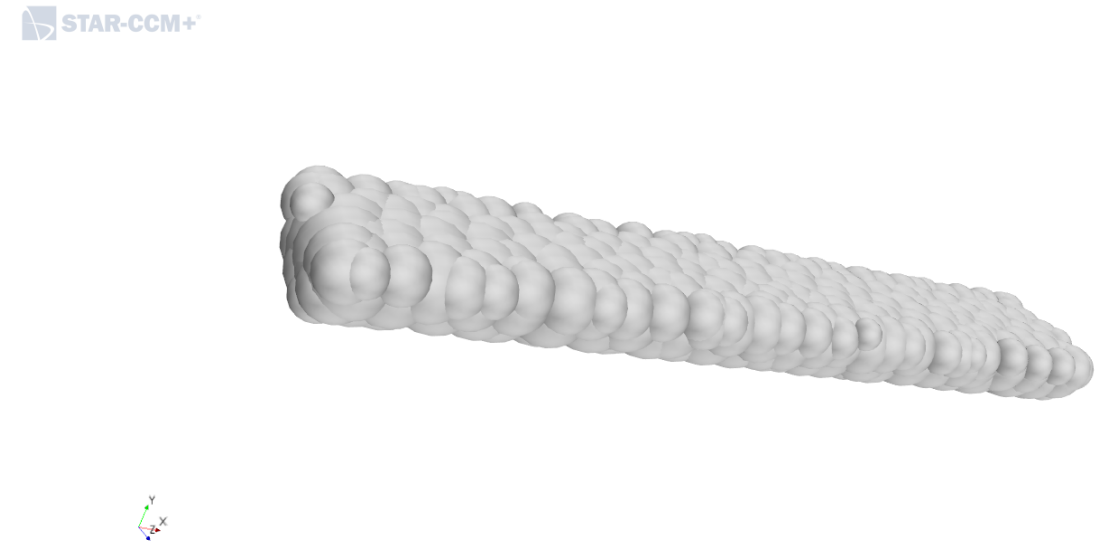

Figure 2.5: Model of medium logs for numerical study.

Chapter 3

NUMERICAL METHODOLOGY

Computational Fluid Dynamics (CFD) is a numerical simulation tool to solve the equations of motion of fluid flow. The applications of CFD are innumerable. It has become a vital tool for industry and research. The flow One can be fully resolved (Direct Numerical Simulation) or limiting assumptions an be incorporated to reduce the computational cost. Even though the computational power required fro successful simulations is large, the constant improvements in parallel computing are making it more manageable to study different flow phenomena through numerically intense computations.
The solution of a CFD problem can be broken up into three main elements [19]:

1. Pre-processor

2. Solver

3. Post-processor

Pre-processor: This step involves defining the computational domain, generating the grid (or mesh), selection of physical and chemical phenomena to be modeled, definition of fluid properties and specification of boundary conditions.
Solver: This step involves converting the differential equations of fluid motion into difference equations (typically through the finite-difference, finite-volume or finite-element methods) and solving them to obtain the flow variables.
Post-processor: The solution obtained in the previous step is visualized and interpreted in this step. This step involves visualizing the domain, obtaining contour plots, particle tracking etc.

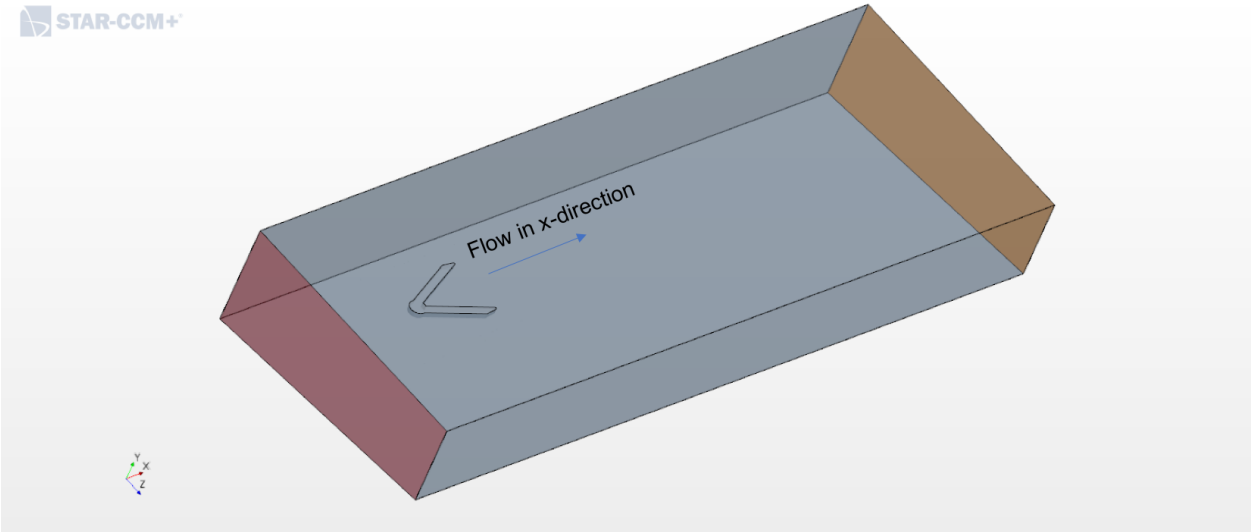

Figure 3.1: Isometric view of the domain.

3.1 Pre-processor

Defining the computational domain

The computational domain is shown in Figure 3.1. Since this study is part of a collaboration with the AHERC, and this study is aimed to complement their fields tests, the computational domain was modeled to look like a river section. The riverbed is sloped to imitate a typical riverbed and look at its effect on the flow. The front-view of the domain is shown in Figure 3.2. Due to this slope of the riverbed, the flow is asymmetrical. The RDDP is placed in the domain as shown in Figure 3.1, centered on the river cross section, so that is far enough from both banks that these do not affect the flow around the RDDP. The domain is long enough to capture the evolution of the velocity deficit and vorticity generated at both the RDDP and the turbine behind it. The flow is in x-direction. Dimensions of the computational domain used are shown in figures 3.3 and 3.4, and those of the RDDP design used in this study are shown in figures 3.5 and 3.6.

Figure 3.2: Inlet of the domain.

Generating the mesh

The computational domain, in which the governing flow equations will be solved, is spatially discretized. The domain is divided into cells or elements (in the case of the CFD methods used here, the control volumes). The governing equations are solved for these elements, using velocity and pressure at the face centers to calculate forces and fluxes, and solve for variable values at the volume centers.

The number of cells is important in the accuracy of the solution. A higher number of cells, that is a finer mesh, is required if high resolution and accuracy is desired for the numerical solution. However, as the number of cells increases, the computational cost also increases. The solution takes longer to converge. So there is an optimum where the mesh size is fine enough to give an acceptable solution, but not too big to require unreasonable computational resources. For this study, a structured mesh has been used. Structured mesh are preferred to limit excessive numerical diffusion. The mesh in the region of interest has to be fine in order to capture the solution accurately. The mesh elsewhere can be relatively coarser. In this study, the region of interest is the region around the RDDP where the logs interact with

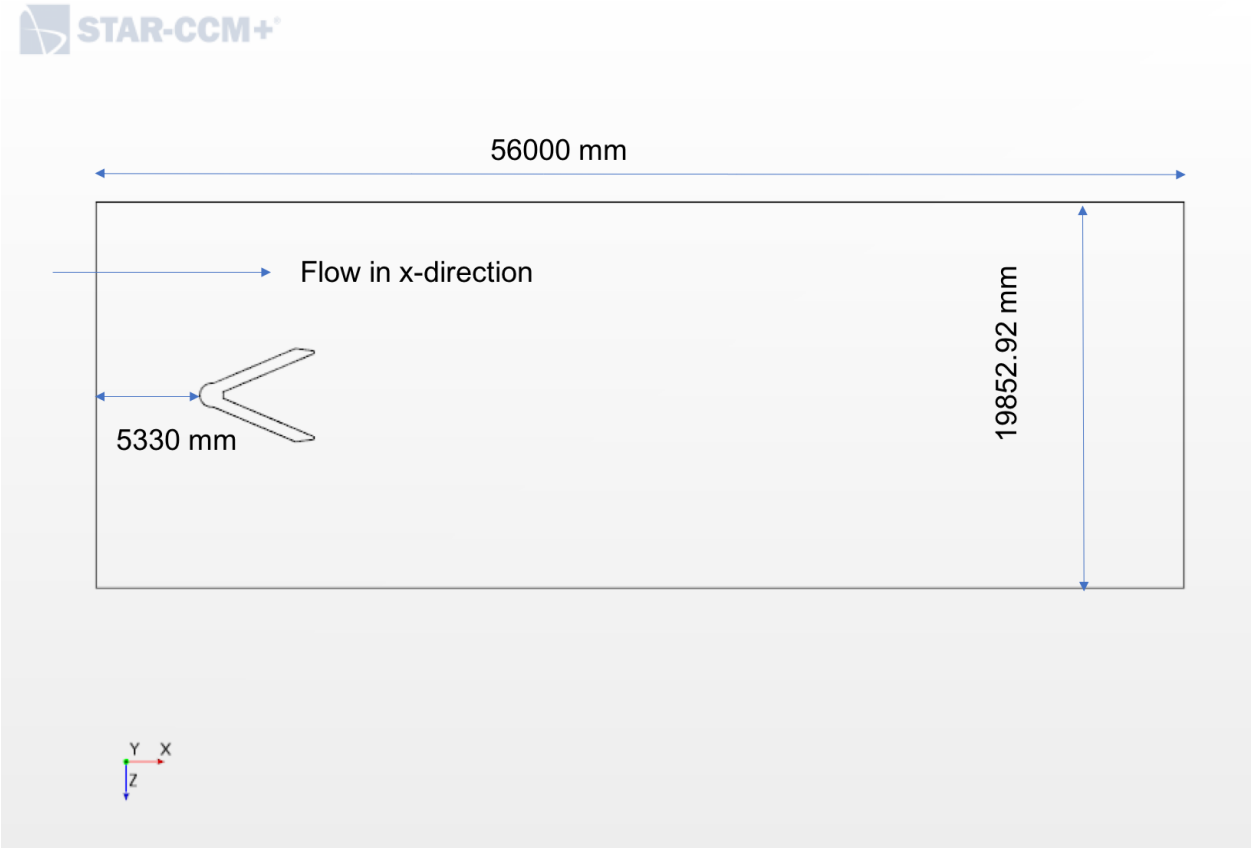

Figure 3.3: Dimensions of Domain: Top View.

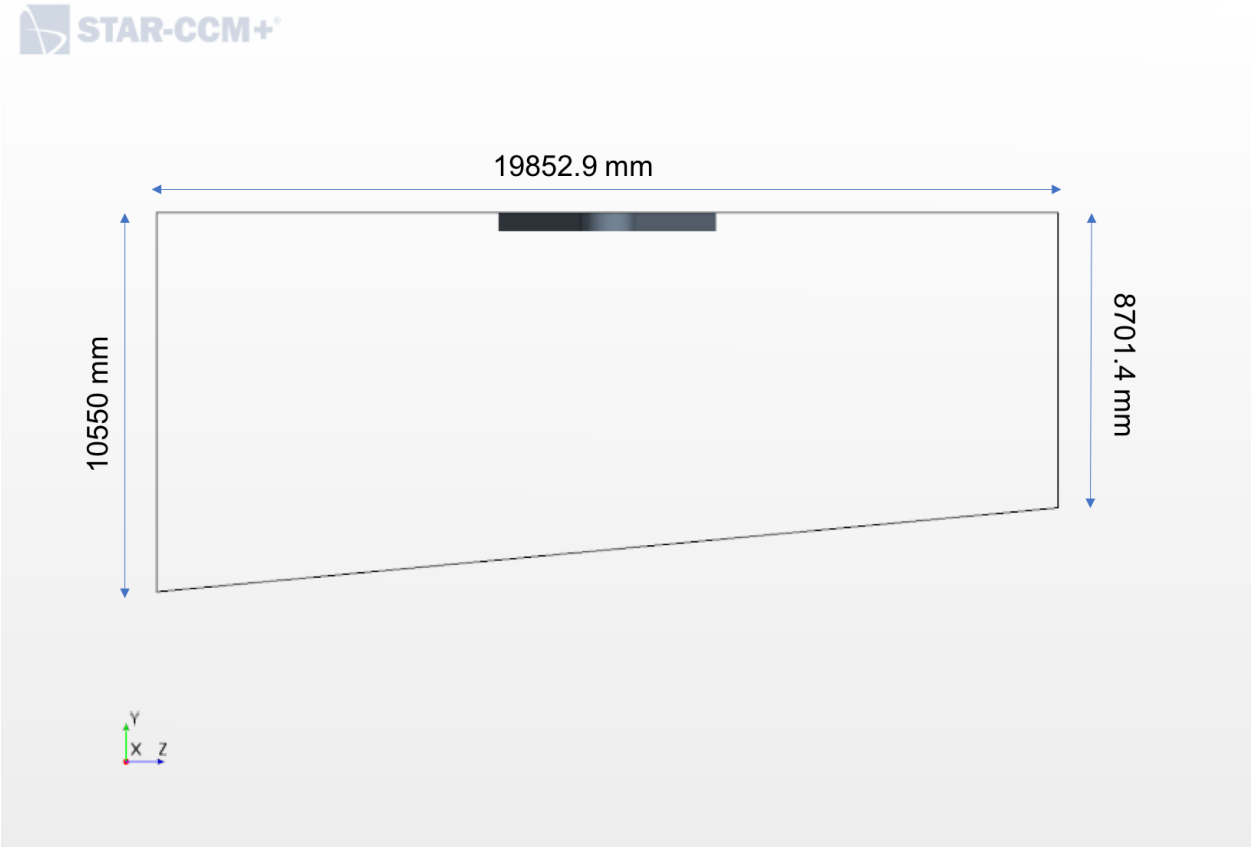

Figure 3.4: Dimensions of domain: Front View.

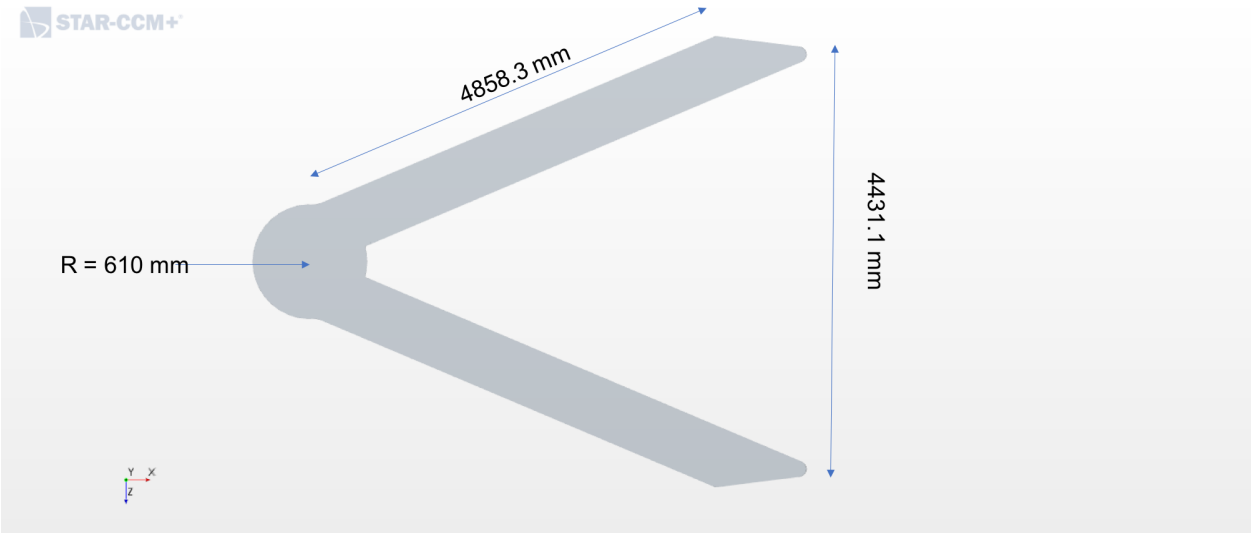

Figure 3.5: Dimensions of RDDP: Top View.

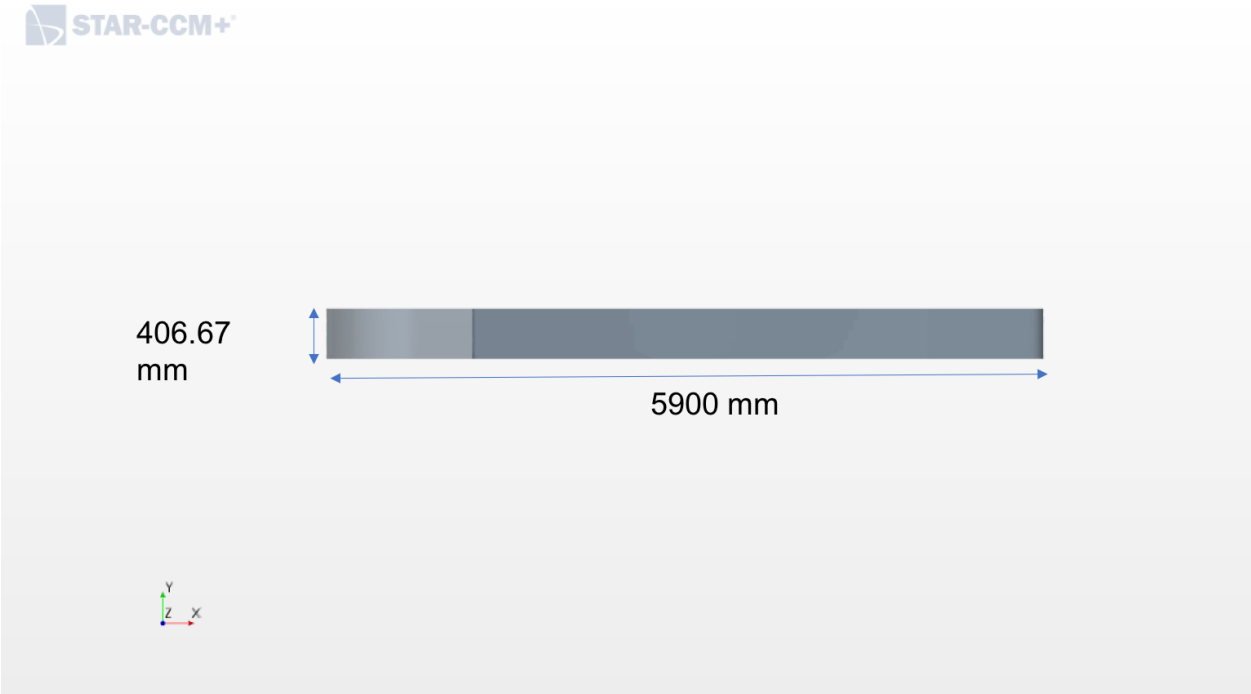

Figure 3.6: Dimensions of RDDP: Side View.

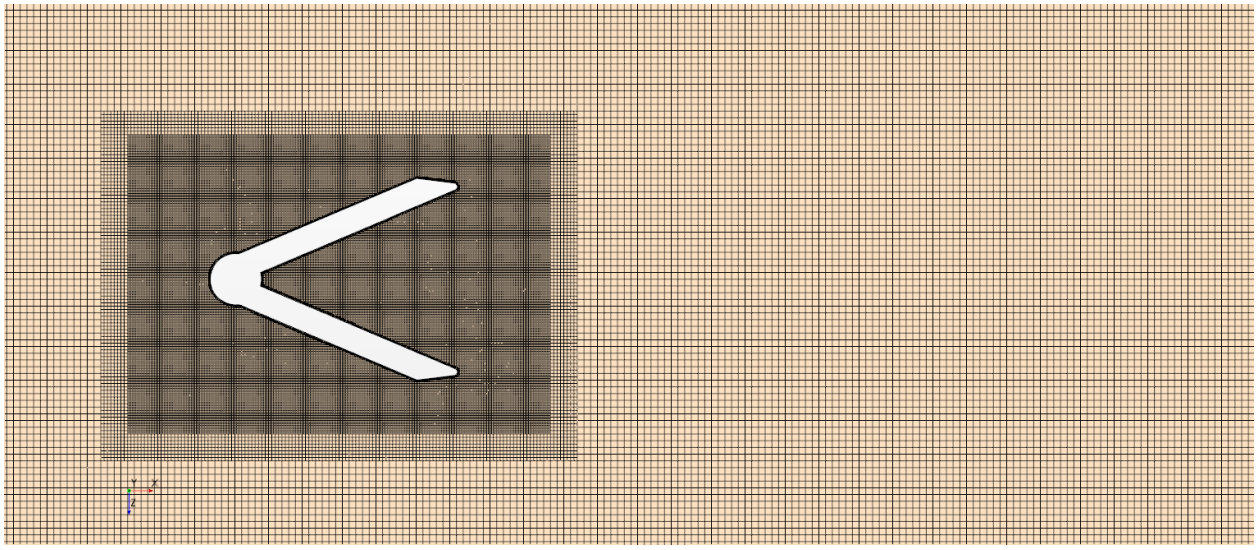

Figure 3.7: Multiple structured meshes in the domain.

the RDDP and also the region behind the RDDP where the vortices are shed and the wake evolves. A satisfactory numerical solution in this domain, under the flow conditions listed above, is achieved nesting multiple structured grids with increasingly large cells in the region of interest and the rest of the domain, as shown in Figure 3.7.

Trimmed cells have been used for meshing which are predominantly hexahedral cells. The trimmed cell mesher provides robust and efficient method of producing high quality meshes [8]. The trimmed cell mesher has various advantages [8]:

- minimal cell skewness
- offers custom refinement controls
- surface quality independence

A base size of 0.16 m is specified. This base size acts as a reference size, from which refinements can be specified. A mesh with this base size is generated in the entire domain.

Subdomains are created around the RDDP, in which the refinements are to be made. Subdomain 2 is created around the RDDP, where the size of the cells is reduced to 30% of the base size. To ensure a smooth transition between the two meshes, the region between them is automatically refined to avoid abrupt changes in cell sizes.

Prism layers are used on the immediate vicinity of the RDDP walls to accurately capture the boundary layer. Prism layers contain orthogonal prismatic cells. Prism layers provide better cross-stream resolution without incurring in excessive stream-wise resolution [7]. Gradients of flow parameters are steep in the boundary layer and prism layers resolve these gradients accurately. Numerical diffusion is also reduced near the walls. The first cell height is 5 mm. The total prism layer height is 50 mm. These settings give y^+ for the first cell inside the boundary layer in this flow in the range of 30 to 300. The definition and significance of y^+ and the values of the first cell from the wall are described in detail in Section 3.2.2. The prism layers generated around the RDDP are shown in Figure 3.8.

To accurately capture the curvature of the element in the front of the RDDP, the core mesh that defines the RDDP geometry is also refined. This is achieved using *Surface Remesher*. A target surface size of 25% of the base size is specified. This controls the size of the cells on the RDDP surface. The curvature of the RDDP sweep is controlled by specifying the *number of points along the circle that defines the front of the RDDP* which is 76 in this case. This reproduces the curvature of the RDDP sweep smoothly. The cell size growth rate from the wall surface is set to 1.2.

Using the settings mentioned above, a mesh with $3,390,955$ cells is generated. This size is found to be sufficient to give accurate results through a grid resolution and independence study. The final volume mesh is shown in Figure 3.9. Figure 3.10 shows a zoomed-in detail of the mesh at the center of the domain. The volume refinement and the prism layers around the RDDP sweep can be clearly seen.

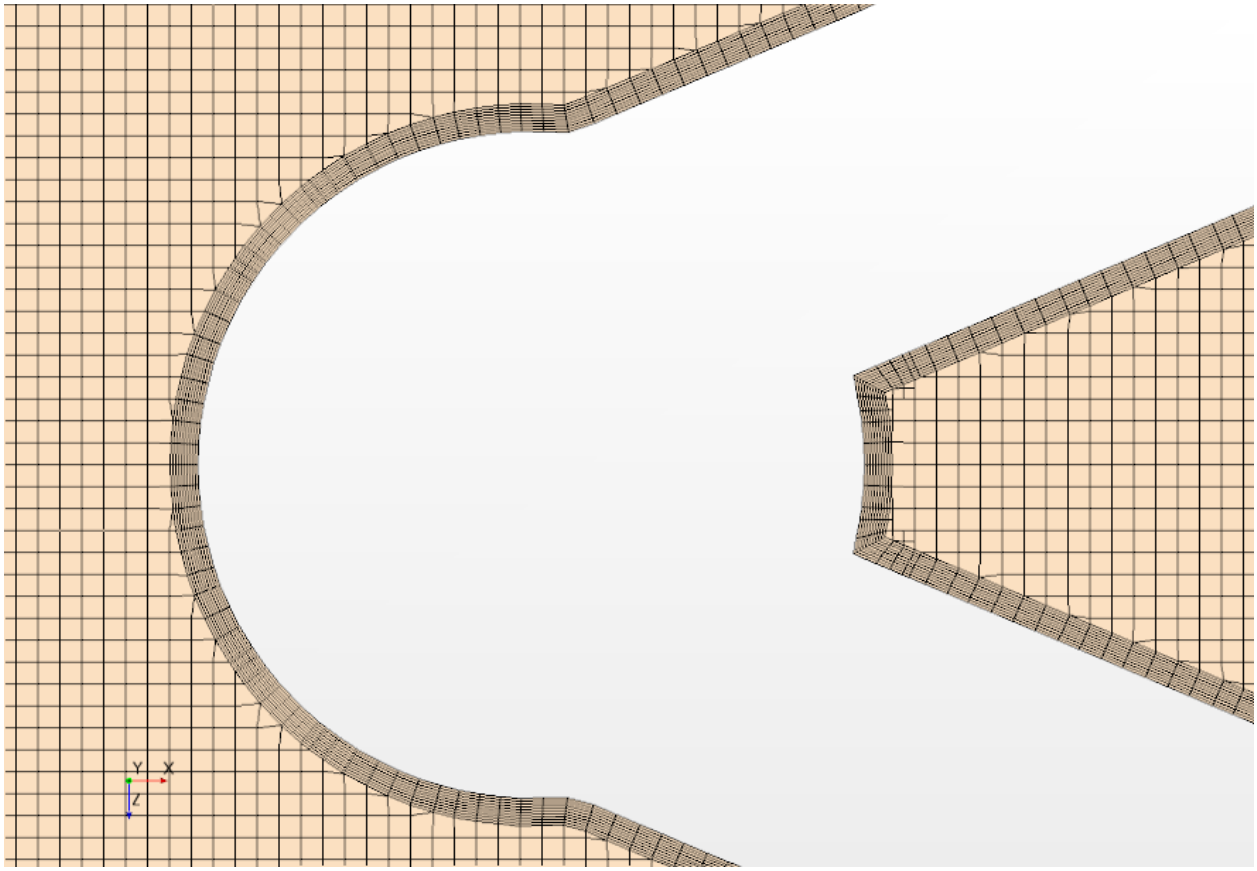

Figure 3.8: Prism Layers around the RDDP to capture the boundary layer accurately.

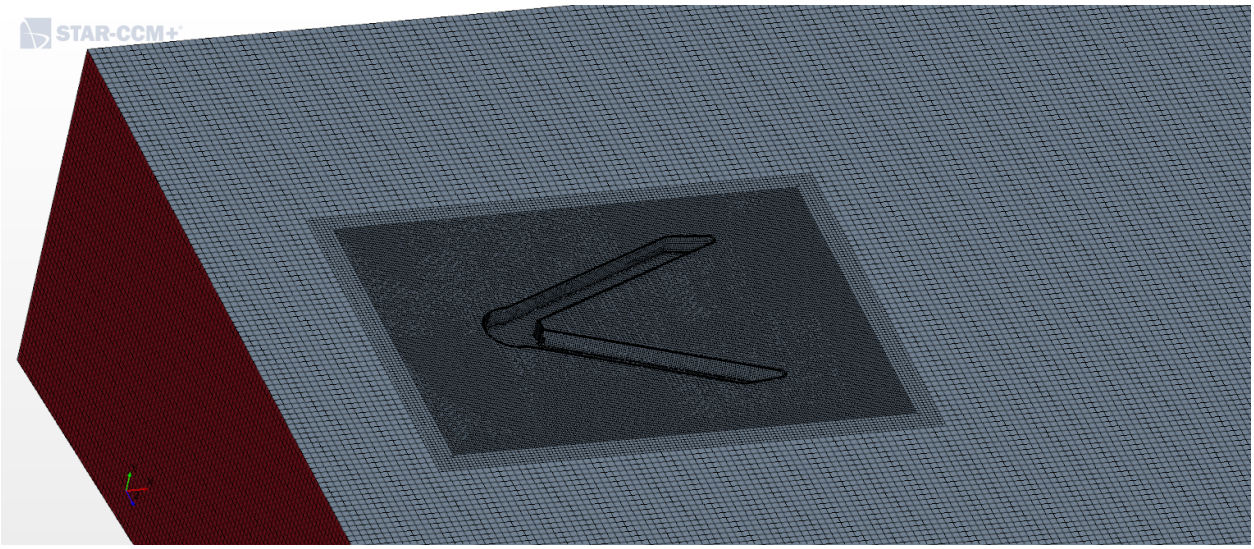

Figure 3.9: Overall Mesh.

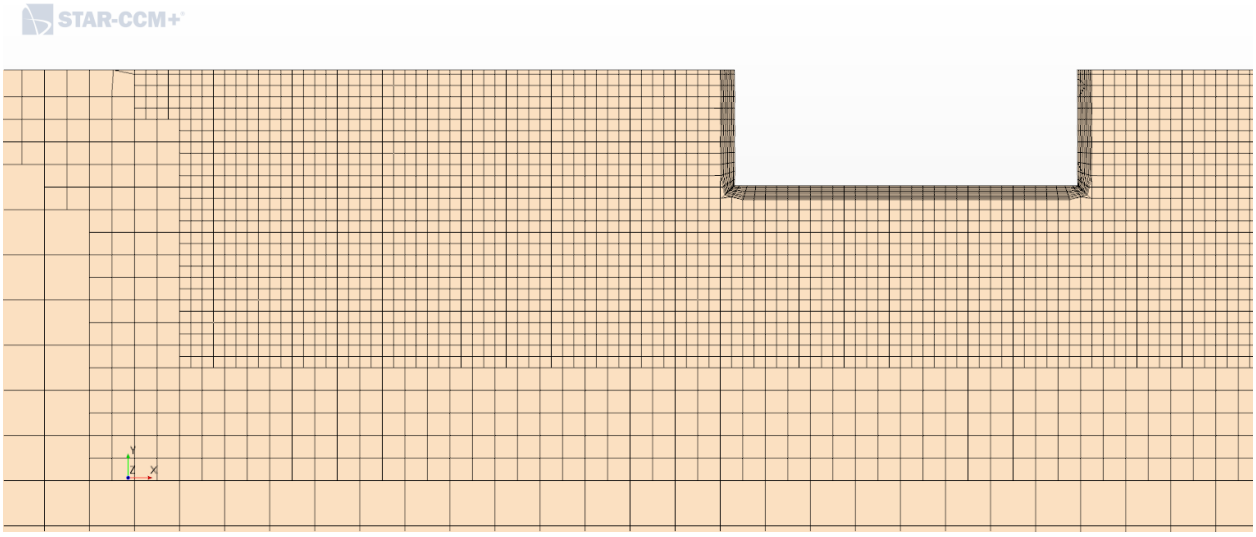

Figure 3.10: A section of the mesh at the center of the domain.

Defining the fluid properties

After the mesh is generated, the next step is to choose the working fluid. Fluid properties such as density viscosity, temperature etc., are defined by this choice. For this study, the working fluid is fresh water at standard atmospheric condition. The flow is three-dimensional and unsteady. Normal gravitational effects are considered.

Defining the boundary conditions

The top, side and bottom of the domain are set as "Slip Walls". Since the boundary layer effects on the river bottom and bank walls are not important in this study, these are set as slip walls so that there is no boundary layer developed that would required millions of computational cells to capture correctly. This saves computational cost and the mesh size. The inlet is set as "Velocity Inlet". The flow direction method is *Boundary Normal*. The velocity is 1 m/s in x-direction. The outlet is set as "Pressure Outlet". The value of pressure is 0.0 Pa gage. The RDDP wall is set as "No-Slip Wall". This leads to development of a boundary layer that is important for this study. The boundary conditions are shown in Figures 3.11 and 3.12.

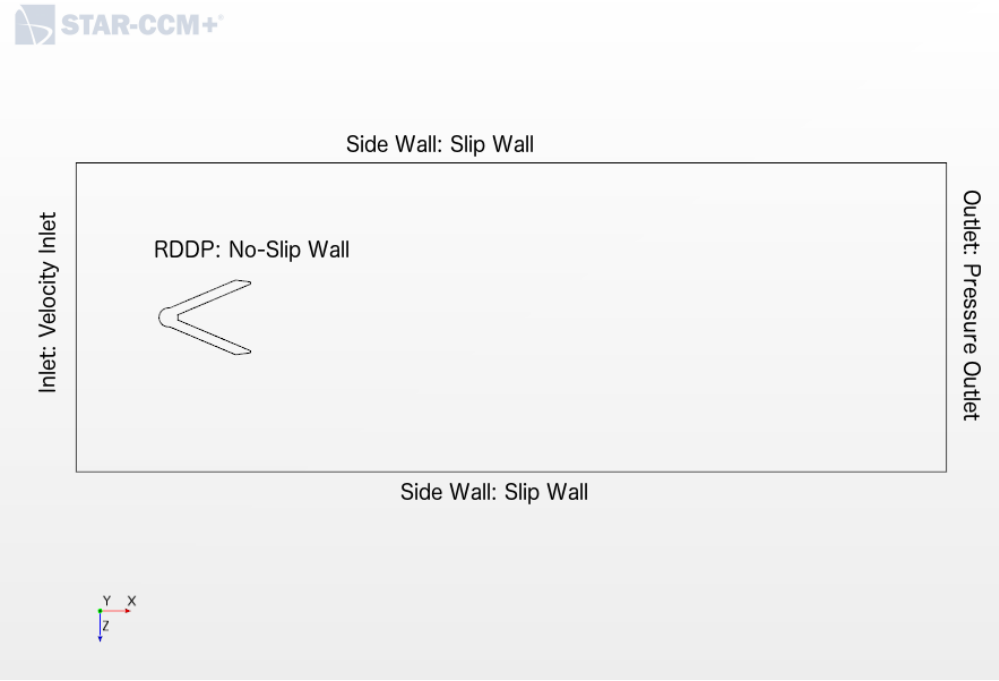

Figure 3.11: Top View of the domain with boundary conditions

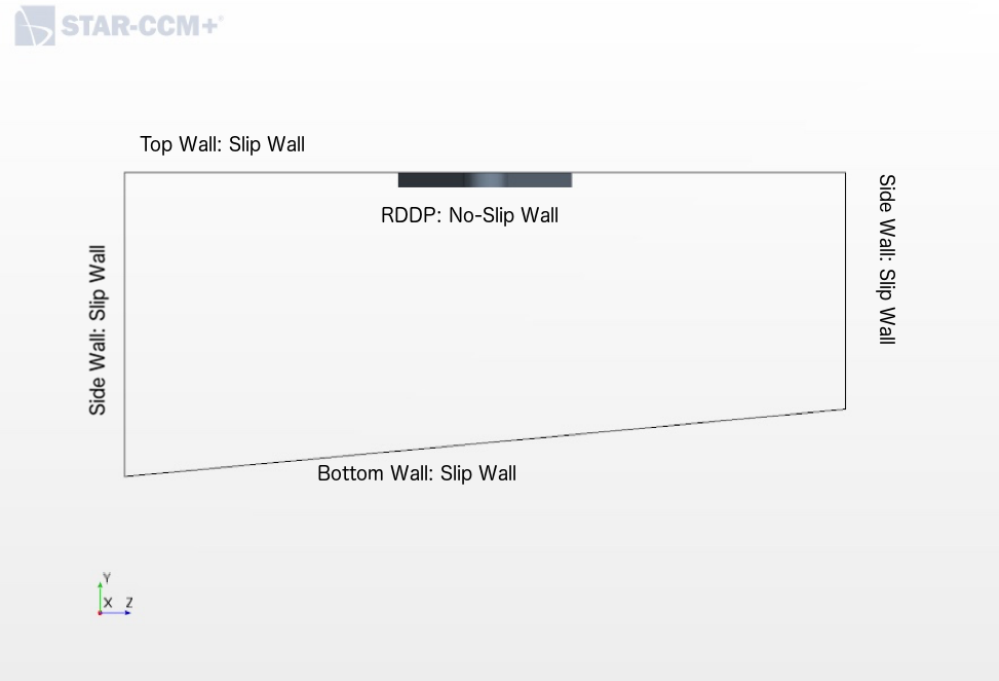

Figure 3.12: Front View of the domain with boundary conditions

3.2 Solver

This study uses the finite volume method (FVM) to discretize the equations equation of motion for the fluid. The equations to be solved for this flow are conservation of mass and momentum (the Navier-Stokes equations). The solution of these equations for a turbulent flow is made specially complex because the velocity fields are chaotic over a large range of temporal and spatial scales. Direct numerical simulation would resolve these fluctuations fully but is computationally too expensive and so far only flows in simple geometries have been solved using this method. We do not yet have the computational power to solve complex geometry problems with this method. One solution to this is to use Reynolds-Averaging to resolve these flows. In this method, the velocity components are decomposed into their mean and fluctuating components. This process of formulating the equation of motion for turbulent flows is known as *Reynolds Decomposition* [16]: Reynolds Decomposition of a scalar variable ϕ

$$\phi = \overline{\phi} + \phi' \tag{3.1}$$

When this scalar variable is velocity, Reynolds decomposition of the velocity becomes

$$\vec{U} = \overline{\vec{U}} + \vec{u}' \tag{3.2}$$

Using this method for conservation equations for an incompressible flow gives: Conservation of mass

$$\nabla \cdot \vec{U} = 0; \nabla \cdot \vec{u}' = 0 \tag{3.3}$$

Conservation of momentum

$$\frac{D\overline{U_i}}{Dt} = \nu \nabla^2 \bar{U_i} - \frac{\partial(\overline{u_i' u_j'})}{\partial x_j} - \frac{1}{\rho}\frac{\partial \overline{p}}{\partial x_i} \tag{3.4}$$

Equations 3.3 and 3.4 are the Unsteady Reynolds Averaged Navier Stokes (URANS) equations. By using Reynolds Decomposition a new term $\overline{u_i' u_j'}$ is introduced. This term is known as the Reynolds Stress term. This is a tensor and has nine components. These nine new terms render the above set of equations incomplete. A turbulence closure model is required

for the problem to be closed, with the same number of equations as unknowns, Thus, there is a need to introduce new equations in order to solve the system of equations.

3.2.1 Turbulence Closure Models

Various turbulence closure models have been developed with their own merits and challenges. Each model has a specific application that is best suited to the physics and numerics in its development. The most commonly used models are the $k-\epsilon$ model and the $k-\omega$ model. Each model computes the Reynolds stress terms $\overline{u_i' u_j'}$ to solve the system of equations described in the previous section.

The $k-\epsilon$ and $k-\omega$ models are two-equation turbulence closure models. The underlying assumption is that there exists a relation between the viscous stresses and Reynolds stresses on the mean flow.

The $k-\epsilon$ and $k-\omega$ models are two-equation turbulence closure models. The underlying assumption is that there exists a relation between the viscous stresses and Reynolds stresses on the mean flow.

The $k-\epsilon$ model introduces two equations: one for turbulent kinetic energy k and another for rate of dissipation of turbulent kinetic energy ϵ. One of the advantages of this method is that it works well for free shear flows [19]. It does not perform well for weak shear flows like the far-region of wakes and mixing layers, and swirling flows. It fails to resolve wall bounded flows and adverse pressure gradients in the flow [19]. It also introduces numerical stiffness in the solution in the viscous sub-layer. To overcome this issue, Wilcox introduced a new model where he considered the turbulence frequency ω as a second variable for closure, instead of ϵ [19]. The viscous near-wall treatment of this model is superior to the $k-\epsilon$ model. It also accounts well for the effects of stream-wise pressure gradients [16]. However, this model fails for external aerodynamics and aerospace applications as the results depend strongly on the assumed free-stream value of ω [19].

To overcome the shortcomings of $k-\epsilon$ and $k-\omega$ models, Menter developed a hybrid model that acts as $k-\omega$ in the near wall region and $k-\epsilon$ model in the fully turbulent region far

from the wall [19]. This is achieved by implementing a blending function in the ω equation. The blending function is zero close to the wall (the model behaves as $k-\omega$ model) and equal to one away from the walls (the model behaves as $k-\epsilon$ model).This model is referred to as the Shear Stress Transport $k-\omega$ model (SST $k-\omega$) [16].

The performance of the SST $k-\omega$ model is superior in adverse pressure gradient flows, free shear flows and zero pressure gradient flows. It is used frequently for general purpose CFD problems. This study uses the SST $k-\omega$ model for solution of RANS equations using the commercial software STAR-CCM+ V12. The default parameters for the turbulence model provided by STAR-CCM+ have been used.

3.2.2 Near Wall Modeling

Walls are a source of shear and vorticity in the flow. The no-slip boundary condition imposes high sear in the velocity and its effect on the velocity must be captured by the model. The region close to the wall can be divided into different sub-layers. A non-dimensional wall distance can be defined to characterize each sublayer. This non-dimensional wall distance is referred to as y *plus*, and denoted as y^+.

$$y^+ = \frac{u_\tau y}{\nu} \tag{3.5}$$

Where u_τ is the friction velocity, y is the nearest wall distance, and ν is the kinematic viscosity.

Very close to the wall is the *viscous sub-layer*. In this layer, viscous effects dominate the flow. The fluid velocity at the solid no-slip surface is zero. Turbulent eddying motions can not exist close to the wall. This layer is very thin ($y^+ < 5$) [19]. In the layer outside the viscous sub-layer ($30 < y^+ < 300$) turbulent (Reynolds) stresses dominate. This layer is called the *log-law layer* [19]. There is a *buffer layer* ($5 < y^+ < 30$) between the viscous sub-layer and the log-law layer. In this region, both viscous and Reynolds stresses are of similar magnitude [19].

It is very important to capture the effects of viscous and inertial forces in these regions.

The physical transport in these regions occurs on a much smaller scale compared to other length scales in the flow. This requires having a high resolution mesh in these regions for an accurate solution.

The flow in these regions can be modeled using two different approaches. One method is to completely resolve the viscous sub-layer. This approach is known as "near-wall modeling" approach or "low-y^+" approach. The mesh resolution required is very high. This method is computationally very expensive. The other approach is to use wall-functions to model the viscous sub-layer and the buffer layer. Here, these two regions are not resolved and modeled using the wall-functions. This method is called the "wall-function" approach or "high-y^+" approach. For this approach, the mesh resolution required for accurate capturing of the wall flow dynamics with the models is y^+ in the range: $30 < y^+ < 300$. In this study the "high-y^+" approach has been used.

3.2.3 Discrete Element Method

The discrete element method (DEM) was established by Cundall and Strack [2] and is an extension of Lagrangian modeling methodology to include dense particle flows. Lagrangian multiphase models are used to design and track the flow path of dispersed particles in a continuous phase [6]. A Lagrangian frame of reference describes the path of the particles as they traverse the domain. Equations of motion are written for each individual particle. Individual particles are not resolved on the Eulerian field but the interaction of the phases are modeled [6].

The interaction between the Lagrangian and the Eulerian phase can be modeled in two ways. In the first method, the Eulerian phase parameters are not affected by the presence of the Lagrangian phase. This is called "One-way Coupling". In the other method, each phase has an influence on the other. This method is called "Two-way Coupling". In the current study, One-way coupling is used.

STAR-CCM+ uses Lagrangian-Eulerian approach where the conservation equations for the

dispersed phase are written for individual particle in Lagrangian form allowing tracking of each particle. The conservation equations for the continuous phase are written in Eulerian form and are modified to take into account the presence of the dispersed phase [6].

In this study, the Haider and Levenspiel drag force model is used to model the drag force on the particles. This method is used for non-spherical particles. The drag coefficient in this model depends on the particle Reynolds number and the particle sphericity [6]

$$C_d = \frac{24}{Re_p}(1 + ARe_p^B) + \frac{C}{1 + \frac{D}{Re_p}} \tag{3.6}$$

where ϕ is the particle sphericity and:

$$A = 8.1716e^{-4.0655\phi}$$

$$B = 0.0964 + 0.5565\phi$$

$$C = 73.690e^{5.0746\phi}$$

$$D = 5.3780e^{6.2122\phi}$$

STAR-CCM+ uses multiple sphere shapes to represent non-spherical shapes. The DEM model used is based on classical mechanics based on soft-particle formulation where particles are allowed to overlap [5]. The contact force is proportional to the overlap, and the material and geometric properties of the particle. The contact force model is based on the spring-dashpot model. The repulsive force pushing the particles apart is generated by the spring, and the viscous damping is represented by the dashpot. Contact forces are modeled using the Hertz Mindlin No-slip contact model [5]. This model is a variant of the non-linear spring-dashpot model. This model was found to be computationally efficient [5]. In this study, as the particle-particle and particle-wall collisions are not expected to be perfectly elastic and linear, this model is used. In addition to this, a rolling friction coefficient is applied, using the Rolling Resistance model provided by STAR-CCM+, to model any rolling motion of the particles.

The DEM model only simulates solid particles. STAR-CCM+ offers different types of solid particles like Spherical particles, Coarse Grain particles, Composite particles, Particle clumps, and Cylindrical particles. Of these, Composite particles are used in this study as the logs are non-spherical and half-cylinders. The composite particles model uses multiple spheres to represent a non-spherical shape. The spheres are joined together and fixed, and do not separate during simulation [3]. Model of the composite particles (logs) used for this study is shown in Figure 2.5. Using composite particles, various particle shapes can be created.

Interaction of particles with wall boundaries can be set using the phase boundary. The **DEM Mode** option in the phase boundary models the interaction such that the particles contact and rebound off the boundary. The **Boundary Properties** specify the material properties at the boundary. These properties influence how particle-boundary interactions behave. In this study, the material properties of oak wood are specified: $\rho_{wood} = 600kg/m^3$. The Young's modulus has been set to $1e10^9\ Pa$ to reduce the numerical stiffness. Thanks to this approximate value of Young's modulus, it was sufficient to resolve the motion in 20,000 DEM time sub-steps. Increasing the value of Young's modulus beyond this value led to high numerical stiffness and the logs did not move after being injected. In this study, logs are sequentially injected from each location. The injection times are adjusted to avoid logs getting piled up on the RDDP.

Particles are injected at positions specified by the user. The injection velocity, particle diameter, particle orientation, flow rate, and position can be specified.

3.3 Evaluation Parameters

The simulations in this study are conducted using STAR-CCM+ V12. The governing equations are solved using a cell-centered control-volume space discretization method. Implicit unsteady solver is used. A time step of $5e^{-4}\ s$ is used, as it was found to be a good compromise of stability and accuracy with numerical cost for this study, through a temporal time-step independence analysis. For the DEM solver, a collision time scale of 0.2 is used to

Table 3.1: Evaluation parameters

STAR-CCM+ Solver Settings	
Turbulent Model	SST (Menter) $k-\omega$
Convection Scheme	Second Order
Transient Formulation	Implicit Unsteady Second Order
Flow Model	Segregated
Gradient Method	Hybrid Gauss-LSQ
Limiter Method	Venkatakrishnan
Relaxation Scheme	Gauss-Seidel
$k-\omega$ Turbulence Under-relaxation Factor	0.8
$k-\omega$ Turbulent Viscosity Under-relaxation Factor	1
Pressure Under-relations Factor	0.2
Velocity Under-relaxation Factor	0.8

resolve the motion of the particles. Other solver parameters are given in table 3.1

Chapter 4

RESULTS AND DISCUSSION

4.1 Flow field analysis

Prior to the main focus of the study: the analisys of the floating logs trajectories and forces, the flow field is described and analyzed. The flow field was simulated in STAR-CCM+ with the flow field settings discussed in Chapter 3. River flow was simulated for 20 s of physical time.

The velocity magnitude is described via contour plots on a plane that passes through the center of the submerged part of the RDDP, as shown in Figure 4.1. The flow decelerates as it approaches the RDDP and then accelerates around the RDDP sweep. Water flows below the sweep and the first section of the RDDP, emerging behind it. There is a flow separation region behind the sweep and the pontoons as the upwelling flow comes from underneath and leaves a recirculating bubble in the proximity of the inner wall. The velocity recovers behind the sweep. The corresponding pressure field is shown in Figure 4.2. There is a stagnation point right in front of the RDDP sweep as expected. Flow is brought to a complete stop here, raising the static pressure to its maximum possible value on the water surface (representing the rise in water height above the mean water level that would happen in reality, not captured here because the water surface is assumed flat and fixed at its mean level.

Vortices are shed from this region as shown in Figure 4.4. Vorticity can also be seen to accumulate along the boundary later growing on RDDP pontoons upstream walls. Periodic vortices are being shed downstream from the pontoons, as the blunt trailing edge leads to separated flow and the vorticity created along the boundary layer rolls onto itself in that adverse pressure gradient region. The vortices diffuse far behind RDDP. Fast-Fourier transform of the velocity signal behind RDDP show the leading vortex shedding frequency of

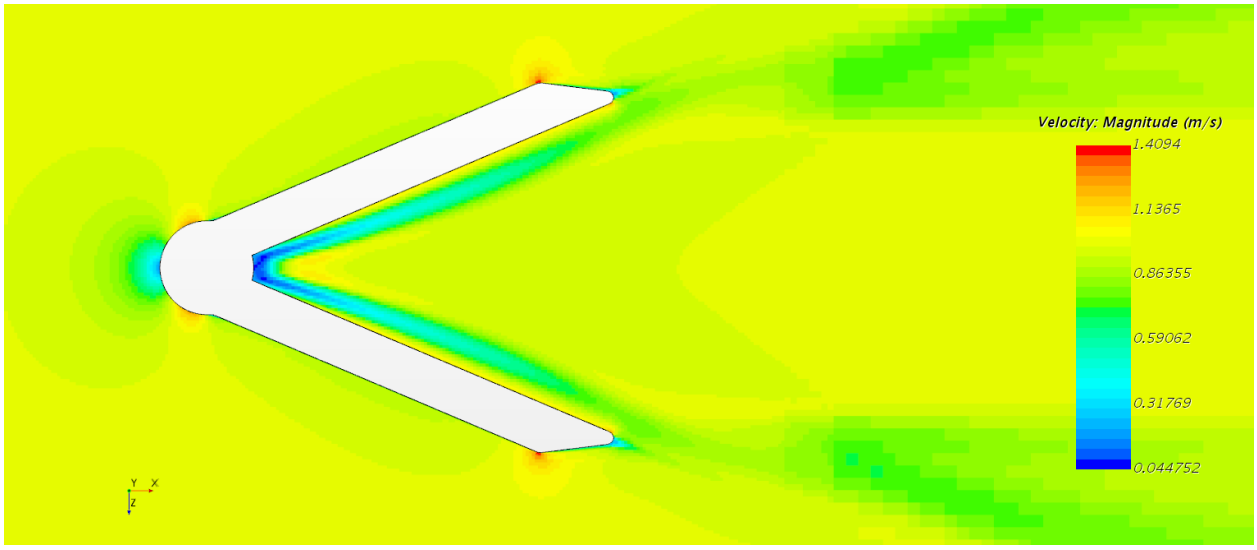

Figure 4.1: Velocity Magnitude Contour on a section that passes through the center of RDDP.

0.6 Hz in Figure 4.5. From the movie visualizing show the vortices being shed every 1.6667 s. The Strouhal number for this flow is 0.32.

Presence of vortices can also be observed in the streamlines around the RDDP (shown in Figure 4.6). The streamlines are seeded at the inlet from points on a horizontal plane that passes through the center of RDDP, at mid-depth. The streamlines are colored by velocity magnitude. Some streamlines go below the RDDP pontoons and start to swirl up as soon as they cross under. Figure 4.7 shows the same phenomenon from a different perspective. Swirling up of the streamlines can be clearly seen. Figure 4.8 shows this in top view.

The flow field near the RDDP very close to the top of the domain (the water surface) is slightly different from that at the mid-depth of the RDDP. Water doesn't go below RDDP pontoons and curl up. The streamlines can be seen in Figure 4.9. Water accelerates as it flows horizontally around the sweep and then along the pontoons as seen in Figure 4.10.

Streamlines along the RDDP surface are shown in Figure 4.11. This surface is a projection of

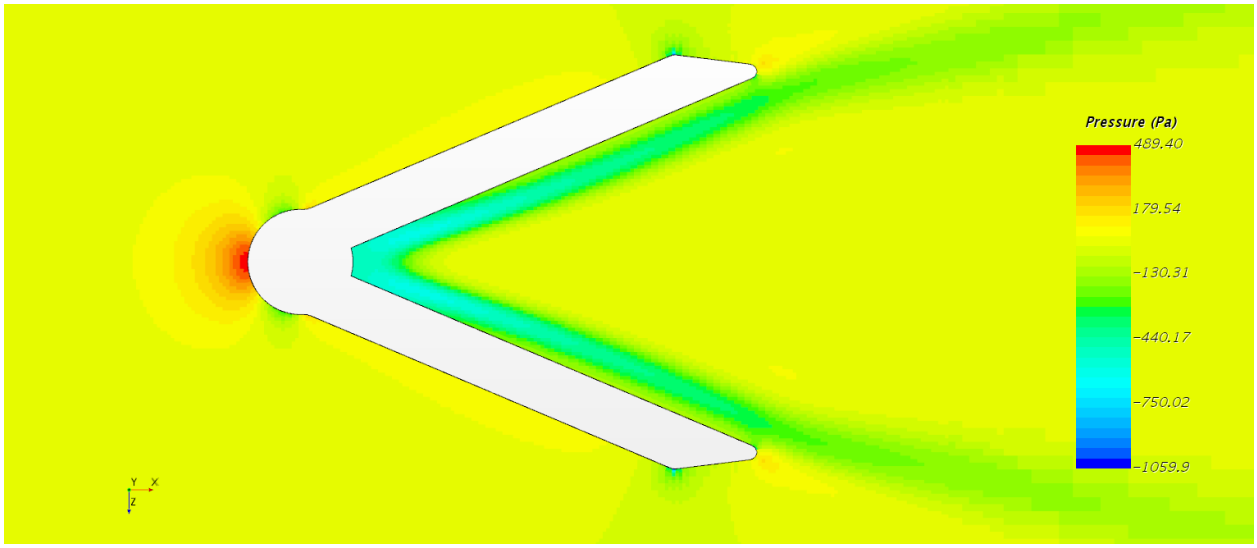

Figure 4.2: Pressure field on a section that passes through the center of RDDP.

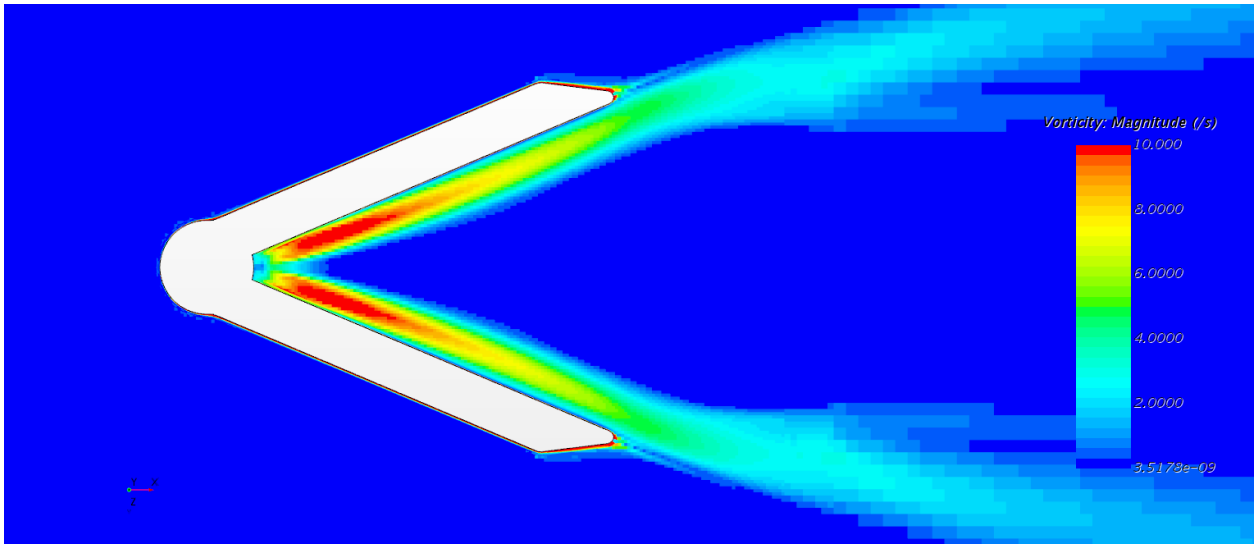

Figure 4.3: Vorticity Magnitude Contour on a section that passes through the center of RDDP.

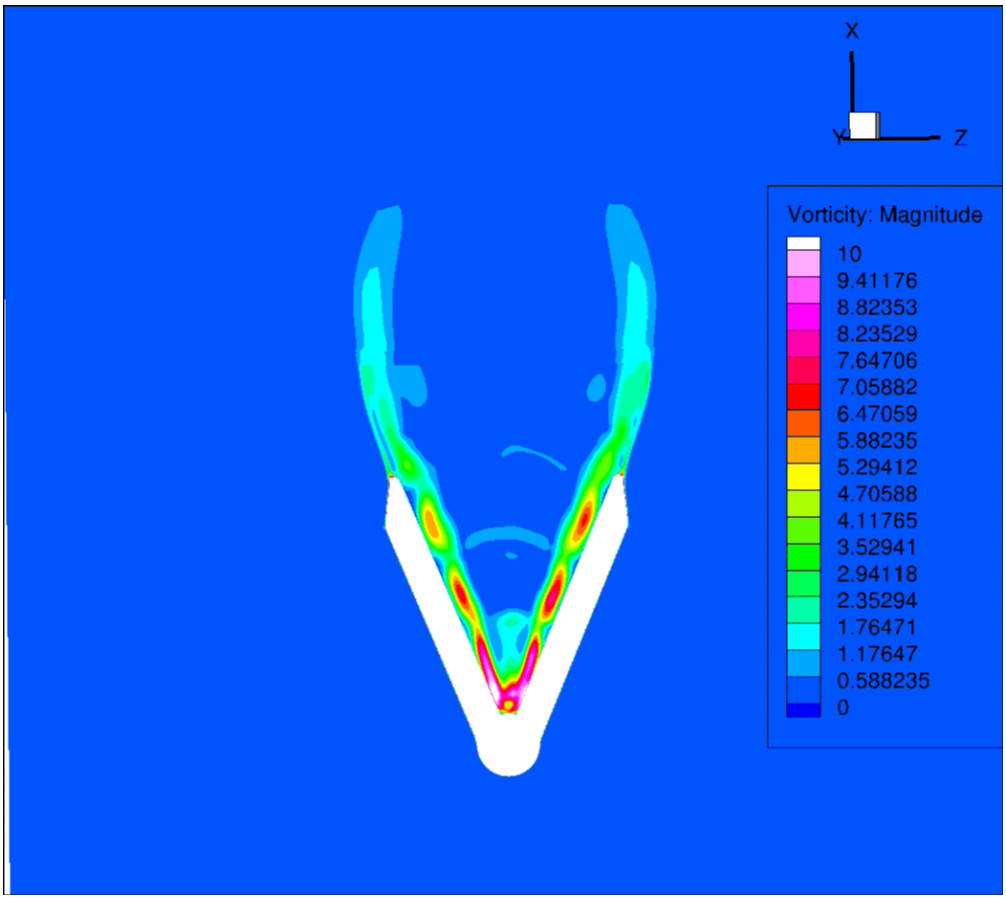

Figure 4.4: Vortices being shed from behind RDDP sweep.

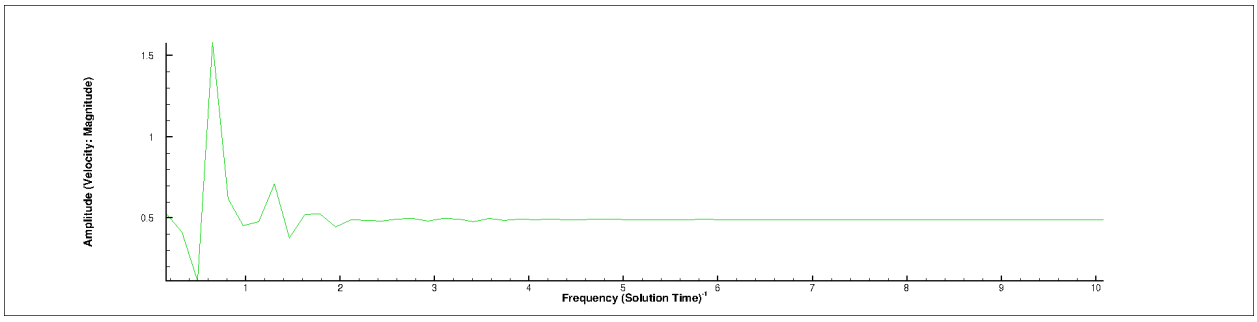

Figure 4.5: FFT analysis of velocity magnitude behind RDDP to obtain vortex shedding frequency.

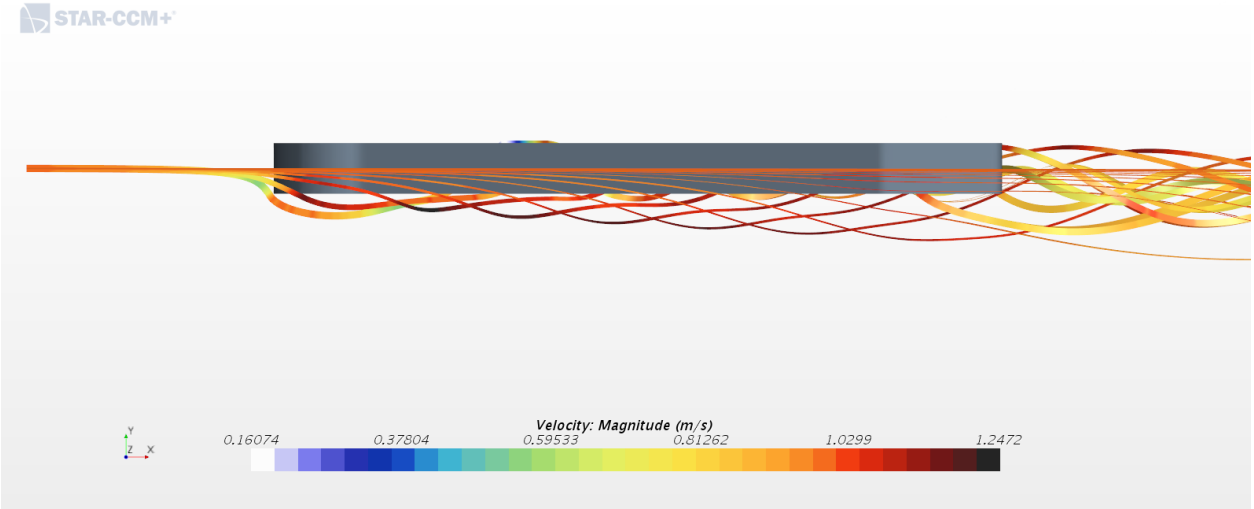

Figure 4.6: Streamlines around RDDP. Streamlines are originating from points on a section that passes through the center of RDDP.

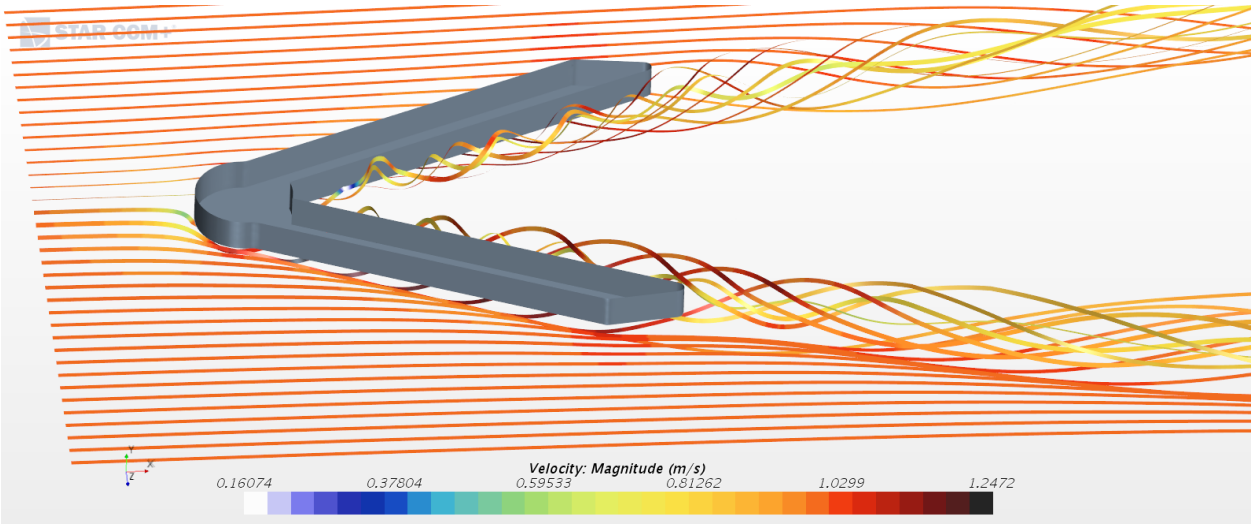

Figure 4.7: Streamlines around RDDP. Streamlines are originating from points on a section that passes through the center of RDDP.

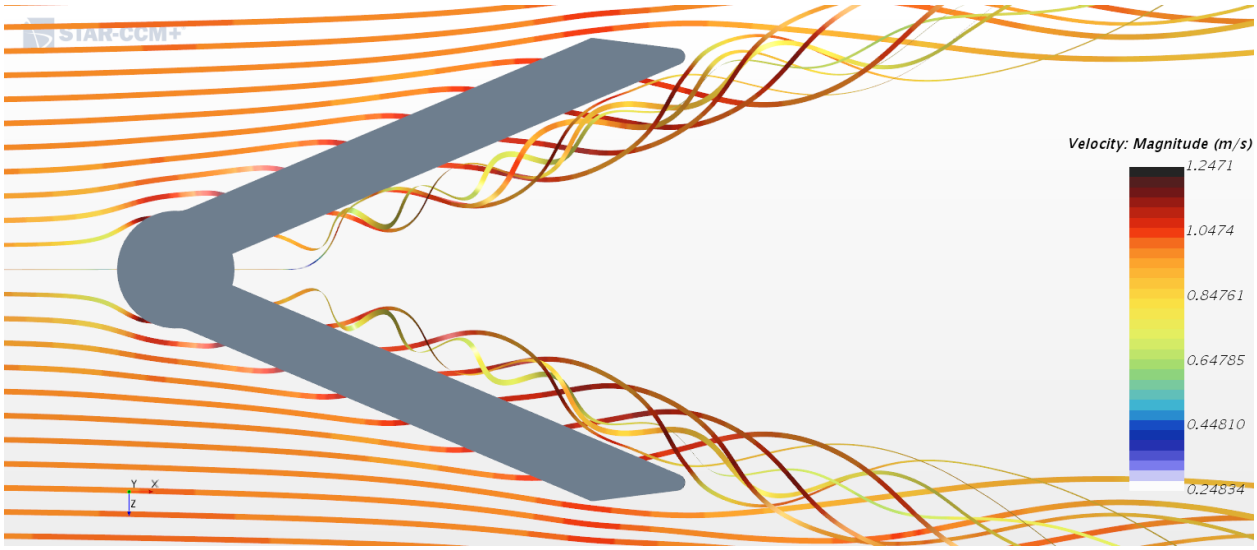

Figure 4.8: Streamlines around RDDP. Streamlines are originating from points on a section that passes through the center of RDDP.

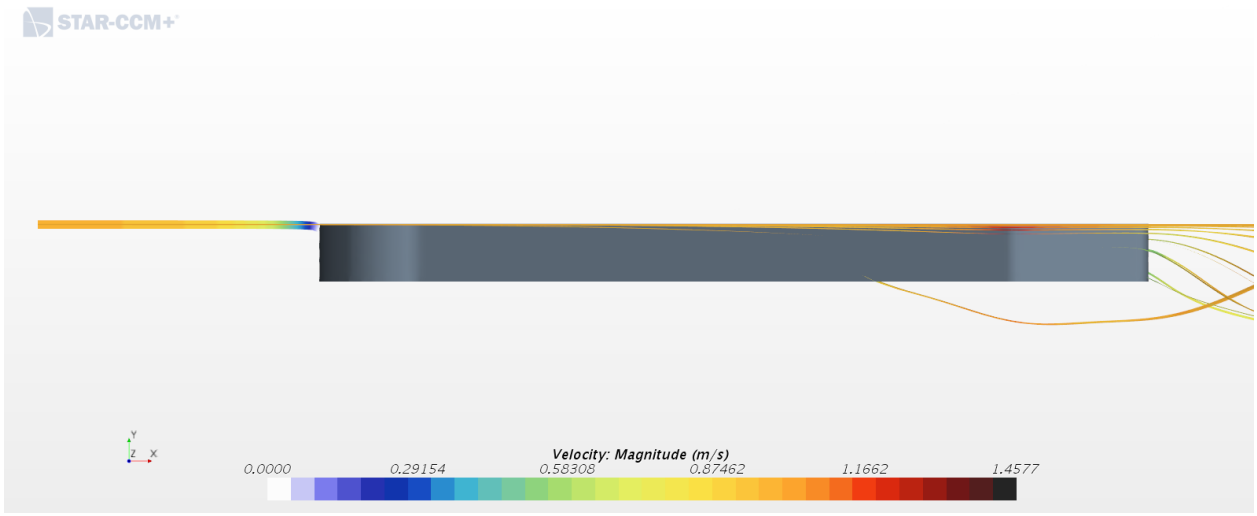

Figure 4.9: Streamlines around RDDP very close to top of the domain.

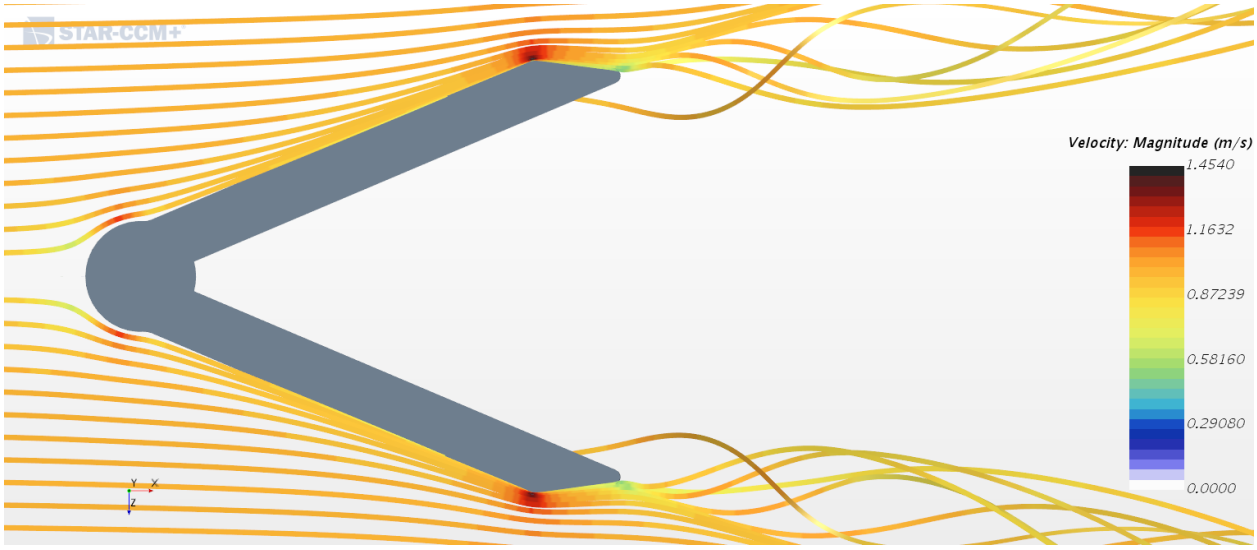

Figure 4.10: Streamlines around RDDP very close to top of the domain.

the RDDP wall offset 0.05 m from the actual immersed boundary. Streamlines flow around the pontoons and only a few of them submerge, passing underneath them. A recirculation zone can be seen at the bottom of the RDDP. Water recirculates there and then emerges from behind the sweep.

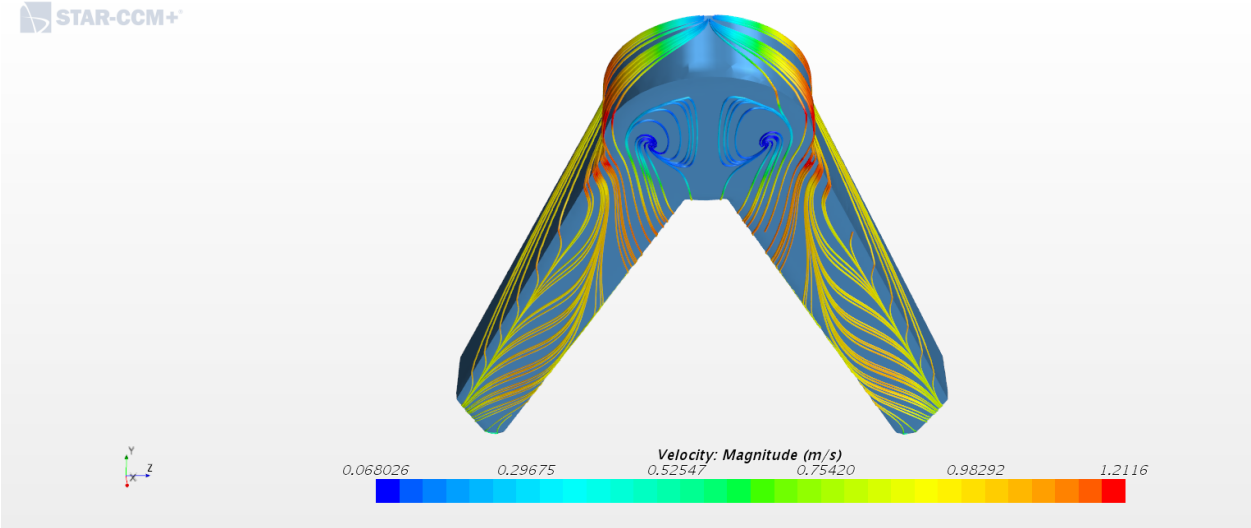

Figure 4.11: Streamlines on an iso-surface of RDDP.

4.2 Analysis of impact of logs on RDDP

Impact of logs (debris) on the RDDP was simulated by the DEM model in STAR-CCM+, with the settings described in the previous chapter. Two sizes of logs (maintaining volume constant) were used in the analysis. The lengths values were 1 m and 2 m, with the log radius modified accordingly to maintain constant mass. For simplicity in the presentation of the results, the lengths have been non-dimensionalized by dividing the lengths by 2 m. The two cases thus are referred to as 0.5L (1 m case) and 1L (2 m case). In addition to changing the log length, the flow velocity has also been varied, with three values explored: 0.5 m/s, 1 m/s and 2 m/s. Analysis is done for these six combinations of log lengths and flow velocities as show in Table 4.1. The effects of log size and flow velocity on the forces on the RDDP are studied in the following.

The logs are injected into the flow from fifteen locations upstream of the RDDP, as shown in Figure 4.12. The logs shown are of Size 1L, for scale. The numbering is to identify the log injection positions. The color scale shows the distance from the centroids of the logs to

Table 4.1: Six combinations of log sizes and flow velocities of the analysis

V = 0.5 m/s, Size: 0.5L	V = 0.5 m/s, Size: 1L
V = 1.0 m/s, Size: 0.5L	V = 1.0 m/s, Size: 1L
V = 2.0 m/s, Size: 0.5L	V = 2.0 m/s, Size: 1L

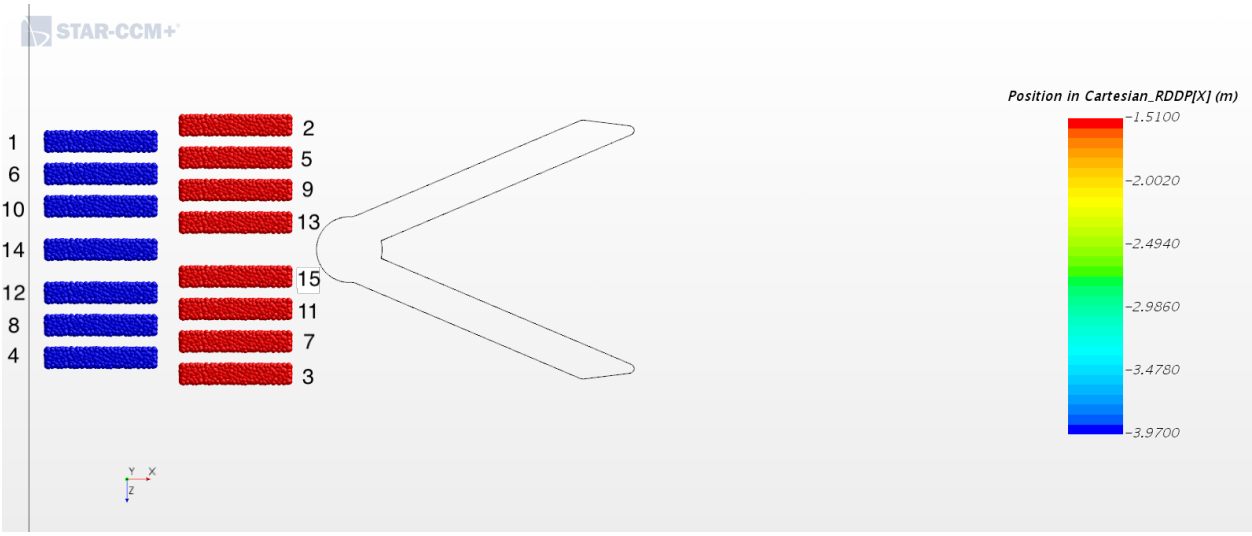

Figure 4.12: Positions of log injection.

front end of RDDP sweep. Henceforth, the logs will be labeled according to their injection position number indicated in Figure 4.12. The positions are chosen to represent the statistical variation range possible for logs interacting with the RDDP, while avoiding logs piling up on each other. Logs are injected in groups of four (a group of three for the last three logs) starting from logs 1, 2, 3, and 4. The log groups are injected at different times to avoid overlap.

4.2.1 Forces on RDDP

Forces on the RDDP due to impact of the logs are measured for every log and every condition in the study matrix. The magnitude of the force and each component are measured. A probability distribution function (PDF) for the force statistics is obtained for each condition. While analyzing the forces on RDDP, unusually high forces were recorded of the order of mega newtons. Acceleration due to such high force would be higher than 1000g, where g is the gravitational acceleration on Earth. This is clearly not realistic and is the result of a numerical error in the DEM model. The reason maybe the default recommended high DEM time scale parameter (time scale for calculating particle motion) of 0.2 With a high DEM time step, the trajectory of the logs is not fully resolved, which leads to higher acceleration of the logs than reasonably expected. This shows up as a high force being calculated by the DEM. These high forces have been filtered based on the log acceleration they would produce. Different filters have been applied for different flow velocities. For $V = 0.5\ m/s$, forces with acceleration greater than 1g are filtered. Forces greater than 1g in this case have a probability of nearly zero and thus the filter does not alter the statistics significantly. Since the force is expected to be proportional to the square of the flow velocity, according to a drag force with a constant drag coefficient at very large Reynolds numbers, the filtering for the higher river flow velocities has been applied as a quadratic ratio to the base case of $0.5\ m/s$. For $V = 1\ m/s$, the filter is 4g and for $V = 2\ m/s$, the filter is 16g. PDFs for each case are shown after applying the filters. The PDFs are then compared to study the effect of log size and flow velocity on the forces on the RDDP.

Effect of log size on the forces on the RDDP

The effect of log size on the forces on the RDDP are studied as follows: Two log sizes: 0.5L and 1L at three flow velocities were simulated. Figure 4.13 shows the comparison of the PDFs for force magnitude for different sizes when $V = 0.5\ m/s$. As the size increases, the

mean, median and max force increase. The probability of higher forces also increases with size.

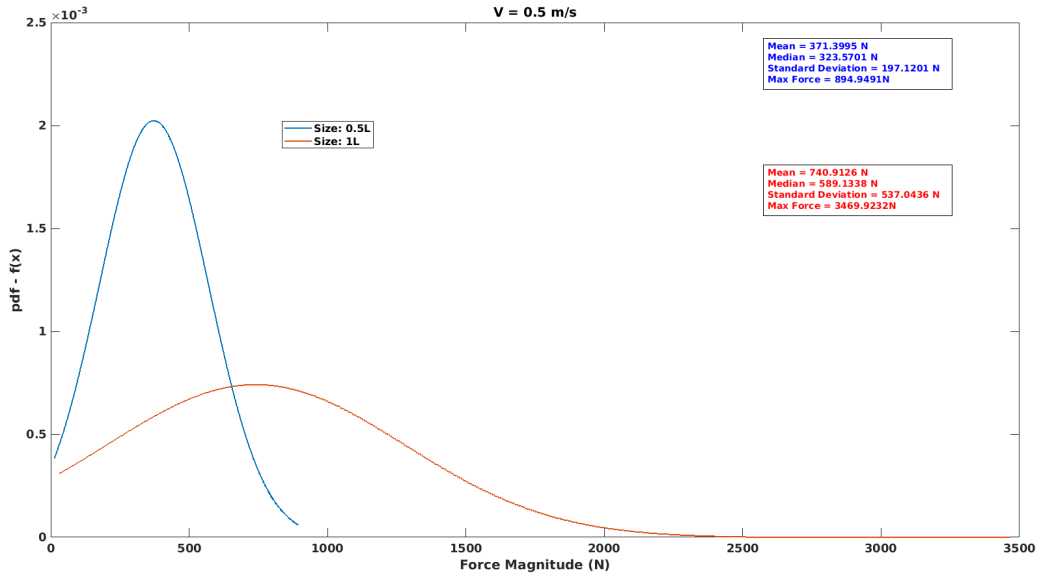

Figure 4.13: Comparison of PDFs of force magnitude for two sizes and $V = 0.5\ m/s$.

Figure 4.14 shows the effect of size on the forces on the RDDP for $V = 1\ m/s$. The probability of forces being around the mean is higher for the longer logs. The PDFs are similar to each other. The median and max force increase with size but the difference is not significant. The mean force is lower for the larger log size than for the smaller log, for this flow velocity.

Figure 4.15 shows the effect of log size on the forces on the RDDP for $V = 2\ m/s$. The distributions are very similar for both sizes. There is a slight variation between the mean, median and max forces.

Figures 4.16, 4.17, and 4.18 show, respectively, the variation of mean, median, and maximum force magnitude with log size for different velocities. The variation of mean, median, and maximum force magnitude is not significant between the two sizes. At low Reynolds numbers ($\mathrm{Re} < 10^6$), increasing the lengths of the logs increases the forces on the logs. At high

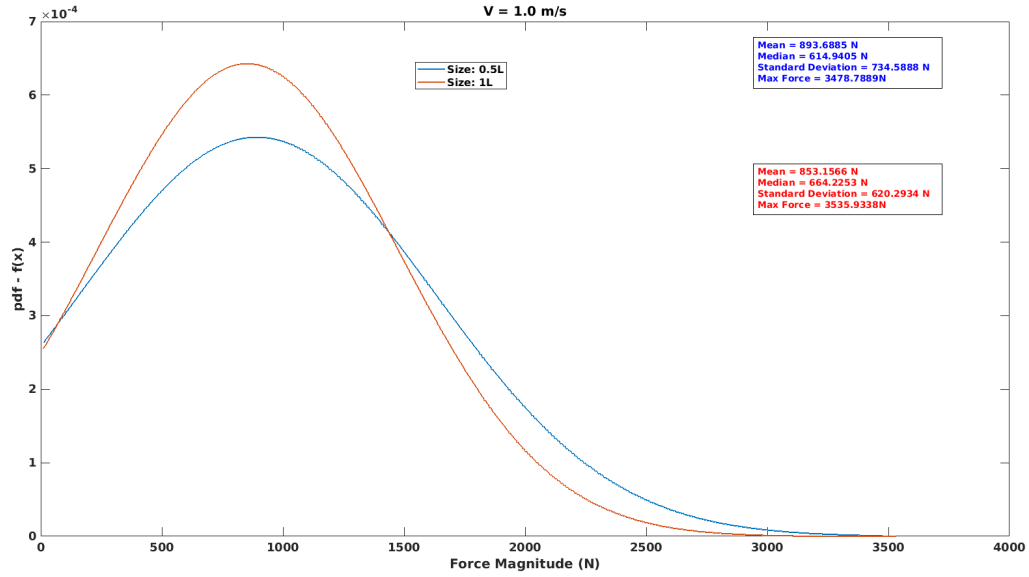

Figure 4.14: Comparison of PDFs of force magnitude for two sizes and $V = 1.0\ m/s$.

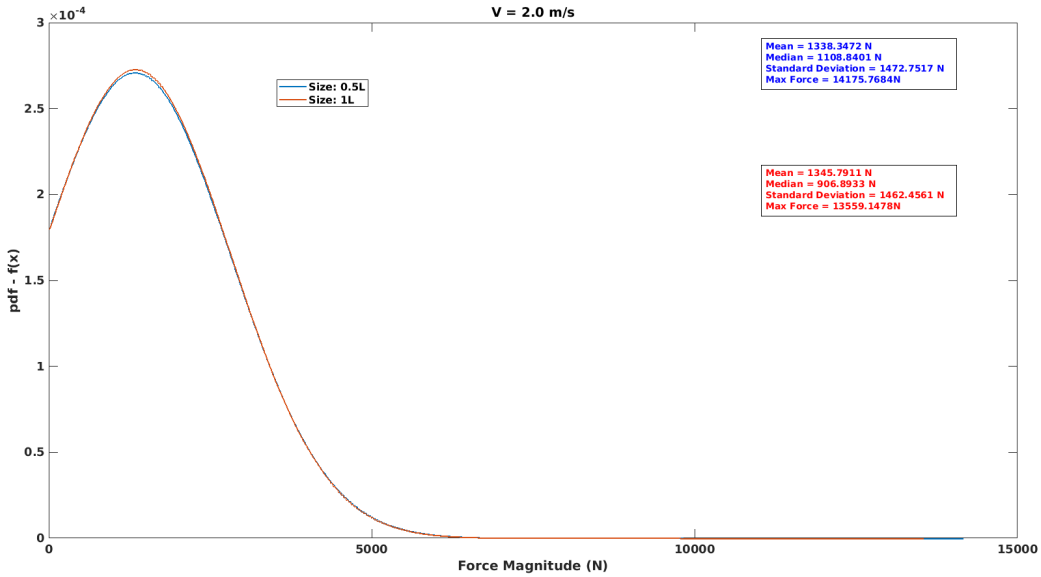

Figure 4.15: Comparison of PDFs of force magnitude for two sizes and $V = 2.0\ m/s$.

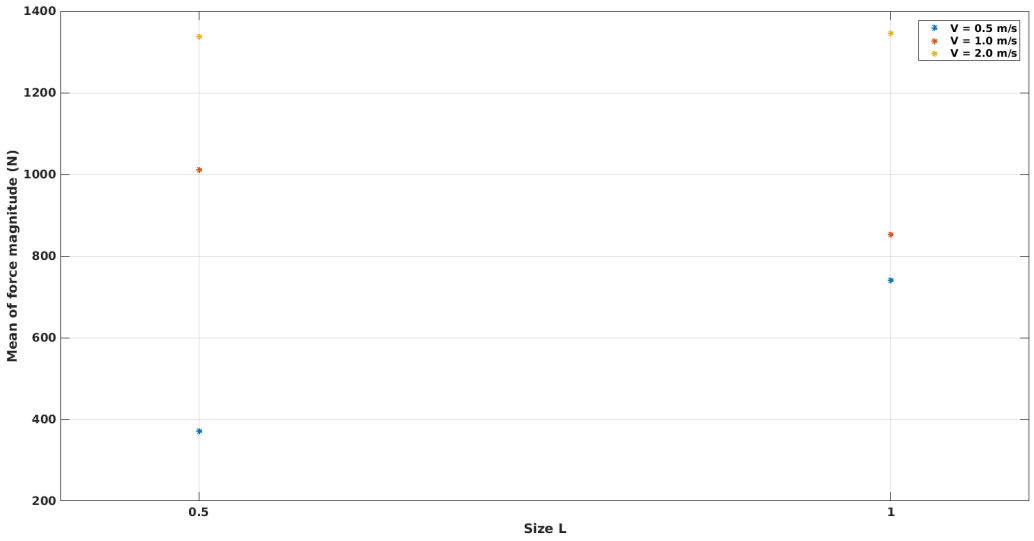

Figure 4.16: Variation of mean force magnitude with log size.

Reynolds numbers ($\mathrm{Re} > 10^6$), changing the lengths of the logs while maintaining the volume constant does not change, to first approximation, the forces on the RDDP. The effect of shape of the debris at these high Reynolds numbers, does not change the hydrodynamic interactions of the logs with the river flow, and thus the forces do not change significantly. The drag coefficient is independent of Reynolds number at such high Reynolds numbers.

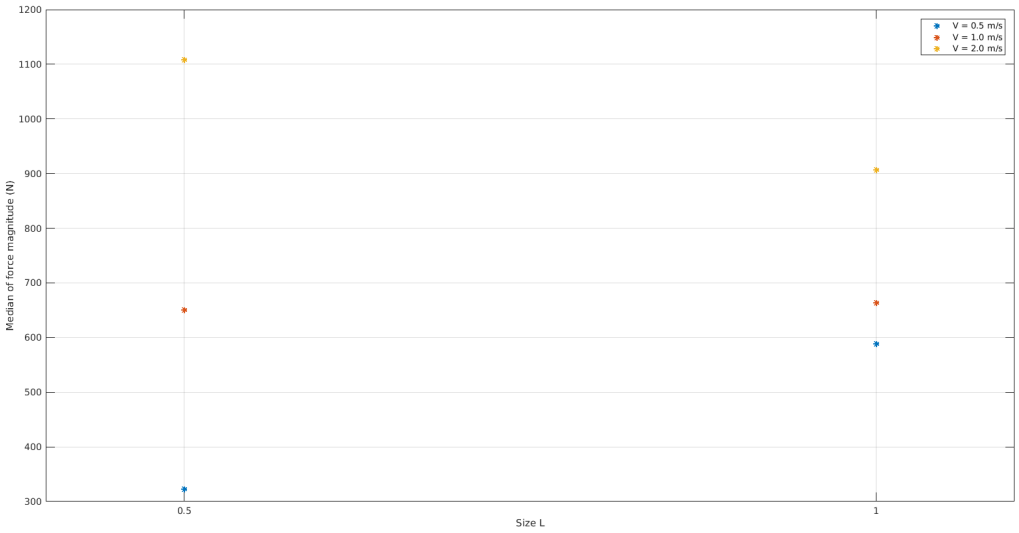

Figure 4.17: Variation of median force magnitude with log size.

Figure 4.18: Variation of maximum force magnitude with log size.

Effect of flow velocity on the forces on the RDDP

The effect of flow velocity on the forces on the RDDP are studied now. Flow velocities of 0.5 m/s, 1 m/s, and 2 m/s are used for this analysis.

Figure 4.19 shows the comparison of the PDFs of force magnitude for the three flow velocities with log size 0.5L. As the flow velocity increases, the probability of larger forces increases. The mean, median, and maximum of force magnitudes also increase. As the flow velocity increases, the momentum of the logs increases, and this influences the impact forces on the RDDP. The probability of smaller forces is higher for the low flow velocity, resulting in a narrower distribution with a much more marked mode at a lower force value. A similar behavior is seen for log size 1L, as shown in Figure 4.20.

Figures 4.21, 4.21, and 4.21 show, respectively, the variation of mean, median, and maximum force magnitude with flow velocity for different log sizes. As explained earlier, when the flow velocity increases, the momentum of the logs increases and so does the impact force. The variation is quadratic as it scales with the the kinetic energy (or the work that the force has to do on the collision to change the trajectory of the log). The mean, median, and maximum force magnitude increase similarly with increasing flow velocity for both log sizes.

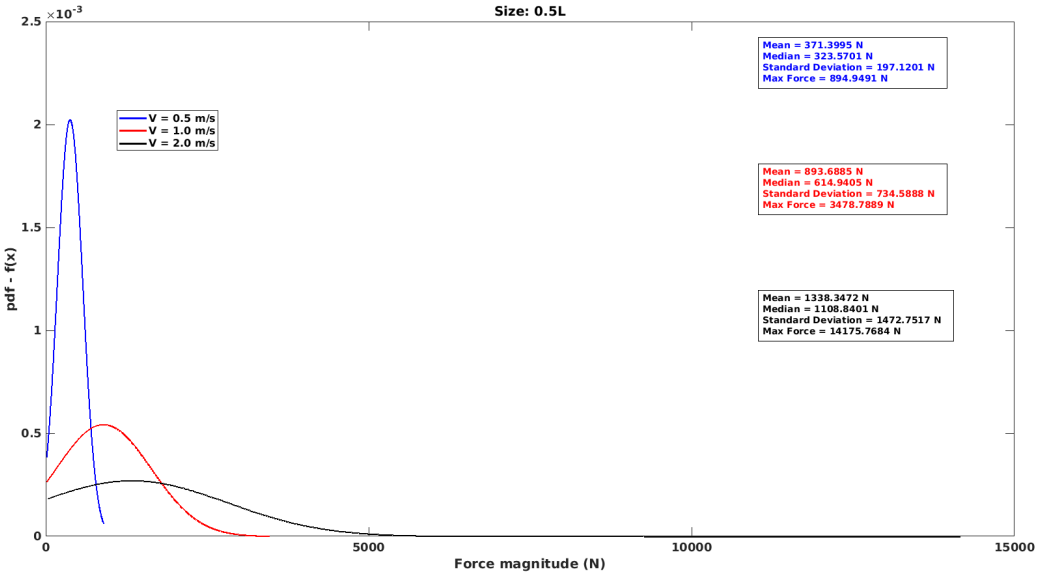

Figure 4.19: Comparison of PDFs of force magnitude for Three velocities with log size 0.5L.

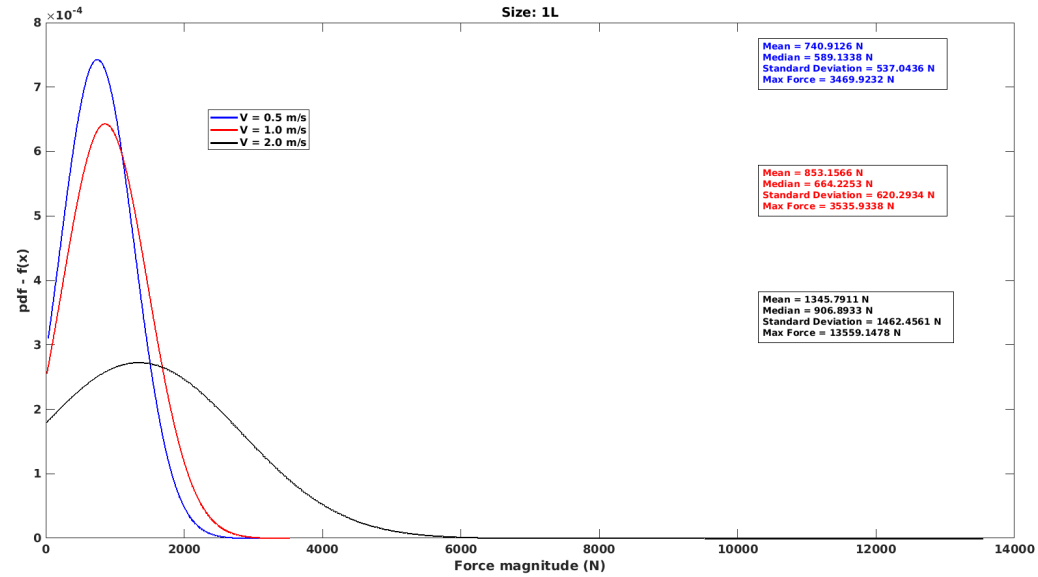

Figure 4.20: Comparison of PDFs of force magnitude for Three velocities with log size 1L.

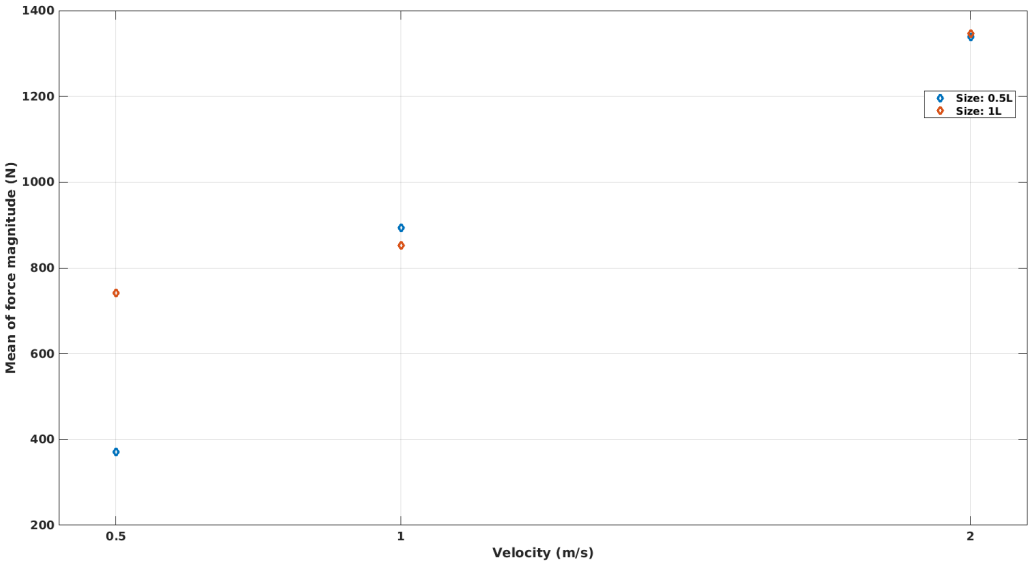

Figure 4.21: Variation of mean force magnitude with flow velocity.

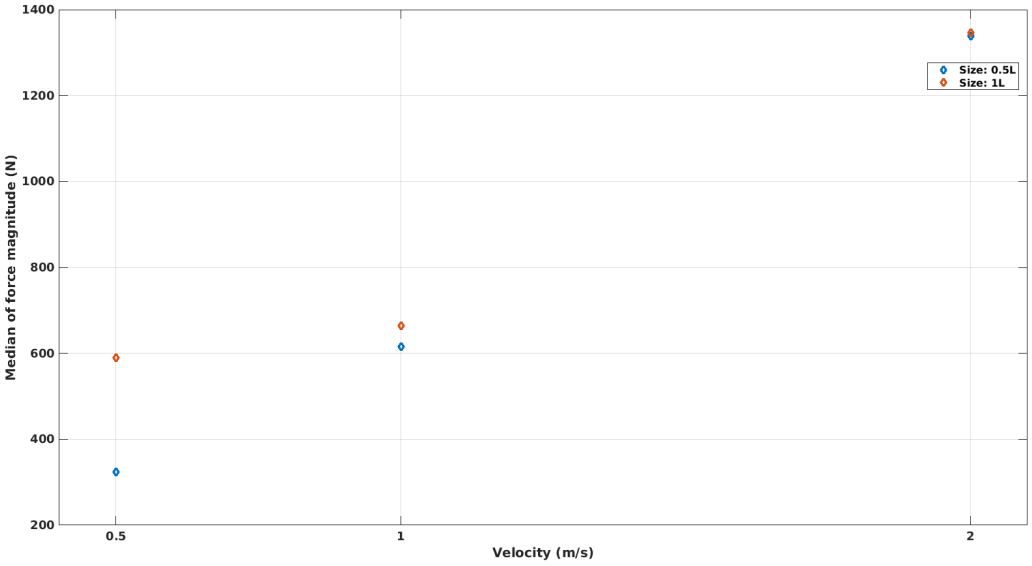

Figure 4.22: Variation of median force magnitude with flow velocity.

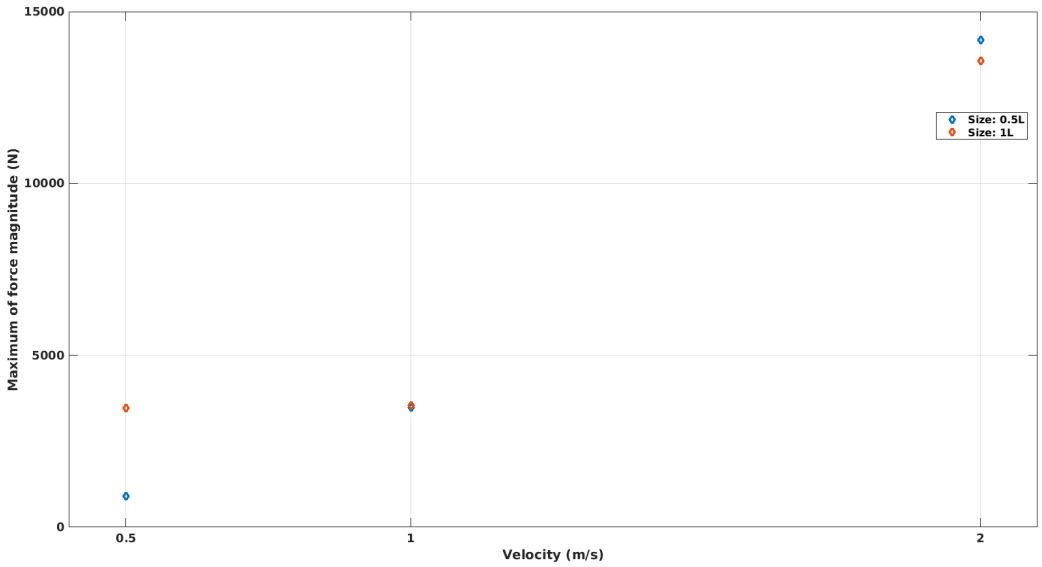

Figure 4.23: Variation of maximum force magnitude with flow velocity.

4.2.2 Forces on logs

The forces calculated on each log include the forces due to impact with the RDDP and the hydrodynamic forces. As shown above, the PDFs of the force distribution are obtained for each log, a combined PDF (ensemble) of force distribution for all logs in obtained and compared for different sizes and flow velocity. Only the forces during the interactions of the logs with the RDDP are considered. Analysis for each log is given in Appendix A

Effect of log size on the forces on the logs

Figure 4.24 shows the comparison of the combined PDFs of the force magnitude for different log sizes at flow velocity $V = 0.5\ m/s$. Logs have a higher probability of forces being around the mean for size 0.5L than that for size 1L. Logs of size 1L have higher probability of smaller-than-mean and larger-than-mean forces.

Figure 4.25 shows the comparison of the combined PDFs of the force magnitude for different

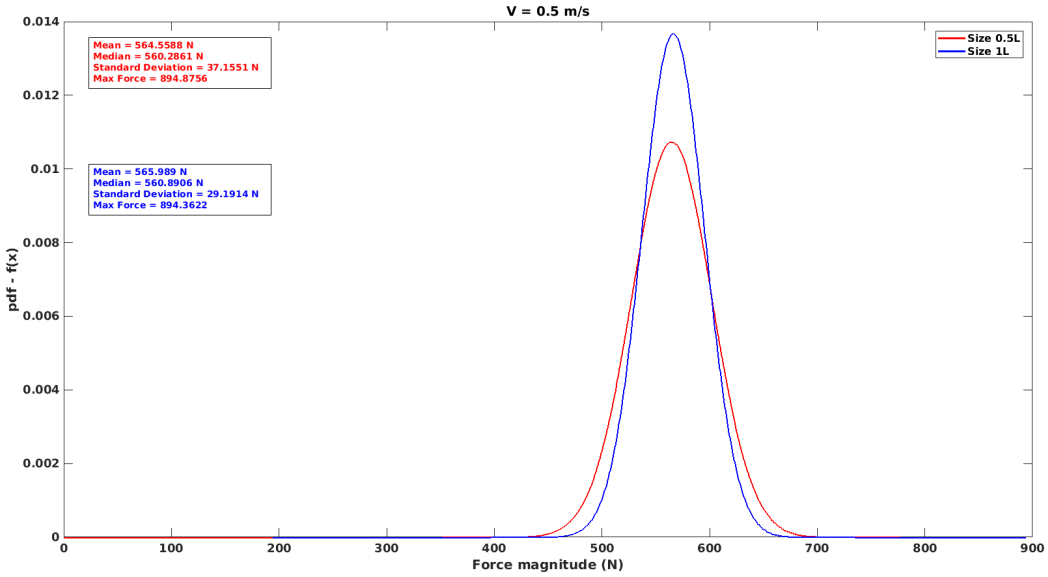

Figure 4.24: Compasrison of combined PDFs of the forces on the logs for different log sizes at $V = 0.5\ m/s$.

log sizes at flow velocity $V = 1.0\ m/s$. The PDFs are very similar to each other.

Figure 4.25 shows the comparison of the combined PDFs of the force magnitude for different log sizes at flow velocity $V = 1.0\ m/s$. The PDFs are very similar to each other with the exception that logs of size 0.5L have a slightly higher probability of forces being around the mean than logs of size 1L.

Figures 4.27, 4.28, and 4.29 show the variation of mean, median, and maximum force magnitude for different log sizes. Mean and maximum force magnitudes remain fairly constant. Median force magnitude increases for $V = 0.5\ m/s$ and $V = 1.0\ m/s$ but decreases for $V = 2\ m/s$.

The above results for variation of forces on the logs with log sizes show that the forces do not change significantly with log sizes at high Reynolds numbers since the drag coefficient is independent of Reynolds number at such high Reynolds numbers.

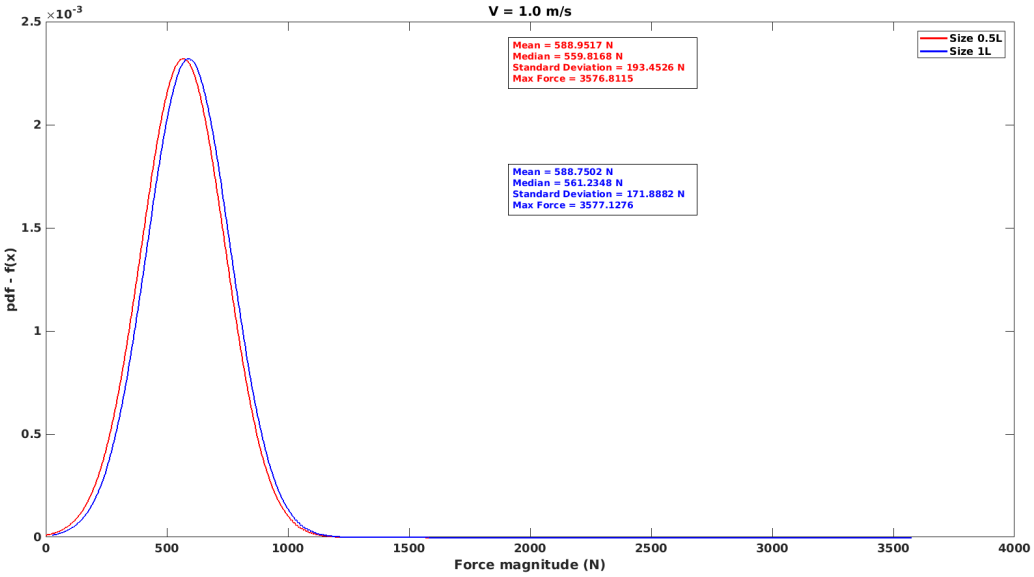

Figure 4.25: Compasrison of combined PDFs of the forces on the logs for different log sizes at $V = 0.5\ m/s$.

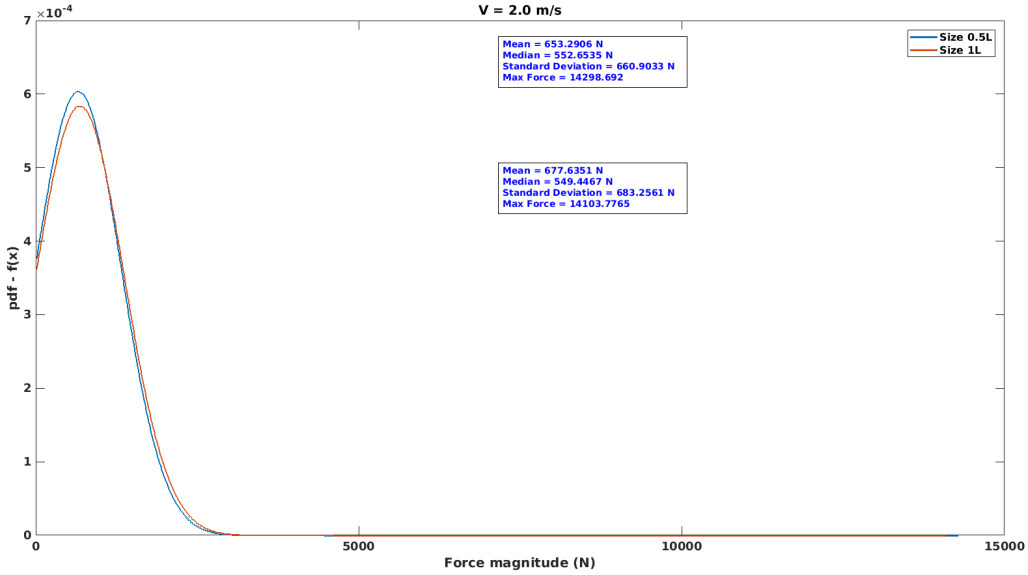

Figure 4.26: Compasrison of combined PDFs of the forces on the logs for different log sizes at $V = 0.5\ m/s$.

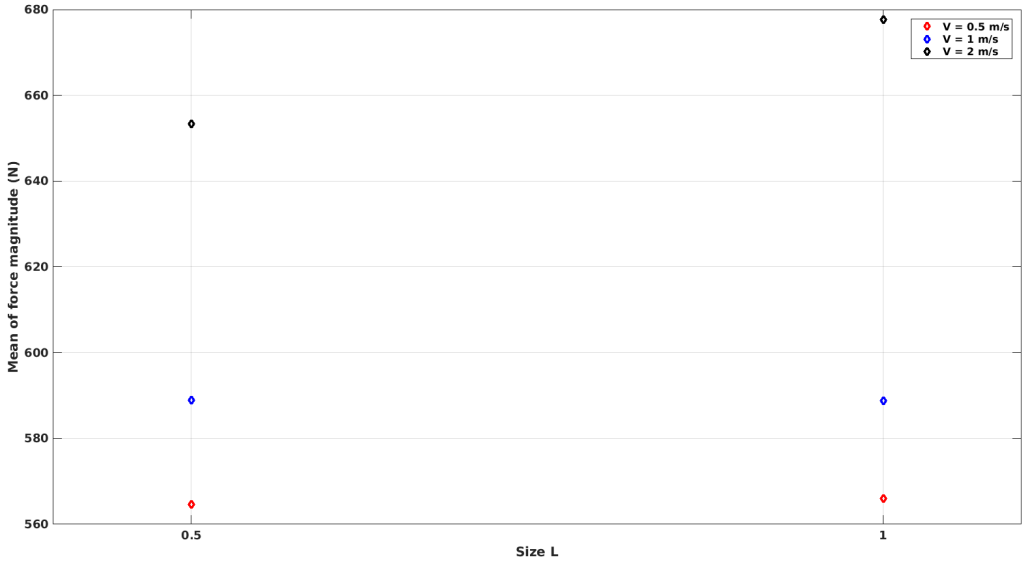

Figure 4.27: Variation of mean force magnitude with log sizes.

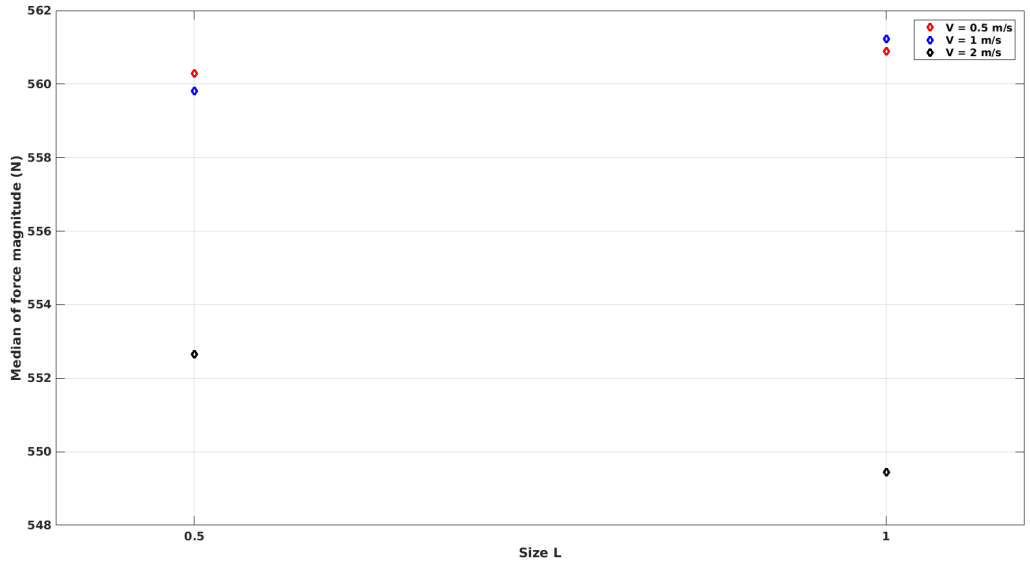

Figure 4.28: Variation of median force magnitude with log sizes.

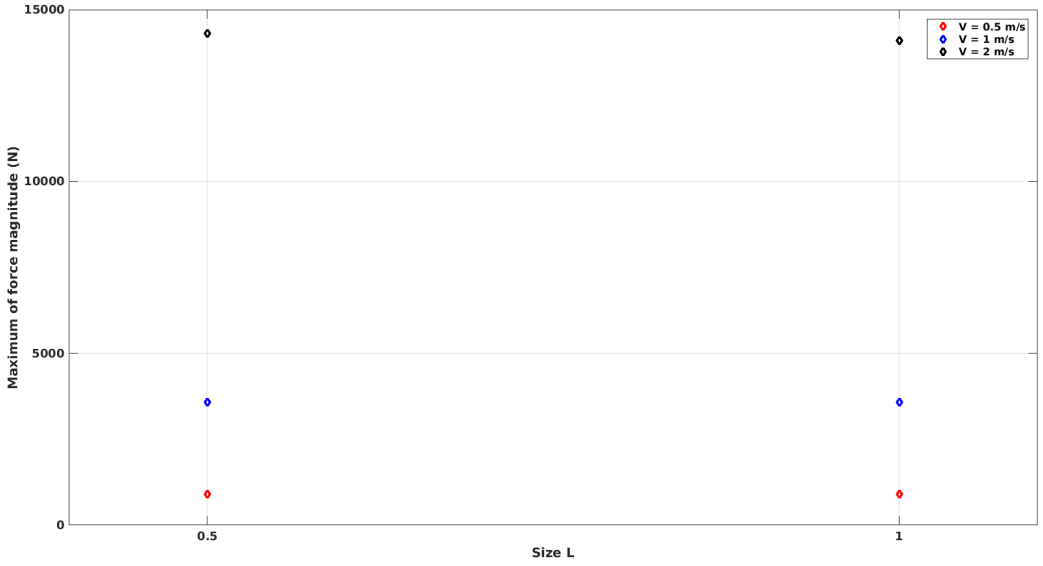

Figure 4.29: Variation of maximum force magnitude with log sizes.

Effect of flow velocity on the forces on the logs

Figures 4.30 and 4.31 shows the comparison of the combined PDFs of the force magnitude for different flow velocities at log sizes 0.5L and 1L respectively. As the flow velocity increases, the probability of higher forces on the logs increases. The momentum of the logs increases with velocity and therefore so does the impact force.

Figures 4.32, 4.33, 4.34 show variation of mean, median, and maximum force magnitude for different flow velocities respectively. The mean and median forces increase with the velocity. Median force decreases for logs of size 1L but increases and then decreases for logs of size 0.5L.

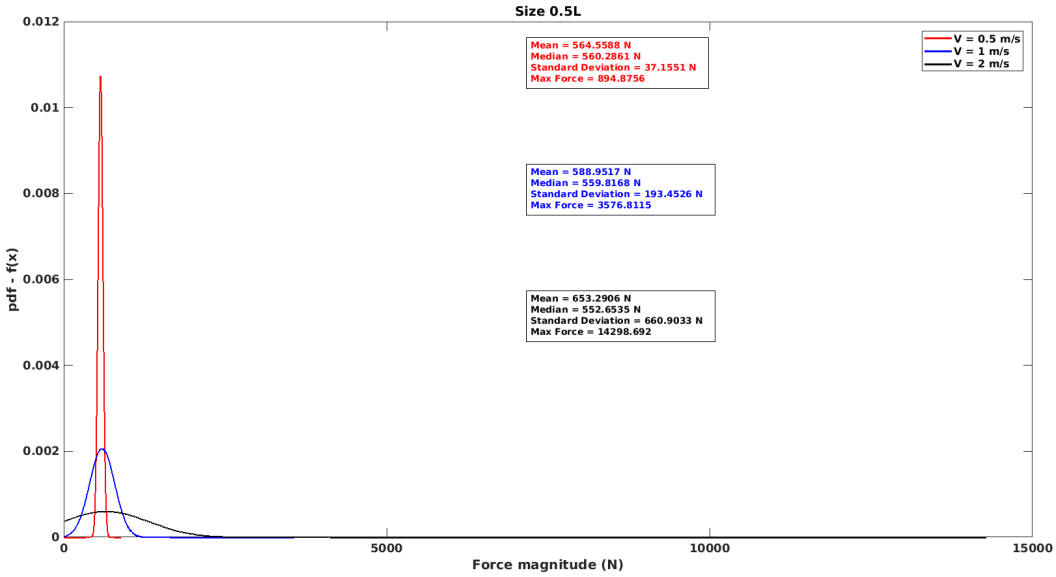

Figure 4.30: Compasrison of the combined PDFs of the forces on the logs for different flow velocities at log size 0.5L.

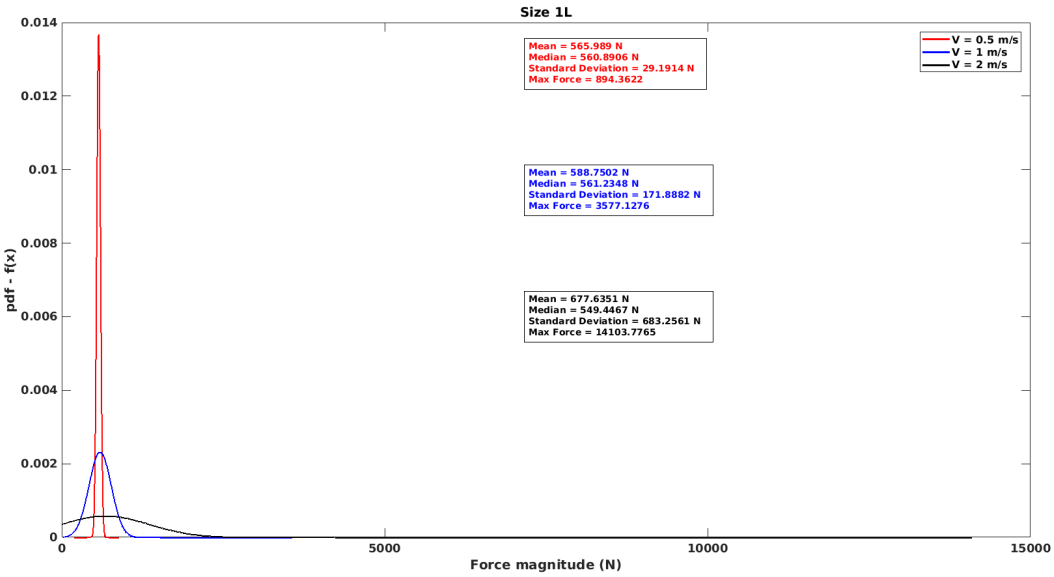

Figure 4.31: Compasrison of the combined PDFs of the forces on the logs for different flow velocities at log size 1L.

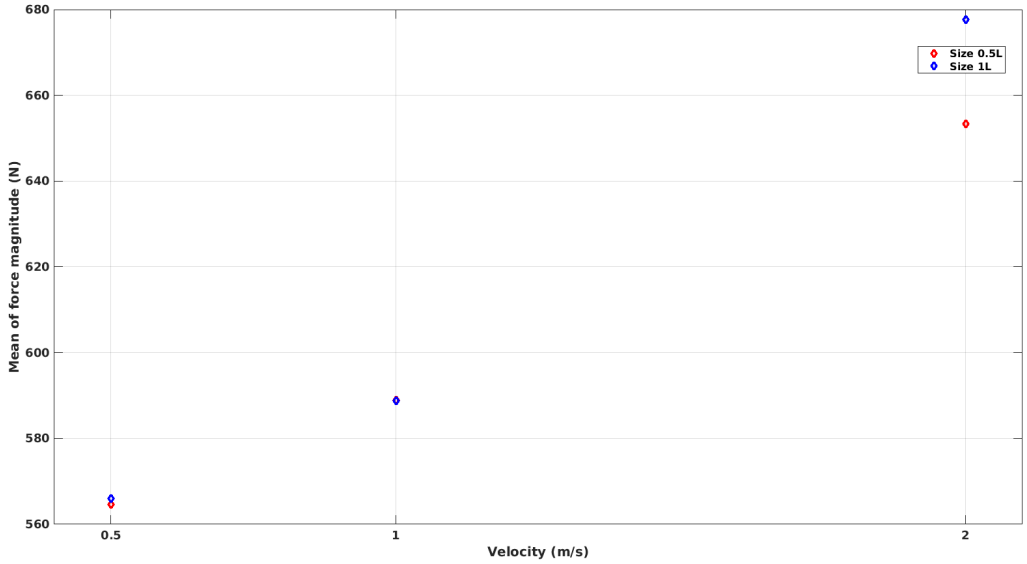

Figure 4.32: Variation of mean force magnitude with flow velocity.

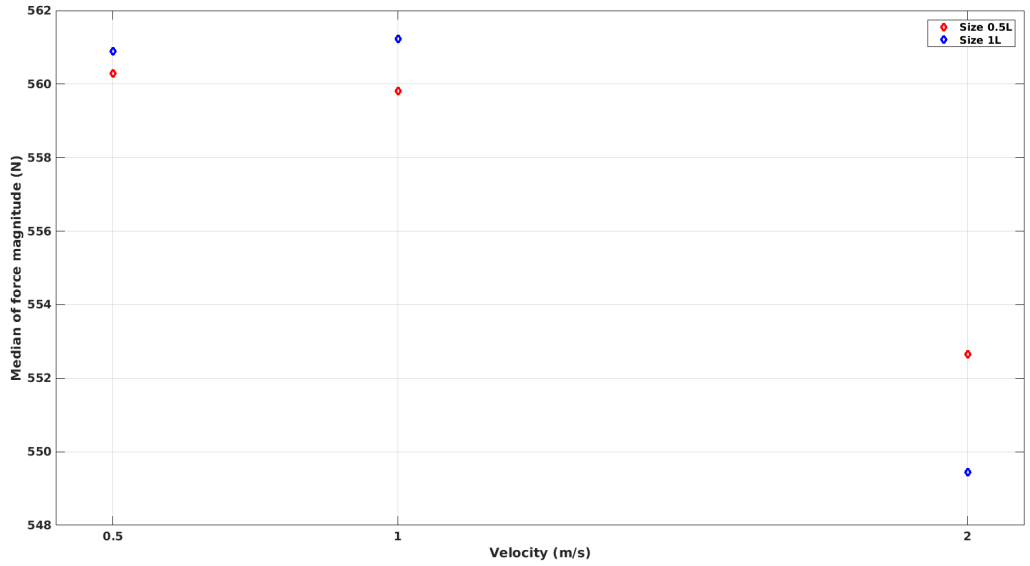

Figure 4.33: Variation of median force magnitude with flow velocity.

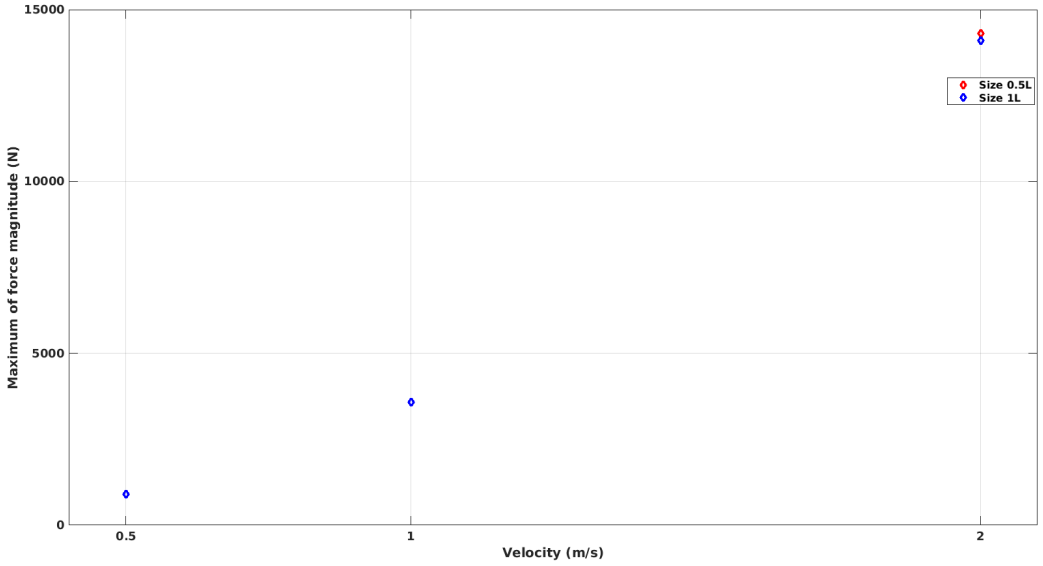

Figure 4.34: Variation of maximum force magnitude with flow velocity.

4.3 Interesting results

4.3.1 Log positions and velocities

Apart from measuring forces on the RDDP and logs, the position and velocities of the logs are also computed throughout the flow domain. Figure 4.35 shows the position along the flow direction and the corresponding force magnitude on Log6 as a function of time, for the case: $V = 1\ m/s$ and Size 1L. Figure 4.36 shows the same information but the position is in the cross-flow direction. Using this information, the position of the log when in contact with the RDDP can be identified. This information can be further used to analyze how the log interacts with the length of the RDDP and which part of RDDP experiences maximum force that can cause structural damage or repeated force that can cause fatigue failure. Figure 4.37 shows the velocity and force magnitudes as a function of time for the same case.

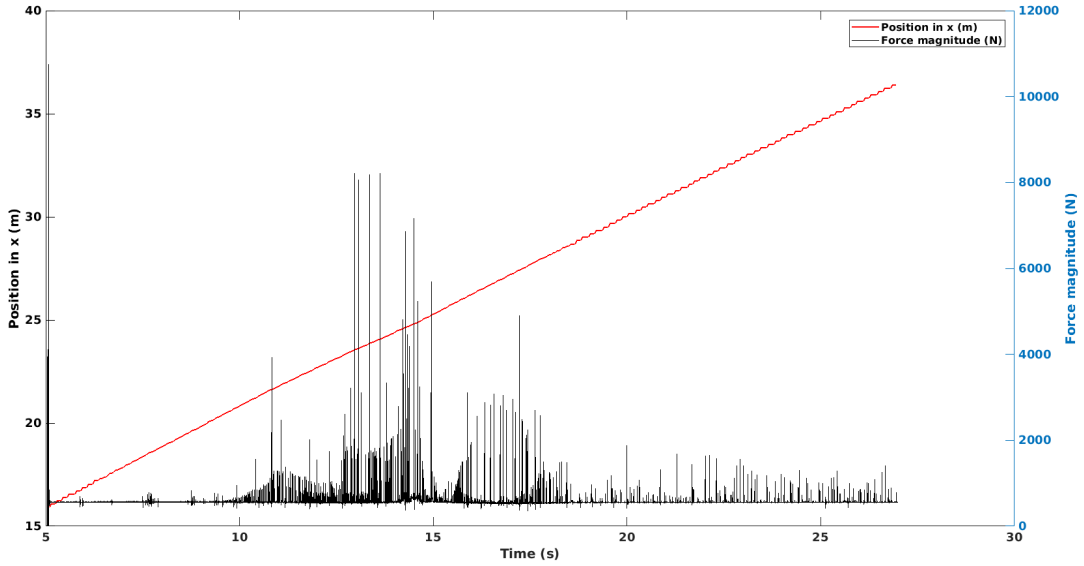

Figure 4.35: Position in flow direction and corresponding force magnitude of Log6 for the case: $V = 1\ m/s$ and Size 1L.

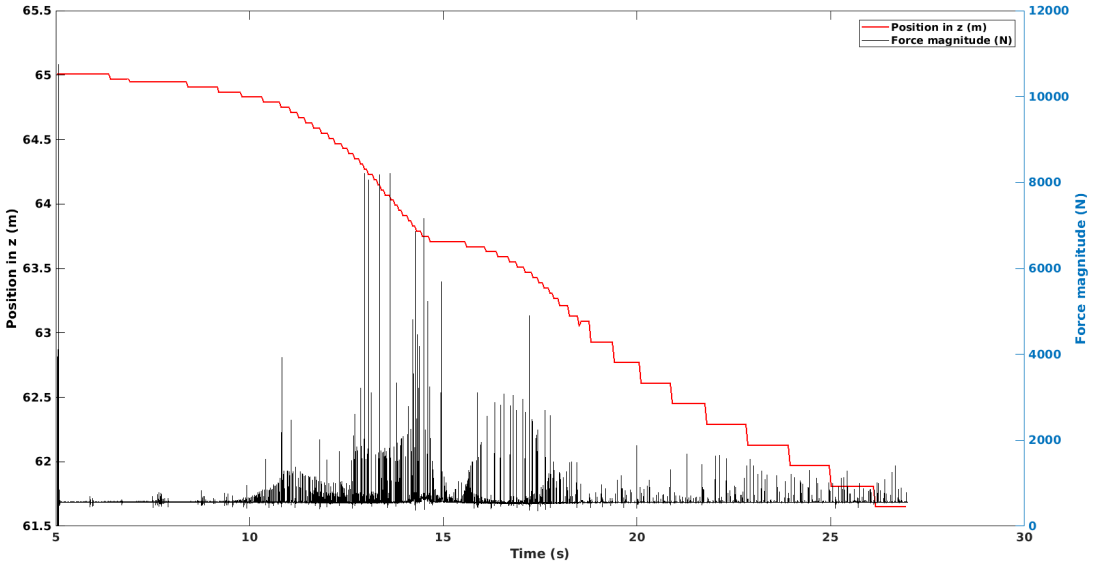

Figure 4.36: Position in cross-flow direction and corresponding force magnitude of Log6 as a function of time for the case: V = 1 m/s and Size 1L.

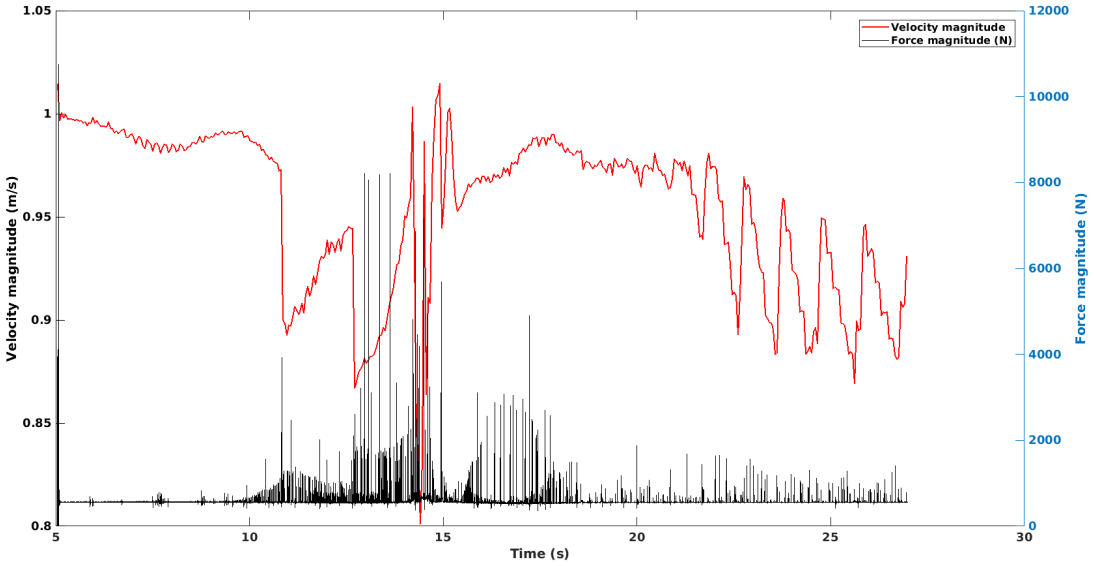

Figure 4.37: Velocity magnitude and corresponding force magnitude of Log6 as a function of time for the case: V = 1 m/s and Size 1L.

4.3.2 Correlation between forces in flow direction and cross-flow direction

While analyzing the forces on the logs in the flow direction and the cross-flow direction, it was noted that there was a correlation between the forces in those directions. When the correlation coefficients were computed, it was noticed that it was positive for logs on the right side of RDDP (Log1, Log2, Log5, Log6, Log9, Log 10, and Log13) when viewed from top and negative for logs on the left side of RDDP (Log3, Log4, Log7, Log8, Log11, Log 12, and Log15). This means that for logs on the right side, when there is force in the positive x-direction (in the direction of flow) there is a force in the positive z-direction (cross-flow direction). The fluid is pushing the logs downstream and towards the RDDP and the RDDP is pushing the logs upstream and away from it. For logs on the left side, this means that the flow is pushing the logs in the downstream (positive x-direction) and towards the RDDP (negative z-direction) while the RDDP is pushing the logs upstream (negative x-direction) and away from it (positive z-direction). For Log14, the correlation coefficient is very small since it is on a head-on collision and the forces on both sides of the log in the cross-flow (z) direction are balanced.

Another interesting observation that was discovered from this analysis is that the slope of the linear fit to the correlation points is between 35 degrees and 42 degrees. There were some outliers in the data that were eliminated as they did not correspond to the collision of the log with the RDDP and therefore did not fit the correlation observations. These outliers are believed to be result of numerical errors and need further investigation. It is interesting that the slope of the line is very close to the opening angle of RDDP (angle between the pontoons), which is 39 degrees. It is believed that the slope of the linear fit should be equal to the RDDP angle. This makes physical sense since the angle with respect to the x-direction at which the RDDP applies force on the log to modify its trajectory and accommodate it to the flow streamlines, and conversely the log applies force on the RDDP, should be parallel to the orientation of the RDDP pontoons. Figure 4.38 shows one example of the correlation between the two components of the force, highlighting the the linear fit and the value of the

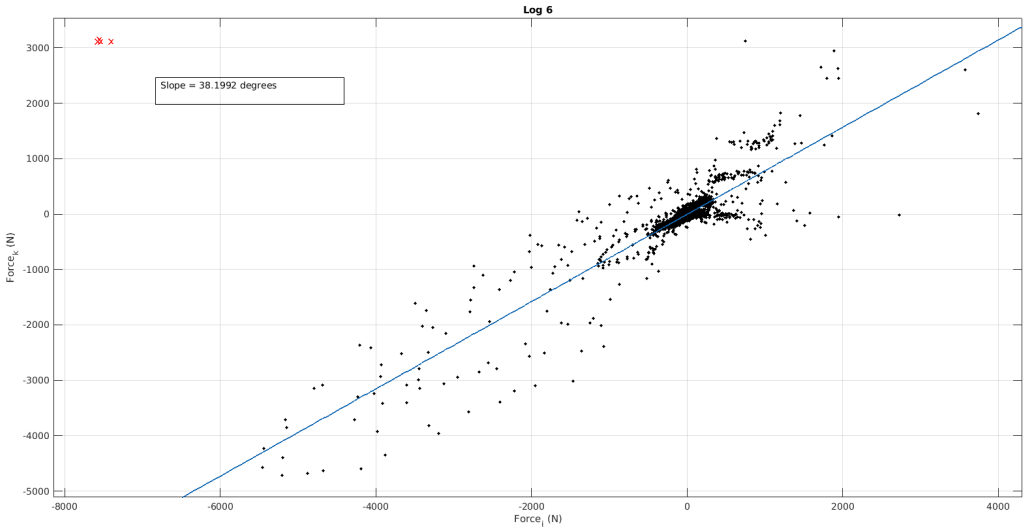

Figure 4.38: Correlation between forces in the flow direction and cross-flow direction for Log6 for the case: $V = 1\ m/s$ and Size 1L.

slope. The outliers are marked in red.

Chapter 5

SUMMARY, CONCLUSIONS, AND FUTURE WORK

One of the main challenges for River Energy Converters (RECs) is river debris. Impact of debris can cause serious structural damage to RECs. To avoid this, number of methods are being used and being developed. Methods currently being used are: using trash racks, using debris deflectors furling, manual debris removal, and using debris booms. Methods currently being developed are: modifying blade designs of turbines to shed debris on impact, and using Research Debris Diversion Platform (RDDP). The later method is being developed by Alaska Hydrokinetic Energy Research Center (AHERC) in collaboration with Alaska Power and Telephone (AP&T) company. Field tests have been conducted by deploying the RDDP in a river testing location. This thesis was conceived to complement the field tests by analyzing impacts from different debris sizes and flow velocities,which are hard to simulate in the field, on a CFD solution. The software used for this study is STAR-CCM+ which is developed by CD-Adapco. Computational Fluid Dynamics (CFD) coupled with the Discrete Element Method is used to simulate the fluid flow and debris impact. Forces on RDDP and logs are measured during the simulation and analyzed. The goal is to study the effects of debris size and flow velocities on forces on RDDP and to obtain a statistical picture of the impact conditions. This will help understand different impact conditions that might cause structural failure of the RDDP. This information can be used in improving the structural strength of the RDDP to improve performance.

5.1 Numerical Methodology

To flow field was simulated in STAR-CCM+ V12, a commercial CFD software. The Unsteady Reynolds Averaged Navier-Stokes (URANS) equations with SST $k-\omega$ turbulence closure

model were solved over a highly detailed three-dimensional mesh. The logs were simulated as discrete element particles. Appropriate contact models were used to model the particle-particle and particle-wall interactions. The analysis was done for two log sizes (log length L = 1 m and 2 m) and three flow velocities (V = 0.5 m/s, 1 m/s, and 2 m/s).

5.2 Forces on RDDP

Forces on RDDP due to impacts from logs were measured during the simulation. The results were then compared for all six cases. It was found that at high Reynolds numbers ($Re > 10^6$) changing the lengths of the logs while maintaining the volume constant does not change, to first approximation, the forces on the RDDP. The effect of shape of the debris at these high Reynolds numbers, does not change the hydrodynamic interactions of the logs with the river flow, and thus the forces do not change significantly.

Changing the flow velocity has a more profound effect on the forces on the RDDP due to log impact. The behavior is consistent with the theoretical predictions: As the flow velocity increases, the momentum of the logs increases and so does the impact force. This results in larger forces being measured for larger flow velocities as seen in the results. The mean, median, and maximum of force magnitude all scale quadratically with flow velocity as expected since kinetic energy (or the work that must be done by the force during the collision) is proportional to the square of velocity.

5.3 Forces on logs

Forces measured on the logs include forces due to impact with the RDDP and also hydrodynamic forces. At low Reynolds numbers, increasing the lengths of the logs increased the forces on the logs. At high Reynolds numbers, the variation in log lengths did not have a significant effect on the forces on the logs.

Changing the flow velocity showed the expected behavior. Increasing the flow velocity increases the momentum of logs and, thus, impact forces.

Hydrodynamic forces also increase with increase in size and flow velocity. Increasing the log

size increases the area in contact with the fluid thus increasing the drag on the logs. Drag forces varies as square of velocity for high Reynolds number for blunt objects. As the flow velocity is increased, the drag force increases quadratically in the results shown.

5.4 Numerical discrepancies

While analyzing the forces on the RDDP and the logs, unusually high forces were recorded. Acceleration due to such high forces was greater than 1000g, where g is acceleration due to gravity. Clearly, such forces are not realistic. Forces analyzed in this study have been filtered based on the acceleration (ratio of the computed acceleration to the gravitational acceleration). Even though a definitive reason for such numerical discrepancy hasn't been found, one reason might be the default recommended DEM time scale parameter equal to 0.2 which is high compared to all other characteristic time scales for this case. The motion of the logs might not be fully resolved and might have resulted in unrealistically high forces.

1. The Rayleigh time-step.

2. The duration of impact of two spheres.

3. The time that a particle takes to move 1/10th of the length of the radius of the particle.

The DEM time-step is determined as the minimum of the three timescales above [4]. The three timescales depend on particle velocity and, thus, the DEM time step depends on the flow regime. If the flow regime changes from more transient phase to a more steady state or change in any other sense, the DEM time-step may change. Since the flow in this study is unsteady and varies over the domain, the DEM time-step might be influenced by the flow. This might have resulted in the motion of logs not being fully resolved and unusually high forces. The Rayleigh timescale also depends on the radius of particles. Composite particles in this study are made up of a number of small spheres of different radius. This also might have influenced the DEM time-step. The radius of the spheres can be manually controlled

but it is time consuming when the number of spheres in large (200 in this study).

Another factor which might have influenced the DEM time-step is the number of sub-steps. The default number is 20,000 which seems high in general but maybe not sufficient for this case. The number of sub-steps is the number of sub-iterations that the DEM model takes to resolve the motion of particles between two flow time steps. Increasing this number increases the computational time and so this has been left to the default value in this study. This needs further investigation.

In addition to the two log sizes presented in this thesis, a third log size of 1.8L (Length = 3.6 m) was also analyzed for the three flow velocities. Initially, a log size of 2L (Length = 4 m) was simulated but the logs were not injected by the model due to a limitation having to do with the high aspect ratio. Log injection was successful for a size of 1.8L, so this was the larger size explored. This highlighted a drawback of the DEM model, which was unable to simulate high aspect ratio objects. For each flow velocity, at least one of the logs penetrated the RDDP wall (wall boundary-condition), which is unrealistic. An example is shown in Figure 5.1. In this case, a couple of logs penetrated the RDDP wall and as a result the logs got stuck there. This led to a pile up of logs. Since this is a numerical error due to some limitation in the DEM model, results for this log size have not been presented in this thesis. The aspect ratio for this size is about 25. When STAR-CCM+ Resource Support was contacted about this, their response was that this is a known limitation in the behavior of the model at high aspect ratios. A clear solution to the limitation presented by this behavior is not available yet and needs further investigation. One reason might be the high DEM timescale parameter.

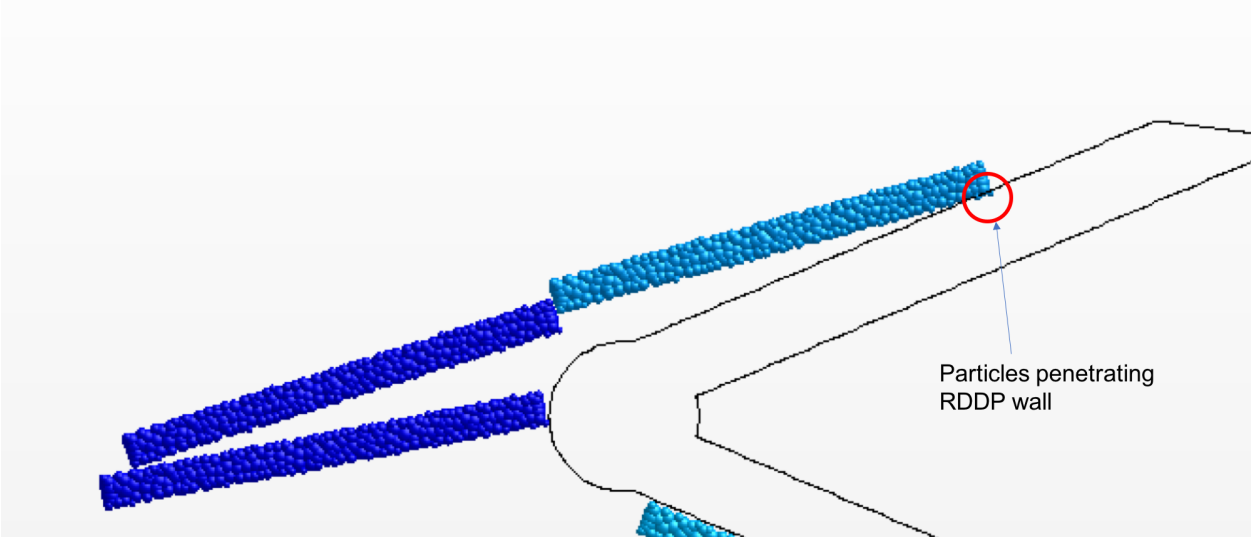

Figure 5.1: Particles penetrating RDDP wall for log size 1.8L.

5.5 Conclusion and Future Work

In this thesis, a numerical method was tested to simulate debris impact on a hydrokinetic debris diverter (RDDP) design. Analysis of the forces on the RDDP and the logs has been performed for different log sizes and flow velocities. The conclusion is that at high Reynolds numbers (Re $> 10^6$) increasing the size of logs did not vary the forces on the RDDP and the logs significantly. Increasing the flow velocity profoundly increases the forces on RDDP, and the logs. A statistical picture of the impact conditions was also obtained. Probability of forces due to impact from logs from different initial conditions was obtained. This information can be used in improving the structural design of the RDDP. There were a few numerical discrepancies in the code that require further investigation but the major contributor for this might be the DEM timescale parameter.

The current study contributes only to a part of study of RDDP performance. There is a lot that can be done in this research project. The flow fields can be analyzed in detail to identify the possible locations for placement of RECs. In this study, a simplified model of the RDDP was used. A study can be conducted with the actual model of RDDP, for example including

the rotating RDDP sweep to model interactions of the RDDP pontoons with the rotating sweep. The study can be setup in a domain that mimics an actual field location. It is not practical to store the flow-field data and used in another simulation within STAR-CCM+. For each simulation, the flow field has to be fully computed for about 20 s of physical time, which takes around two weeks on 48 processors. A code that makes it practical to store the flow field so that it can be used with a number of different combinations of log sizes, injection positions, times, etc, would significantly improve on the statistical description of the forces acting on the RDDP. This would reduce the total computation time from weeks to less than 24 hours, as the DEM is the computationally inexpensive part o the study. Different orientations of the logs could be studied, to imitate actual river conditions. There is so much more that this research can contribute. The goal of this thesis is to provide an initial study that can be used to further the research in this field. This research aims to contributes to development of river energy as a viable source of renewable energy source on a commercial scale.

BIBLIOGRAPHY

[1] J. Bradely, D. Richards, and C.Bahner. Debris Control Structures Evaluation and Countermeasures. *Department of Transportation Federal Highway Administration, Salem, OR*, 2005.

[2] P. A. Cundall and O. D. L. Strack. A discrete numerical model for granular assemblies. *Geotechnique*, 29(1):47–65, 1979.

[3] STAR-CCM+ Documentation. Composite particles model, 2017.

[4] STAR-CCM+ Documentation. Dem time step, 2017.

[5] STAR-CCM+ Documentation. Discrete element method, 2017.

[6] STAR-CCM+ Documentation. Lagrangian multiphase flow, 2017.

[7] STAR-CCM+ Documentation. Prism layer mesher, 2017.

[8] STAR-CCM+ Documentation. Trimmed cell mesher, 2017.

[9] STAR-CCM+ Documentation. Wall treatment, 2017.

[10] R. B. Haehnel and S. F. Daly. Maximum impact force of woody debris on floodplain structures. 2002.

[11] T. J. Hall. Numerical simulation of a cross flow marine hydrokinetic turbine. Master's thesis, University of Washington, 2012.

[12] T. Javaherchi. *Numerical investigation of Marine Hydrokinetic Turbines: methodology development for single turbine and small array simulation, and application to flume and full-scale reference models*. PhD thesis, University of Washington, 2012.

[13] J. B. Johnson, J. L. Kasper, J. Schmid, P. Duvoy, A. Kulchitsky, M. Mueller-Stoffels, N. Konefal, and A. C. Seitz. Surface debris characterization and mitigation strategies and their impact on the operation of river energy conversion devices on the tanana river at nenana, alaska. *Alaska Center for Energy and Power, Alaska Hydrokinetic Energy Research Center*, 2015.

[14] J. B Johnson, J. Schmid, J. L. Kasper, A. C. Seitz, and P. Duvoy. Protection of in-river hydrokinetic power-generating devices for surface debris in alaskan rivers. *University of Alaska Fairbanks, Fairbanks, AK, 61 pp*, 2014.

[15] P. C. Lagasse. Effects of debris on bridge pier scour. *National Cooperative Highway Research Program*, 2010.

[16] S. B. Pope. Turbulent flows. *Cambridge University Press*, 2008.

[17] D. Sale, A. Aliseda, and Y. Li. Simulation of hydrokinetic turbines in turbulent flow using vortex particle methods. In *Proceedings of the 2nd Marine Energy Technology Symposium*, Seattle, WA, April 2014.

[18] R. N. Tyler. River debris: Causes, impacts, and mitigation techniques. 2011.

[19] H. K. Versteeg and W. Malalasekera. An introduction to computational fluid dynamics: The finite volume method (2nd edition). *Pearson Publications*, 2007.

[20] N. Wallerstein and C. Thorne. Debris control at hydraulic structures in selected areas of europe. *University of Nottingham, England: University of Nottingham, Department of Geography*, 1995.

Appendix A

FORCES ON LOGS

Log1

This is the log that is injected from location 1 as shown in Figure 4.12. It is inject at the same time as logs 2, 3, and 4.

Figure A.1 shows the comparison of the PDFs of the force magnitude for different log sizes at V = 0.5 m/s. Log1 has a higher probability of smaller-than-mean forces when the length is 1L than for 0.5L. The probability of the force being around the mean is higher for size 1L than for 0.5L. The variation of PDFs is because of different injection times. The amount of time any log interacts with RDDP is different for each case. This causes the PDFs to not follow the expected behavior.

Figure A.2 shows the comparison of the PDFs of the force magnitude of for different log sizes at V = 1.0 m/s. The behavior is similar to that at V = 0.5 m/s.

Figure A.3 shows the comparison of the PDFs of force magnitude for different log sizes at V = 2.0 m/s. The PDFs are very similar to each other, almost overlapping.

Figures A.4, A.5, and A.6 show the variation of mean, median, and maximum force magnitude on Log1 for different log sizes. Mean and median forces do not vary much with log size. Maximum of force magnitude increases but the variation is very small.

Figures A.7 and A.8 show the comparison of the PDFs of Log1 force magnitude for different flow velocities, for the two sizes studied. As the velocity increases, the probability of higher forces on the log increases. The momentum of the logs increases with velocity and therefore so does the impact force.

Figures A.9, A.10, and A.11 show the variation of mean, median, and maximum force of magnitude, on Log1, at different flow velocities. The mean and maximum force increase

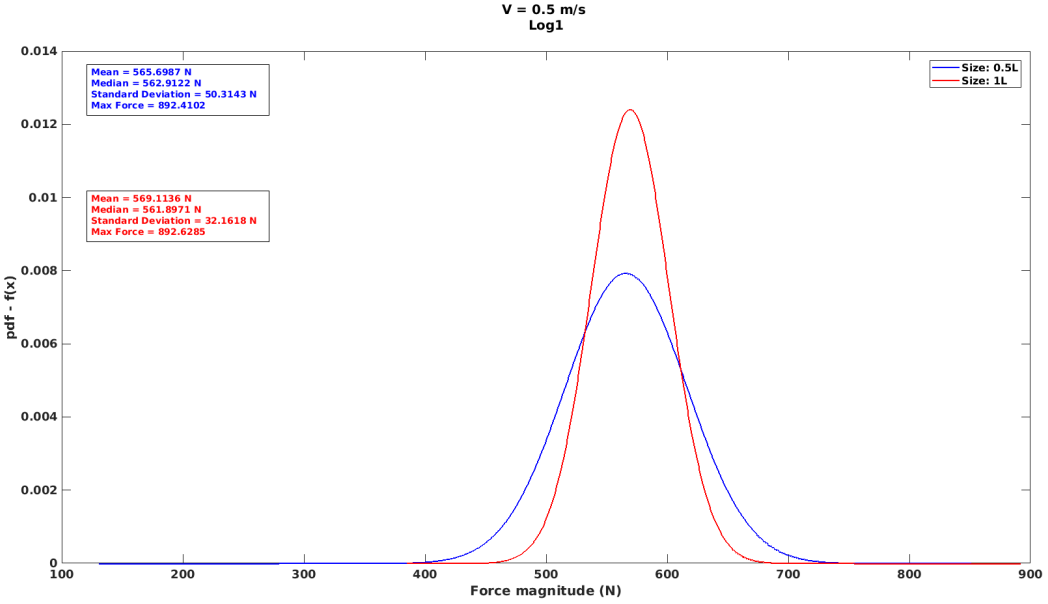

Figure A.1: Comparison of PDFs of forces on Log1 at V = 0.5 m/s.

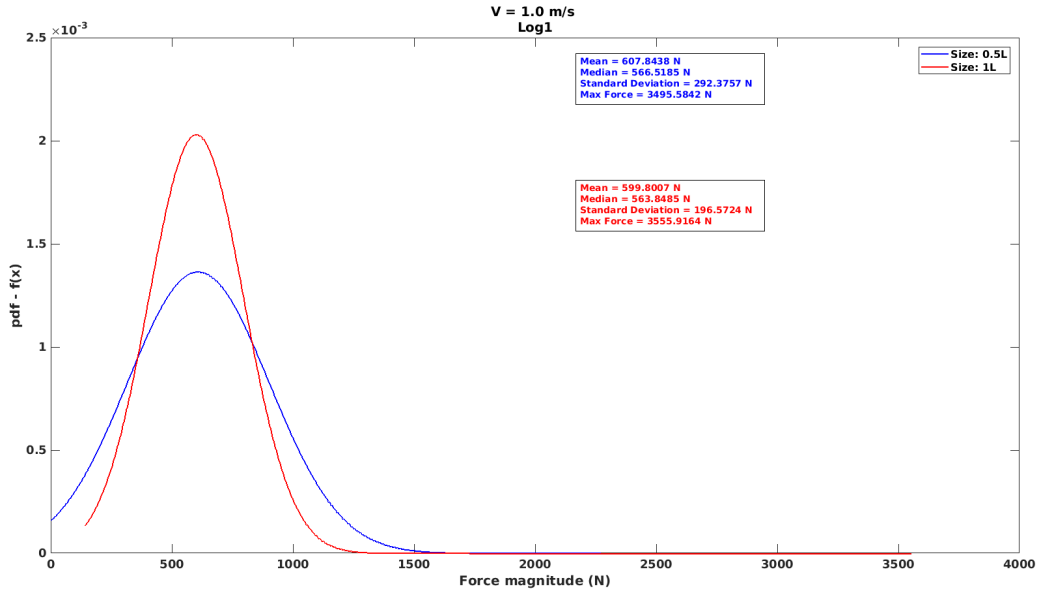

Figure A.2: Comparison of PDFs of forces on Log1 at V = 1.0 m/s.

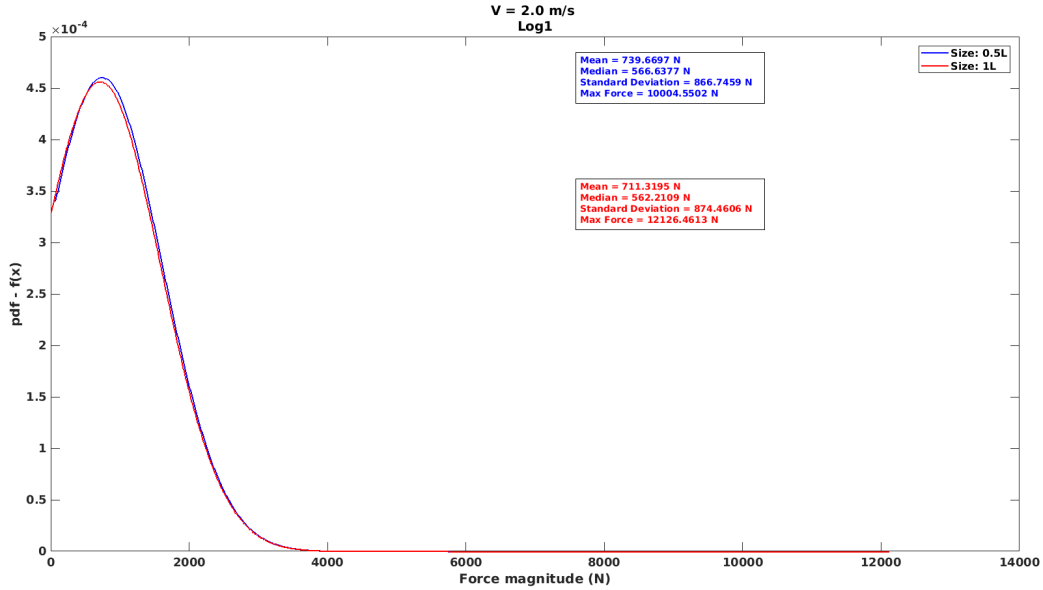

Figure A.3: Comparison of PDFs of forces on Log1 at V = 2.0 m/s.

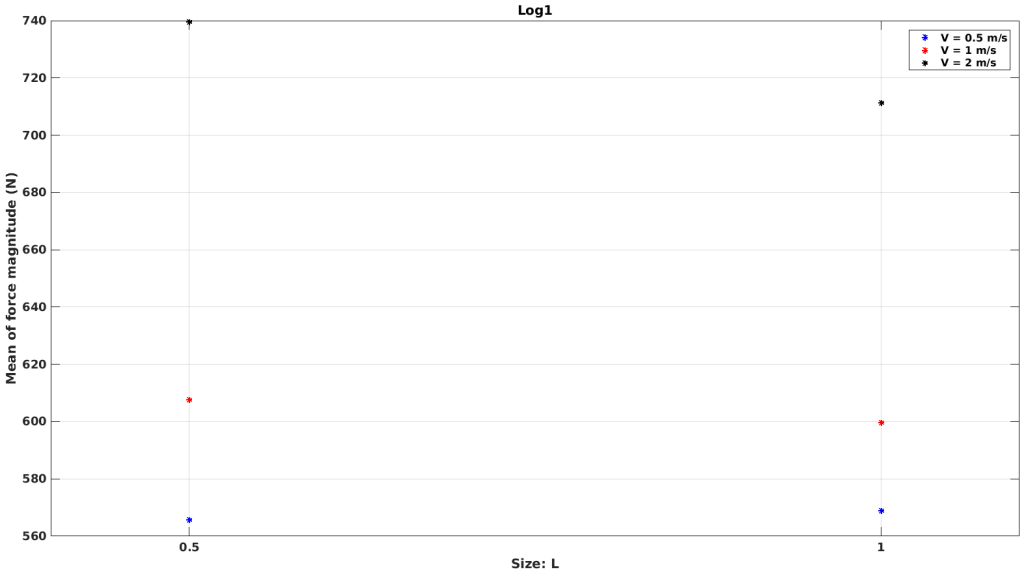

Figure A.4: Variation of mean force magnitude with log size for Log1.

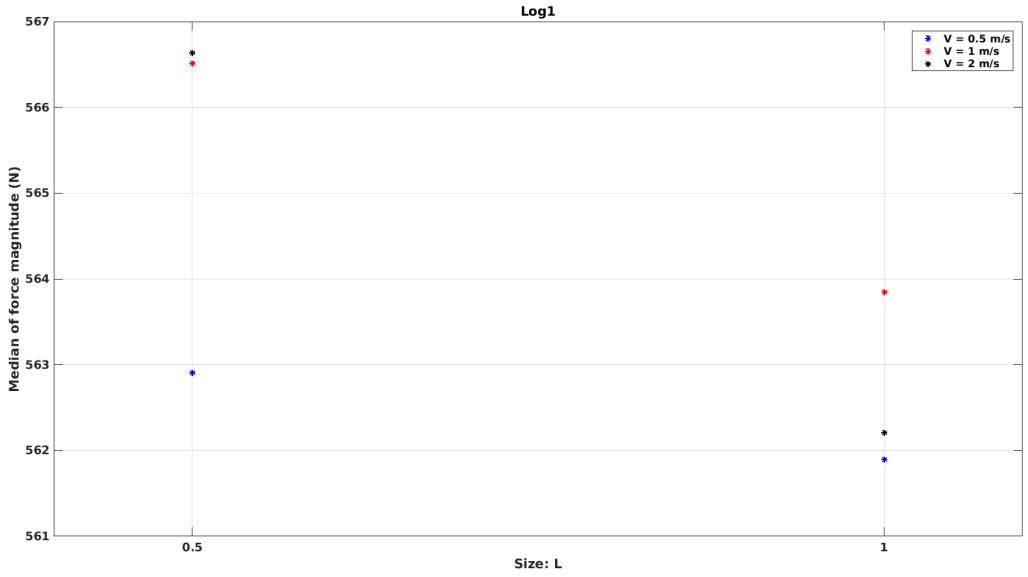

Figure A.5: Variation of median force magnitude with log size for Log1.

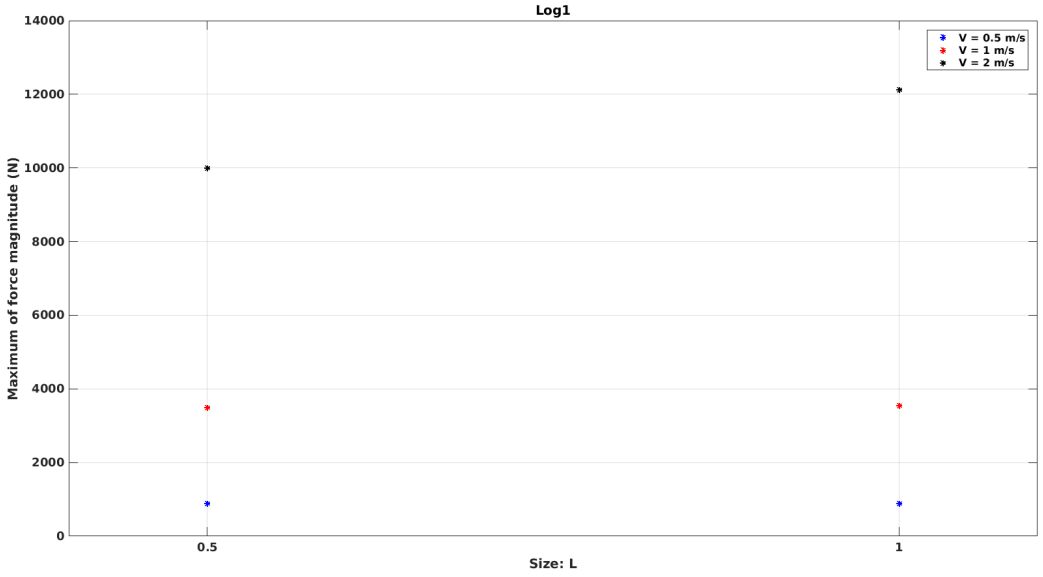

Figure A.6: Variation of maximum force magnitude with log size for Log1.

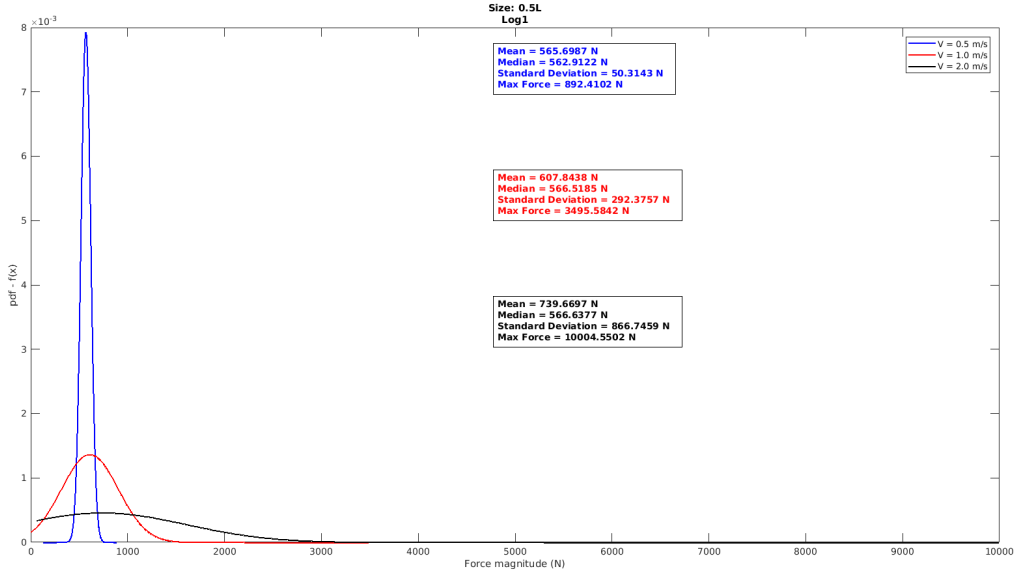

Figure A.7: Comparison of PDFs of forces on Log1 of size 0.5L.

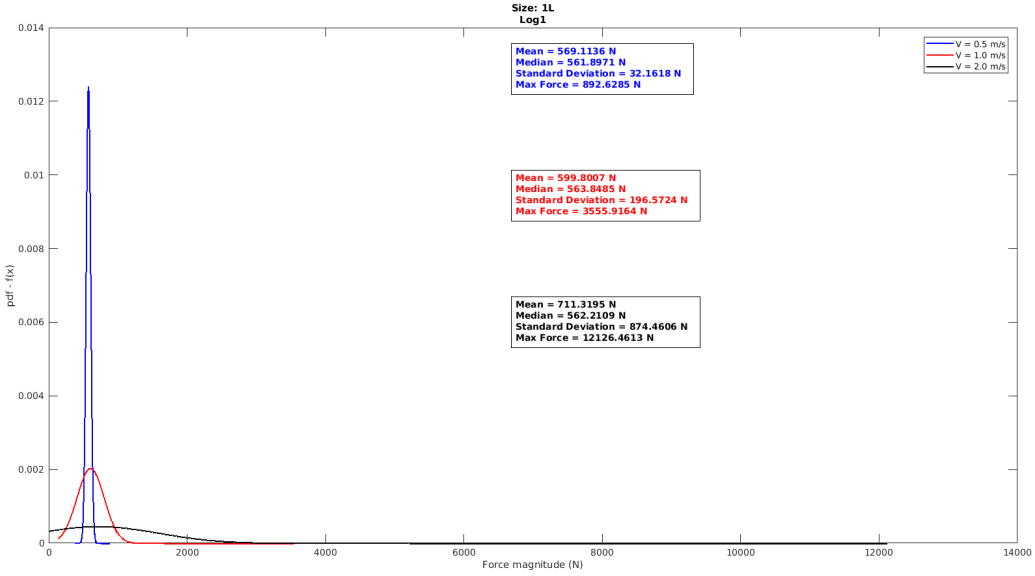

Figure A.8: Comparison of PDFs of forces on Log1 of size 1L.

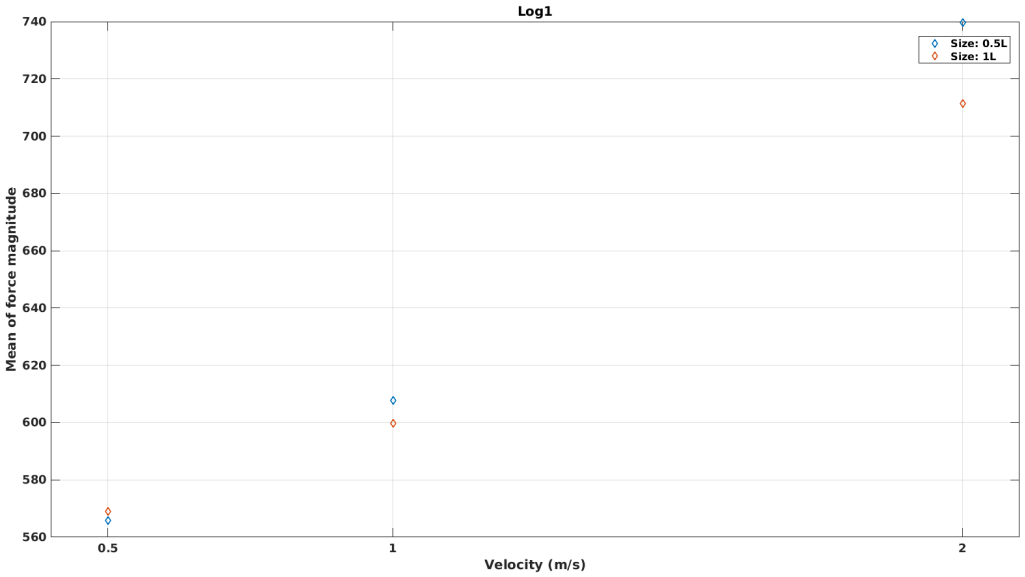

Figure A.9: Variation of mean force magnitude with flow velocity for Log1.

with increase in flow velocity.

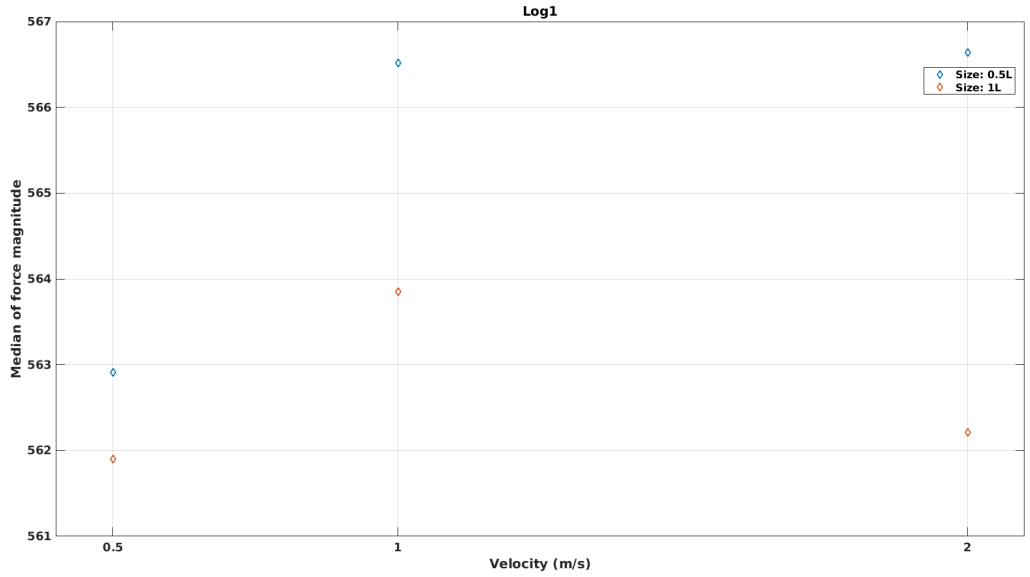

Figure A.10: Variation of median force magnitude with flow velocity for Log1.

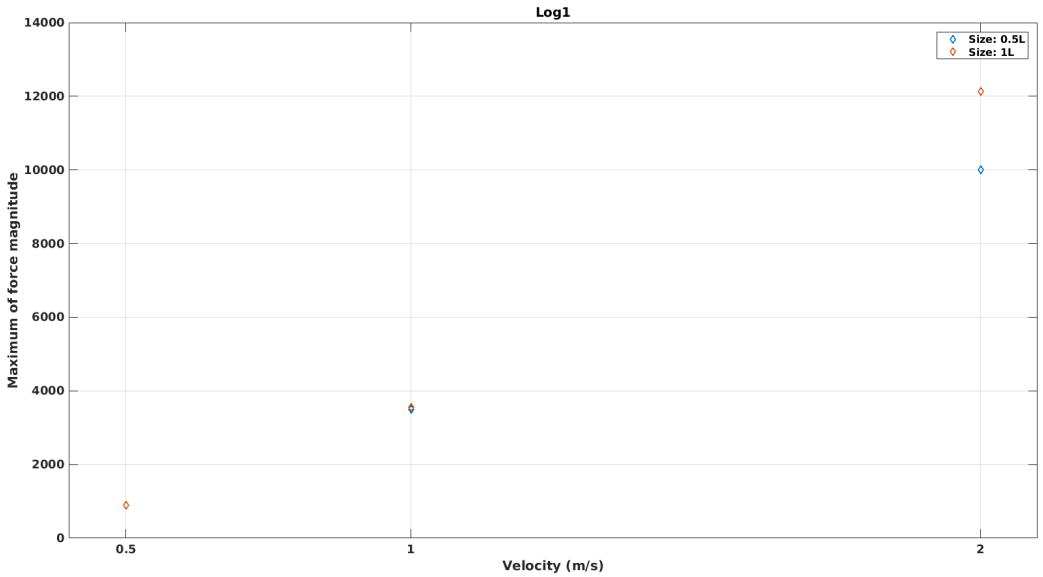

Figure A.11: Variation of maximum force magnitude with flow velocity for Log1.

Log2

This is the log that is injected from location 2 as shown in Figure 4.12. It is injected at the same time as logs 1, 3, and 4.

Figure A.12 shows comparison of PDFs of magnitude of forces for different log sizes at V = 0.5 m/s. Log2 of size 0.5L has higher probability of smaller than mean forces than that of size 0.5L. Probability of force being around the mean forces is higher for size 1L than size 0.5L.

Figure A.13 shows the comparison of the PDFs of the force magnitude of forces for different log sizes at V = 1.0 m/s. The behavior is similar to that at V = 0.5 m/s.

Figure A.14 shows the comparison of the PDFs of Log2 force magnitude for different log sizes at V = 2.0 m/s. Probability of the forces being around the mean is higher for log size 0.5L than that for size 1L.

Figures A.15, A.16, and A.17 show variation of mean, median, and maximum of force magnitude on Log2 at different log sizes. Mean and median forces do not vary much with log size. Maximum force shows a decreasing trend.

Figures A.18 and A.19 show the comparison of the PDFs of Log2 force magnitude for the two log sizes at different flow velocities. As the velocity increases, the probability of higher forces on log increases. The momentum of logs increases with velocity and therefore so does the impact force.

Figures A.20, A.21, and A.22 show variation of mean, median, and maximum of force magnitude on Log2 at different flow velocities. All three quantities show an increasing trend with velocity. The variation is quadratic.

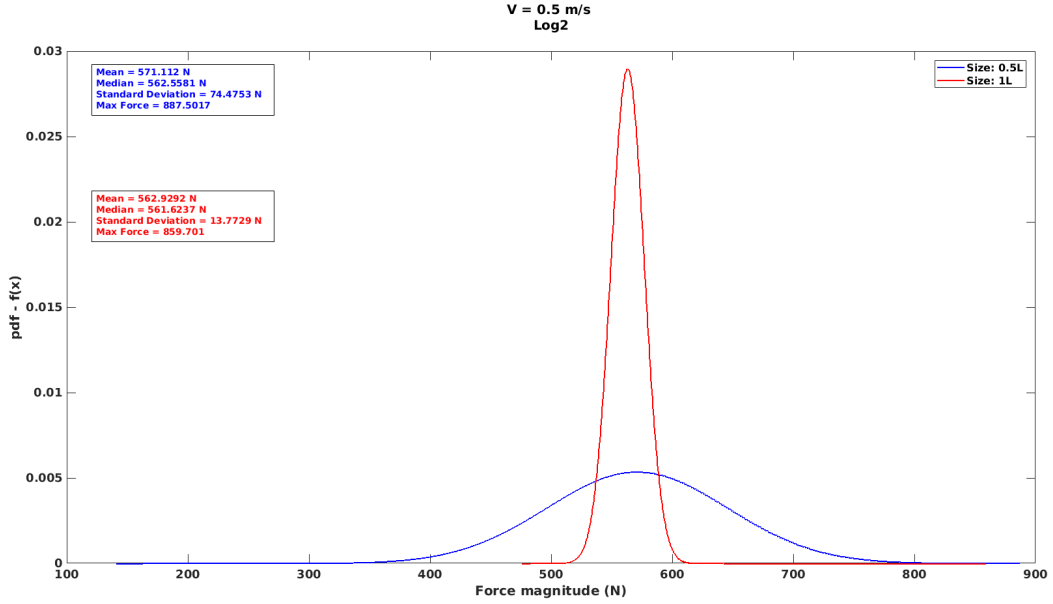

Figure A.12: Comparison of the PDFs of the forces on Log2 at V = 0.5 m/s.

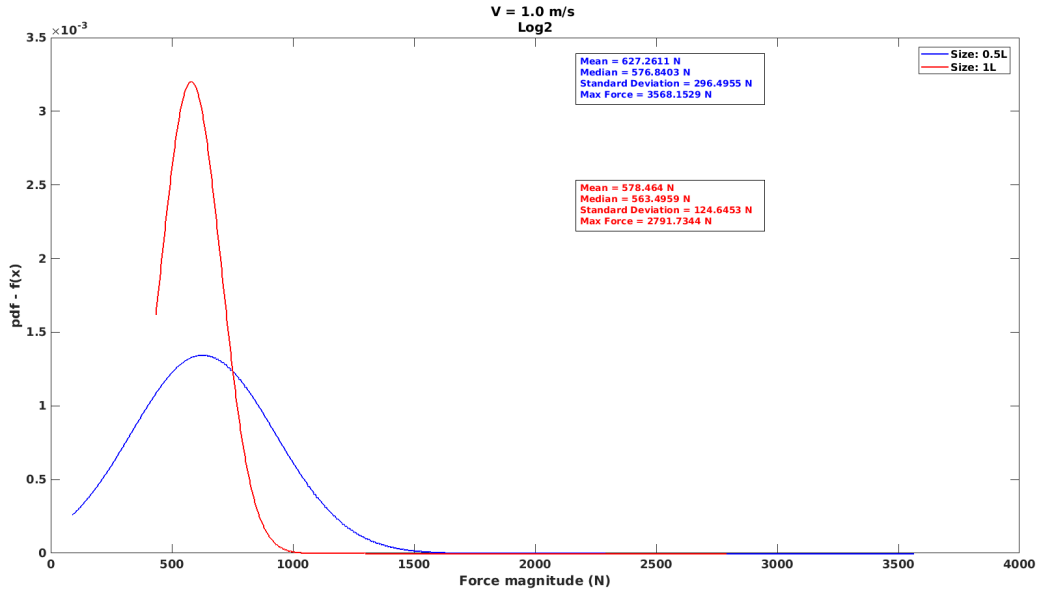

Figure A.13: Comparison of the PDFs of the forces on Log2 at V = 1.0 m/s.

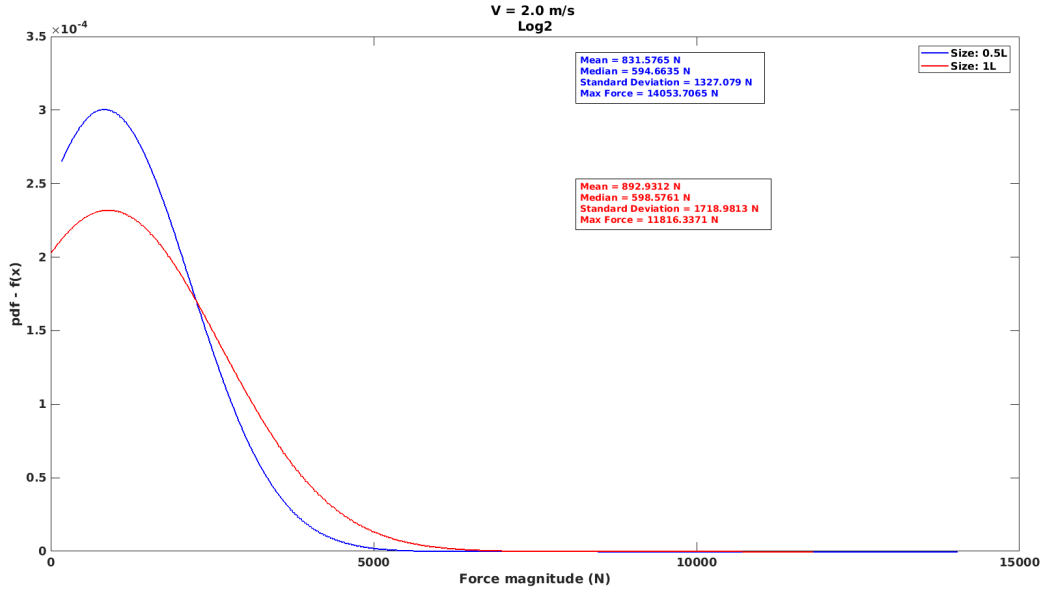

Figure A.14: Comparison of the PDFs of the forces on Log2 at V = 2.0 m/s.

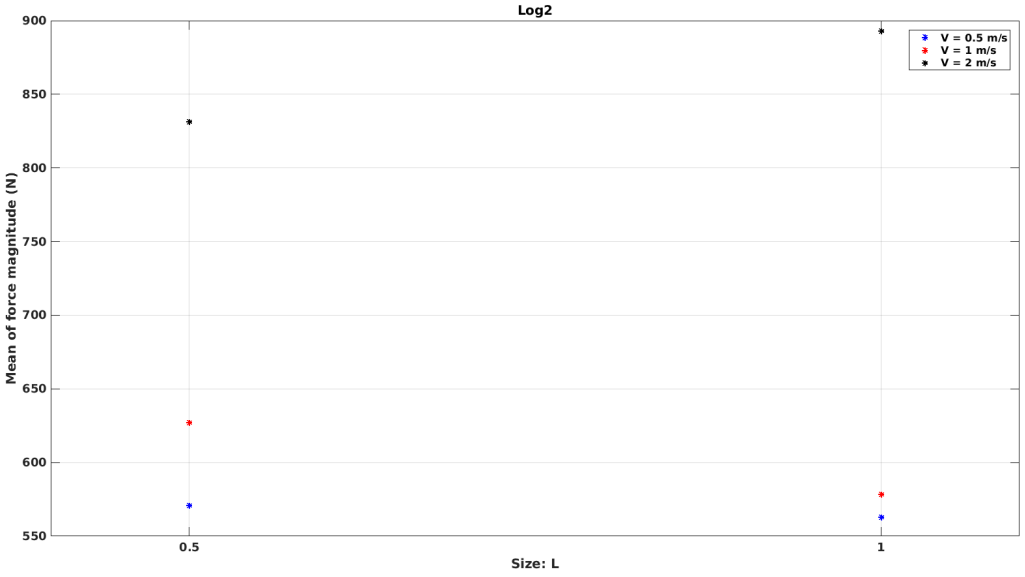

Figure A.15: Variation of mean force magnitude with log size for Log2.

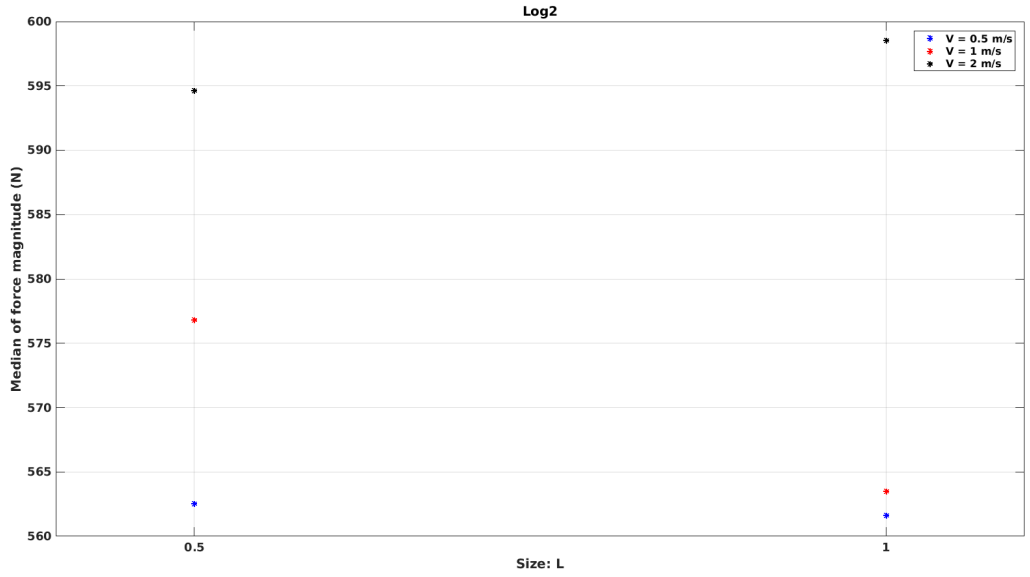

Figure A.16: Variation of median force magnitude with log size for Log2.

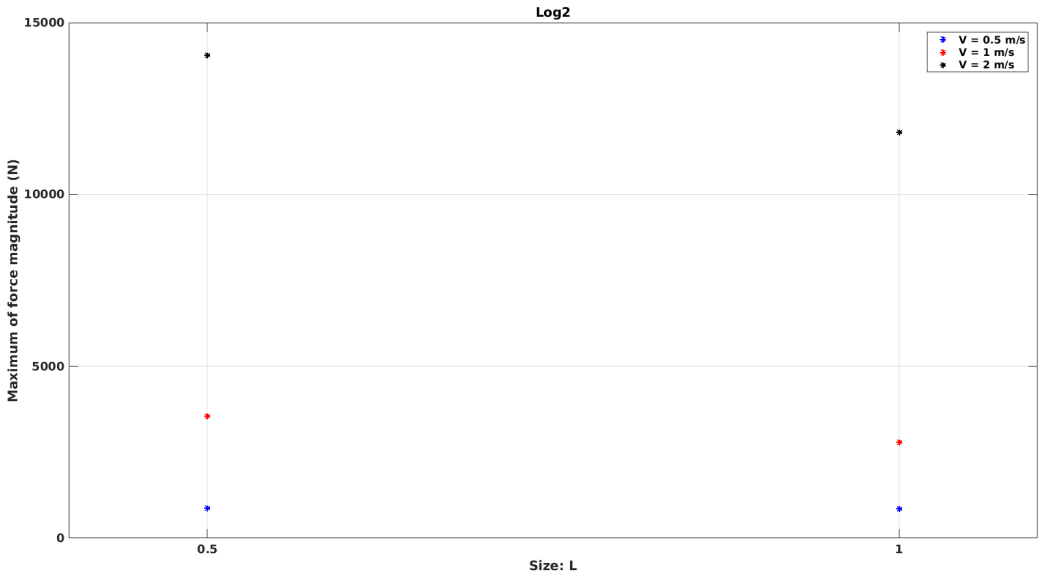

Figure A.17: Variation of maximum force magnitude with log size for Log2.

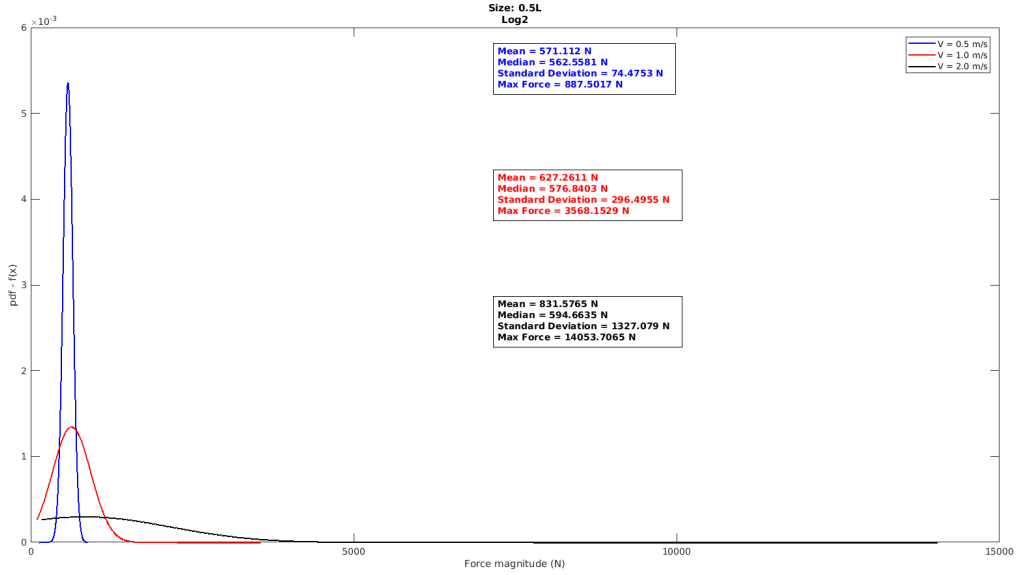

Figure A.18: Comparison of the PDFs of the forces on Log2 of size 0.5L.

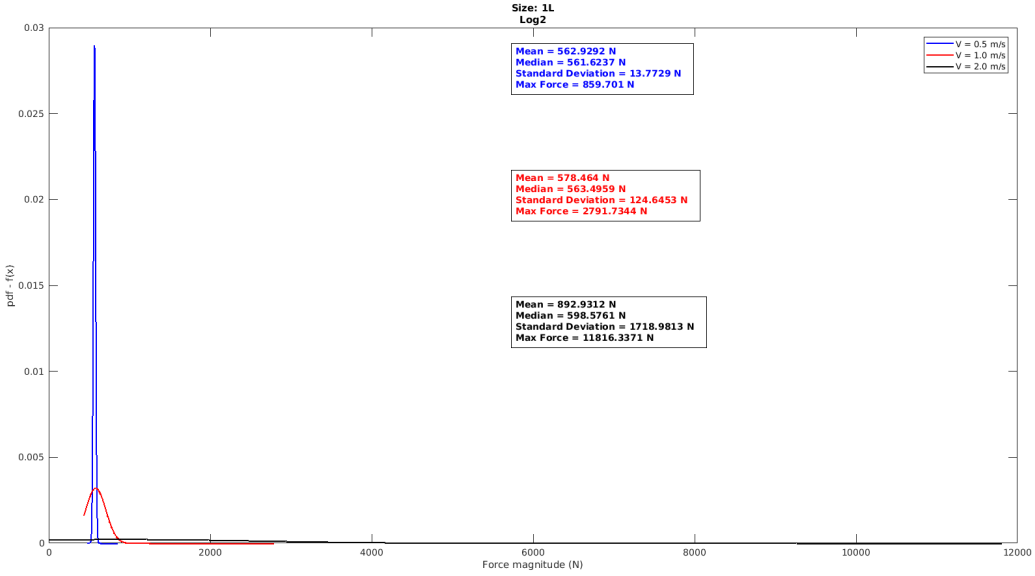

Figure A.19: Comparison of the PDFs of the forces on Log2 of size 1L.

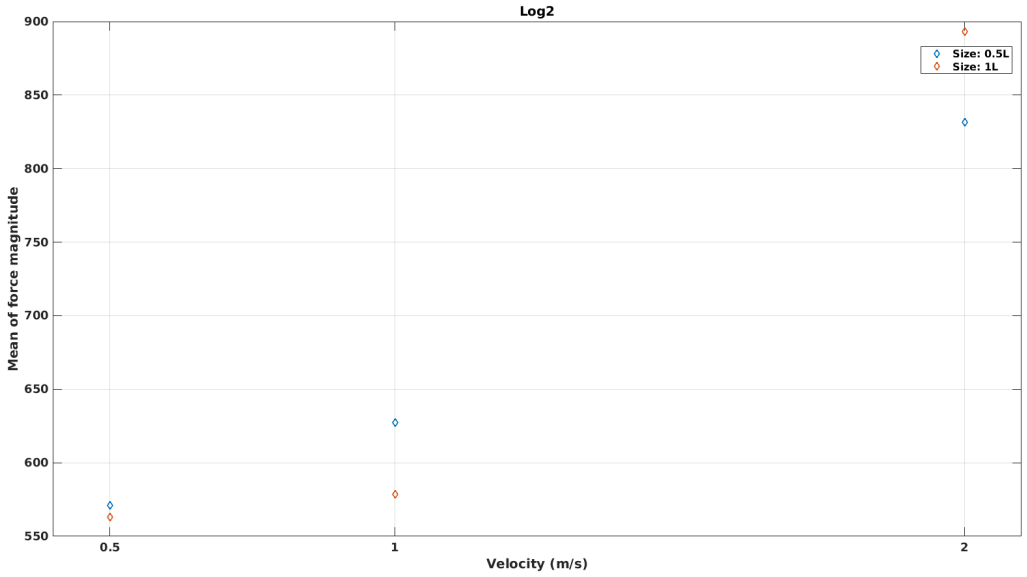

Figure A.20: Variation of mean force magnitude with flow velocity for Log2.

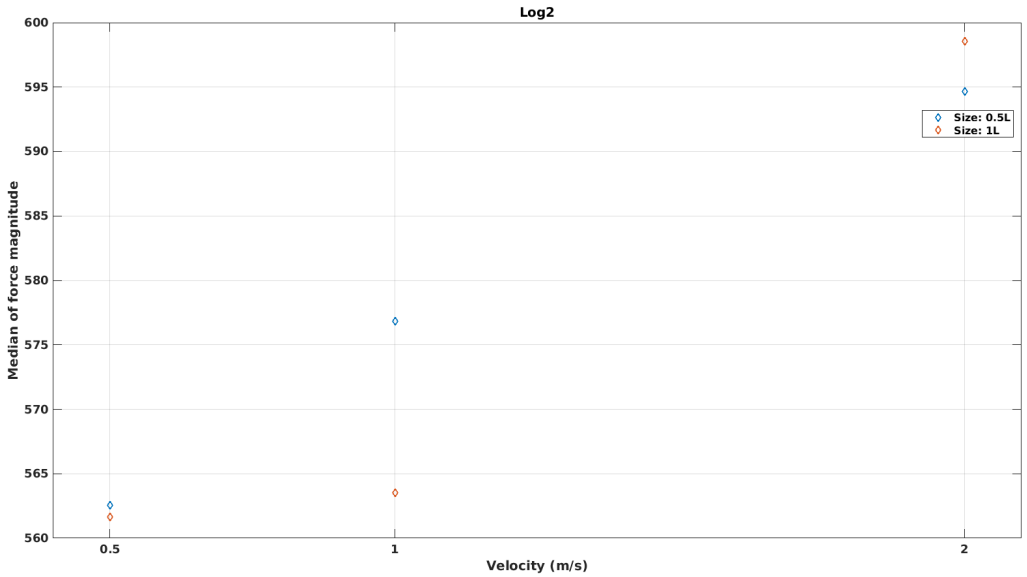

Figure A.21: Variation of median force magnitude with flow velocity for Log2.

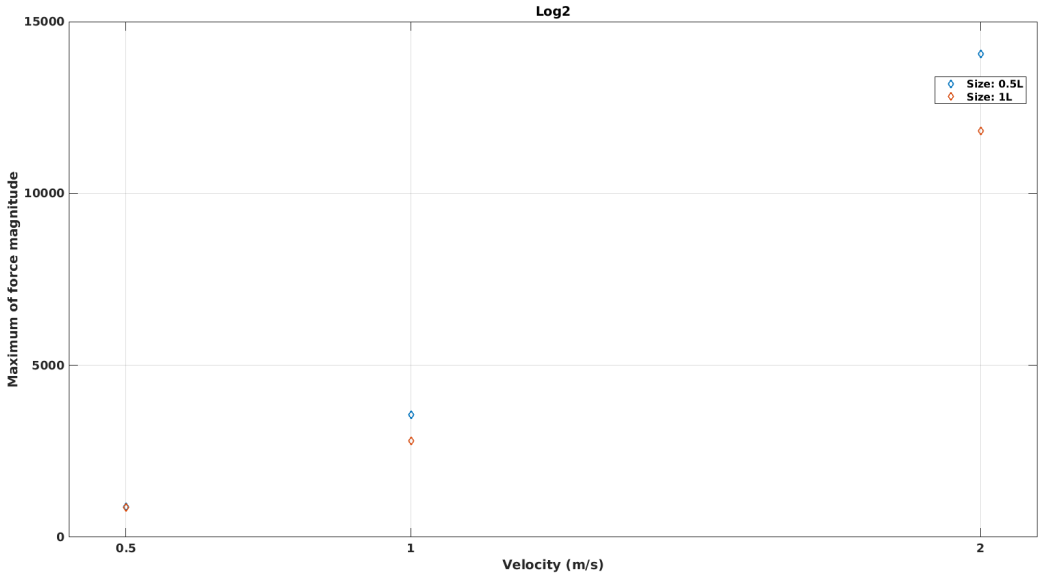

Figure A.22: Variation of maximum force magnitude with flow velocity for Log2.

Log3

This is the log that is injected from location 3 as shown in Figure 4.12. It is injected at the same time as logs 1, 2, and 4.

Figure A.23 shows the comparison of the PDFs of the force magnitude for different log sizes at V = 0.5 m/s. Log3 of size 0.5L has higher probability of forces being around the mean than that for size 1L. Log of size 1L has higher probability of forces being large.

Figure A.24 shows the comparison of the PDFs of the force magnitude for different log sizes at V = 1.0 m/s. The PDFs are very similar for forces larger than mean force. Log of size 1L has forces greater than 500N.

Figure A.25 shows the comparison of the PDFs of Log3 force magnitude for different log sizes at V = 2.0 m/s. The probability of forces being around the mean is higher for log size 1L than that for size 1L. Log of size 0.5L has higher probability of forces being large.

Figures A.26, A.27, and A.28 show the variation of mean, median, and maximum of force

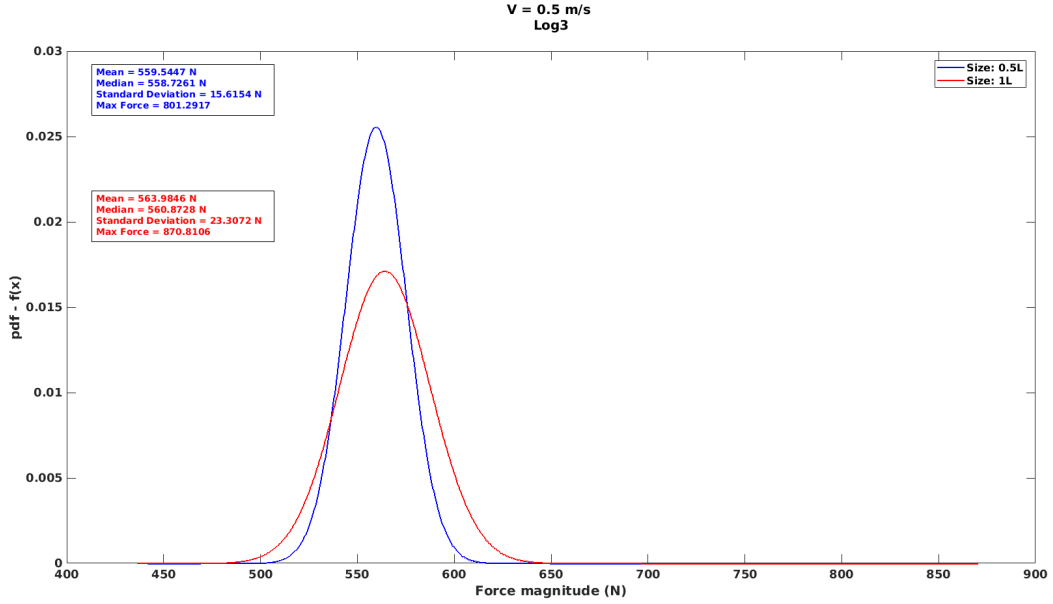

Figure A.23: Comparison of the PDFs of the forces on Log3 at V = 0.5 m/s.

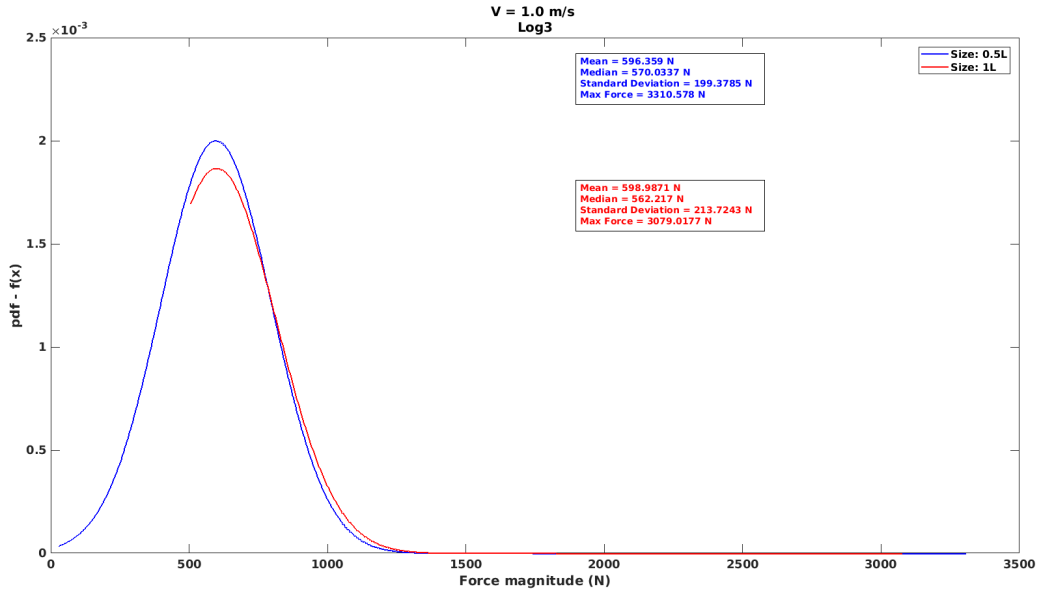

Figure A.24: Comparison of the PDFs of the forces on Log3 at V = 1.0 m/s.

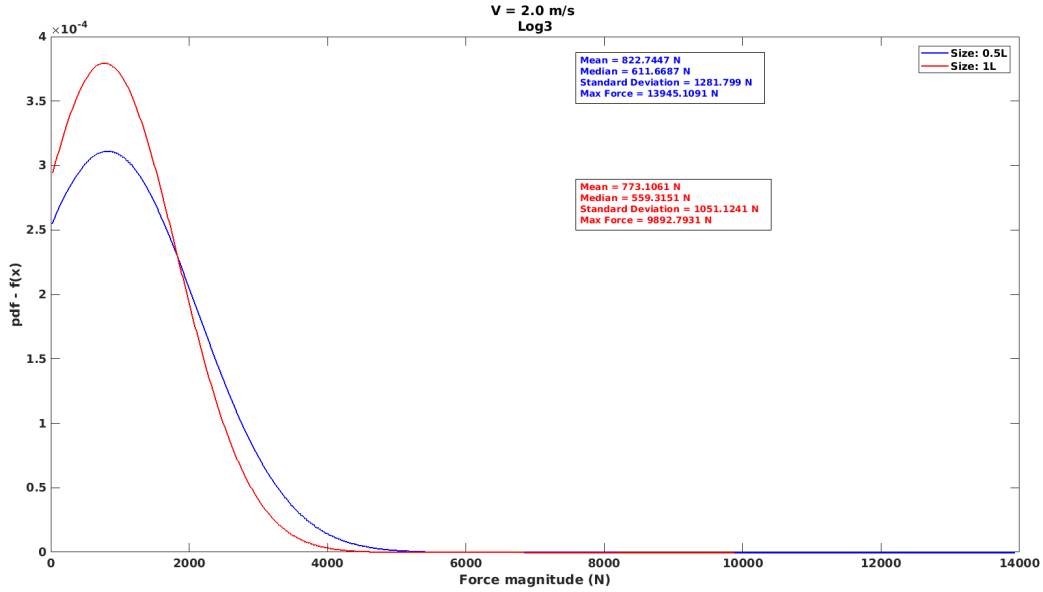

Figure A.25: Comparison of the PDFs of the forces on Log3 at V = 2.0 m/s.

magnitude on Log3 at different log sizes. Mean and median forces do not vary much with log size. Maximum force shows a decreasing trend.

Figures A.29 and A.30 show the comparison of the PDFs of Log3 force magnitude for the two log sizes at different flow velocities. As the velocity increases, the probability of higher forces on log increases. The momentum of logs increases with velocity and therefore so does the impact force.

Figures A.31, A.32, and A.33 show the variation of mean, median, and maximum of magnitude of force on Log3 at different flow velocities. Both mean and maximum force show an increasing trend with velocity. The variation is quadratic. Median force for log size 0.5L increases with velocity but for log size 1L it increases at first and then decreases. The variation is not very large.

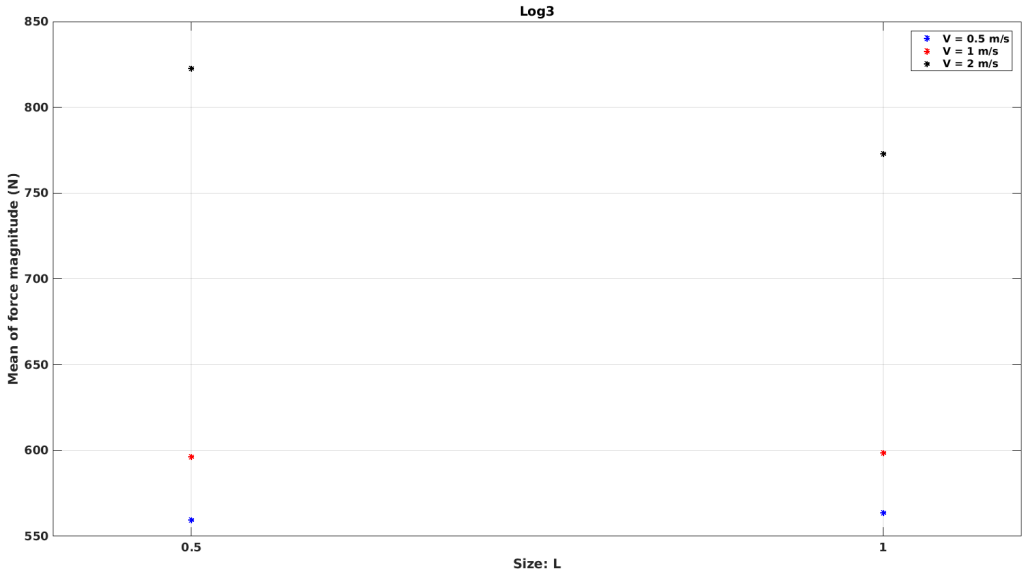

Figure A.26: Variation of mean force magnitude with log size for Log3.

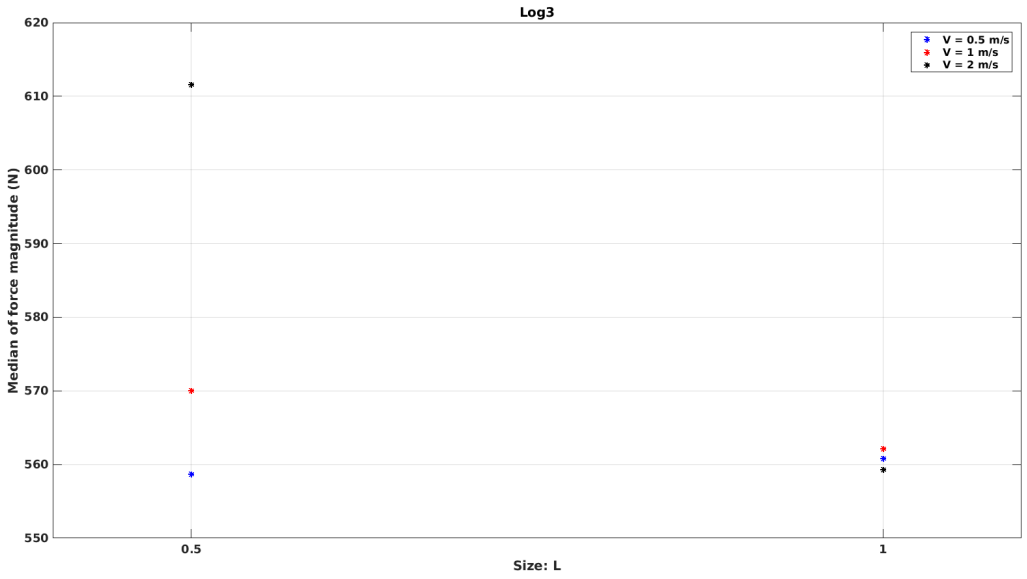

Figure A.27: Variation of median force magnitude with log size for Log3.

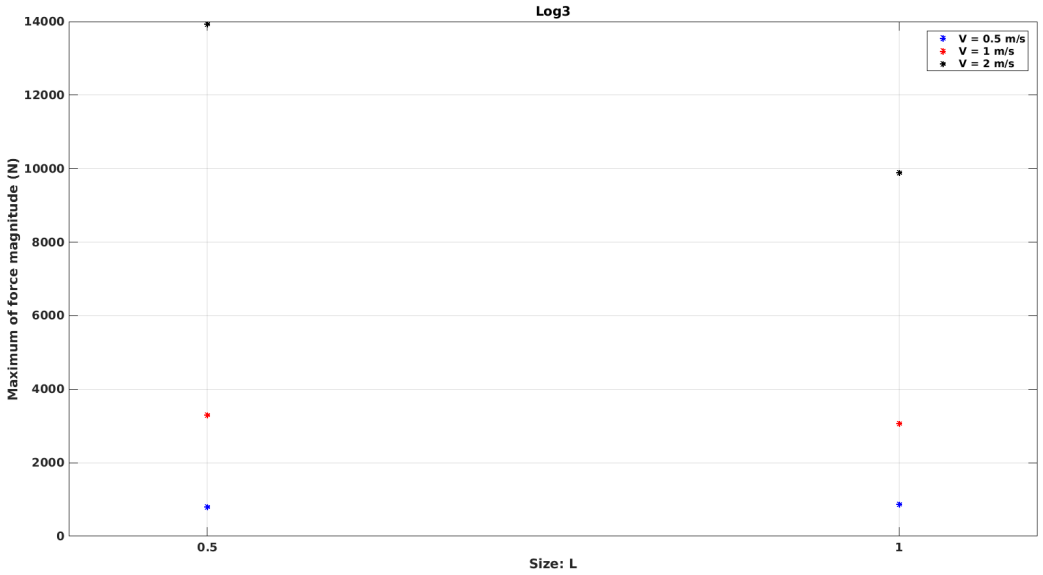

Figure A.28: Variation of maximum force magnitude with log size for Log3.

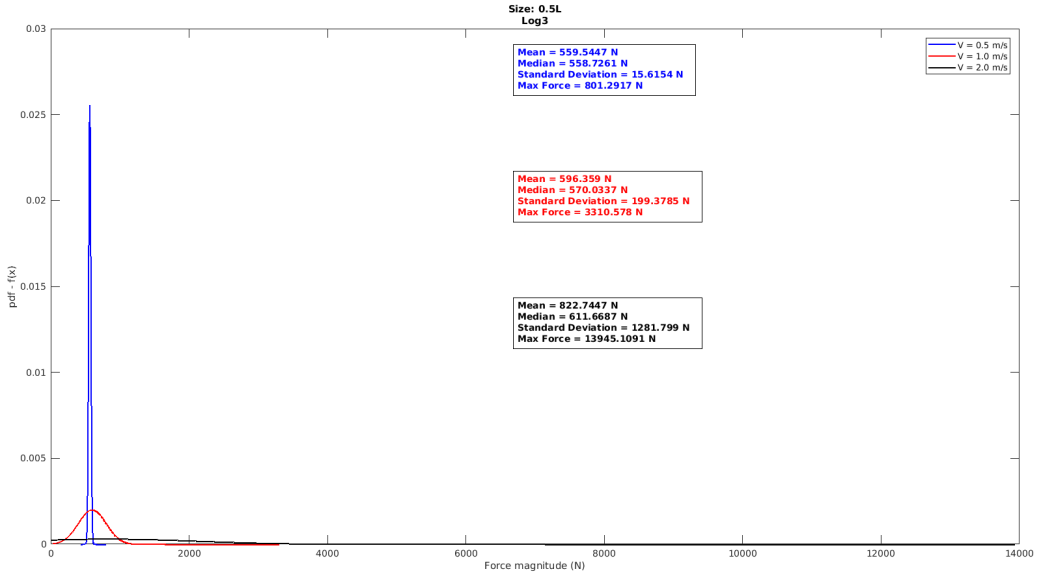

Figure A.29: Comparison of the PDFs of the forces on Log3 of size 0.5L.

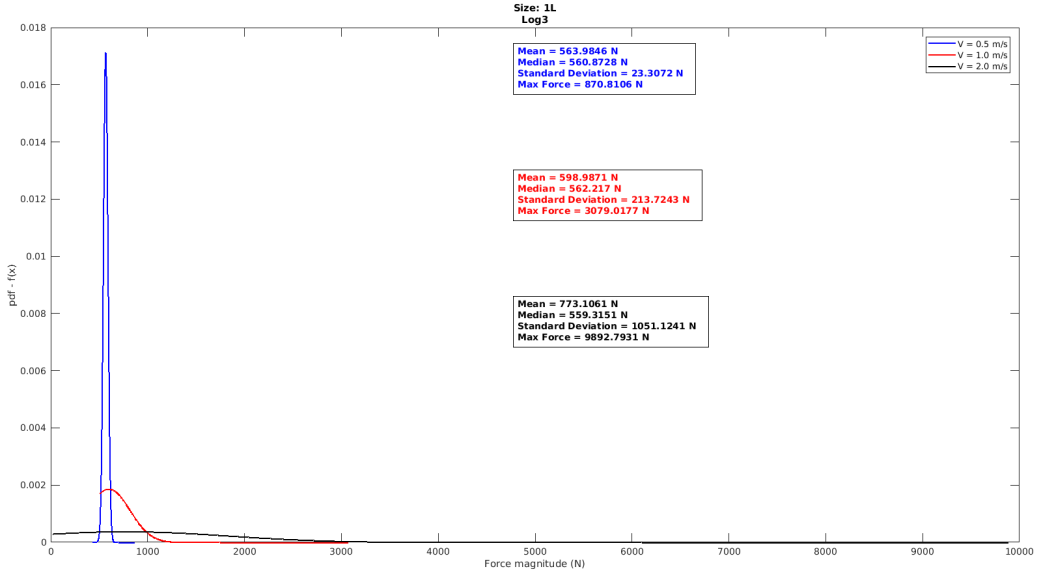

Figure A.30: Comparison of the PDFs of the forces on Log3 of size 1L.

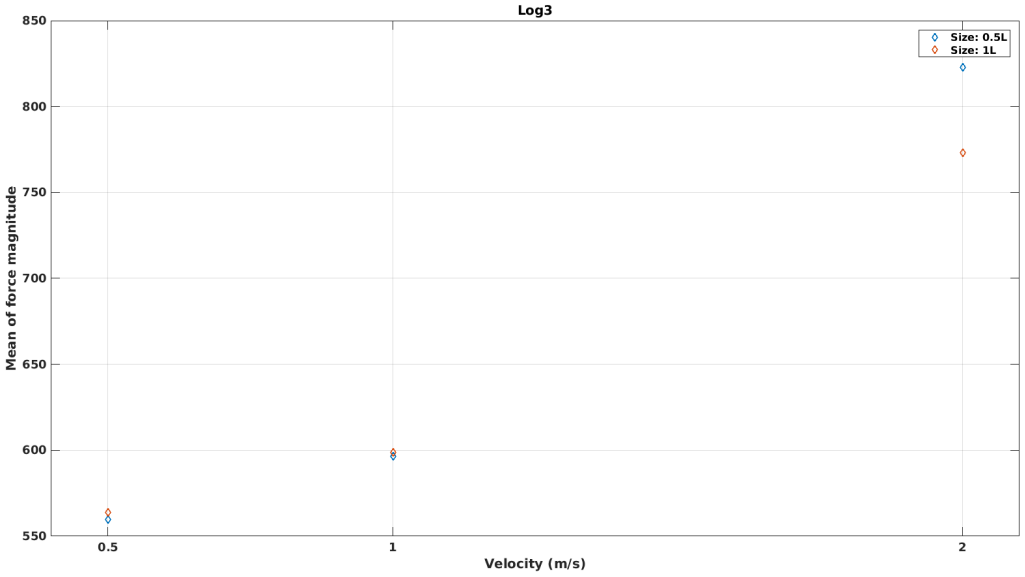

Figure A.31: Variation of mean force magnitude with flow velocity for Log3.

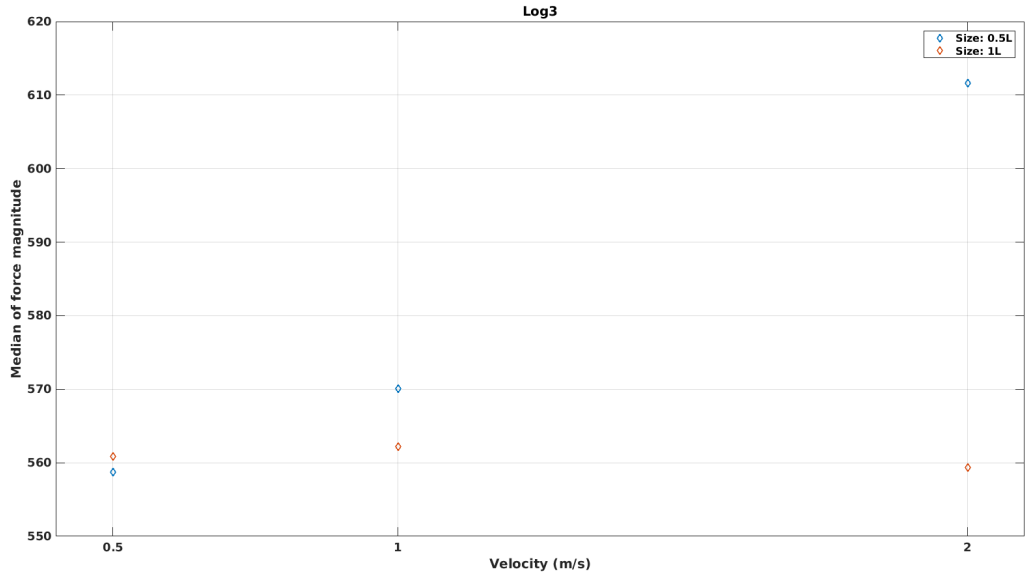

Figure A.32: Variation of median force magnitude with flow velocity for Log3.

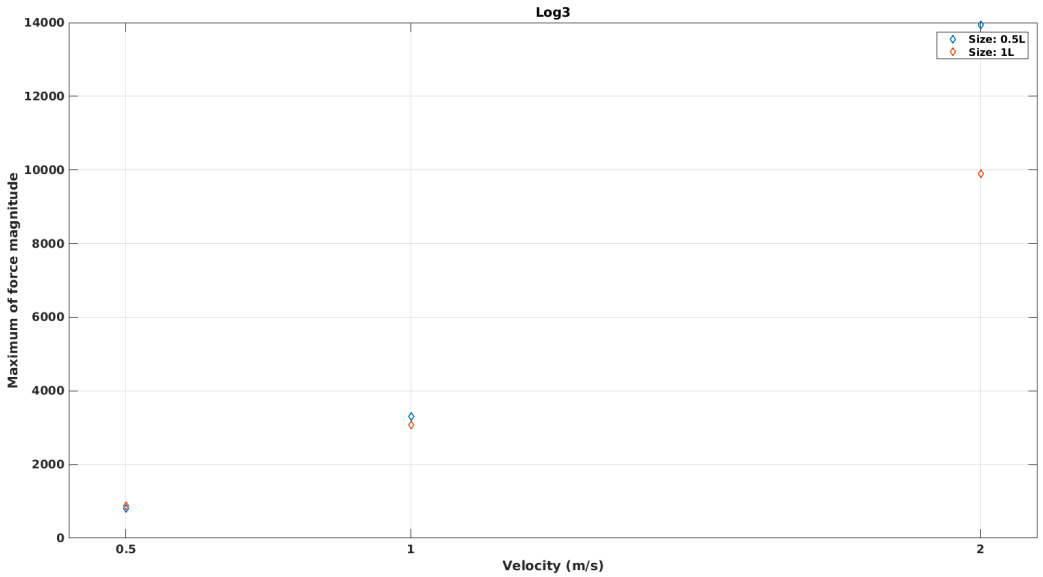

Figure A.33: Variation of maximum force magnitude with flow velocity for Log3.

Log4

This is the log that is injected from location 4 as shown in Figure 4.12. It is injected at the same time as logs 1, 2, and 3.

Figure A.34 shows the comparison of PDFs of the force magnitude for different log sizes at V = 0.5 m/s. Log4 of size 0.5L has a higher probability of forces being around the mean than that for size 1L. Log of size 1L has a higher probability of forces being large and small as well.

Figure A.35 shows the comparison of the PDFs of the force magnitude for different log sizes at V = 1.0 m/s. Log4 of size 1L has higher probability of force being around the mean than that for size 0.5L.

Figure A.36 shows the comparison of the PDFs of Log4 force magnitude for different log sizes at V = 2.0 m/s. Probability of forces being around the mean is higher for log size 1L than that for size 1L. Log of size 0.5L has higher probability of forces being large.

Figures A.37, A.38, and A.39 show the variation of mean, median, and maximum of Log 4 force magnitude for different log sizes. There is no consistency in variation of mean and median force with log size. Maximum force shows an increasing trend with velocity but the variation is very small for V = 0.5 m/s and V = 1 m/s.

Figures A.40 and A.41 show the comparison of the PDFs of Log4 force magnitude for the two log sizes at different flow velocities. As the velocity increases, the probability of higher forces on log increases. The momentum of logs increases with velocities and therefore so does the impact force.

Figures A.42, A.43, and A.44 show the variation of mean, median, and maximum of Log4 force magnitude for different flow velocities. Both mean and maximum force show an increasing trend with velocity. The variation is quadratic. Median force for log size 0.5L shows a decreasing trend.

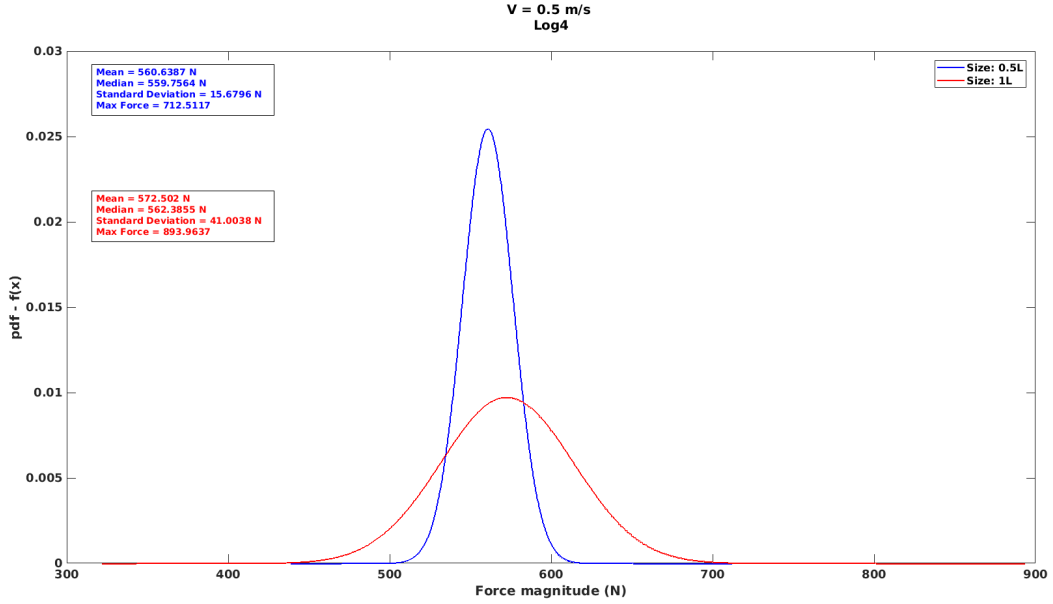

Figure A.34: Comparison of the PDFs of the forces on Log4 at V = 0.5 m/s.

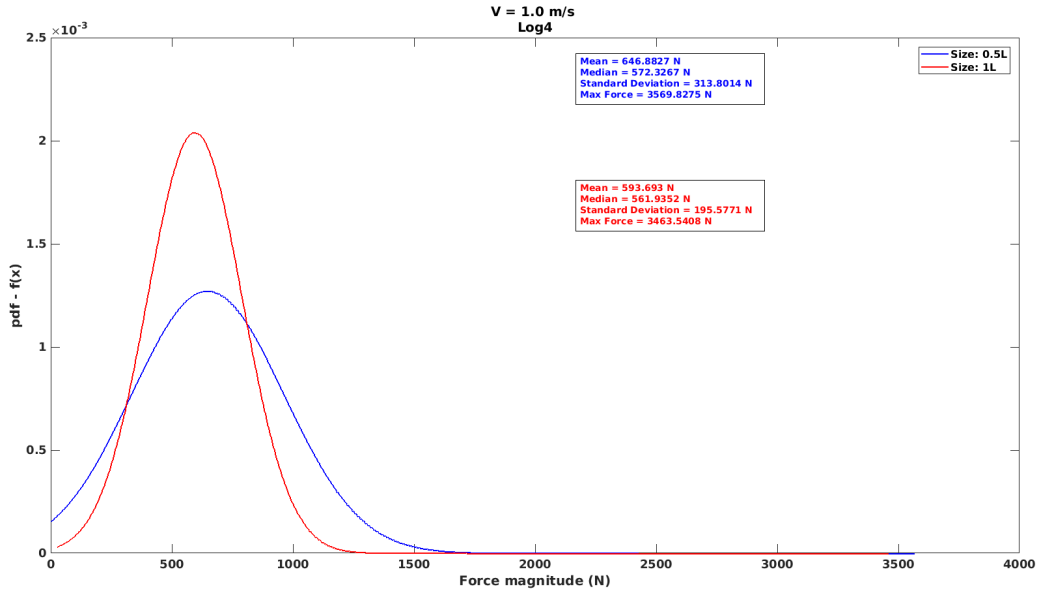

Figure A.35: Comparison of the PDFs of the forces on Log4 at V = 1.0 m/s.

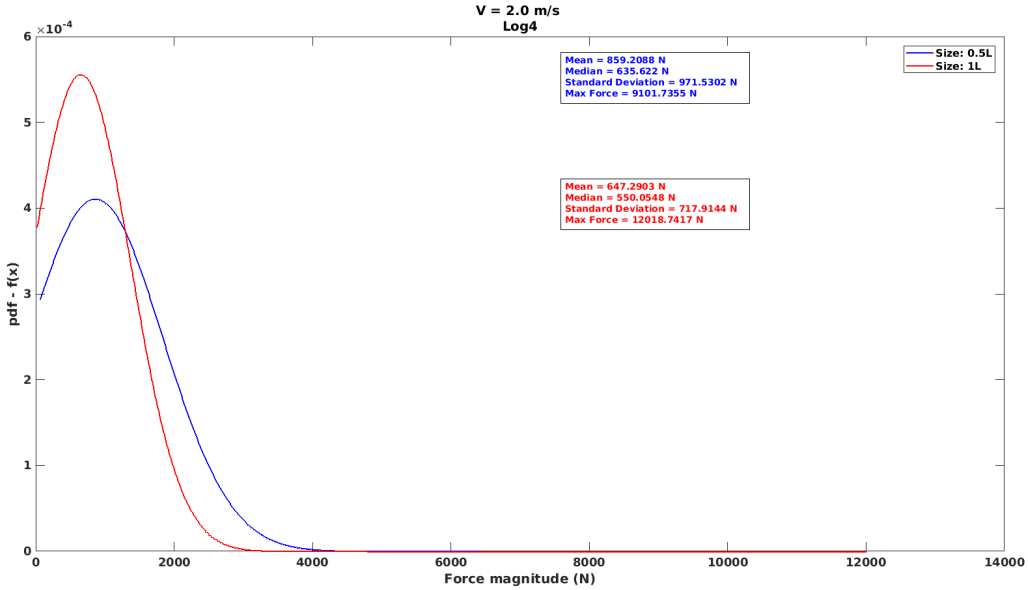

Figure A.36: Comparison of the PDFs of the forces on Log4 at V = 2.0 m/s.

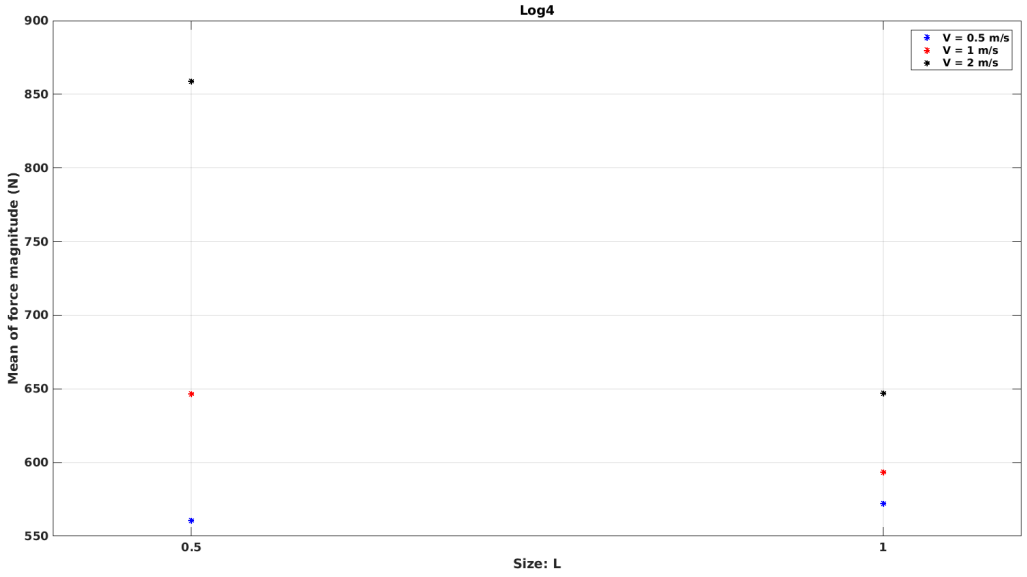

Figure A.37: Variation of mean force magnitude with log size for Log4.

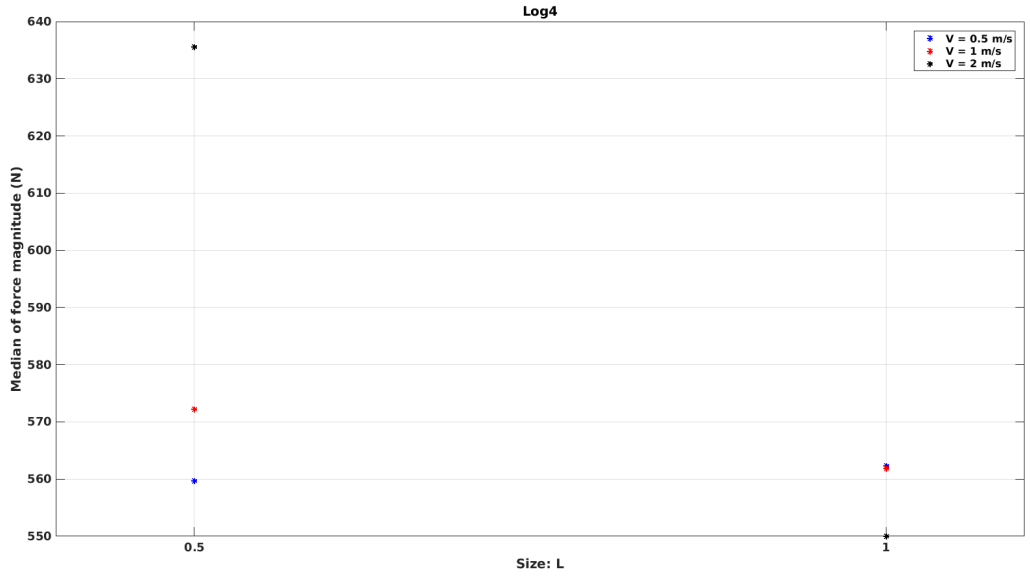

Figure A.38: Variation of median force magnitude with log size for Log4.

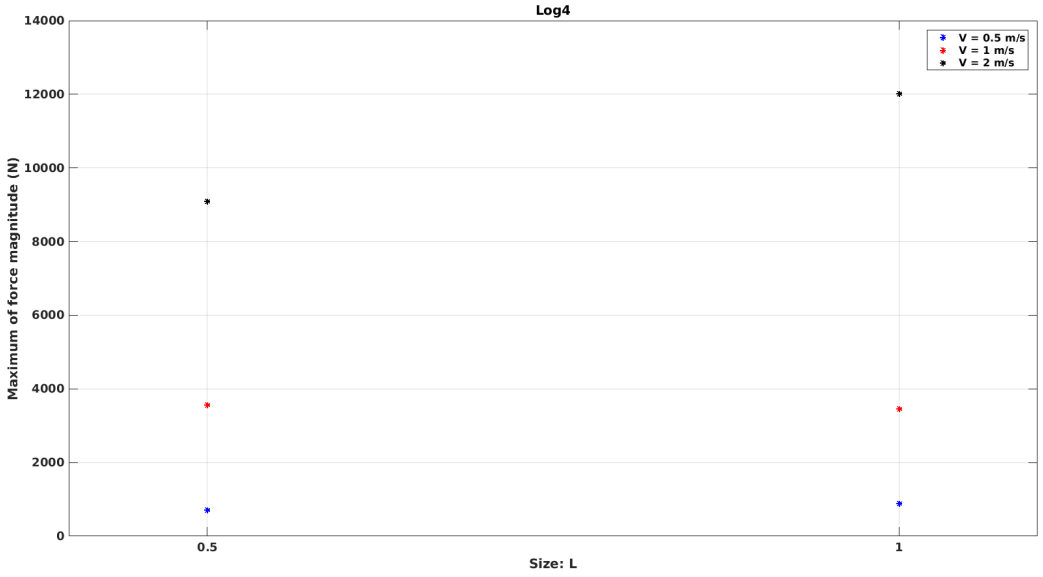

Figure A.39: Variation of maximum force magnitude with log size for Log4.

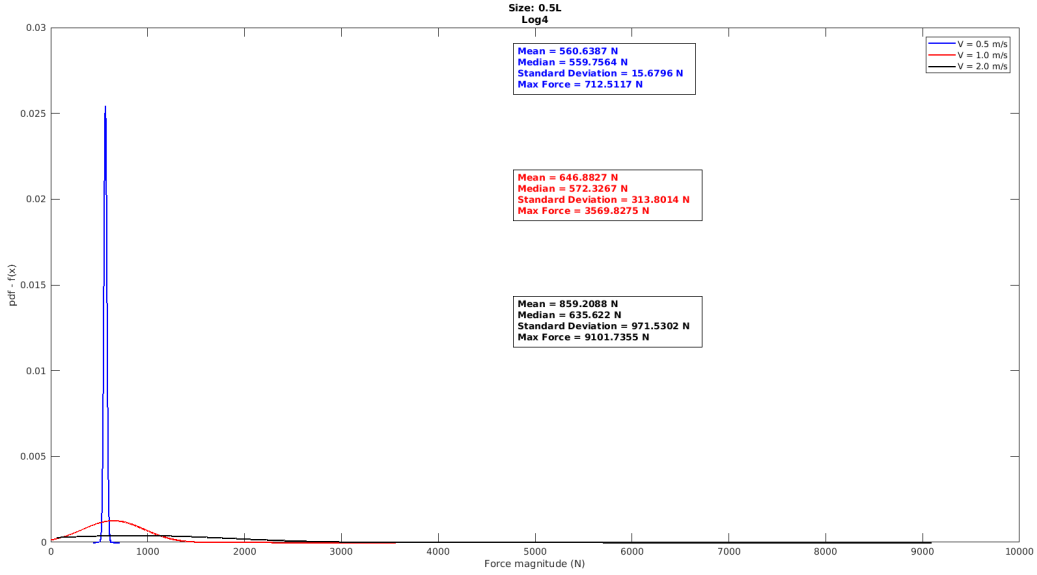

Figure A.40: Comparison of the PDFs of the forces on Log4 of size 0.5L.

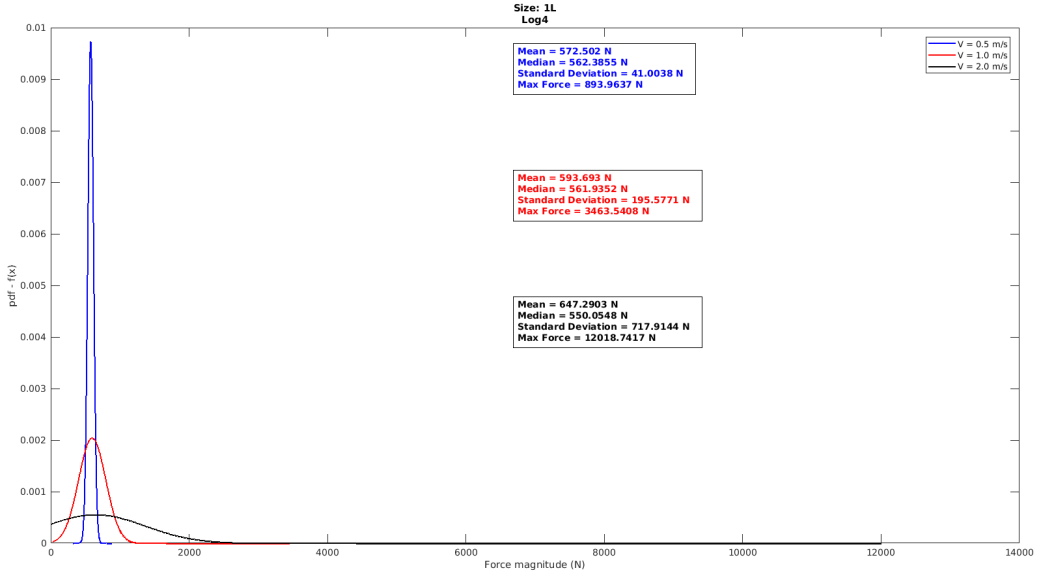

Figure A.41: Comparison of the PDFs of the forces on Log4 of size 1L.

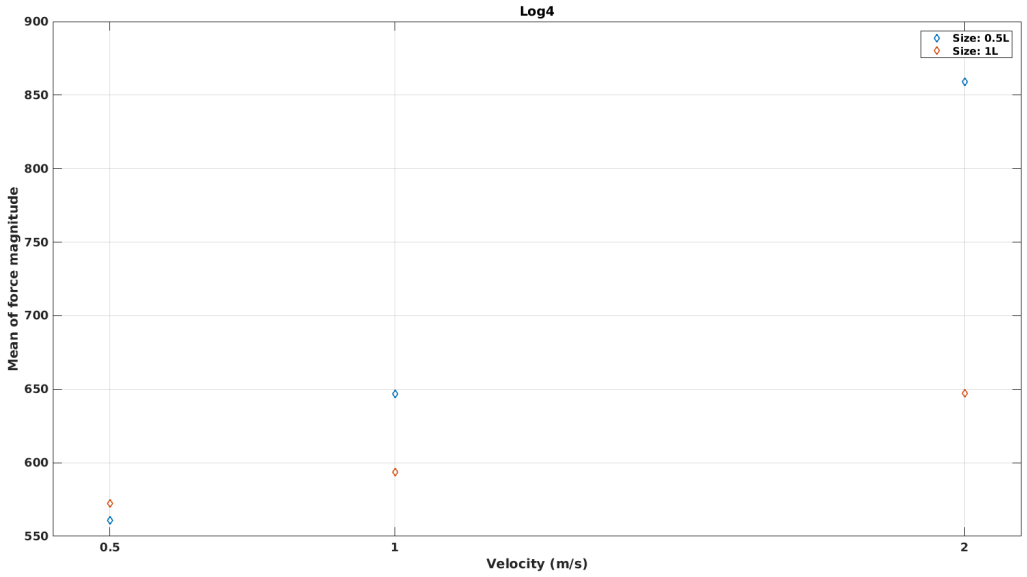

Figure A.42: Variation of mean force magnitude with flow velocity for Log4.

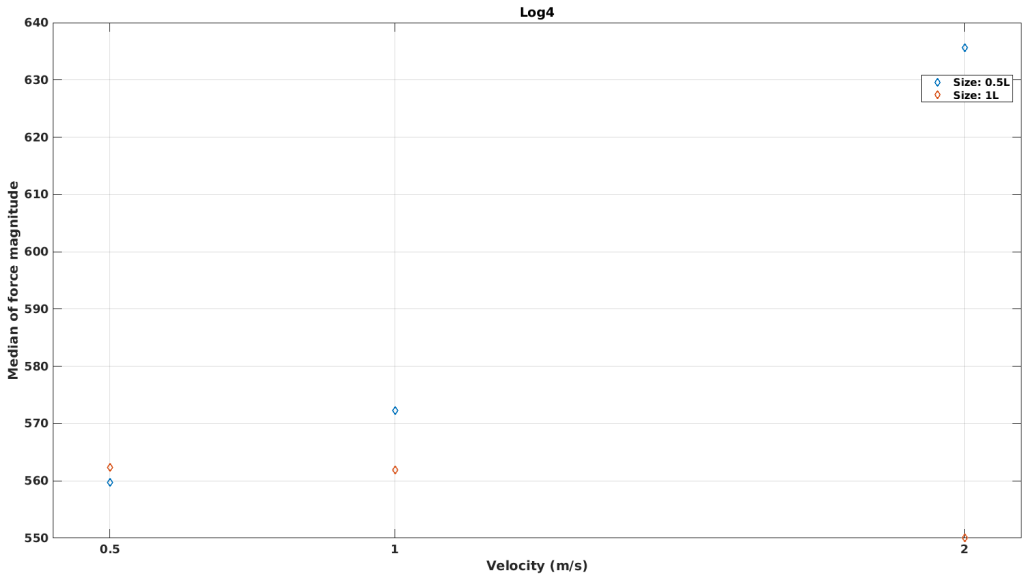

Figure A.43: Variation of median force magnitude with flow velocity for Log4.

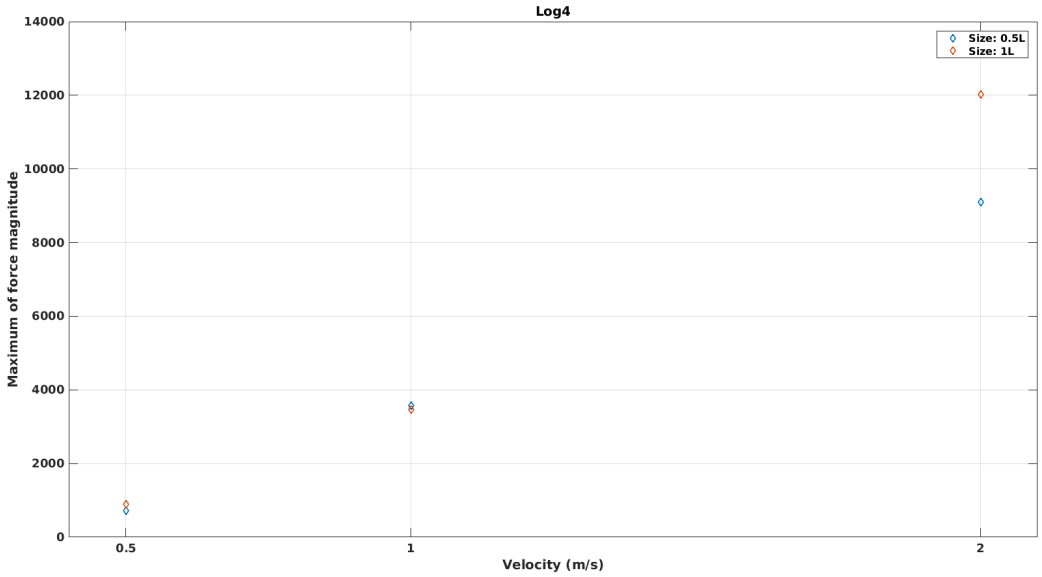

Figure A.44: Variation of maximum force magnitude with flow velocity for Log4.

Log5

This is the log that is injected from location 5 as shown in Figure 4.12. It is injected at the same time as logs 6, 7, and 8.

Figure A.45 shows the comparison of the PDFs of the Log5 force magnitudes for different log sizes at V = 0.5 m/s. Log5 of size 1L has higher probability of forces being around the mean than that for size 0.5L. Log of size 0.5L has higher probability of forces being large and small as well.

Figure A.46 shows the comparison of the PDFs of Log5 force magnitude for different log sizes at V = 1.0 m/s. The PDFs are very similar to each other with Log5 of size 1L having higher probability of force being around the mean.

Figure A.47 shows the comparison of the PDFs of Log5 force magnitude for different log sizes at V = 2.0 m/s. Probability of forces being around the mean is higher for log size 1L than that for size 1L. Log of size 0.5L has higher probability of forces being large.

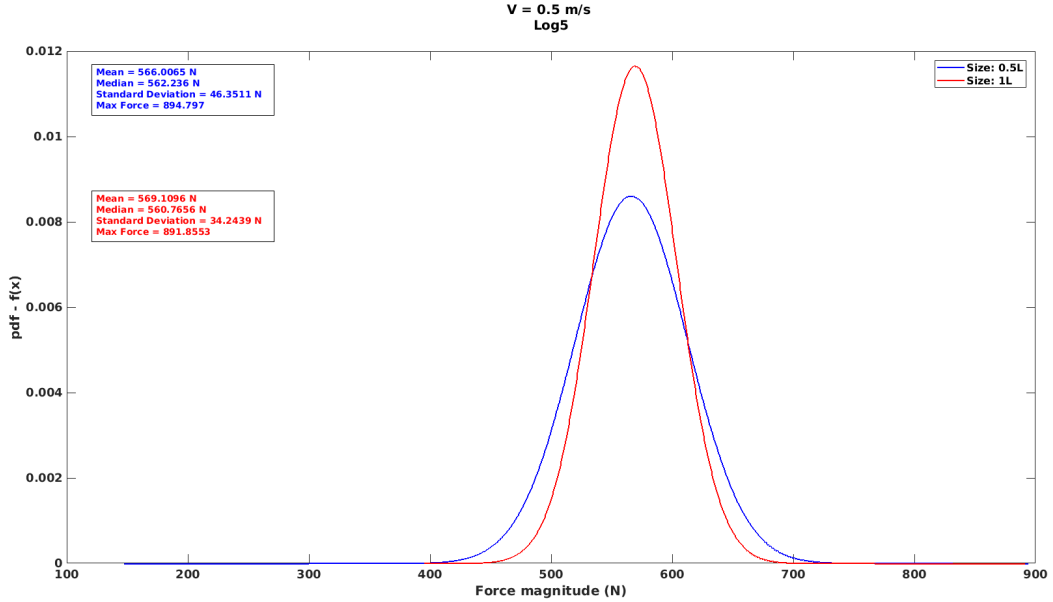

Figure A.45: Comparison of the PDFs of the forces on Log5 at V = 0.5 m/s.

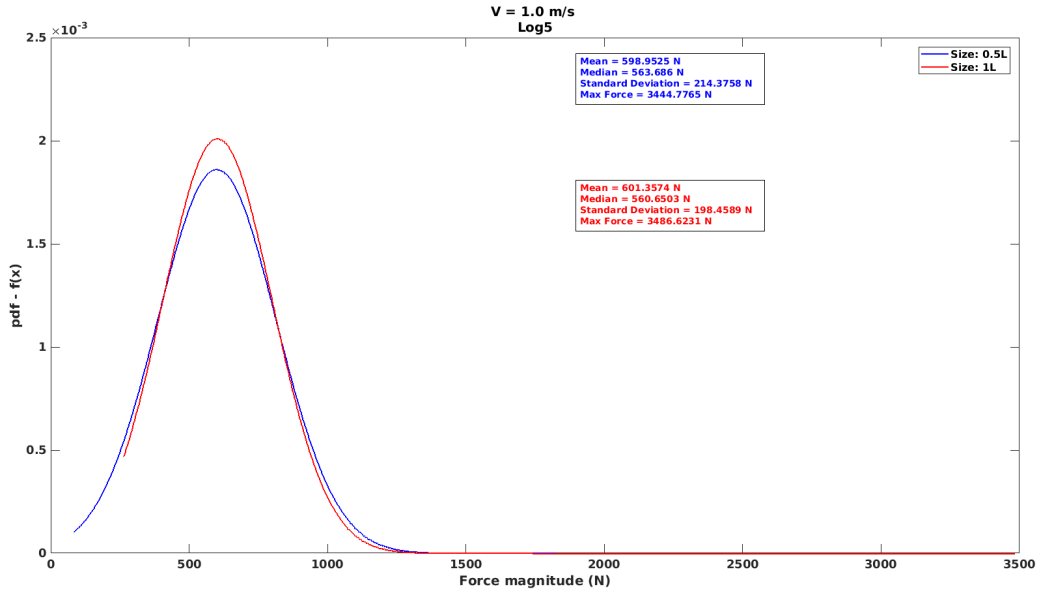

Figure A.46: Comparison of PDFs of forces on Log5 at V = 1.0 m/s.

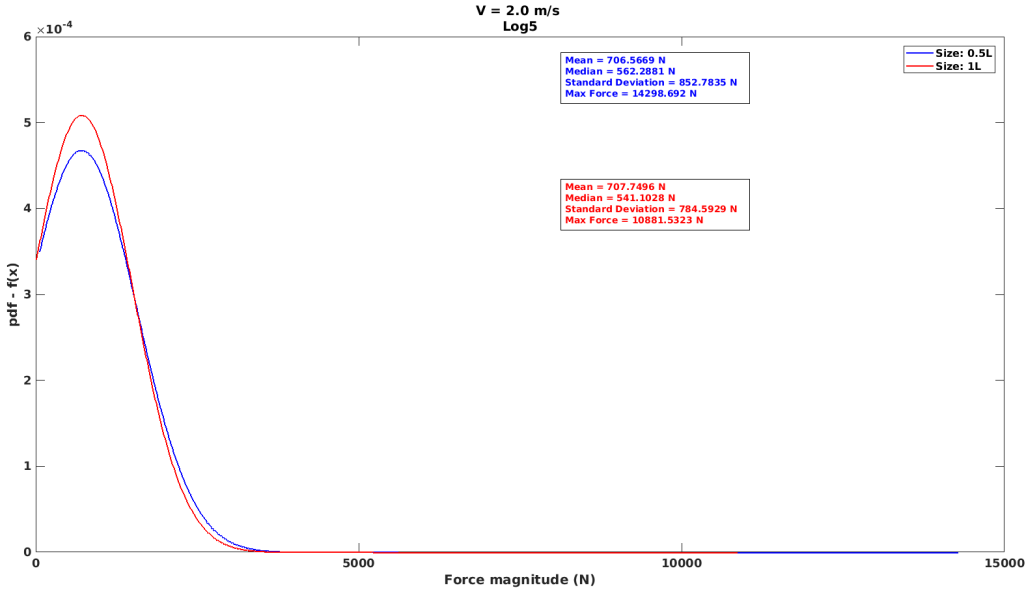

Figure A.47: Comparison of the PDFs of the forces on Log5 at V = 2.0 m/s.

Figures A.48, A.49, and A.50 show the variation of mean, median, and maximum of magnitude of force on Log5 at different log sizes. Mean force increases with size but the variation is very small. Median and maximum forces do not show a consistent behavior.

Figures A.51 and A.52 show the comparison of the PDFs of Log5 force magnitude for the two log sizes at different flow velocities. As the velocity increases, the probability of higher forces on log increases. The momentum of logs increases with velocities and therefore so does the impact force.

Figures A.53, A.54, and A.55 show the variation of mean, median, and maximum of Log5 force magnitude at different flow velocities. Both mean and maximum force show an increasing trend with velocity. The variation is quadratic. Median force for increases at first but then decreases.

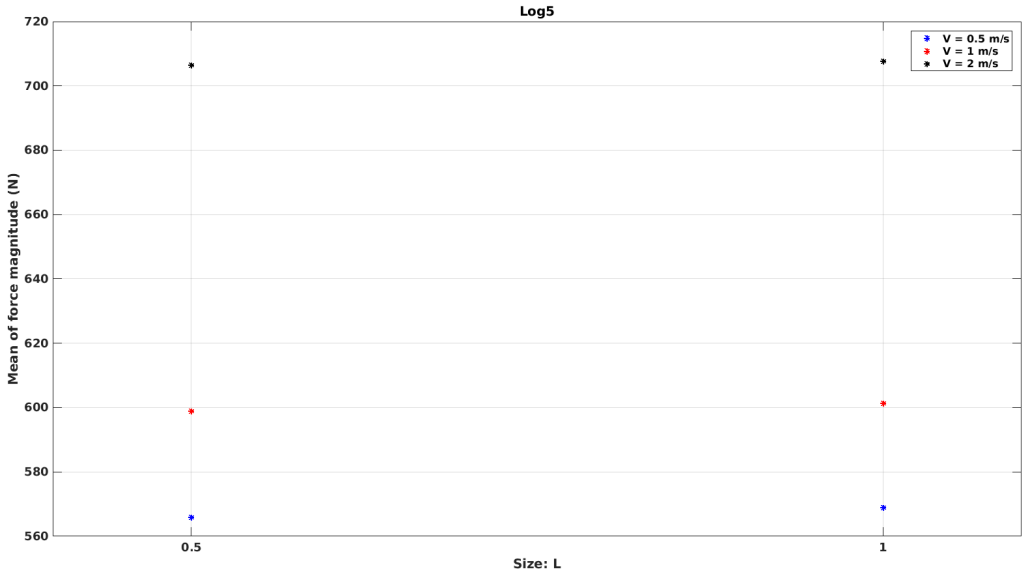

Figure A.48: Variation of mean force magnitude with log size for Log5.

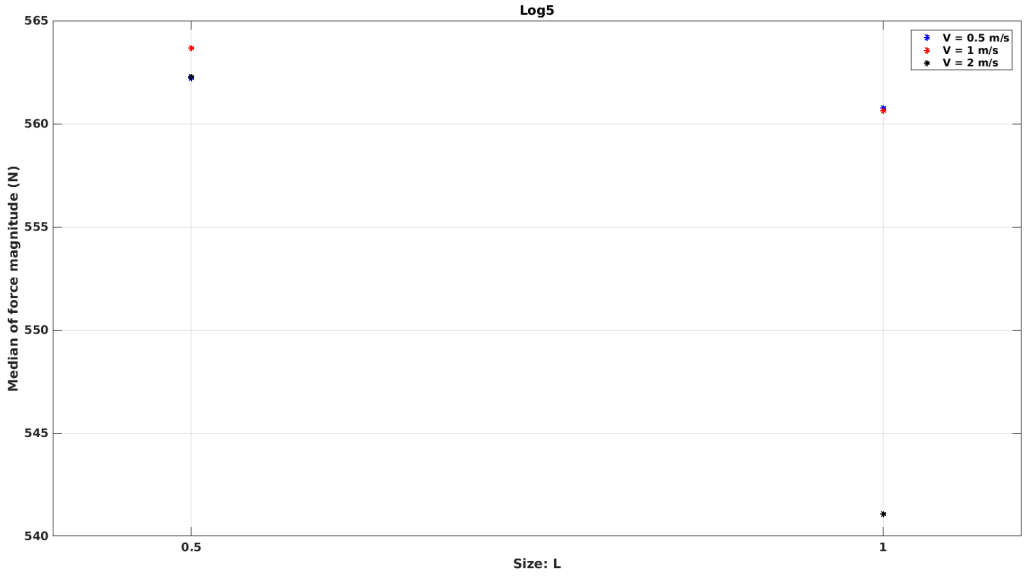

Figure A.49: Variation of median force magnitude with log size for Log5.

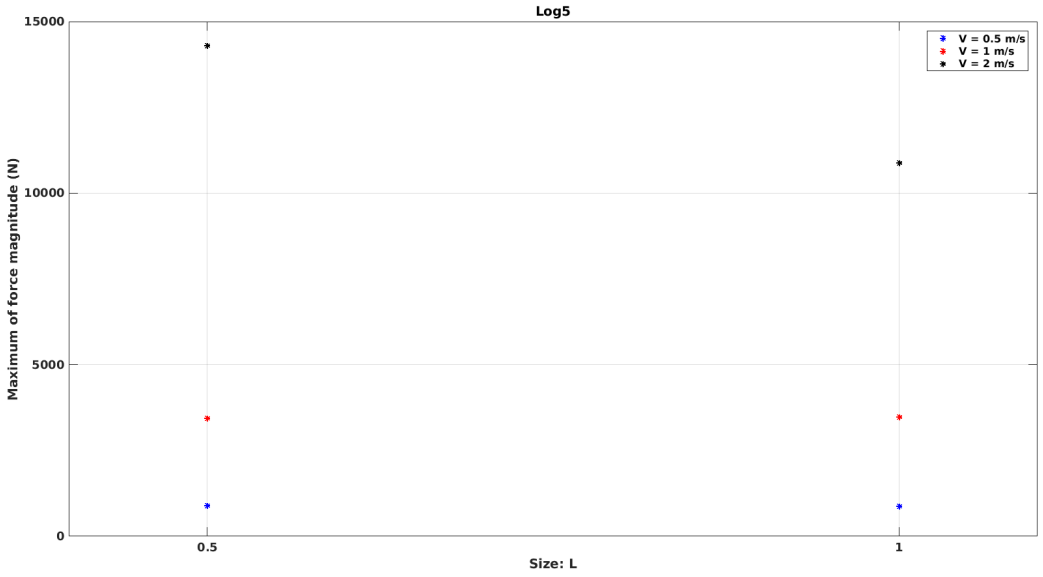

Figure A.50: Variation of maximum force magnitude with log size for Log5.

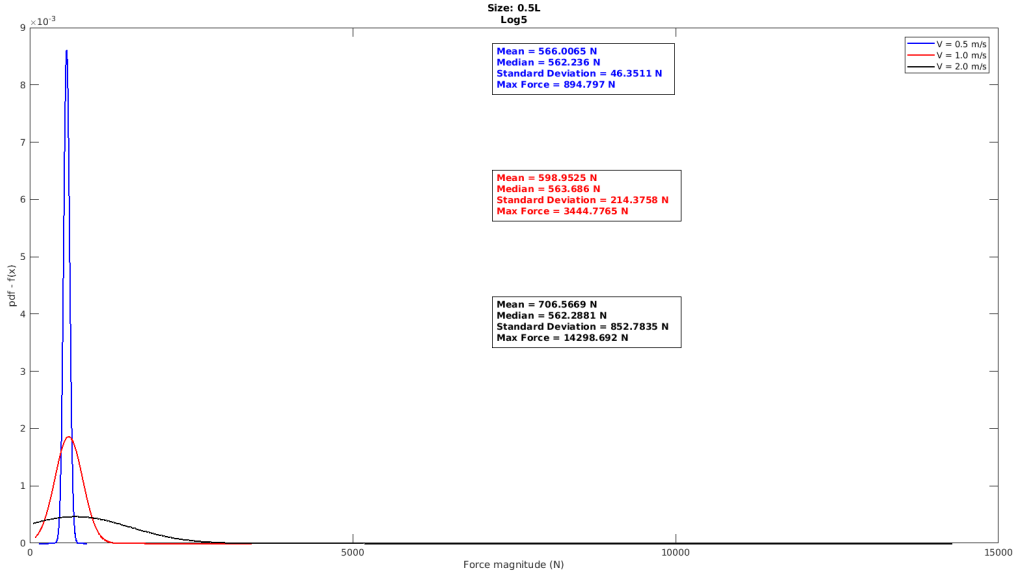

Figure A.51: Comparison of PDFs of forces on Log5 of size 0.5L.

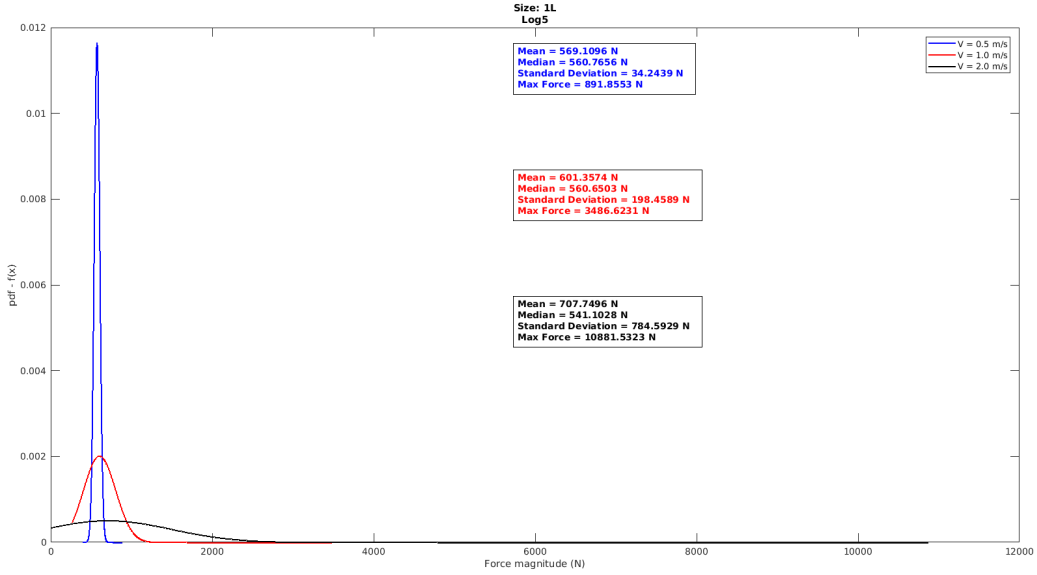

Figure A.52: Comparison of PDFs of forces on Log4 of size 1L.

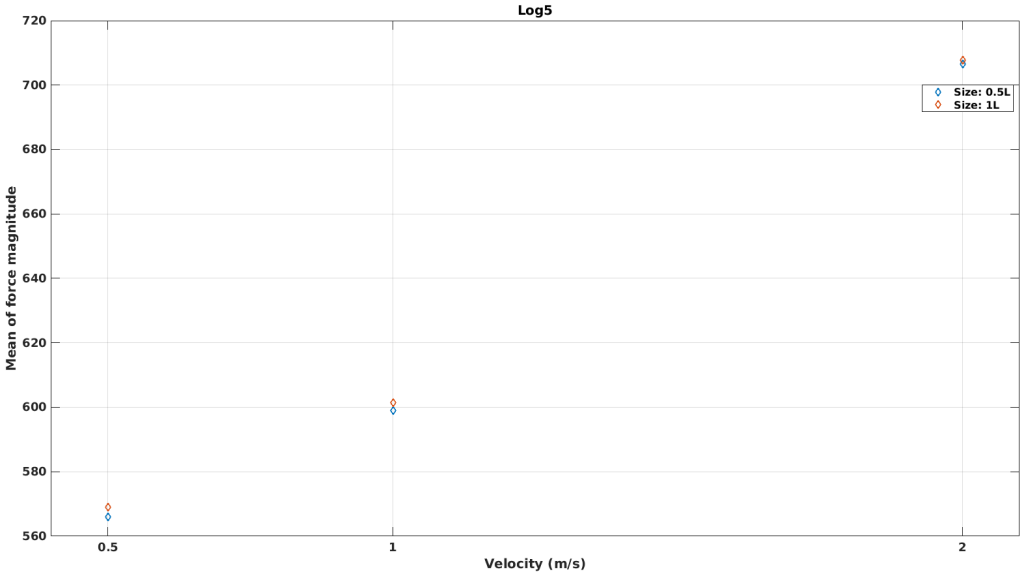

Figure A.53: Variation of mean force magnitude with flow velocity for Log5.

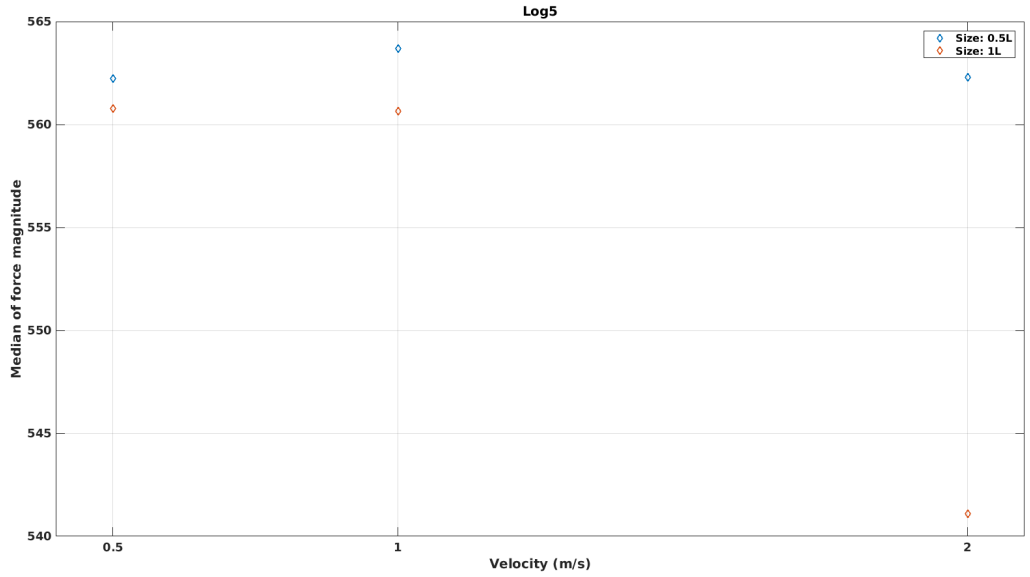

Figure A.54: Variation of median force magnitude with flow velocity for Log5.

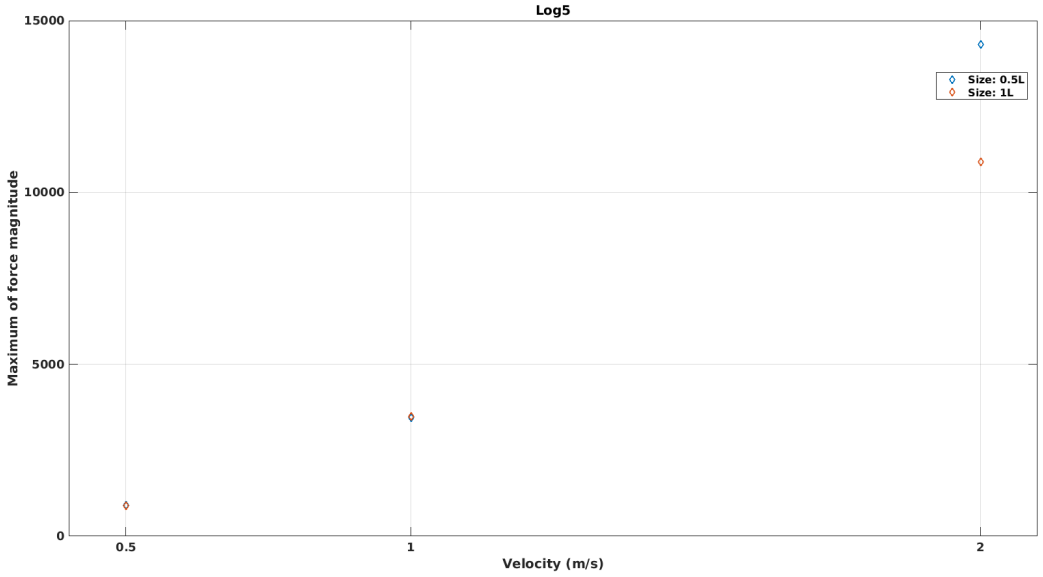

Figure A.55: Variation of maximum force magnitude with flow velocity for Log5.

Log6

This is the log that is injected from location 6 as shown in Figure 4.12. It is injected at the same time as logs 5, 7, and 8.

Figure A.56 shows the comparison of the PDFs of Log6 force magnitude for different log sizes at V = 0.5 m/s. Log6 of size 1L has higher probability of forces being around the mean than that for size 0.5L. Log of size 0.5L has higher probability of forces being large and small as well.

Figure A.57 shows the comparison of the PDFs of the force magnitude for different log sizes at V = 1.0 m/s. The PDFs are very similar to each other with Log6 of size 0.5L having higher probability of forces being lower than the mean.

Figure A.58 shows the comparison of the PDFs of Log6 force magnitude for different log sizes at V = 2.0 m/s. Probability of forces being around the mean is higher for log size 1L than that for size 0.5L. Apart from this, the PDFs are very similar to each other.

Figures A.59, A.60, and A.61 show the variation of mean, median, and maximum of magnitude of force on Log6 at different log sizes. Mean, median and maximum forces do not vary much.

Figures A.62 and A.63 show the comparison of the PDFs of Log6 force magnitude for the two log sizes at different flow velocities. As the velocity increases, the probability of higher forces on log increases. The momentum of logs increases with velocities and therefore so does the impact force.

Figures A.64, A.65, and A.66 show the variation of mean, median, and maximum Lo6 force magnitude at different flow velocities. Both mean and maximum force show an increasing trend with velocity. The variation is quadratic. Median force for increases at first but then decreases but the variation is very small.

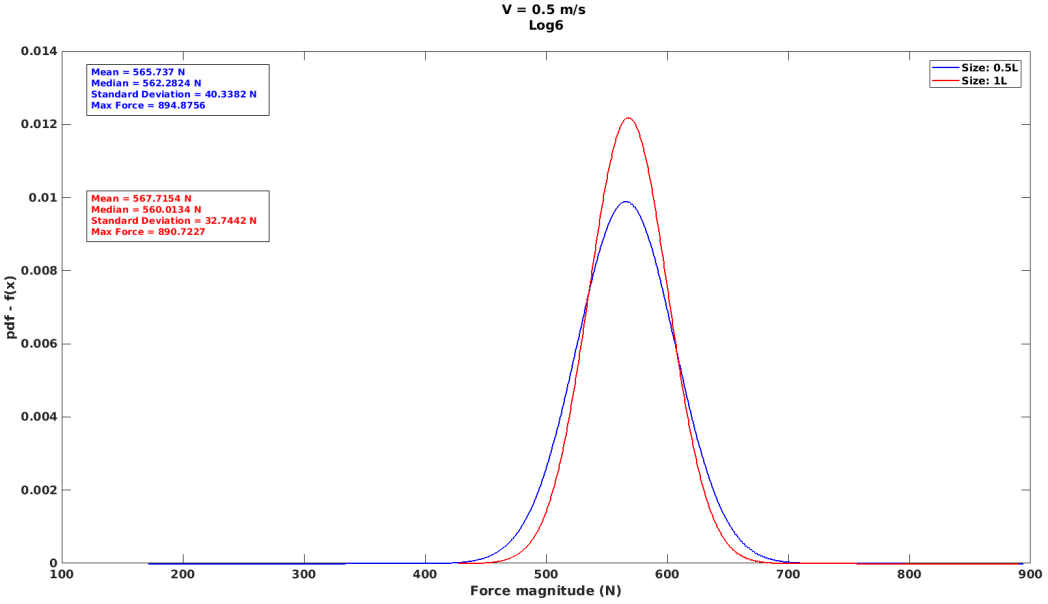

Figure A.56: Comparison of the PDFs of the forces on Log6 at V = 0.5 m/s.

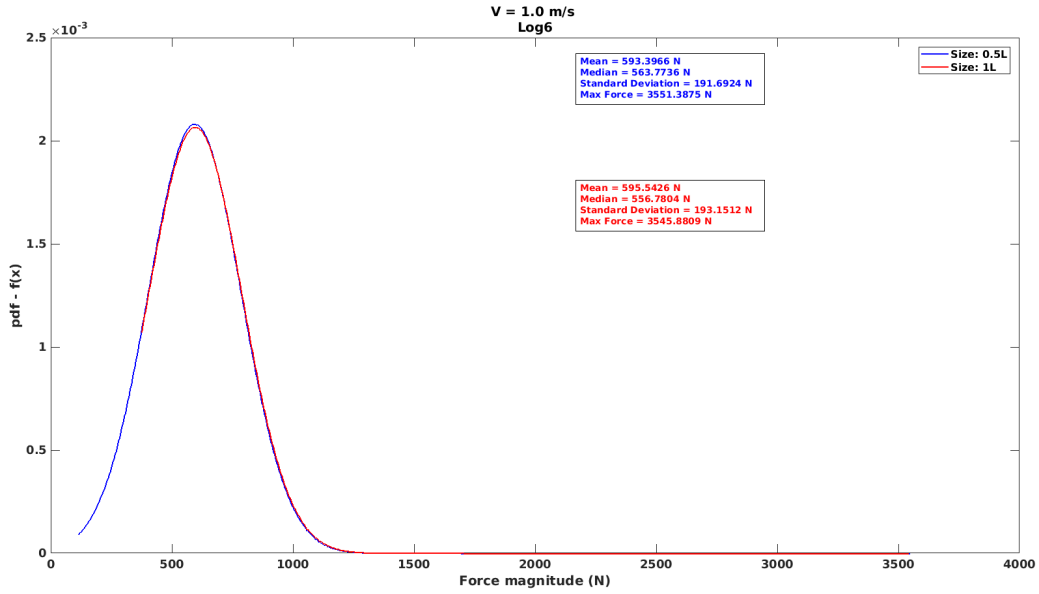

Figure A.57: Comparison of the PDFs of the forces on Log6 at V = 1.0 m/s.

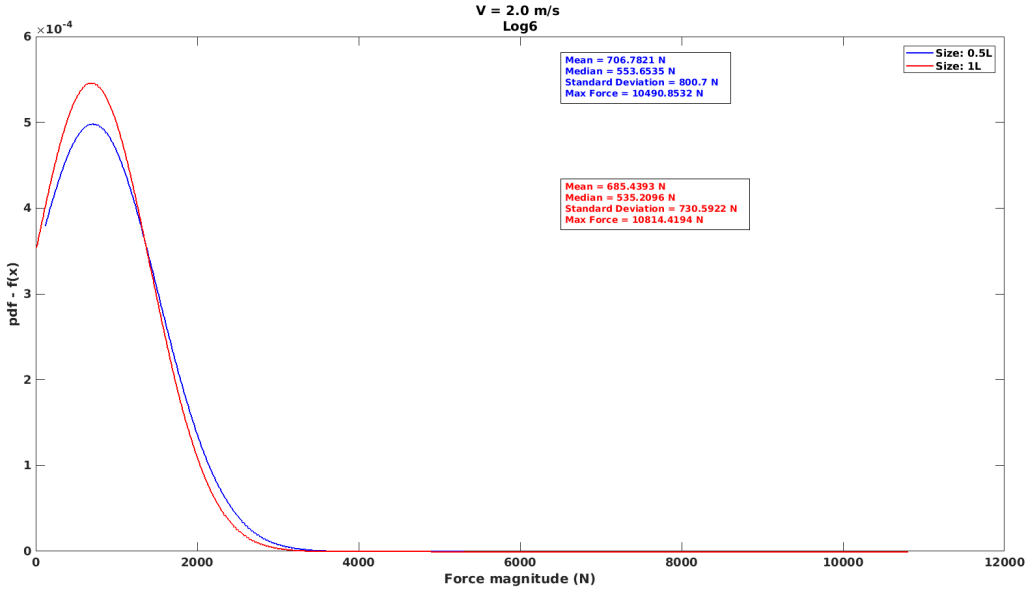

Figure A.58: Comparison of the PDFs of the forces on Log6 at V = 2.0 m/s.

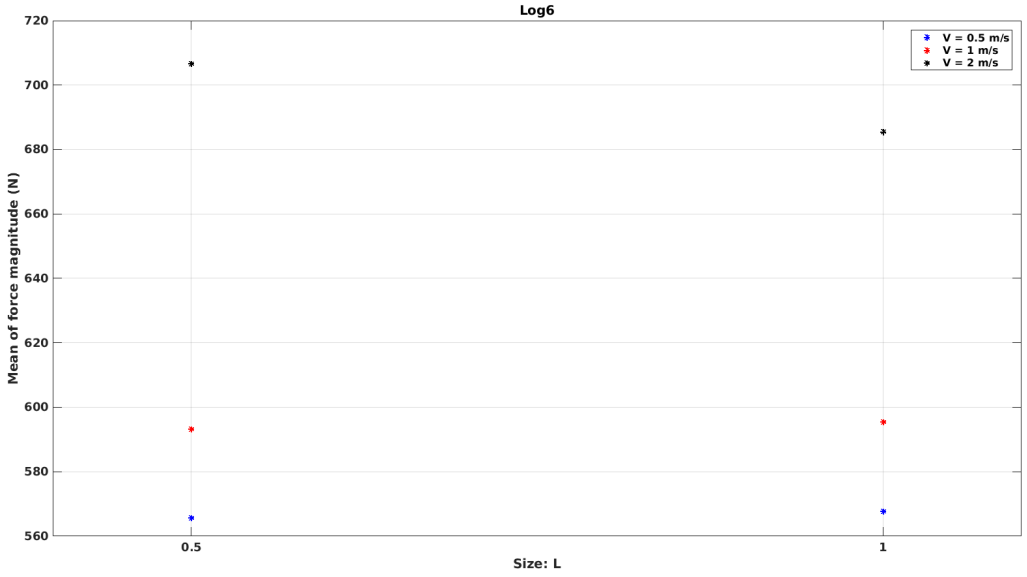

Figure A.59: Variation of mean force magnitude with log size for Log6.

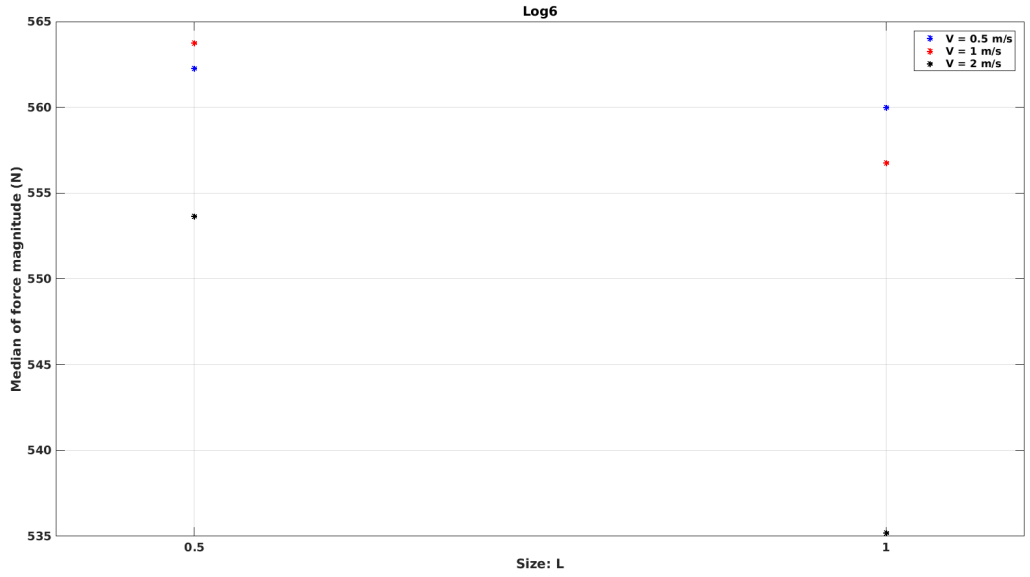

Figure A.60: Variation of median force magnitude with log size for Log6.

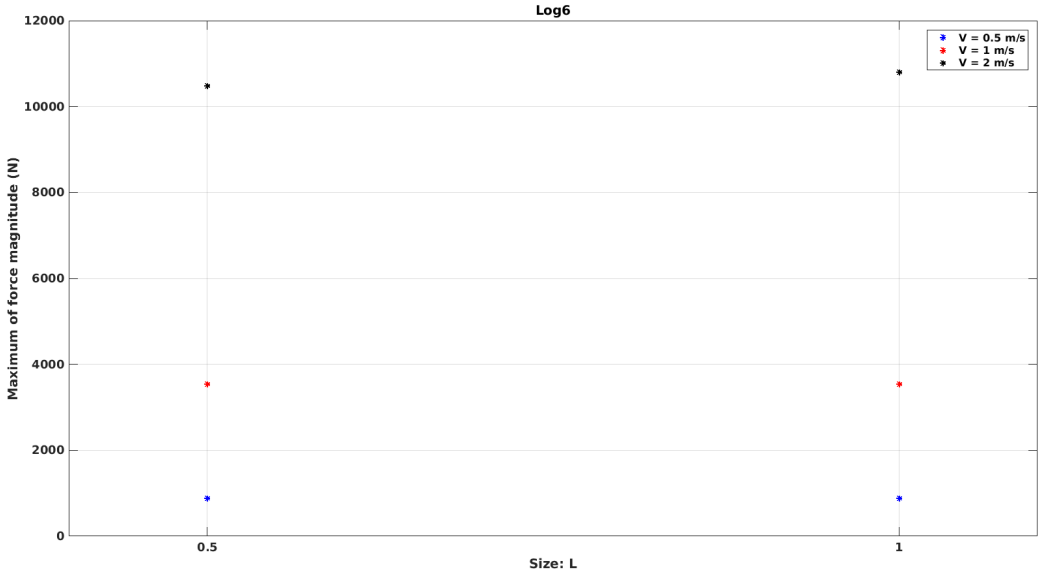

Figure A.61: Variation of maximum force magnitude with log size for Log6.

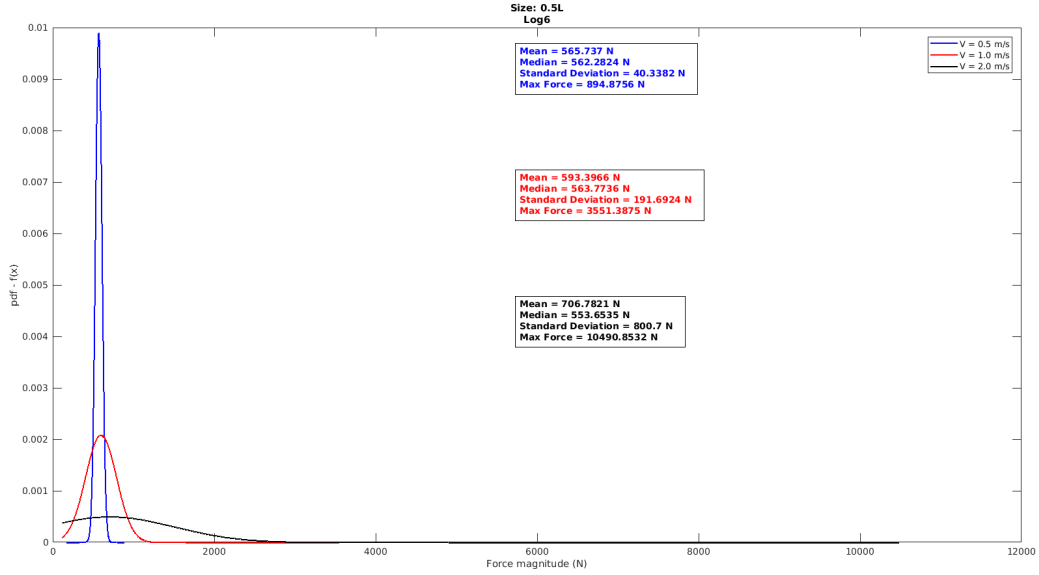

Figure A.62: Comparison of PDFs of forces on Log6 of size 0.5L.

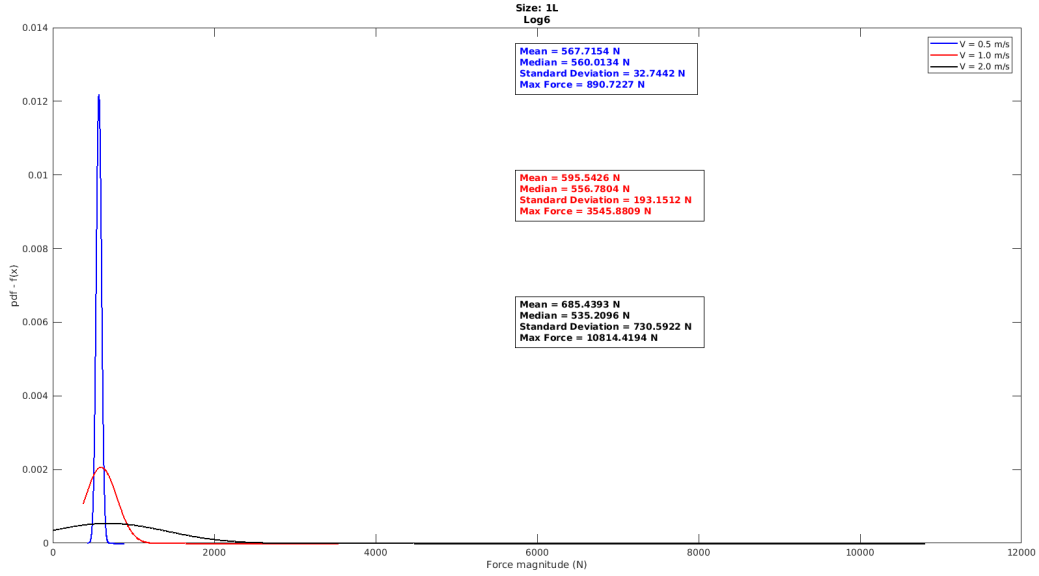

Figure A.63: Comparison of the PDFs of the forces on Log6 of size 1L.

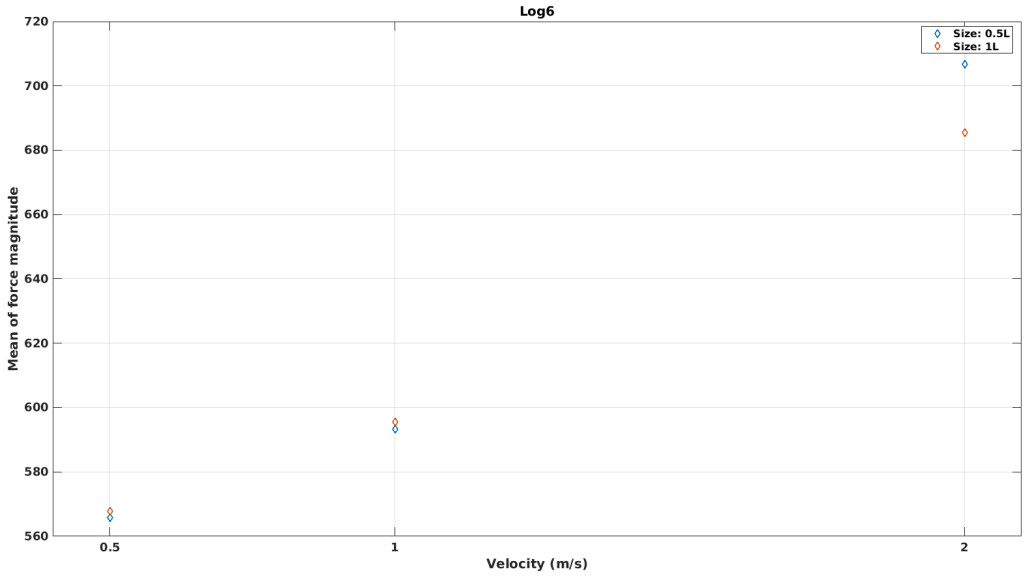

Figure A.64: Variation of mean force magnitude with flow velocity for Log6.

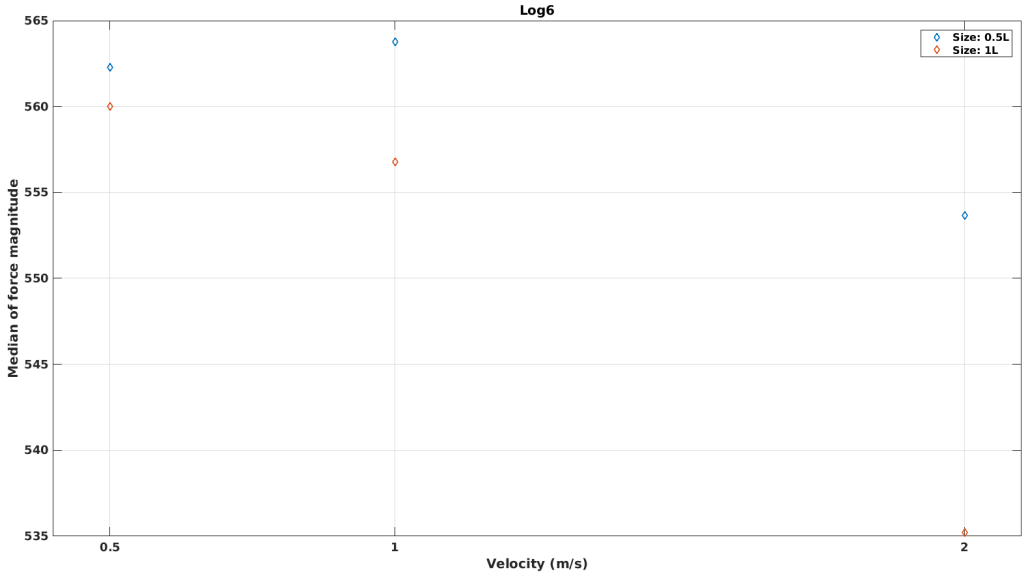

Figure A.65: Variation of median force magnitude with flow velocity for Log6.

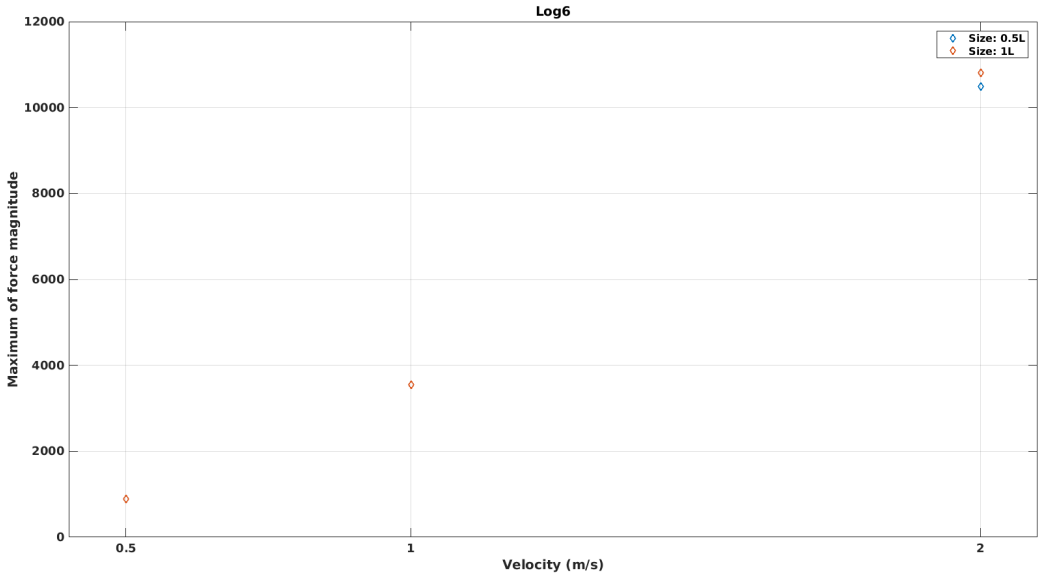

Figure A.66: Variation of maximum force magnitude with flow velocity for Log6.

Log7

This is the log that is injected from location 7 as shown in Figure 4.12. It is injected at the same time as logs 5, 6, and 8.

Figure A.67 shows the comparison of the PDFs of Log7 force magnitude for different log sizes at V = 0.5 m/s. Log7 of size 1L has higher probability of forces being around the mean than that for size 0.5L. Log of size 0.5L has higher probability of forces being large and small as well.

Figure A.68 shows the comparison of the PDFs of Log7 force magnitude for different log sizes at V = 1.0 m/s. The PDFs are very similar to each other with Log7 of size 1L having higher probability of forces being higher than the mean.

Figure A.69 shows the comparison of the PDFs of Log7 force magnitude for different log sizes at V = 2.0 m/s. Probability of forces being around the mean is higher for log size 0.5L than that for size 0.5L. Log7 of size 1L has higher probability of force being large.

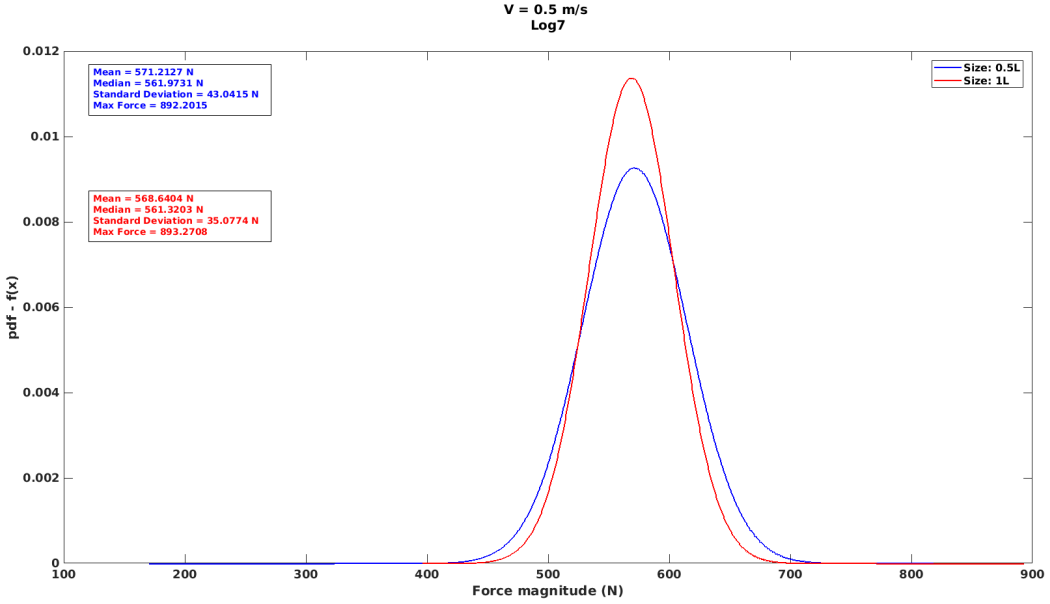

Figure A.67: Comparison of PDFs of forces on Log7 at V = 0.5 m/s.

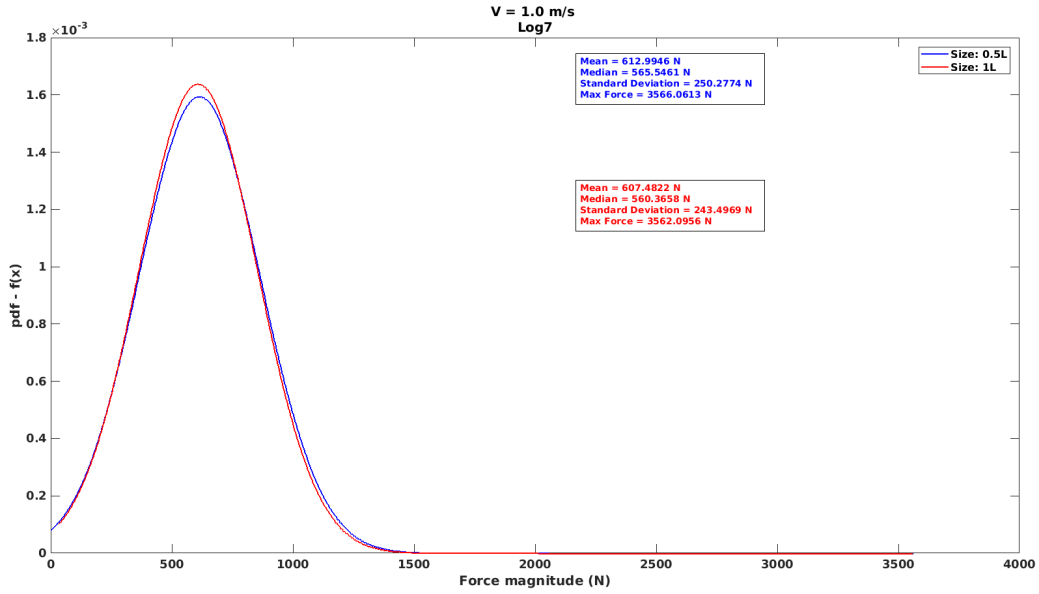

Figure A.68: Comparison of the PDFs of the forces on Log7 at V = 1.0 m/s.

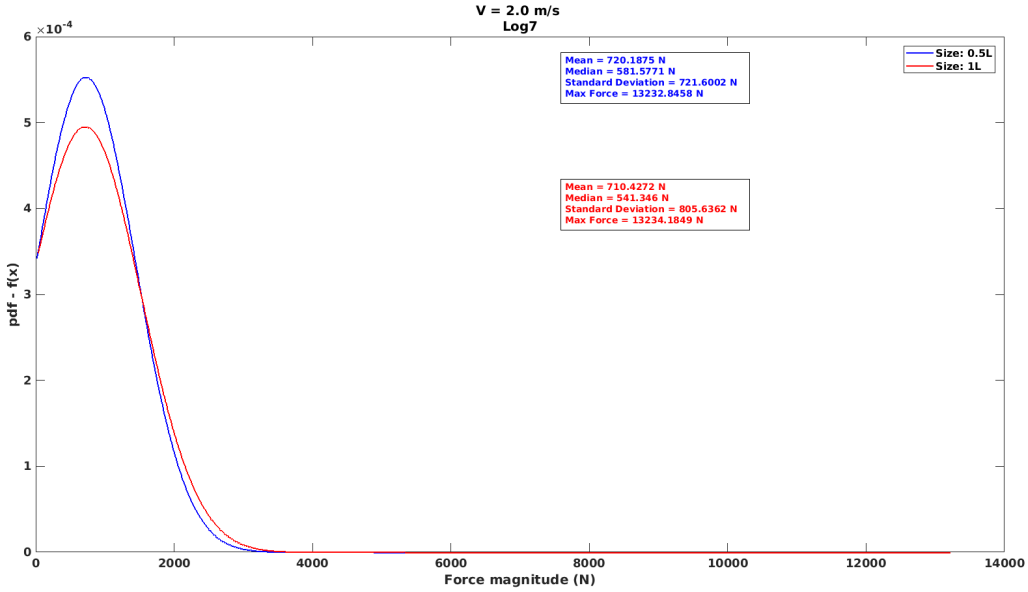

Figure A.69: Comparison of the PDFs of the forces on Log7 at V = 2.0 m/s.

Figures A.70, A.71, and A.72 show the variation of mean, median, and maximum of Log7 force magnitude at different log sizes. Median force does not have a consistent behavior. Mean and Maximum forces remain fairly constant for both cases.

Figures A.73 and A.74 show the comparison of PDFs of Log7 force magnitude for the two log sizes at different flow velocities. As the velocity increases, the probability of higher forces on log increases. The momentum of logs increases with velocities and therefore so does the impact force.

Figures A.75, A.76, and A.77 show the variation of mean, median, and maximum of Log7 force magnitude for different flow velocities. Both mean and maximum force show an increasing trend with velocity. The variation is quadratic. Median force for increases with velocity for size 0.5L but decreases for size 1L.

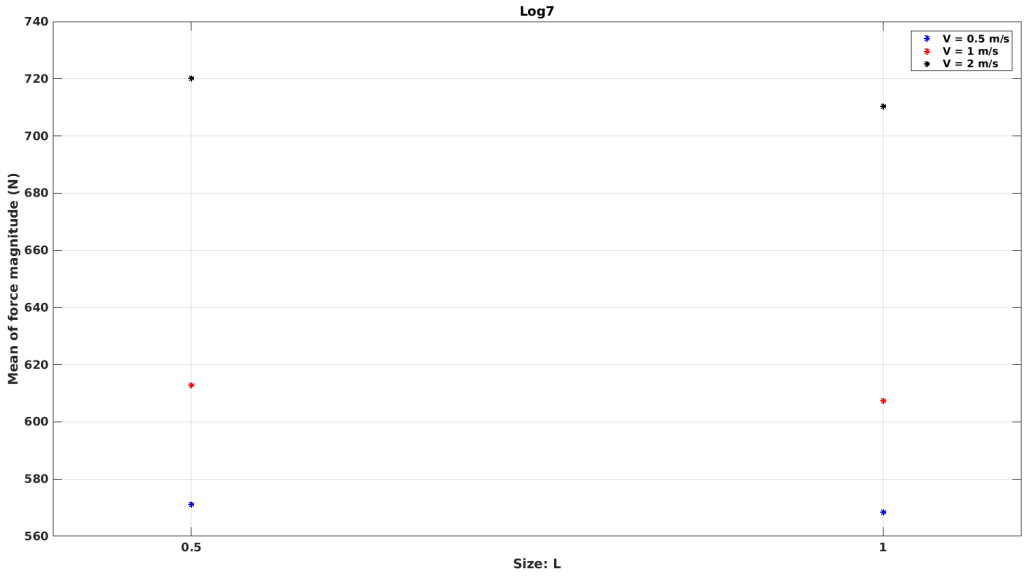

Figure A.70: Variation of mean force magnitude with log size for Log7.

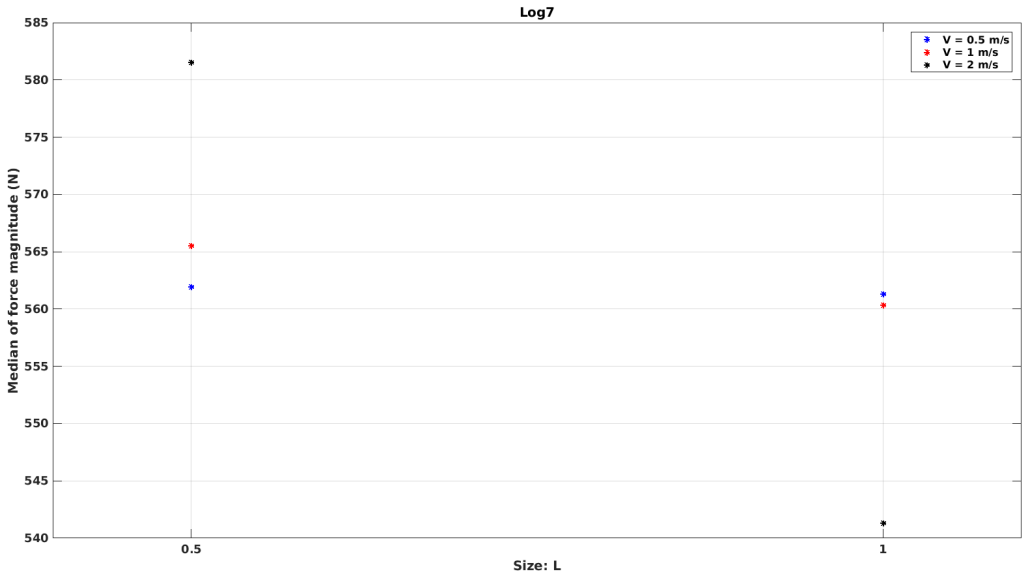

Figure A.71: Variation of median force magnitude with log size for Log7.

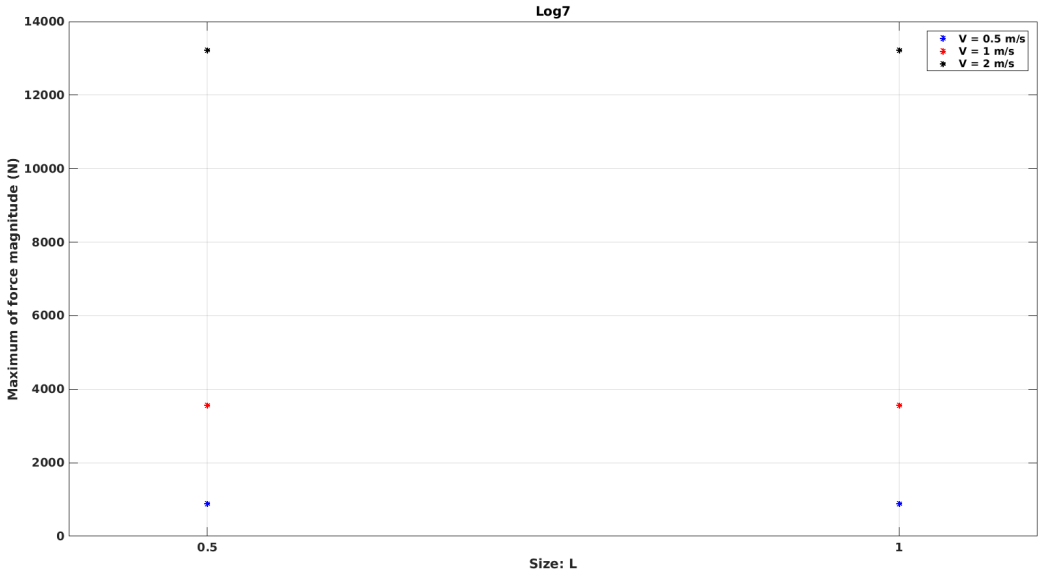

Figure A.72: Variation of maximum force magnitude with log size for Log7.

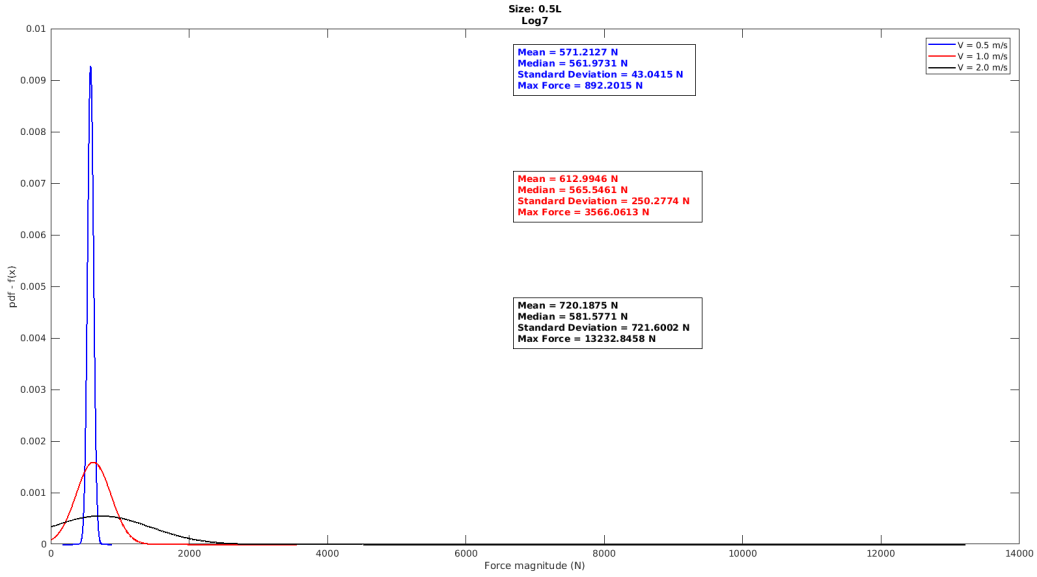

Figure A.73: Comparison of PDFs of forces on Log7 of size 0.5L.

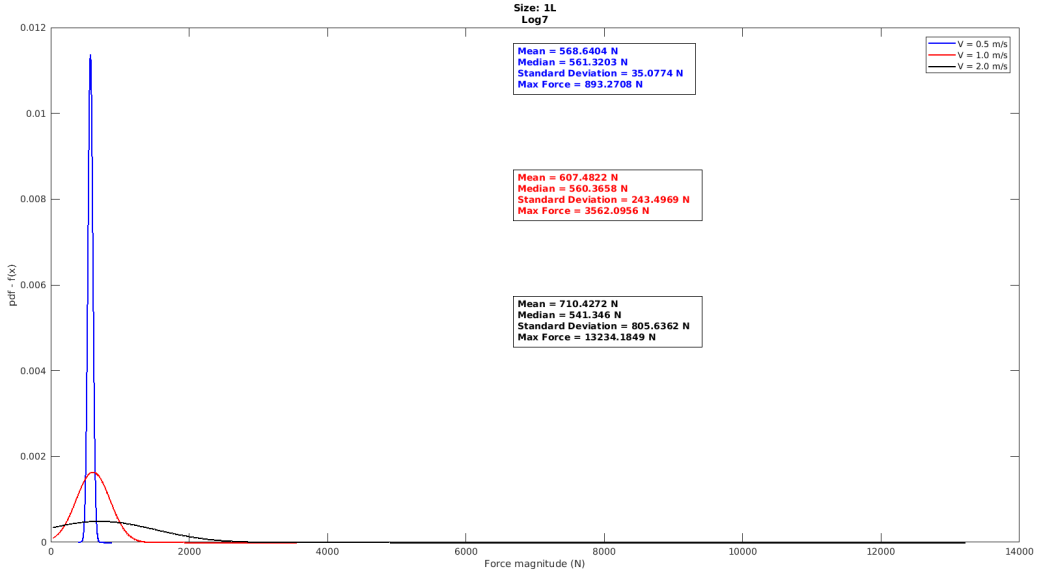

Figure A.74: Comparison of PDFs of forces on Log7 of size 1L.

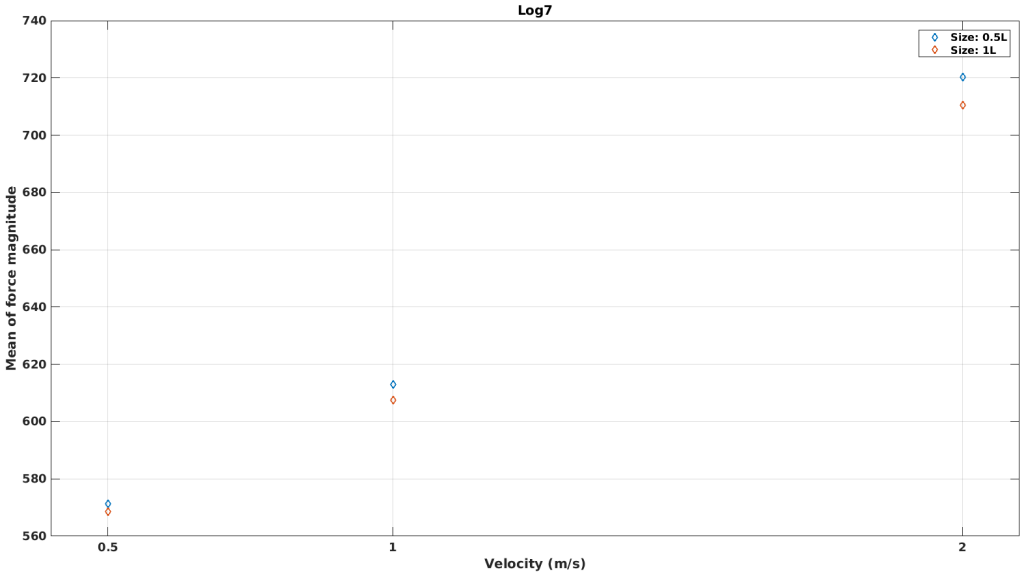

Figure A.75: Variation of mean force magnitude with flow velocity for Log7.

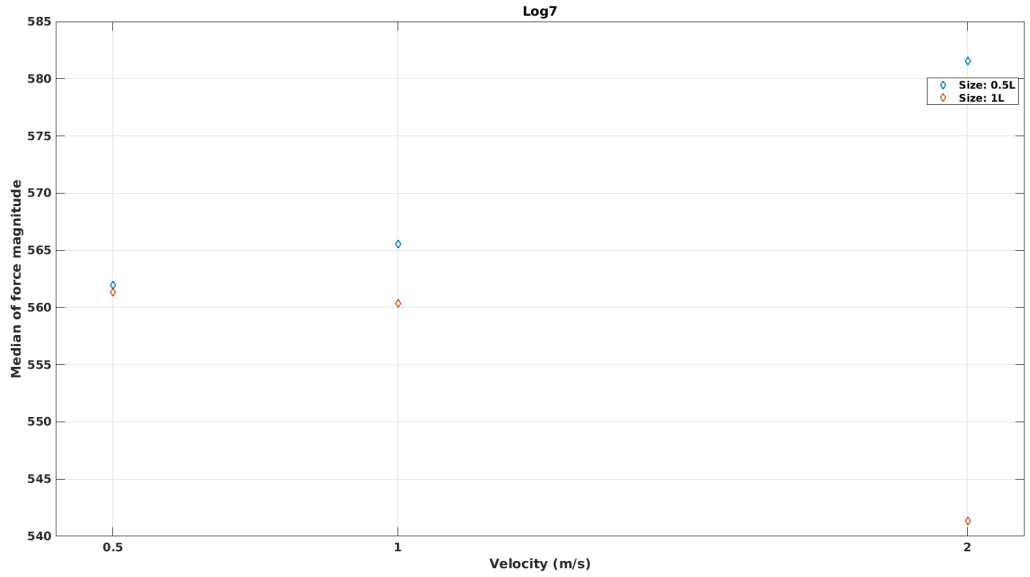

Figure A.76: Variation of median force magnitude with flow velocity for Log7.

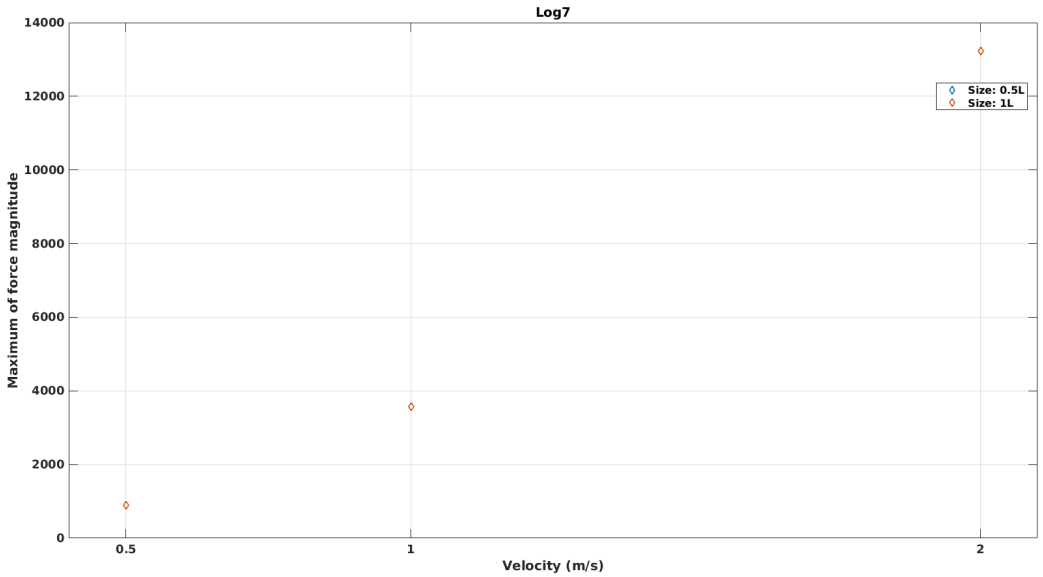

Figure A.77: Variation of maximum force magnitude with flow velocity for Log7.

Log8

This is the log that is injected from location 8 as shown in Figure 4.12. It is injected at the same time as logs 5, 6, and 7.

Figure A.78 shows the comparison of the PDFs of Log8 force magnitude for different log sizes at V = 0.5 m/s. Log8 of size 1L has higher probability of forces being around the mean than that for size 0.5L. Log of size 0.5L has higher probability of forces being large and small as well.

Figure A.79 shows the comparison of the PDFs of the force magnitude for different log sizes at V = 1.0 m/s. Log8 of size 1L has higher probability of force being around the mean. Log of size 0.5L has higher probability of forces being large and small as well.

Figure A.80 shows the comparison of the PDFs of Log8 force magnitude for different log sizes at V = 2.0 m/s. Probability of forces being around the mean is higher for log size 0.5L than that for size 0.5L. Log8 of size 1L has higher probability of force being large.

Figures A.81, A.82, and A.83 show the variation of mean, median, and maximum Log8 force magnitude for different log sizes. Mean force remains fairly constant. Median force shows inconsistent variation. Maximum force shows an increasing trend.

Figures A.84 and A.85 show the comparison of the PDFs of Log8 force magnitude for the two log sizes at different flow velocities. As the velocity increases, the probability of higher forces on log increases. The momentum of logs increases with velocities and therefore so does the impact force.

Figures A.86, A.87, and A.88 show the variation of mean, median, and maximum of Log8 force magnitude for different flow velocities. Both mean and maximum force show an increasing trend with velocity. The variation is quadratic. Median force for decreases with velocity for size 1L but increases and then decreases for size 0.5L.

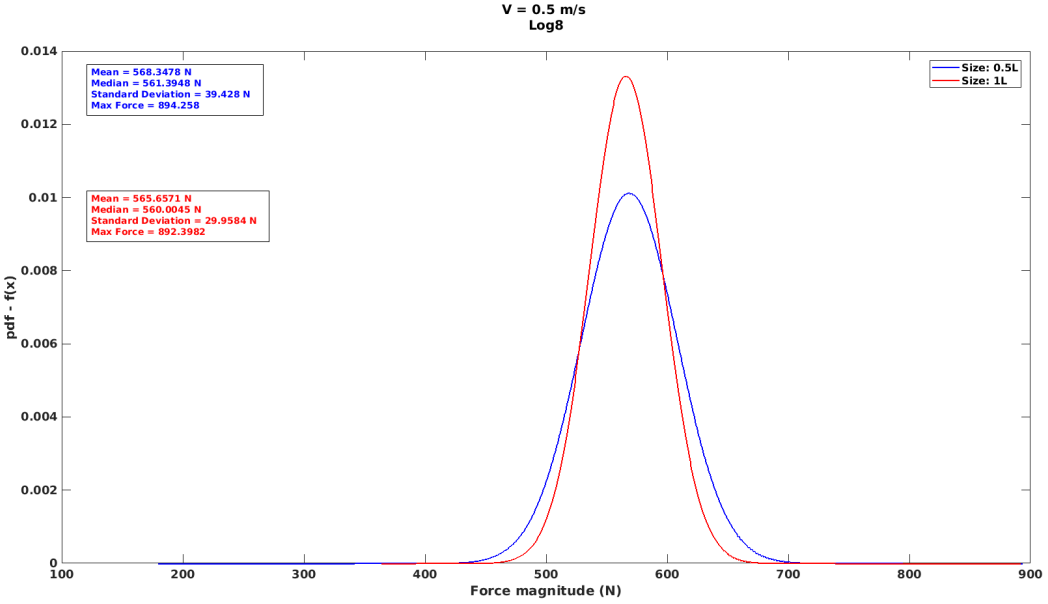

Figure A.78: Comparison of PDFs of forces on Log8 at V = 0.5 m/s.

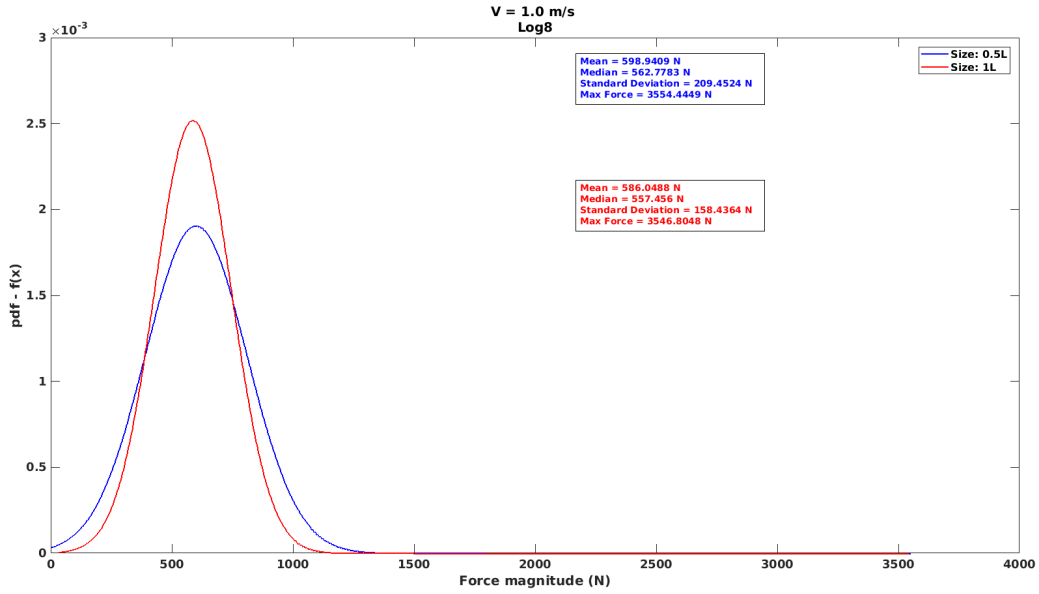

Figure A.79: Comparison of the PDFs of the forces on Log8 at V = 1.0 m/s.

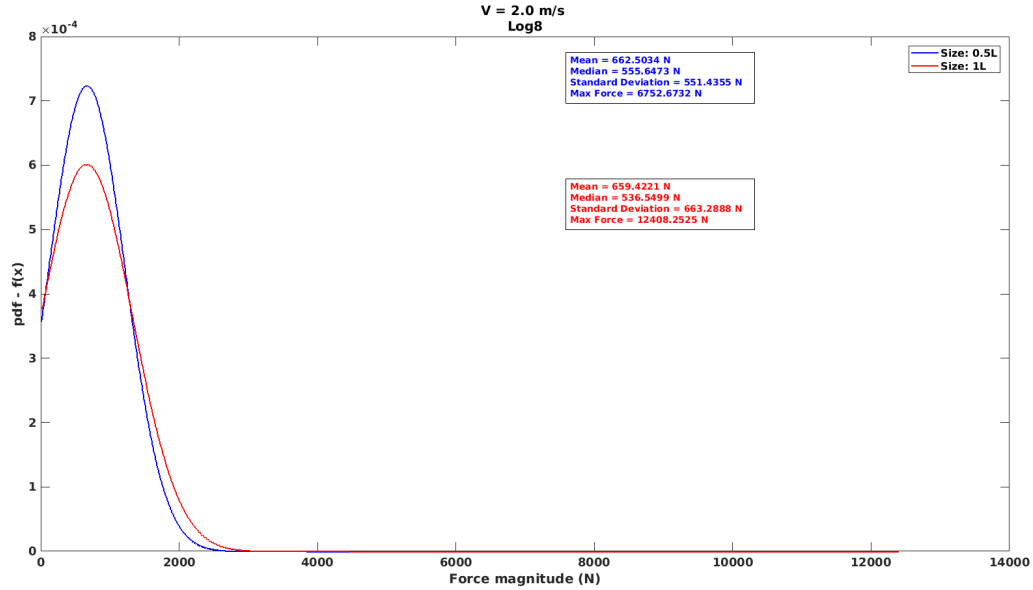

Figure A.80: Comparison of the PDFs of the forces on Log8 at V = 2.0 m/s.

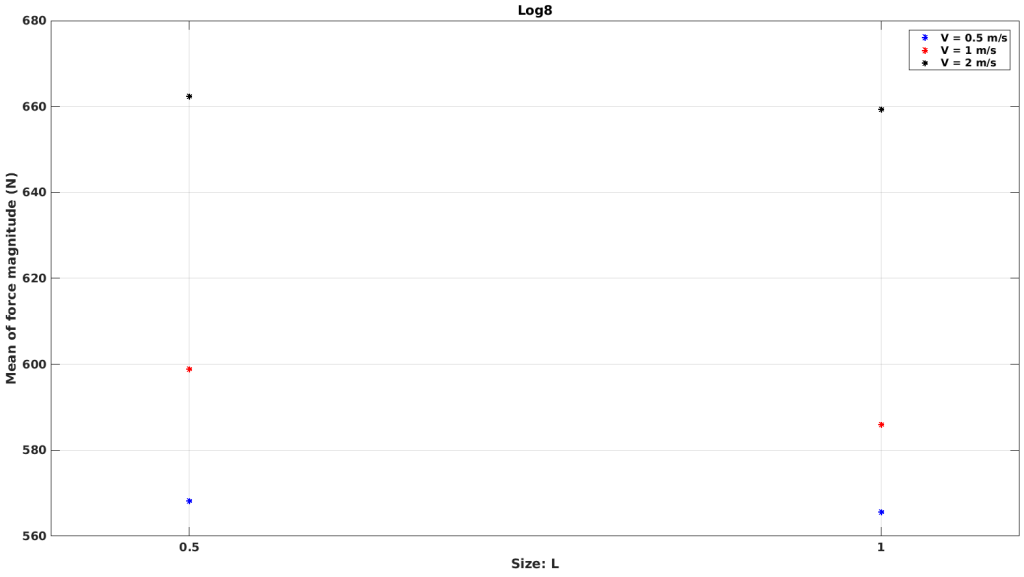

Figure A.81: Variation of mean force magnitude with log size for Log8.

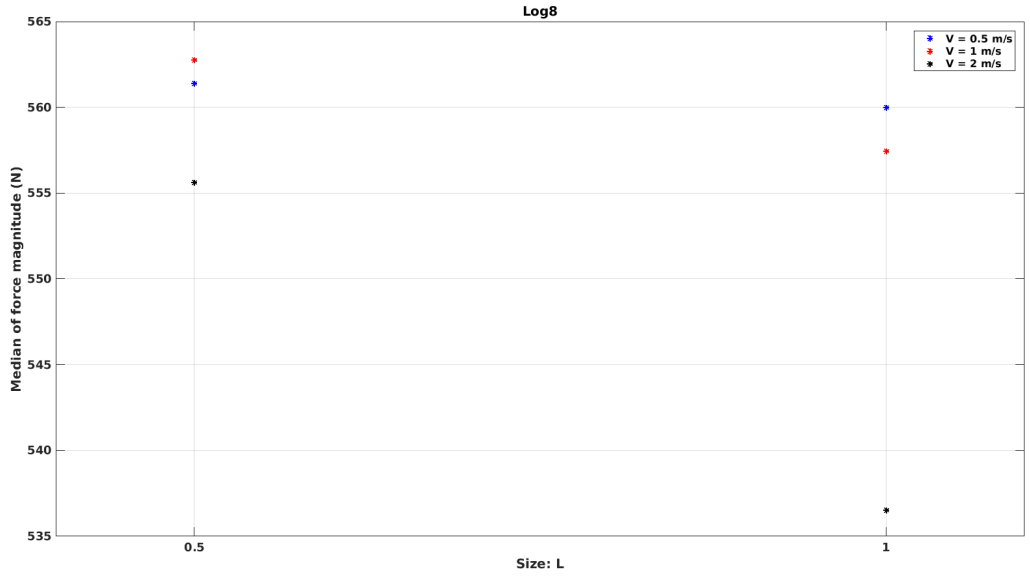

Figure A.82: Variation of median force magnitude with log size for Log8.

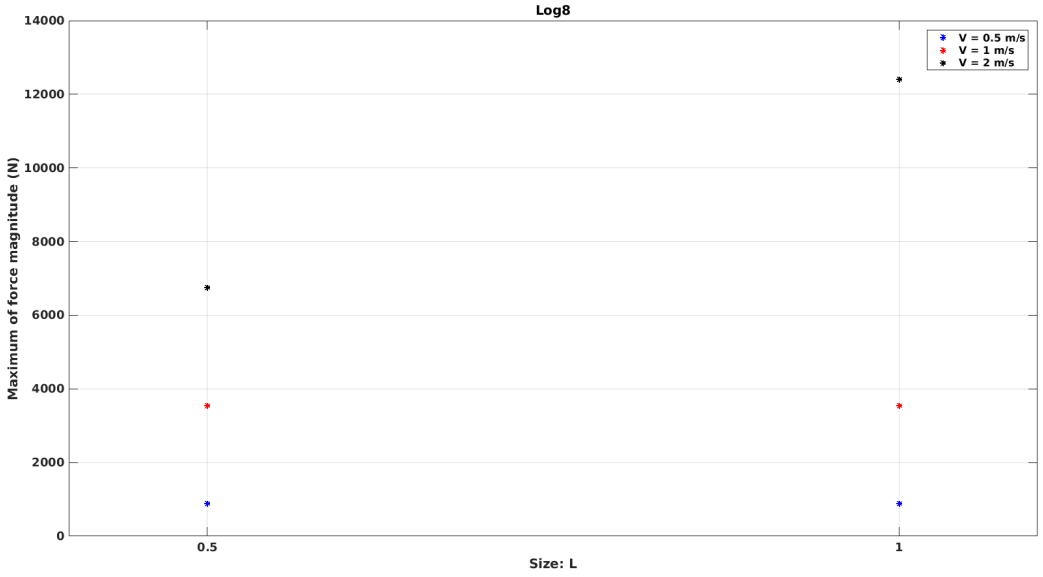

Figure A.83: Variation of maximum force magnitude with log size for Log8.

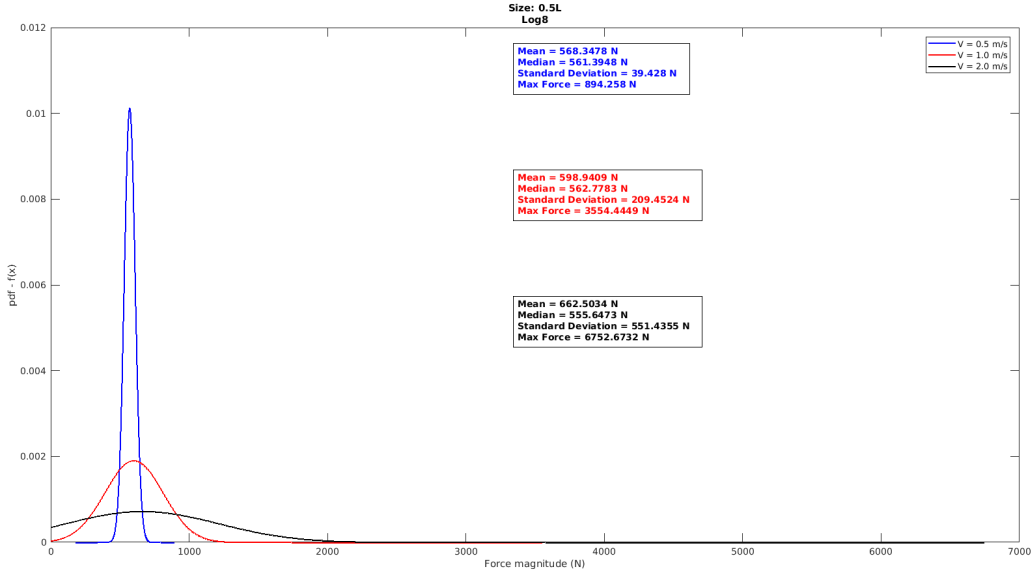

Figure A.84: Comparison of the PDFs of the forces on Log8 of size 0.5L.

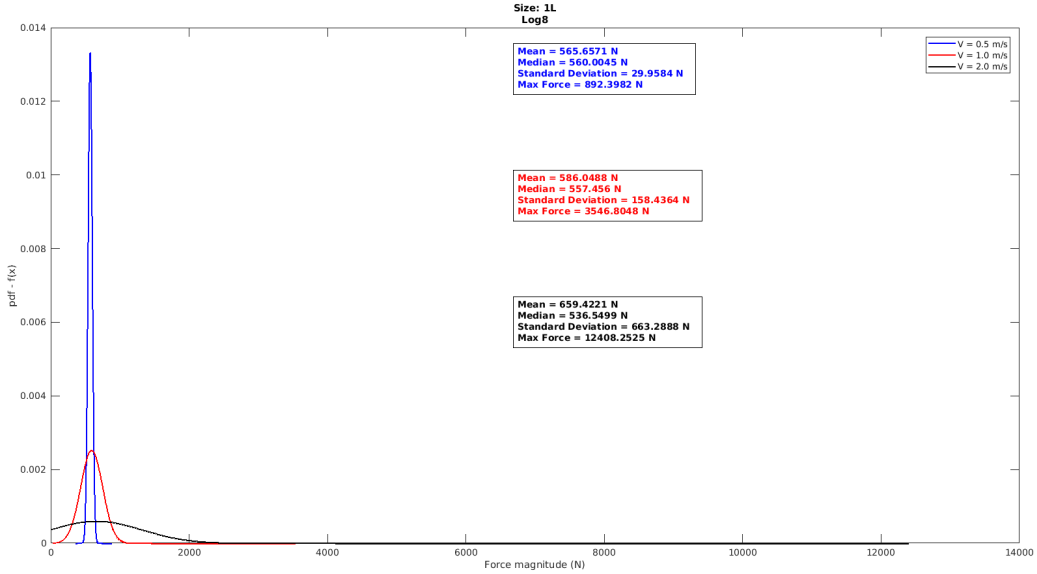

Figure A.85: Comparison of the PDFs of the forces on Log8 of size 1L.

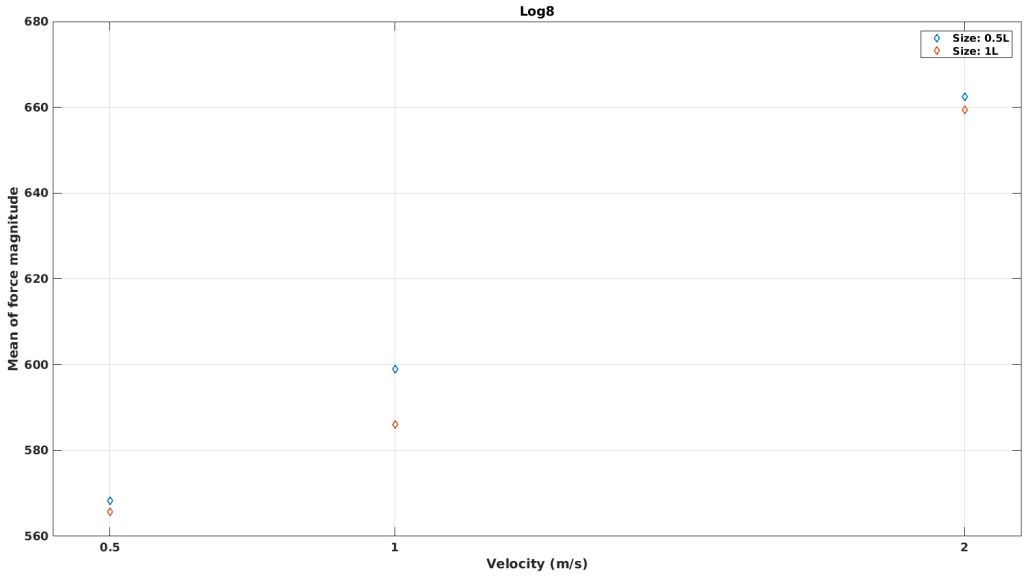

Figure A.86: Variation of mean force magnitude with flow velocity for Log8.

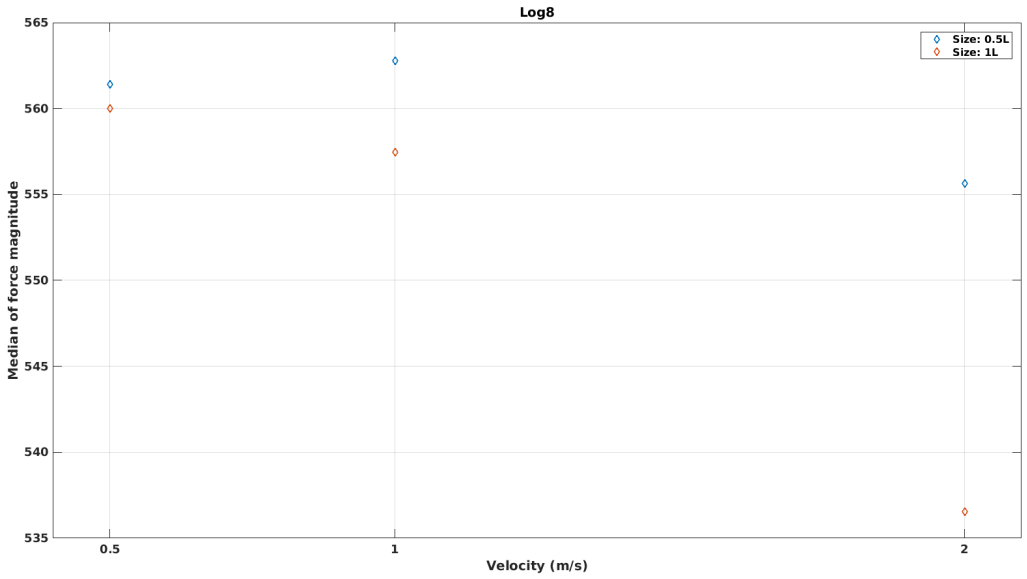

Figure A.87: Variation of median force magnitude with flow velocity for Log8.

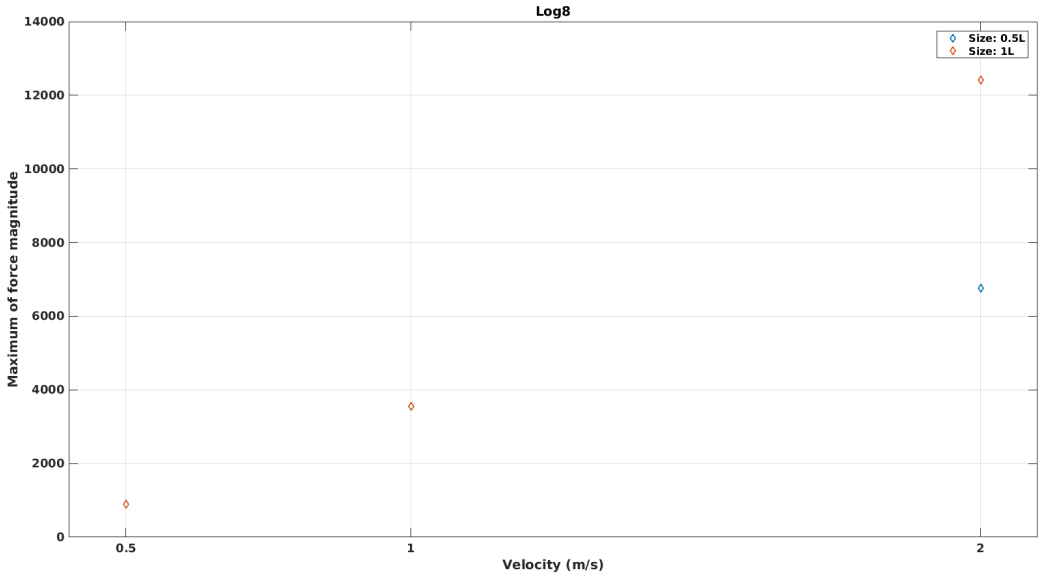

Figure A.88: Variation of maximum force magnitude with flow velocity for Log8.

Log9

This is the log that is injected from location 9 as shown in Figure 4.12. It is injected at the same time as logs 10, 11, and 12.

Figure A.89 shows the comparison of the PDFs of Log9 force magnitude for different log sizes at V = 0.5 m/s. Log9 of size 1L has higher probability of forces being around the mean than that for size 0.5L. Log of size 0.5L has higher probability of forces being large and small as well.

Figure A.90 shows the comparison of the PDFs of the force magnitude for different log sizes at V = 1.0 m/s. The PDFs are very similar to each other but the minimum force for size 0.5L is less than that for size 1L.

Figure A.91 shows the comparison of the PDFs of force magnitude for different log sizes at V = 2.0 m/s. The PDFs are very similar to each other.

Figures A.92, A.93, and A.94 show the variation of mean, median, and maximum of Log9

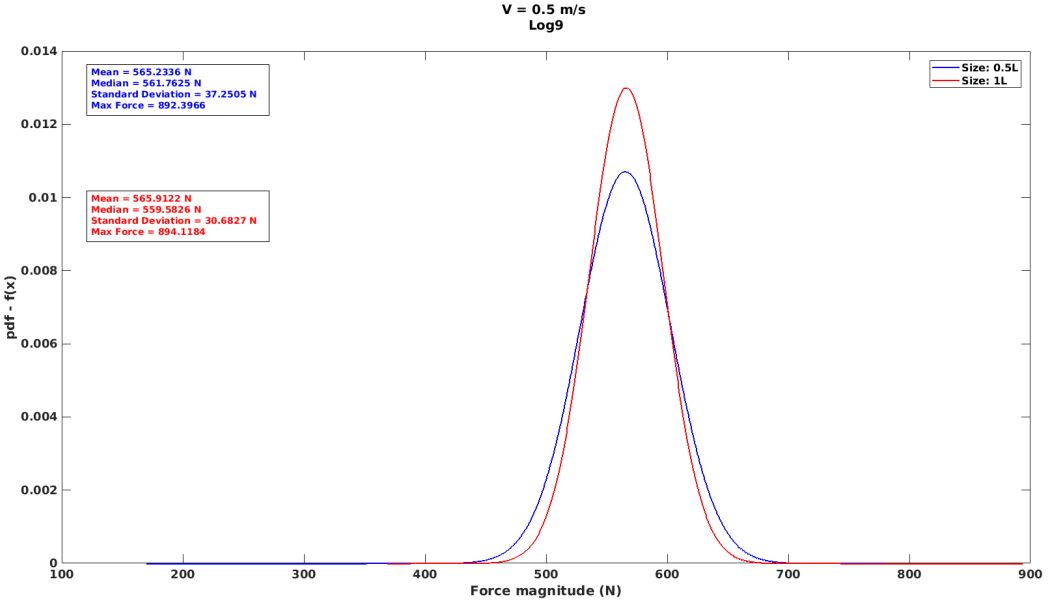

Figure A.89: Comparison of the PDFs of the forces on Log9 at V = 0.5 m/s.

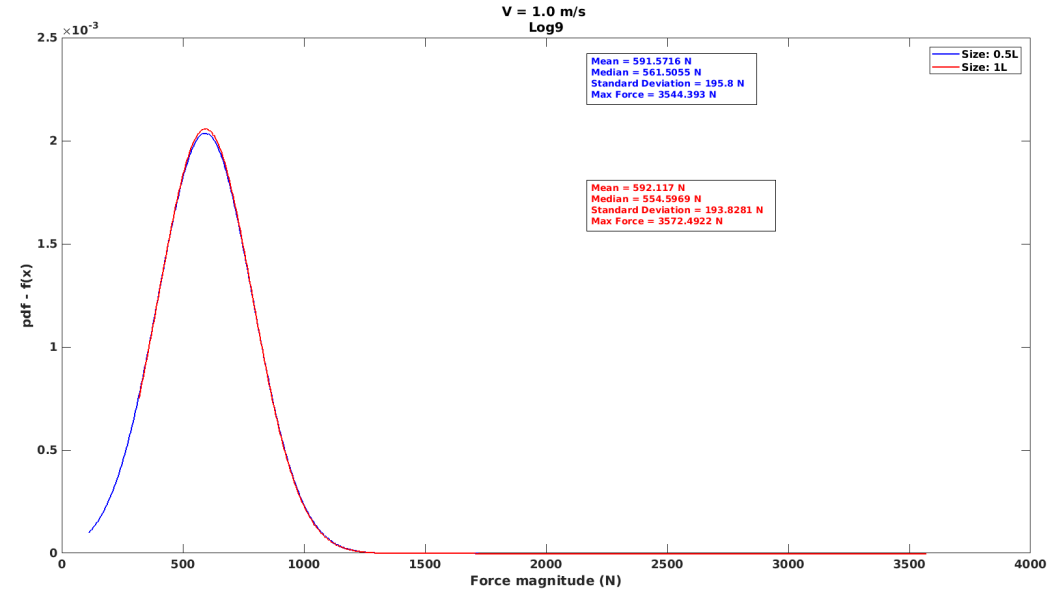

Figure A.90: Comparison of the PDFs of the forces on Log9 at V = 1.0 m/s.

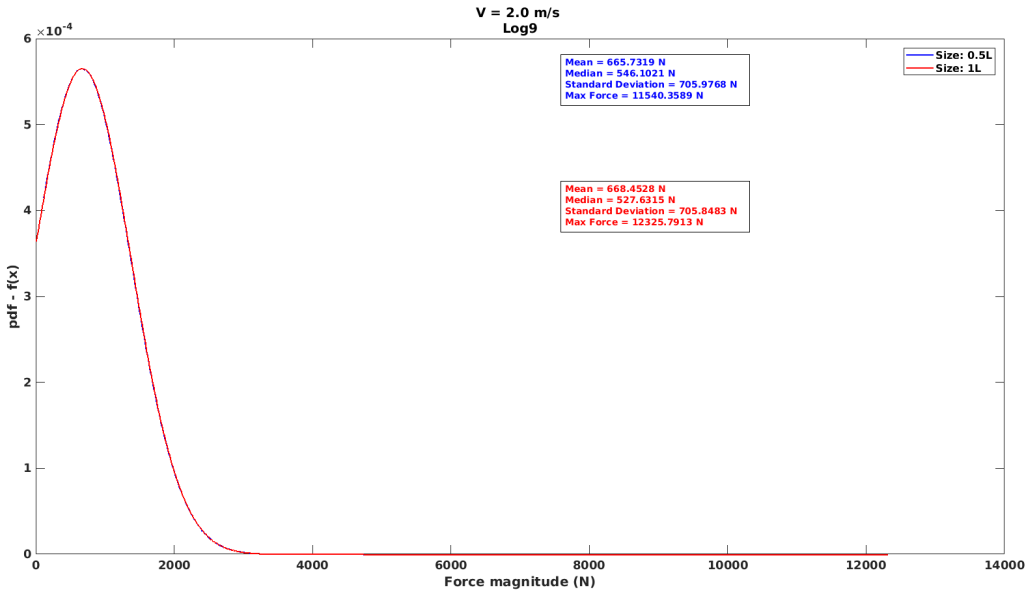

Figure A.91: Comparison of the PDFs of the forces on Log9 at V = 2.0 m/s.

force magnitude for different log sizes. Mean and maximum forces remain fairly constant. Median force shows inconsistent variation.

Figures A.95 and A.96 show the comparison of the PDFs of Log9 force magnitude for the two log sizes at different flow velocities. As the velocity increases, the probability of higher forces on log increases. The momentum of logs increases with velocities and therefore so does the impact force.

Figures A.97, A.98, and A.99 show the variation of mean, median, and maximum Log9 force magnitude for different flow velocities. Both mean and maximum force show an increasing trend with velocity. The variation is quadratic. Median force decreases with velocity.

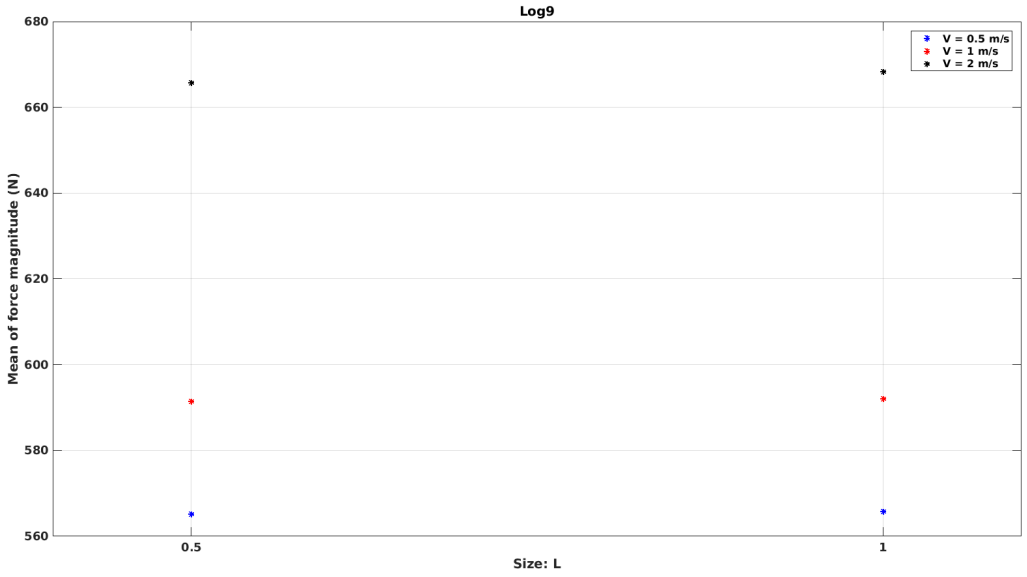

Figure A.92: Variation of mean force magnitude with log size for Log9.

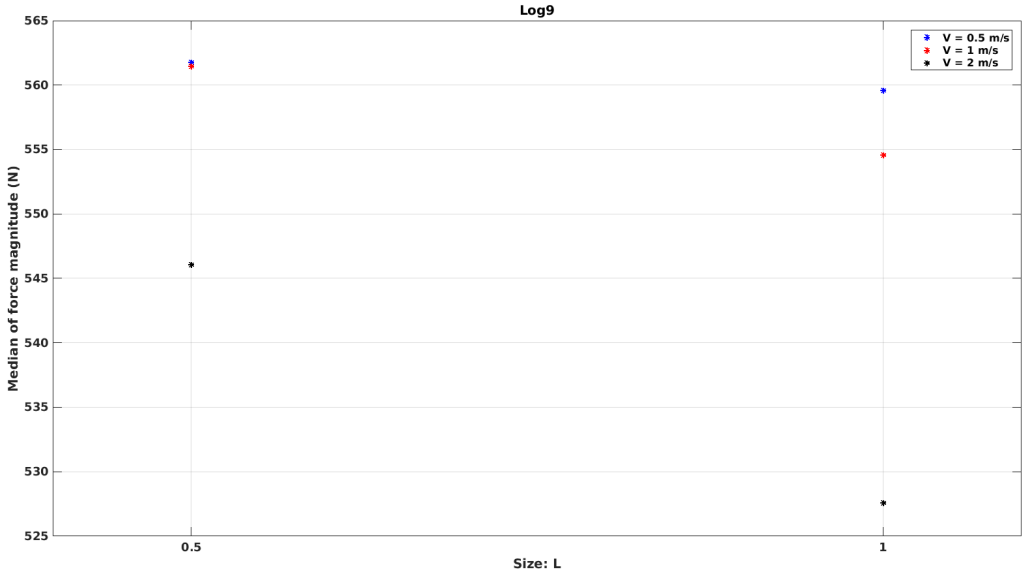

Figure A.93: Variation of median force magnitude with log size for Log9.

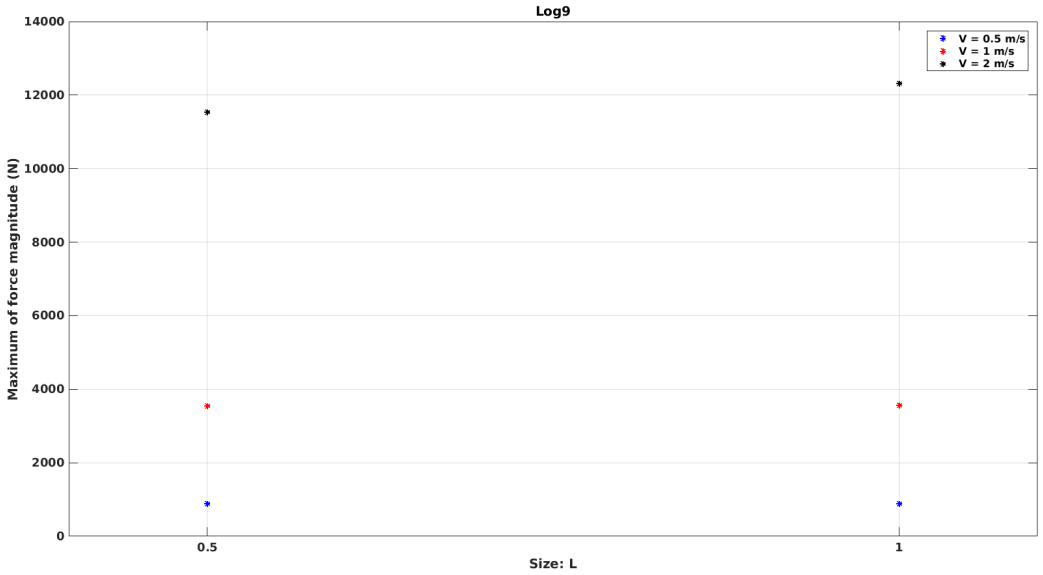

Figure A.94: Variation of maximum force magnitude with log size for Log9.

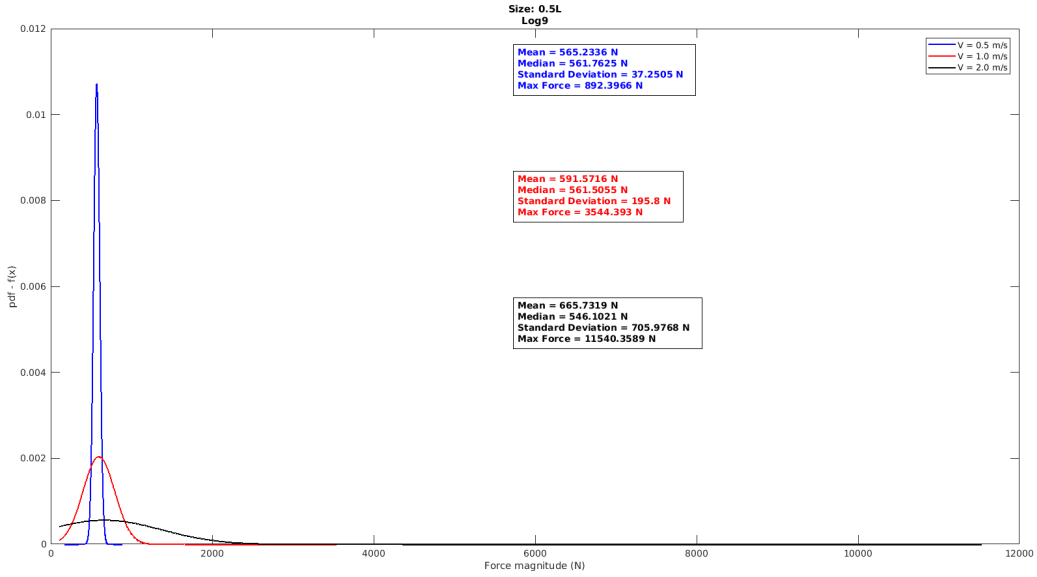

Figure A.95: Comparison of the PDFs of the forces on Log9 of size 0.5L.

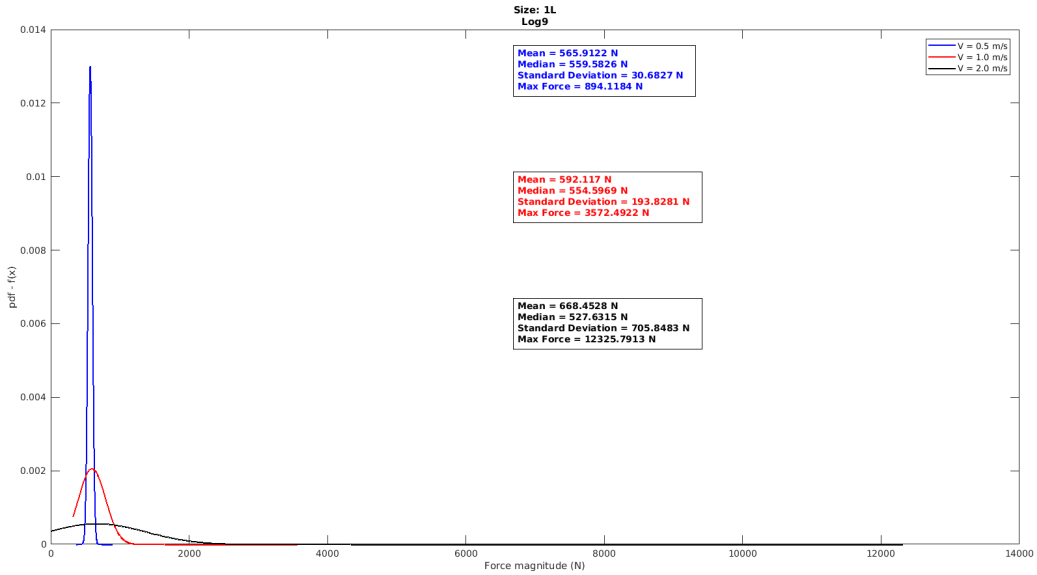

Figure A.96: Comparison of the PDFs of the forces on Log9 of size 1L.

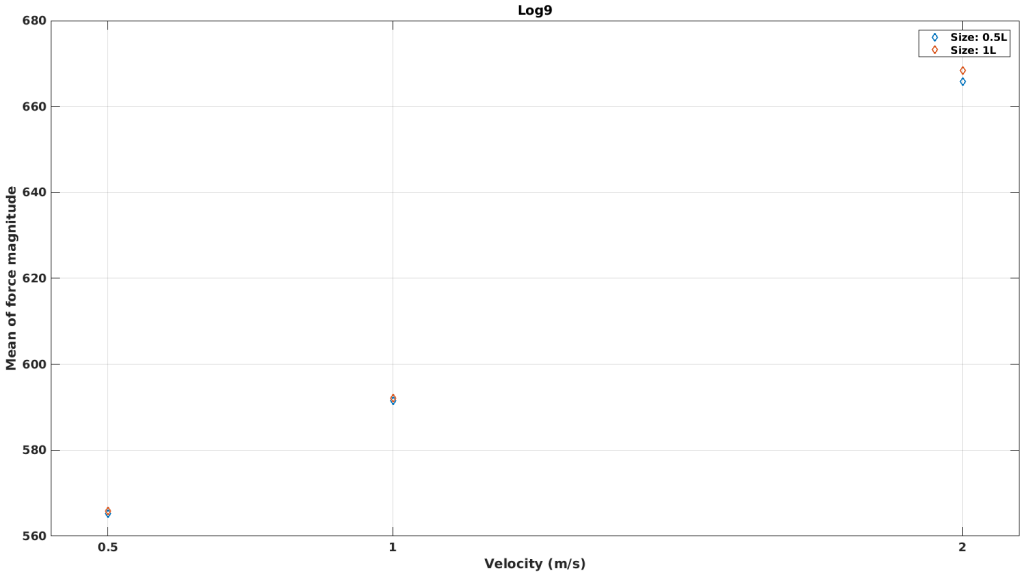

Figure A.97: Variation of mean force magnitude with flow velocity for Log9.

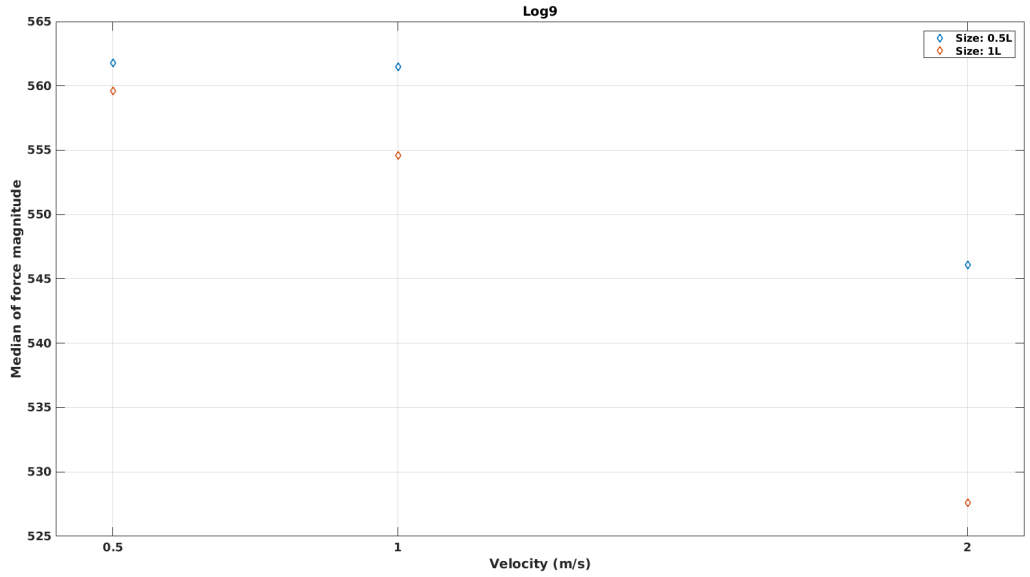

Figure A.98: Variation of median force magnitude with flow velocity for Log9.

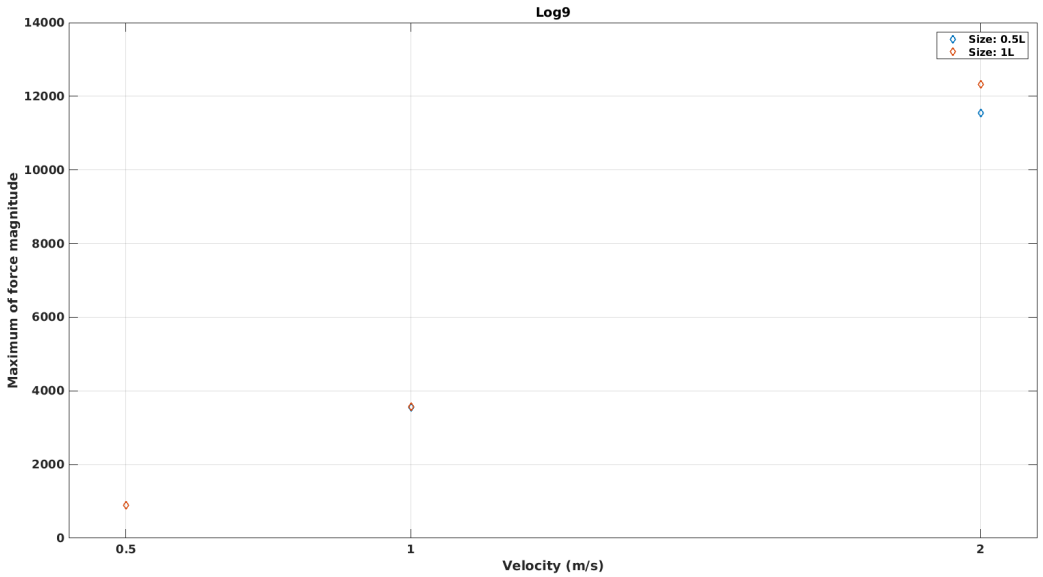

Figure A.99: Variation of maximum force magnitude with flow velocity for Log9.

Log10

This is the log that is injected from location 10 as shown in Figure 4.12. It is injected at the same time as logs 9, 11, and 12.

Figure A.100 shows the comparison of the PDFs of Log10 force magnitude for different log sizes at V = 0.5 m/s. Log10 of size 1L has higher probability of forces being around the mean than that for size 0.5L. Log of size 0.5L has higher probability of forces being large and small as well.

Figure A.101 shows the comparison of the PDFs of Log10 force magnitude for different log sizes at V = 1.0 m/s. Log10 of size 1L has higher probability of force being around the mean than that of size 0.5L. Log10 of size 0.5L has higher probability of large and small forces.

Figure A.102 shows the comparison of the PDFs of Log10 force magnitude for different log sizes at V = 2.0 m/s. Log10 of size 1L has higher probability of force being around the mean than that of size 0.5L. Log10 of size 0.5L has higher probability of large forces and size 1L has higher probability of small forces.

Figures A.103, A.104, and A.105 show the variation of mean, median, and maximum of magnitude of force on Log10 at different log sizes. Mean and maximum forces remain fairly constant. Median force shows a decreasing trend.

Figures A.106 and A.107 show the comparison of the PDFs of Log10 force magnitude for the two log sizes at different flow velocities. As the velocity increases, the probability of higher forces on log increases. The momentum of logs increases with velocities and therefore so does the impact force.

Figures A.108, A.109, and A.110 show the variation of mean, median, and maximum Log10 force magnitude for different flow velocities. Both mean and maximum force show an increasing trend with velocity. The variation is quadratic. Median force decreases with velocity.

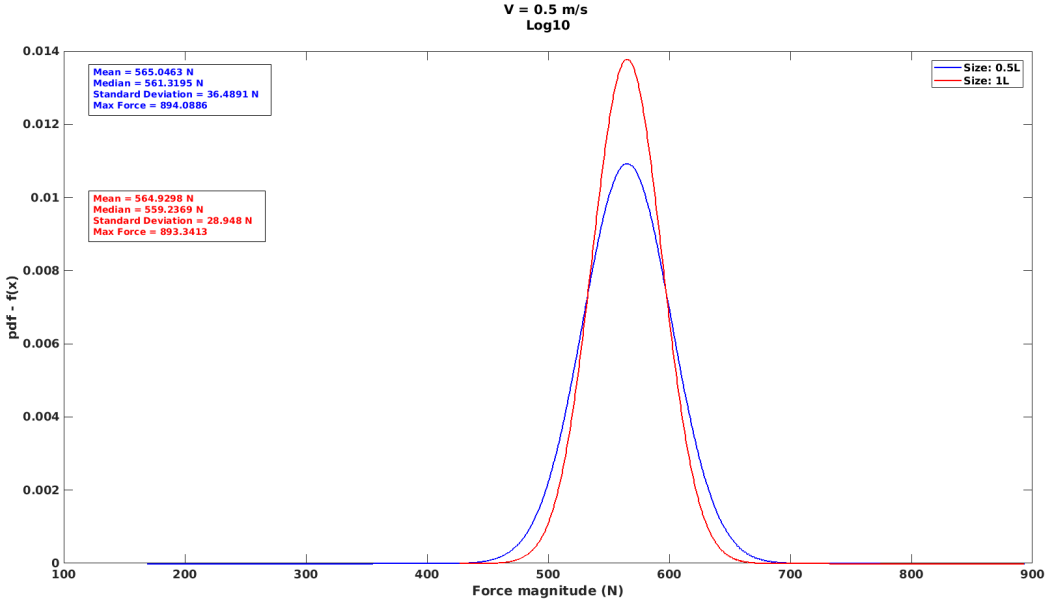

Figure A.100: Comparison of the PDFs of the forces on Log10 at V = 0.5 m/s.

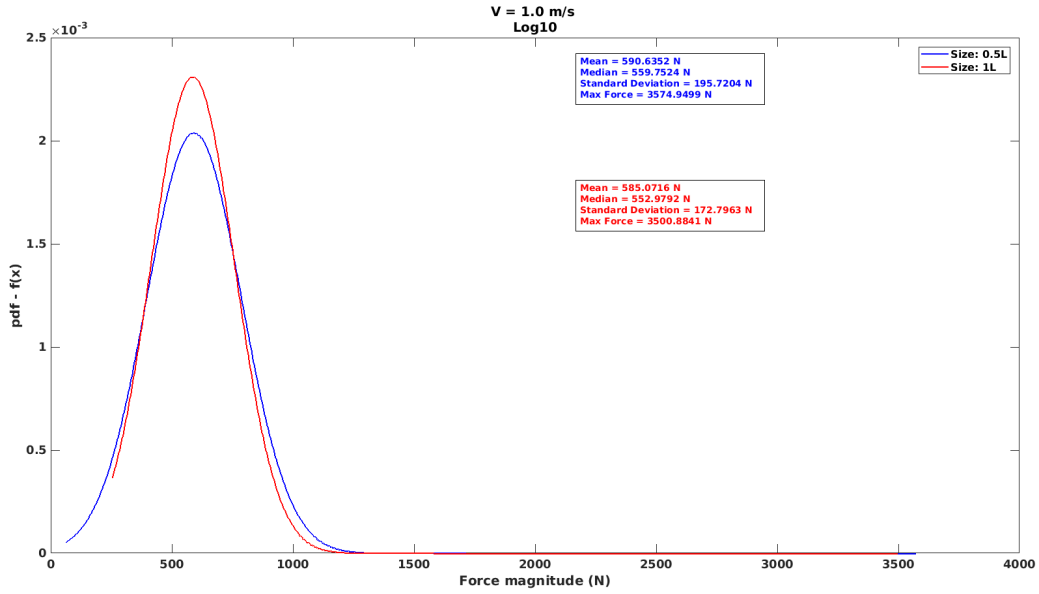

Figure A.101: Comparison of the PDFs of the forces on Log10 at V = 1.0 m/s.

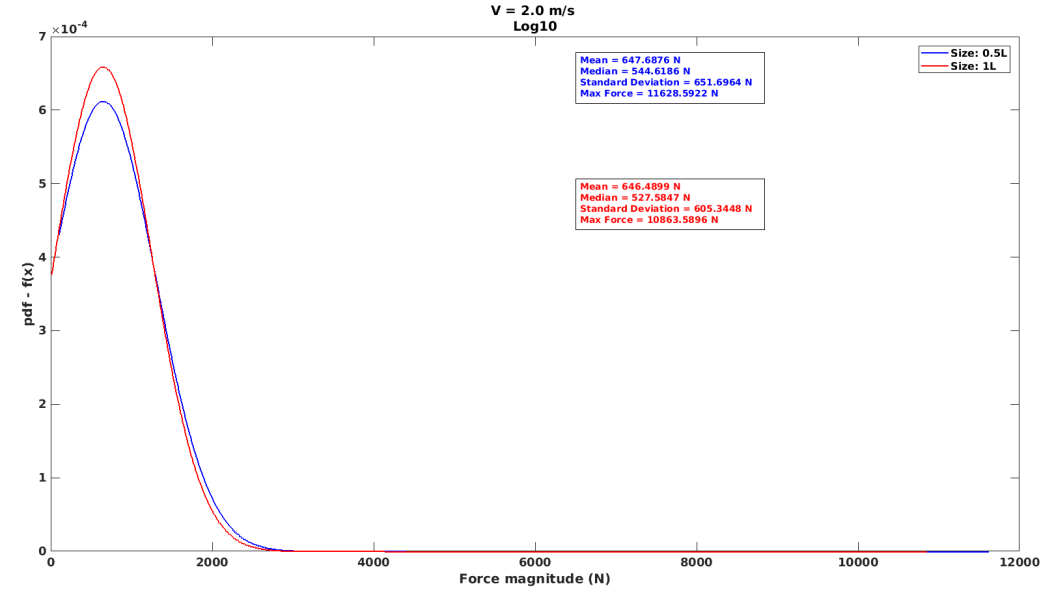

Figure A.102: Comparison of the PDFs of the forces on Log10 at V = 2.0 m/s.

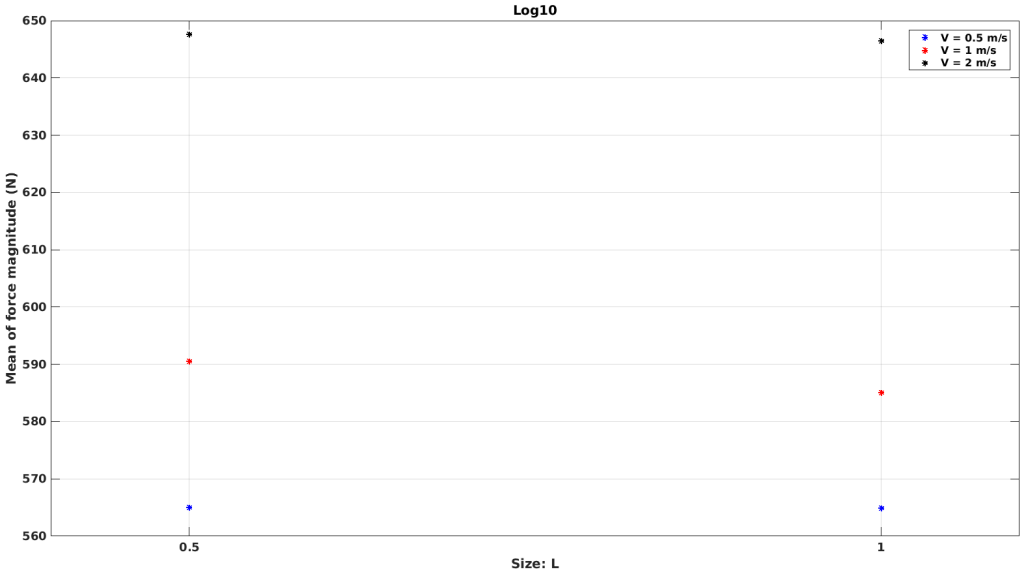

Figure A.103: Variation of mean force magnitude with log size for Log10.

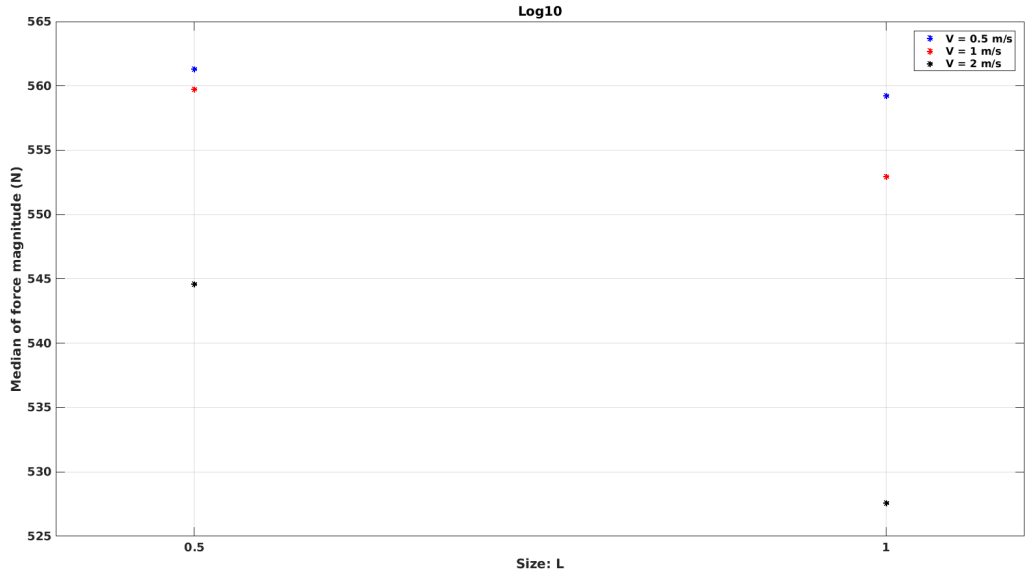

Figure A.104: Variation of median force magnitude with log size for Log10.

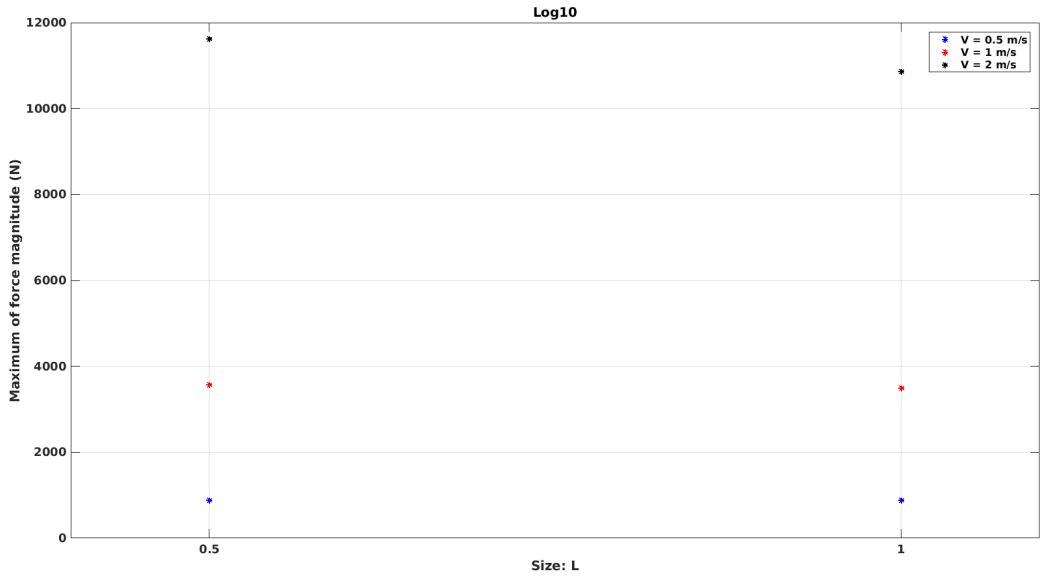

Figure A.105: Variation of maximum force magnitude with log size for Log10.

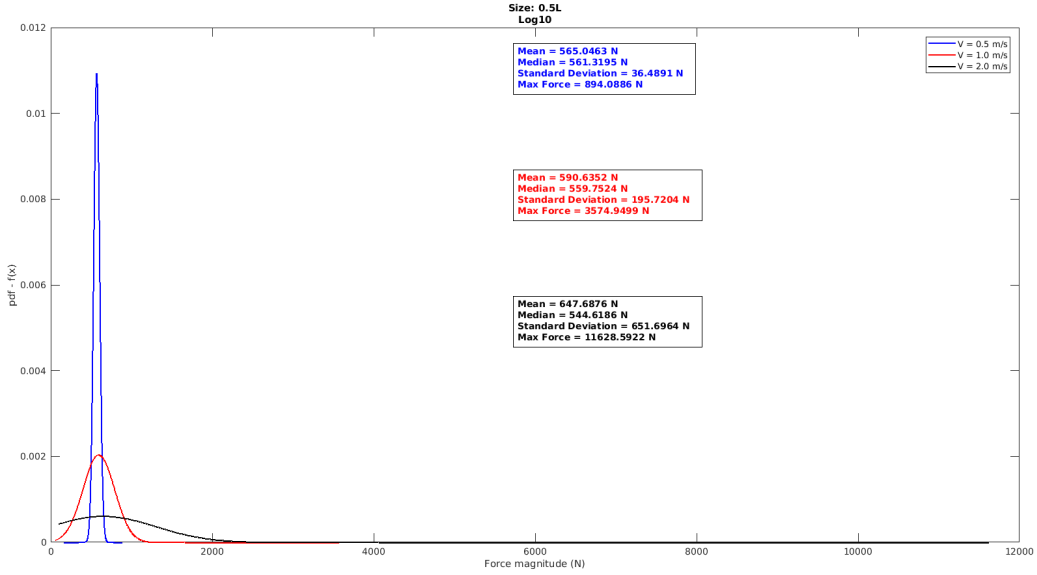

Figure A.106: Comparison of the PDFs of the forces on Log10 of size 0.5L.

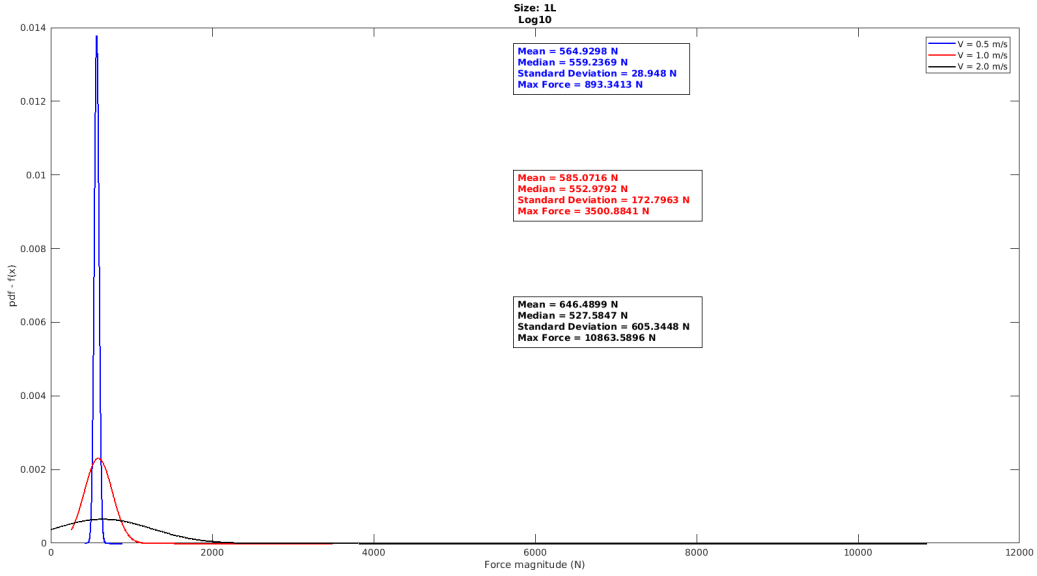

Figure A.107: Comparison of the PDFs of the forces on Log10 of size 1L.

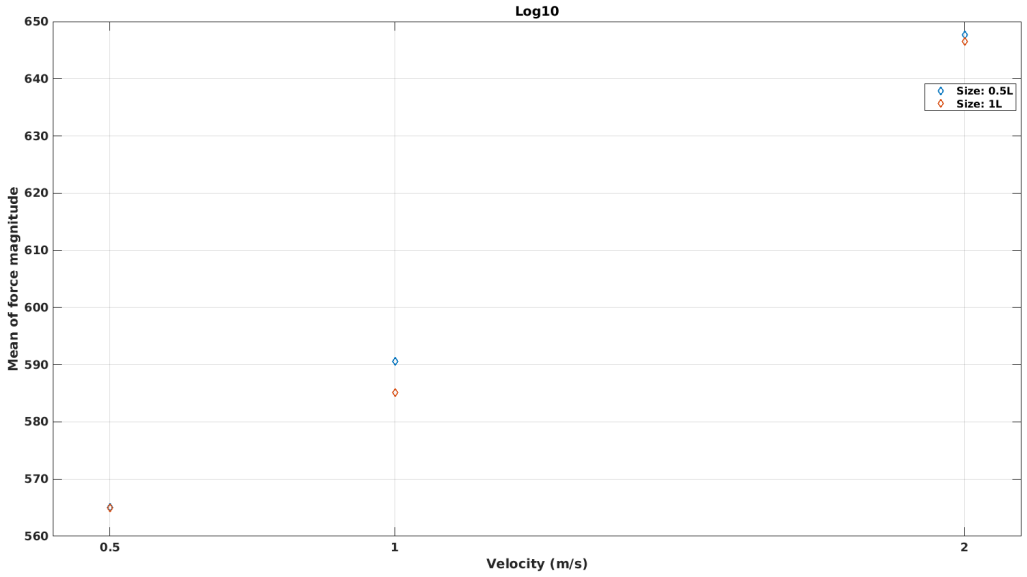

Figure A.108: Variation of mean force magnitude with flow velocity for Log10.

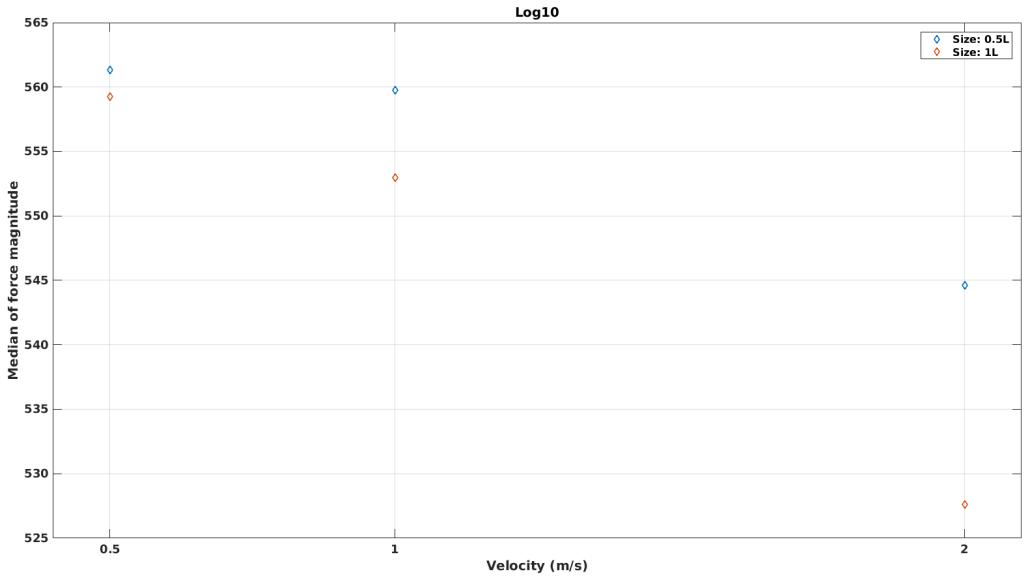

Figure A.109: Variation of median force magnitude with flow velocity for Log10.

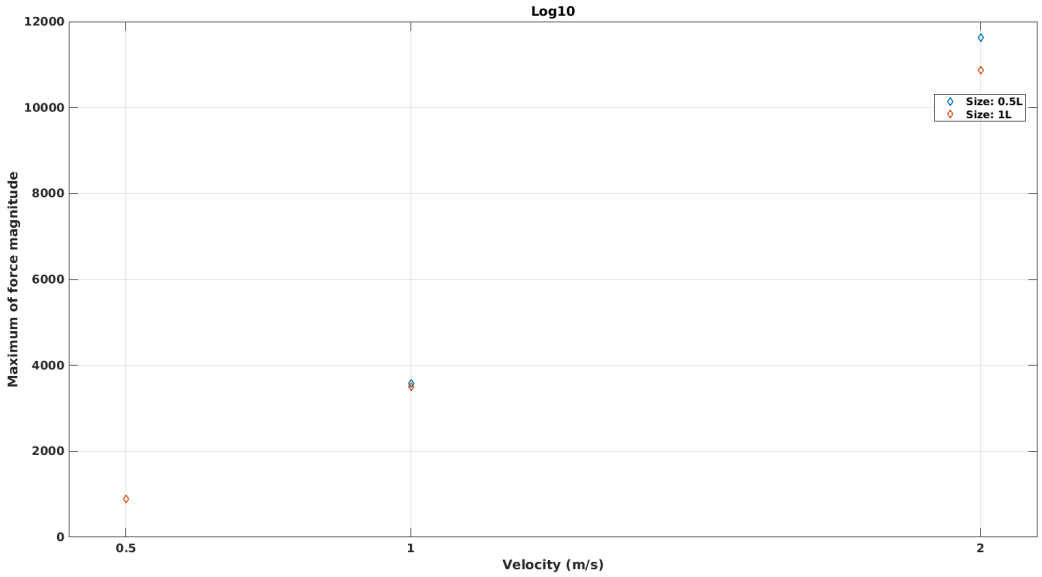

Figure A.110: Variation of maximum force magnitude with flow velocity for Log10.

Log11

This is the log that is injected from location 11 as shown in Figure 4.12. It is injected at the same time as logs 9, 10, and 12.

Figure A.111 shows the comparison of the PDFs of Log11 force magnitude for different log sizes at V = 0.5 m/s. Log11 of size 1L has higher probability of forces being around the mean than that for size 0.5L. Log of size 0.5L has higher probability of forces being large and small as well.

Figure A.112 shows the comparison of the PDFs of Log11 force magnitude for different log sizes at V = 1.0 m/s. Log11 of size 1L has higher probability of force being around the mean than that of size 0.5L. Log11 of size 0.5L has higher probability of large and small forces.

Figure A.113 shows the comparison of the PDFs of Log11 force magnitude for different log sizes at V = 2.0 m/s. Log11 of size 0.5L has higher probability of force being around the mean than that of size 0.5L. Log11 of size 1L has higher probability of large forces.

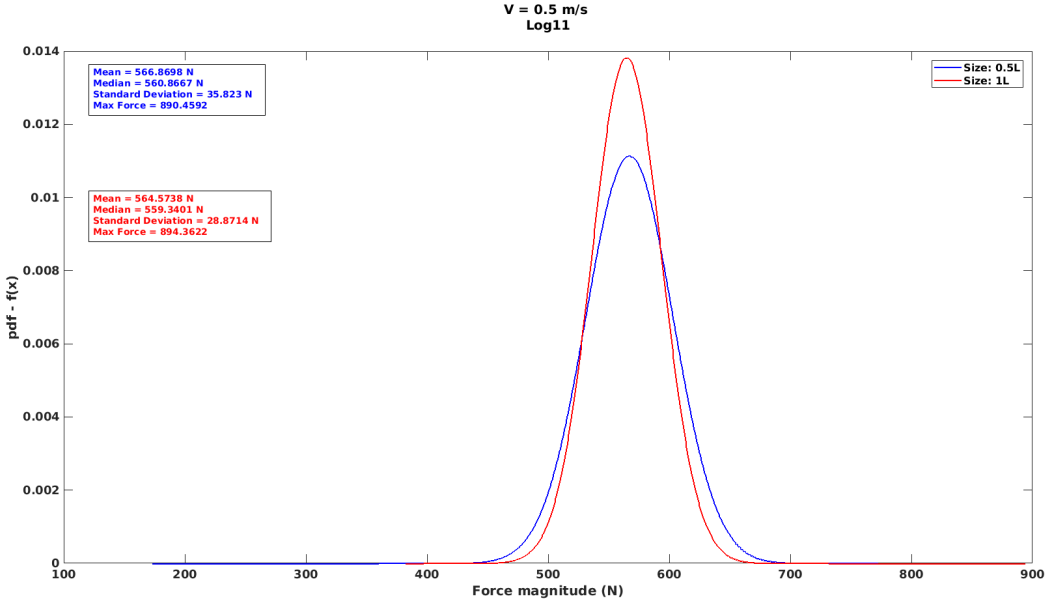

Figure A.111: Comparison of the PDFs of the forces on Log11 at V = 0.5 m/s.

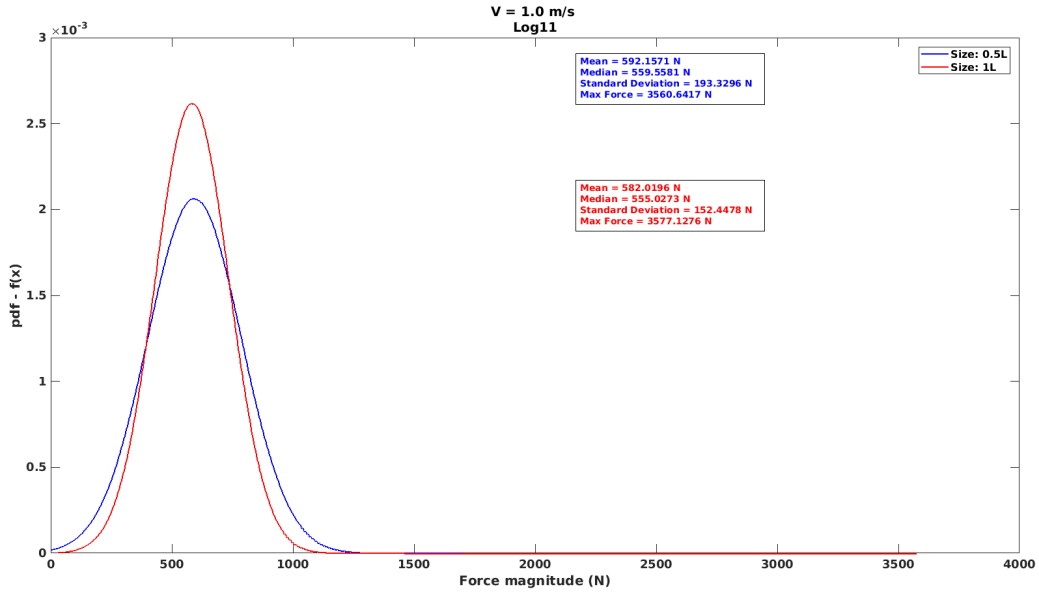

Figure A.112: Comparison of the PDFs of the forces on Log11 at V = 1.0 m/s.

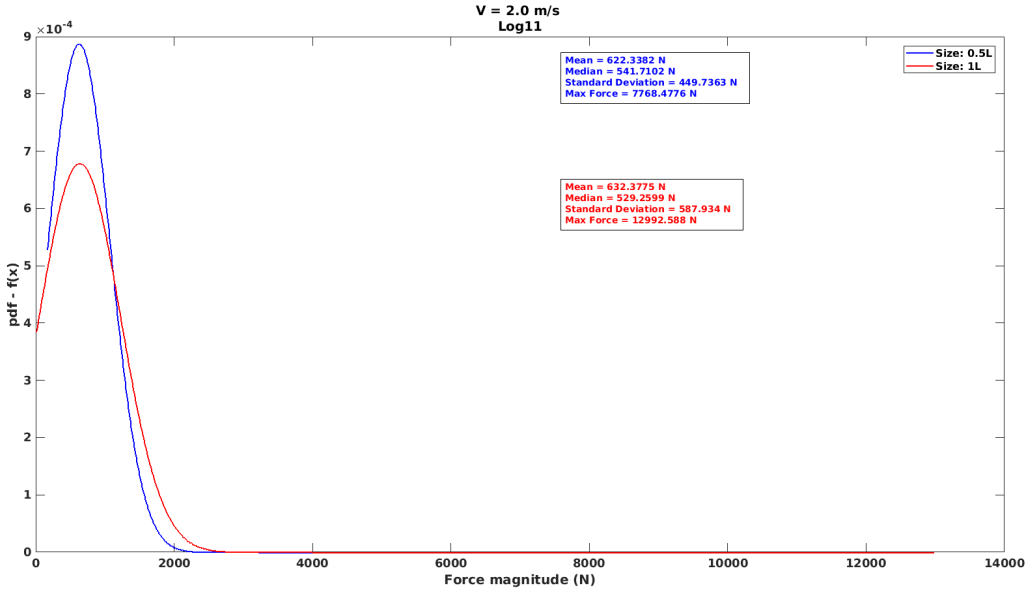

Figure A.113: Comparison of the PDFs of the forces on Log11 at V = 2.0 m/s.

Figures A.114, A.115, and A.116 show the variation of mean, median, and maximum of Log11 force magnitude for different log sizes. Mean force shows inconsistent variation. Median force decreases with log size. Maximum force shows an increasing trend with log size.

Figures A.117 and A.118 show the comparison of the PDFs of Log11 force magnitude for the two log sizes at different flow velocities. As the velocity increases, the probability of higher forces on log increases. The momentum of logs increases with velocities and therefore so does the impact force.

Figures A.119, A.120, and A.121 show the variation of mean, median, and maximum of Log11 force magnitude for different flow velocities. Both mean and maximum force show an increasing trend with velocity. The variation is quadratic. Median force decreases with velocity.

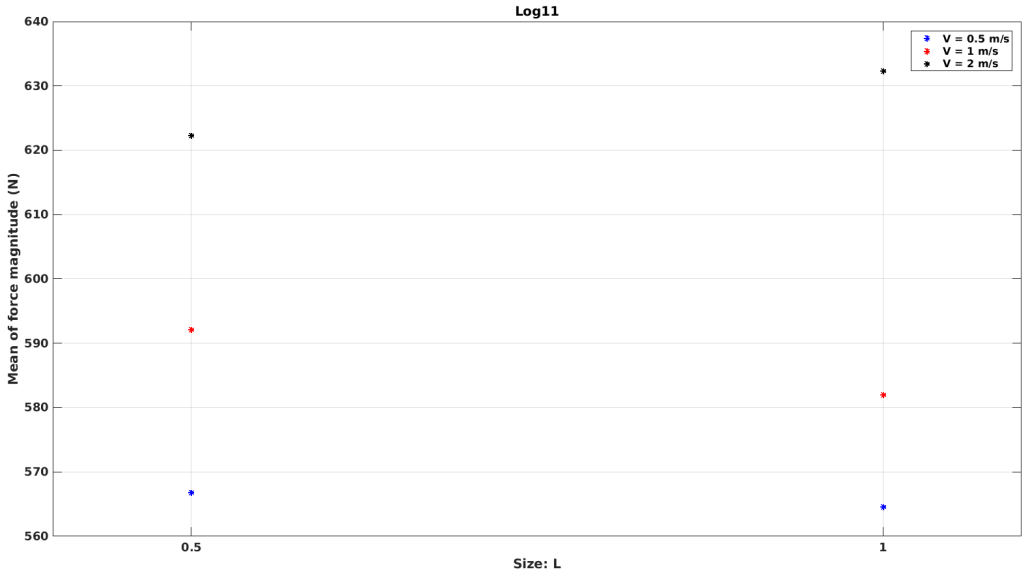

Figure A.114: Variation of mean force magnitude with log size for Log11.

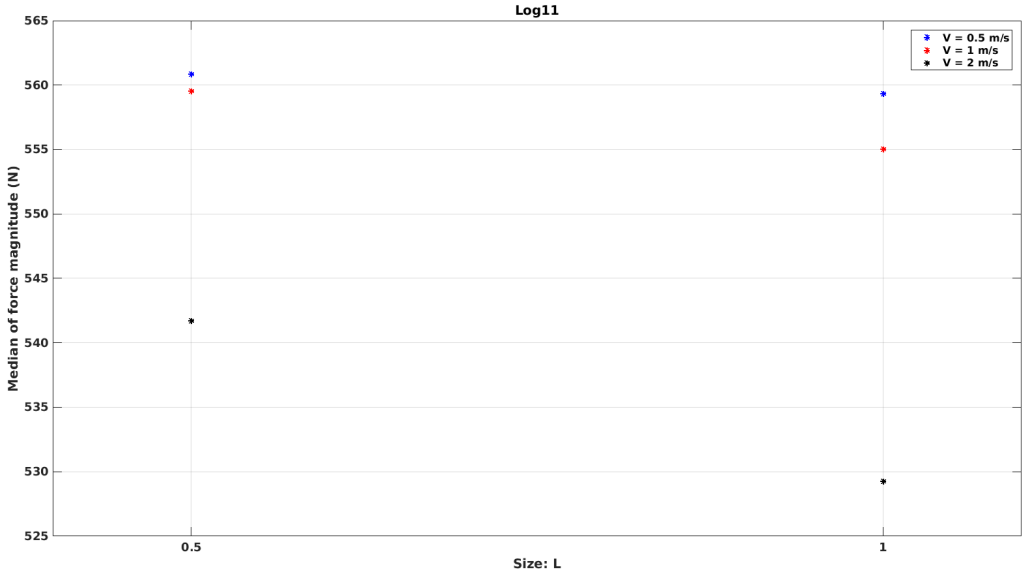

Figure A.115: Variation of median force magnitude with log size for Log11.

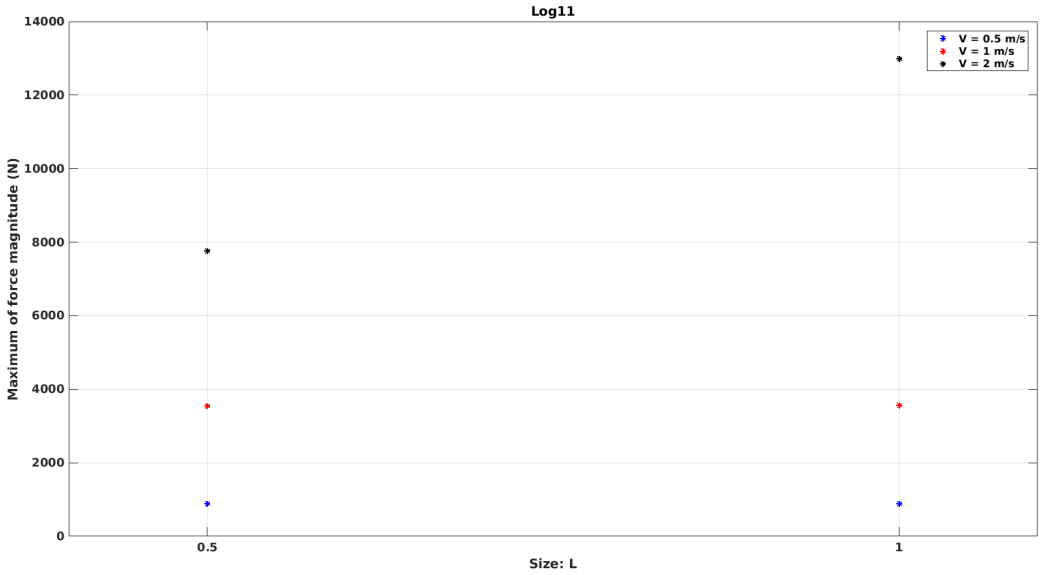

Figure A.116: Variation of maximum force magnitude with log size for Log11.

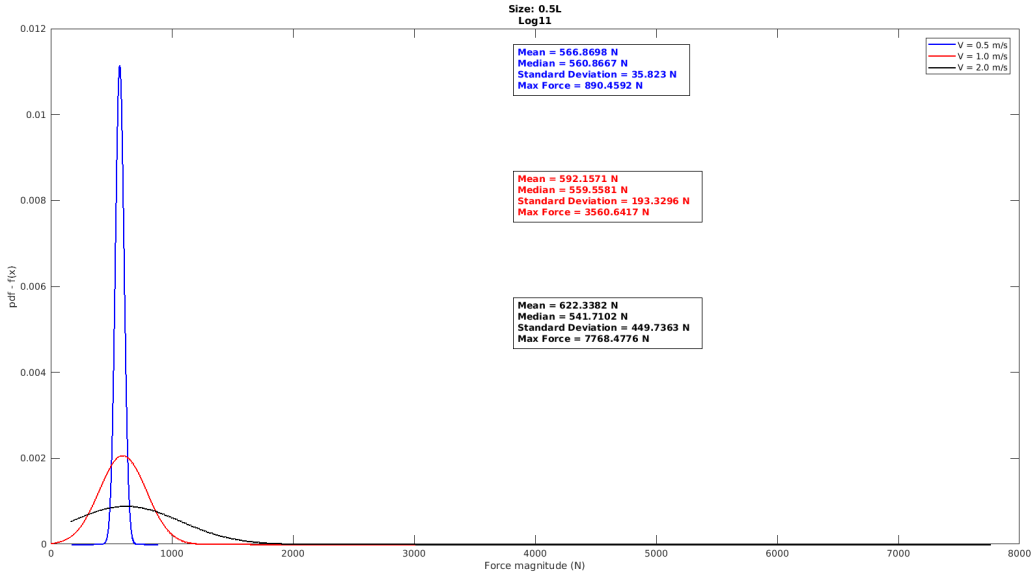

Figure A.117: Comparison of the PDFs of the forces on Log11 of size 0.5L.

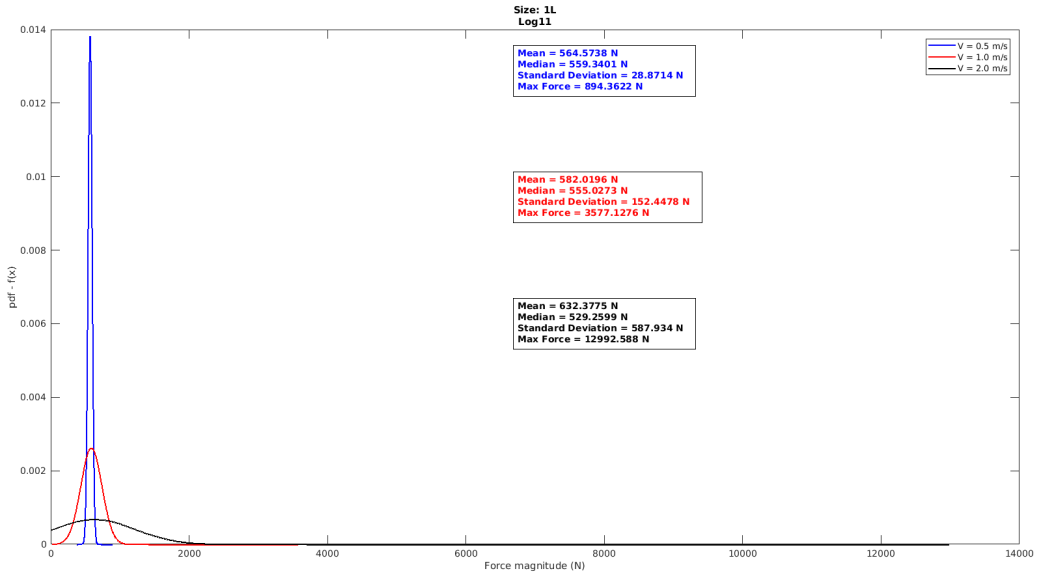

Figure A.118: Comparison of the PDFs of the forces on Log11 of size 1L.

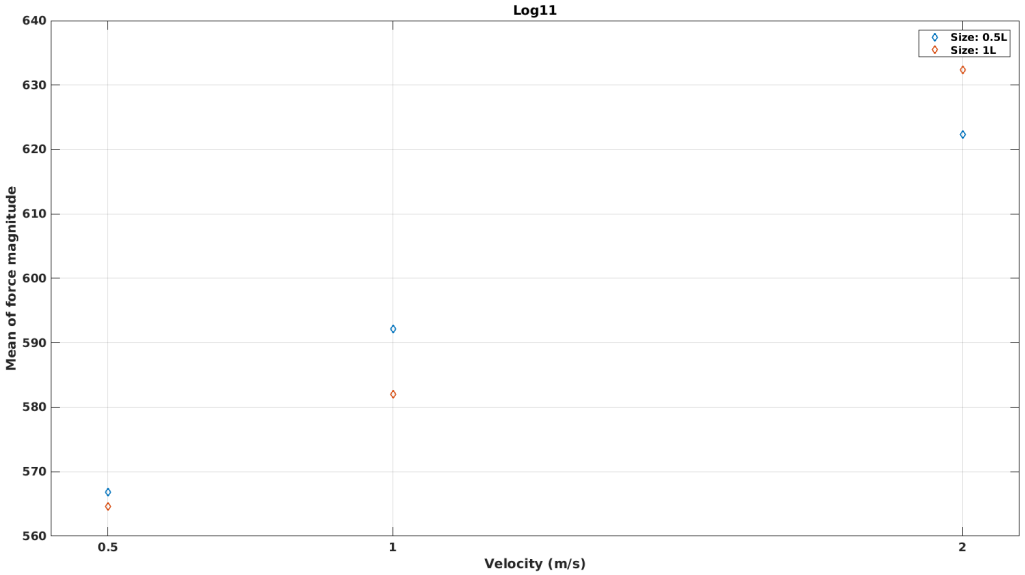

Figure A.119: Variation of mean force magnitude with flow velocity for Log11.

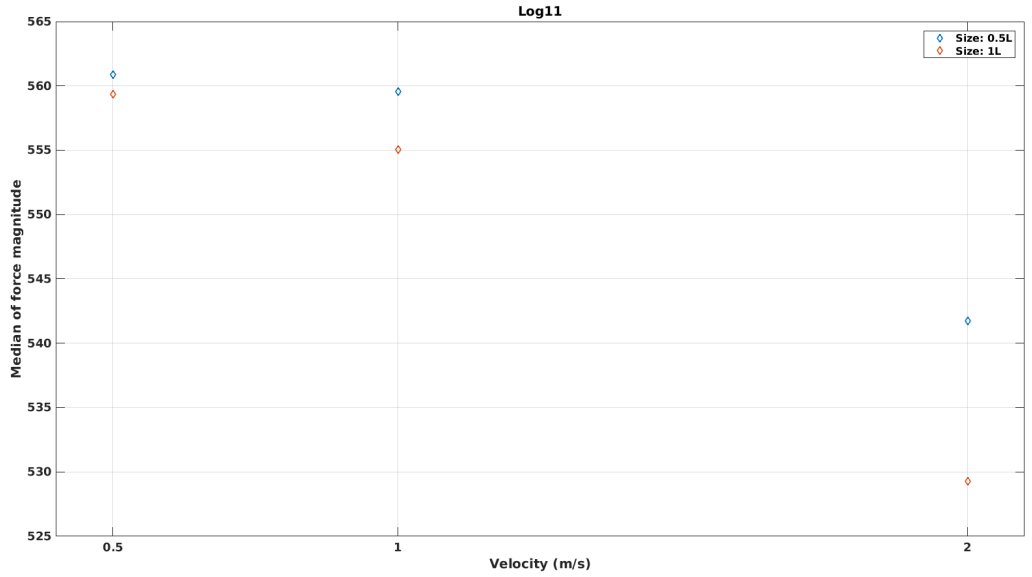

Figure A.120: Variation of median force magnitude with flow velocity for Log11.

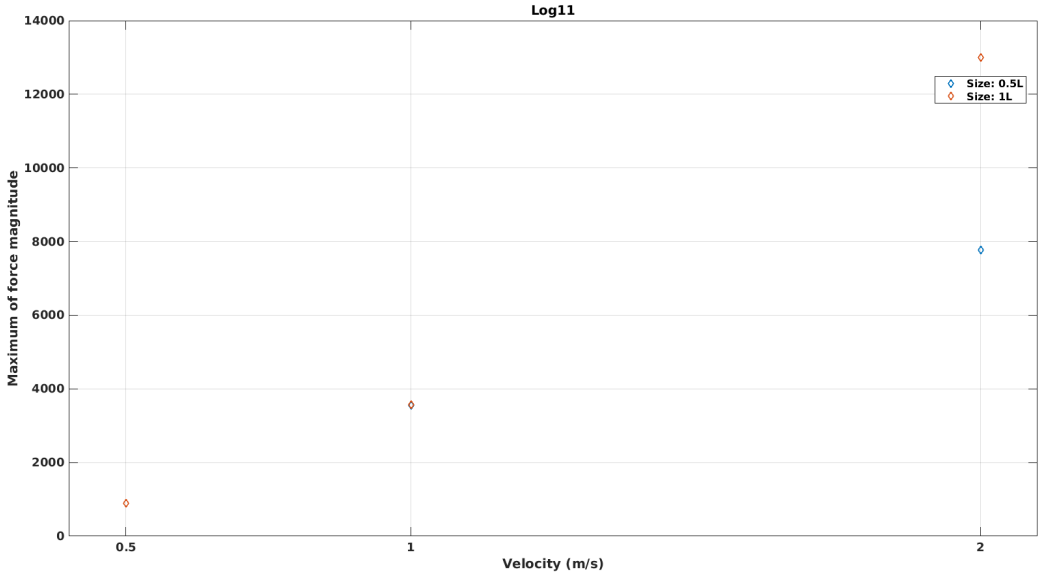

Figure A.121: Variation of maximum force magnitude with flow velocity for Log11.

Log12

This is the log that is injected from location 12 as shown in Figure 4.12. It is injected at the same time as logs 9, 10, and 11.

Figure A.122 shows the comparison of the PDFs of Log12 force magnitude for different log sizes at V = 0.5 m/s. Log12 of size 1L has higher probability of forces being around the mean than that for size 0.5L. Log of size 0.5L has higher probability of forces being large and small as well.

Figure A.123 shows the comparison of the PDFs of Log12 force magnitude for different log sizes at V = 1.0 m/s. Log12 of size 1L has higher probability of force being around the mean than that of size 0.5L. Log12 of size 0.5L has higher probability of large and small forces.

Figure A.124 shows the comparison of the PDFs of Log12 force magnitude for different log sizes at V = 2.0 m/s. Log12 of size 0.5L has higher probability of force being around the mean than that of size 0.5L.

Figures A.125, A.126, and A.127 show the variation of mean, median, and maximum of Log12 force magnitude for different log sizes. Mean and maximum force remain fairly constant. Median force decreases with log size.

Figures A.128 and A.129 show the comparison of the PDFs of Log12 force magnitude for the two log sizes at different flow velocities. As the velocity increases, the probability of higher forces on log increases. The momentum of logs increases with velocities and therefore so does the impact force.

Figures A.130, A.131, and A.132 show the variation of mean, median, and maximum of Log12 force magnitude for different flow velocities. Both mean and maximum force show an increasing trend with velocity. The variation is quadratic. Median force decreases with velocity.

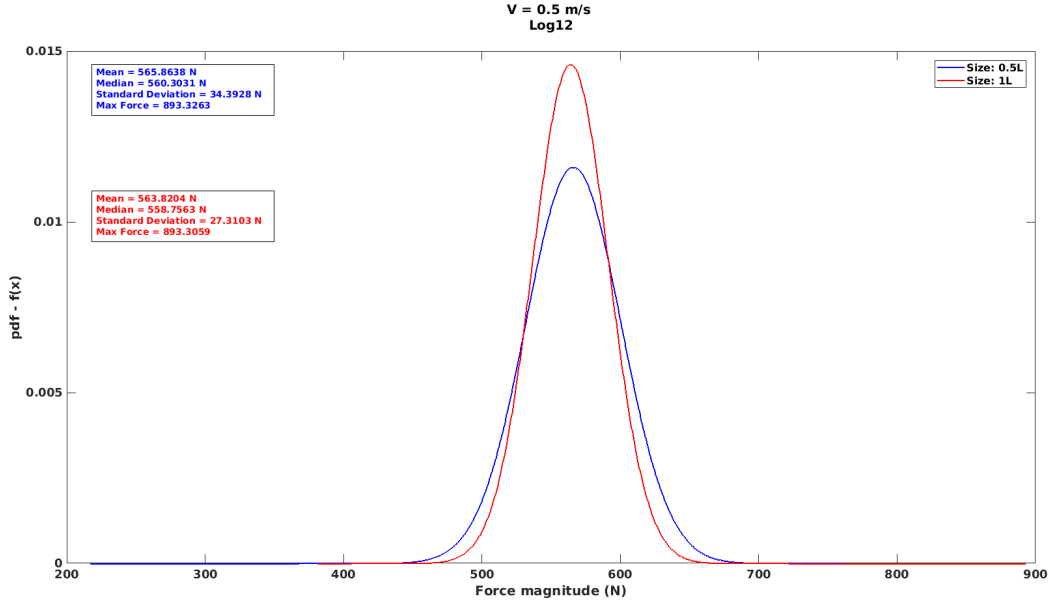

Figure A.122: Comparison of the PDFs of the forces on Log12 at V = 0.5 m/s.

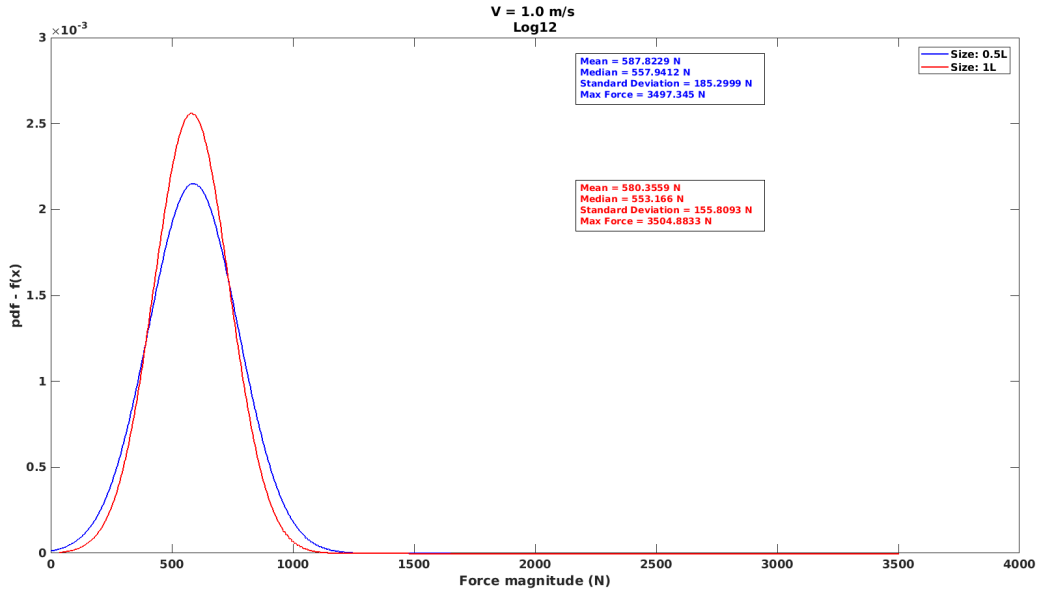

Figure A.123: Comparison of the PDFs of the forces on Log12 at V = 1.0 m/s.

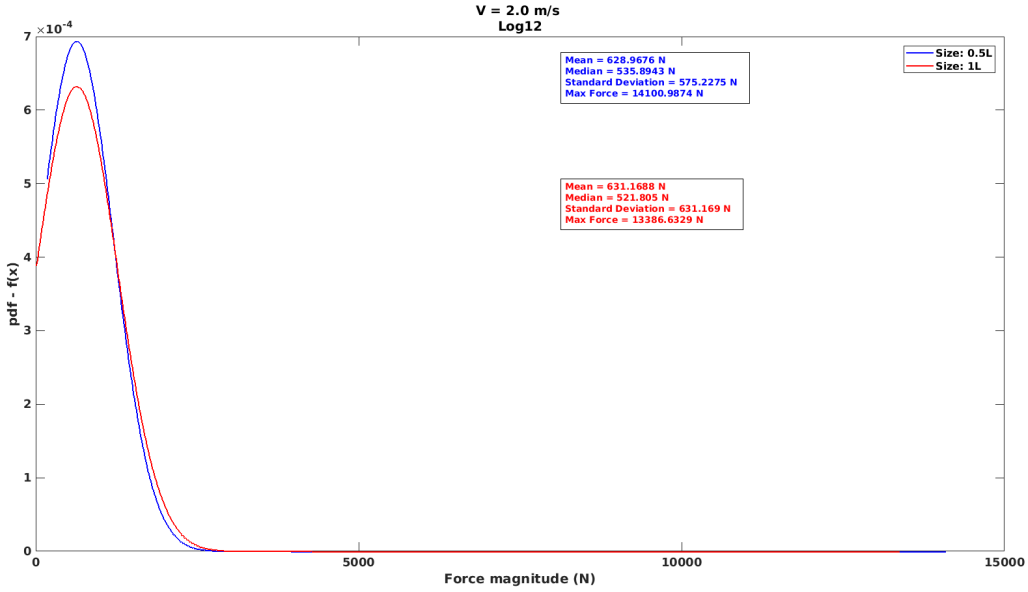

Figure A.124: Comparison of the PDFs of the forces on Log12 at V = 2.0 m/s.

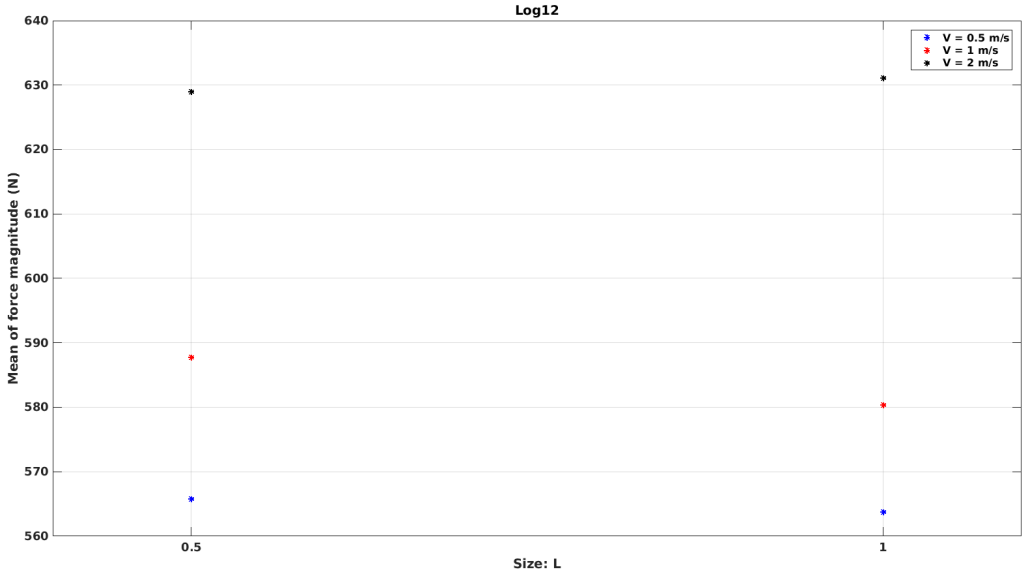

Figure A.125: Variation of mean force magnitude with log size for Log12.

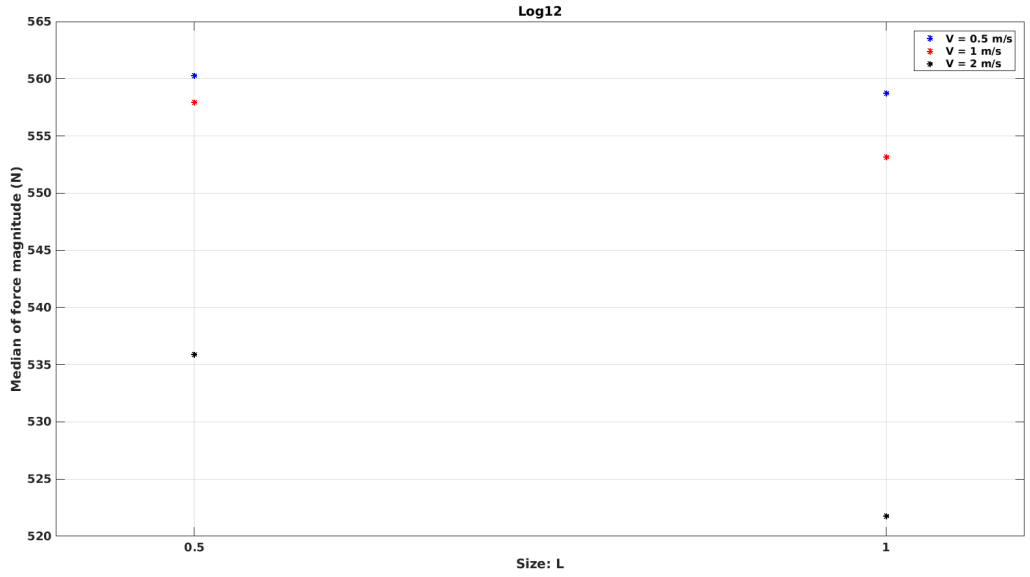

Figure A.126: Variation of median force magnitude with log size for Log12.

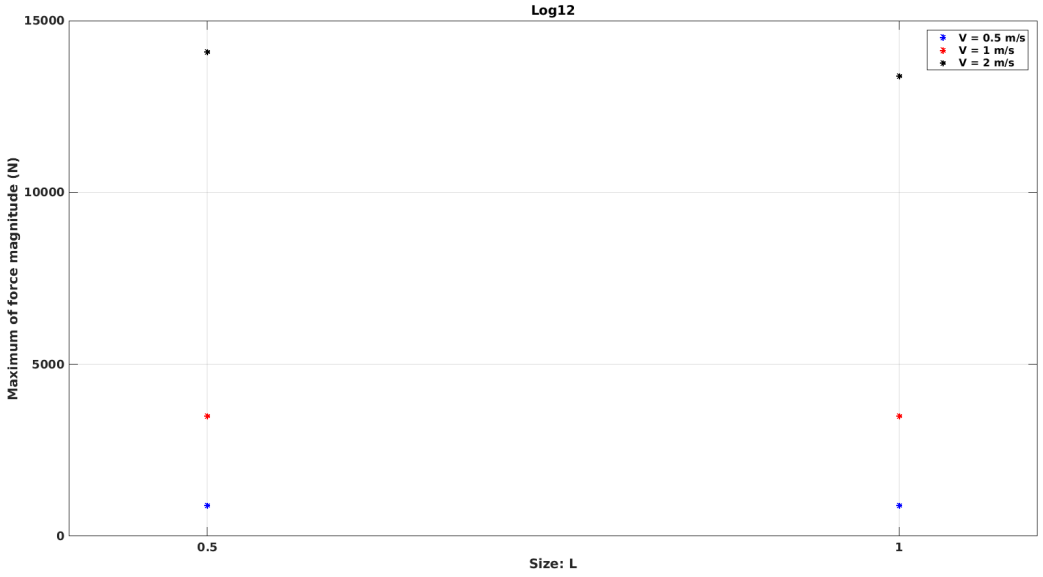

Figure A.127: Variation of maximum force magnitude with log size for Log12.

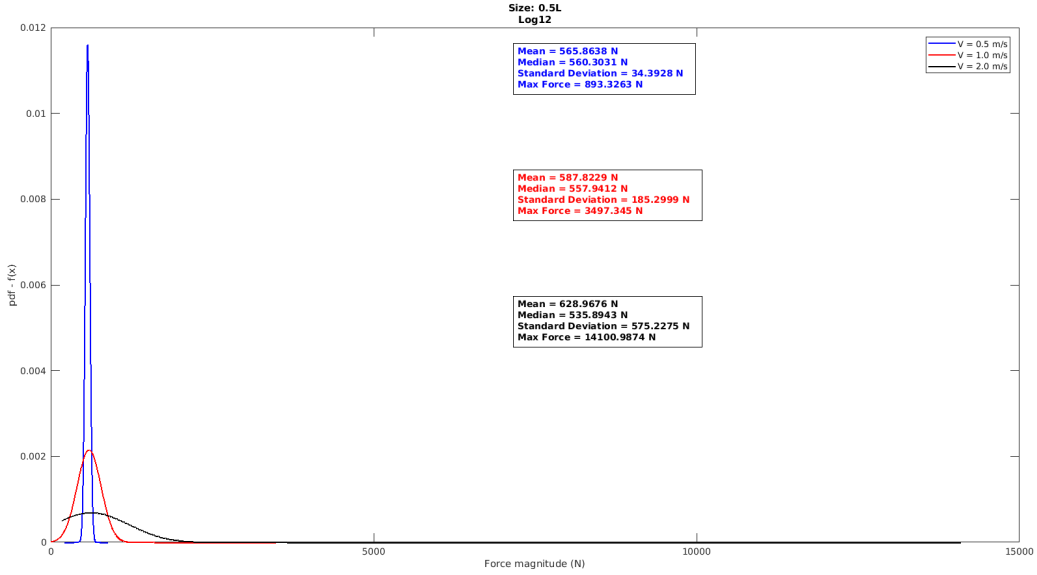

Figure A.128: Comparison of the PDFs of the forces on Log12 of size 0.5L.

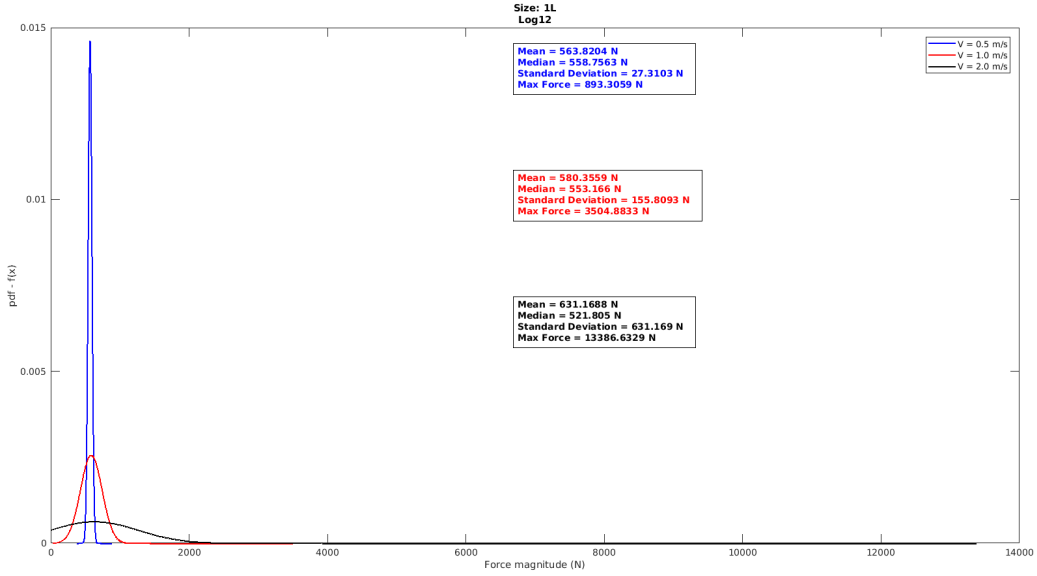

Figure A.129: Comparison of the PDFs of the forces on Log12 of size 1L.

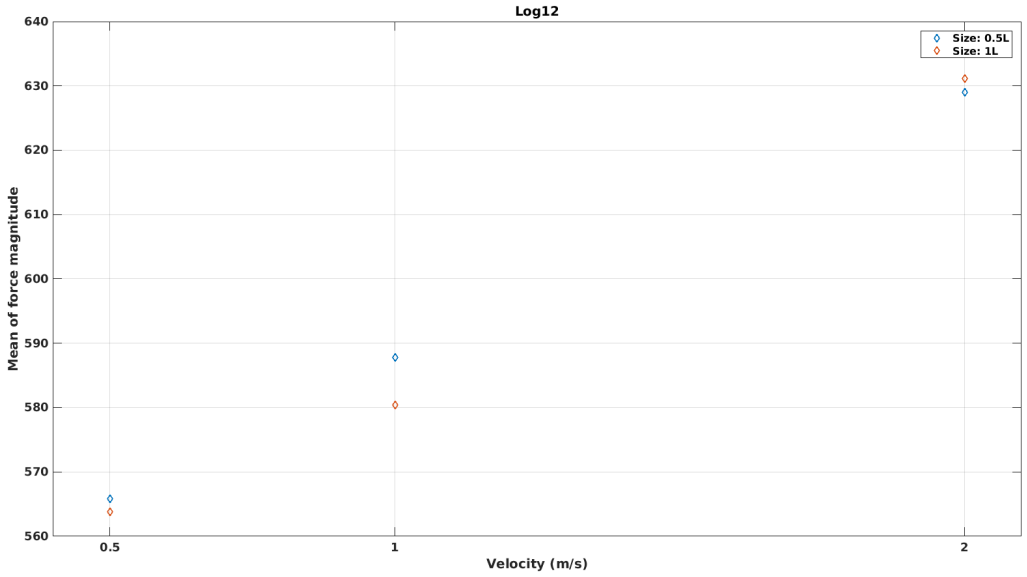

Figure A.130: Variation of mean force magnitude with flow velocity for Log12.

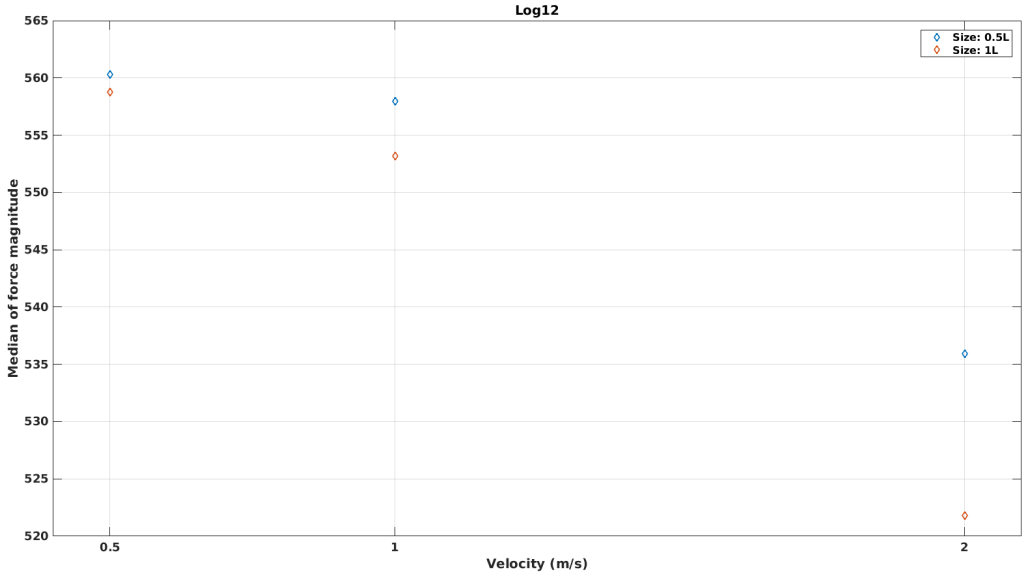

Figure A.131: Variation of median force magnitude with flow velocity for Log12.

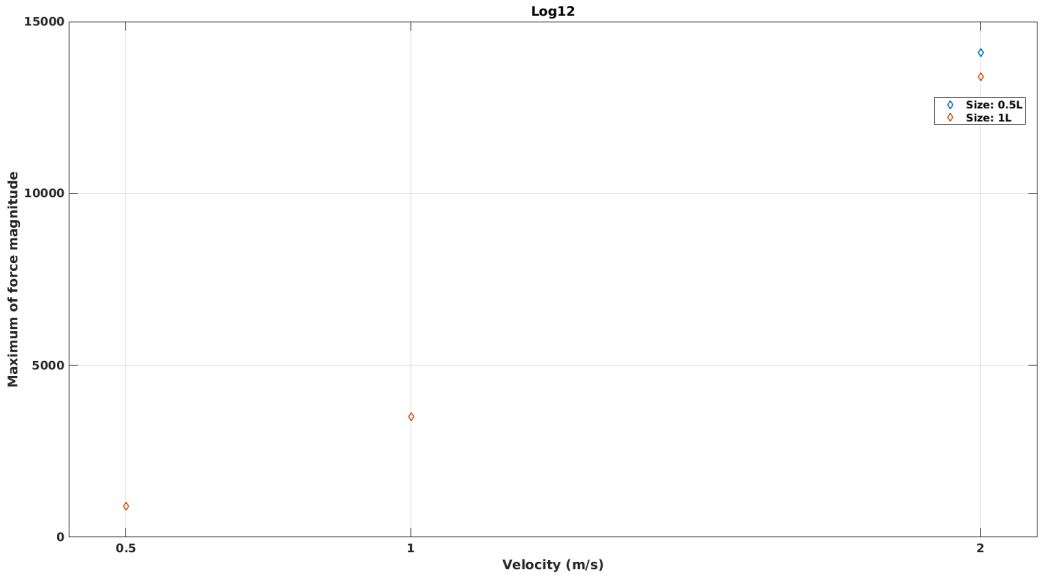

Figure A.132: Variation of maximum force magnitude with flow velocity for Log12.

Log13

This is the log that is injected from location 13 as shown in Figure 4.12. It is injected at the same time as logs 14 and 15.

Figure A.133 shows the comparison of the PDFs of Log13 force magnitude for different log sizes at V = 0.5 m/s. Log13 of size 1L has higher probability of forces being around the mean than that for size 0.5L. Log of size 0.5L has higher probability of forces being large and small as well.

Figure A.134 shows the comparison of Log13 PDFs of the force magnitude for different log sizes at V = 1.0 m/s. Log13 of size 1L has higher probability of force being around the mean than that of size 0.5L. Log13 of size 0.5L has higher probability of large and small forces.

Figure A.135 shows the comparison of the PDFs of Log13 force magnitude for different log sizes at V = 2.0 m/s. The PDFs are very similar to each other.

Figures A.136, A.137, and A.138 show the variation of mean, median, and maximum of

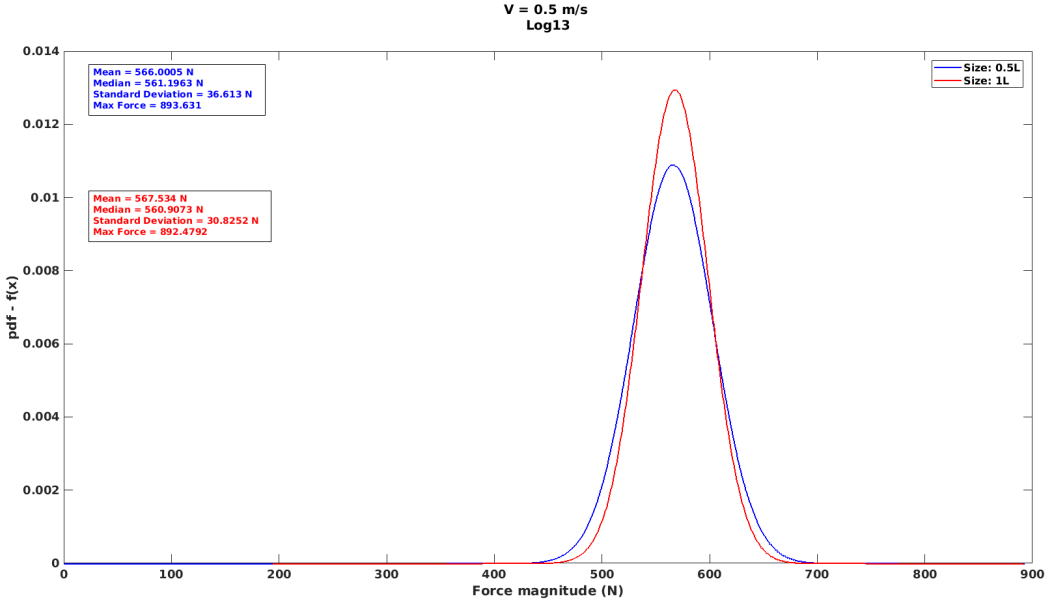

Figure A.133: Comparison of the PDFs of the forces on Log13 at V = 0.5 m/s.

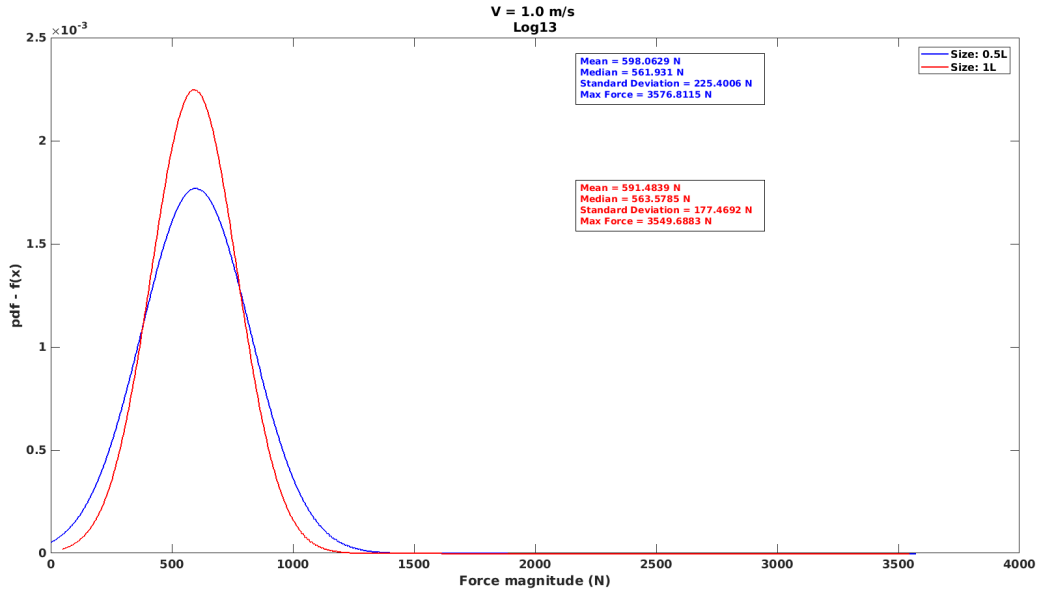

Figure A.134: Comparison of the PDFs of the forces on Log13 at V = 1.0 m/s.

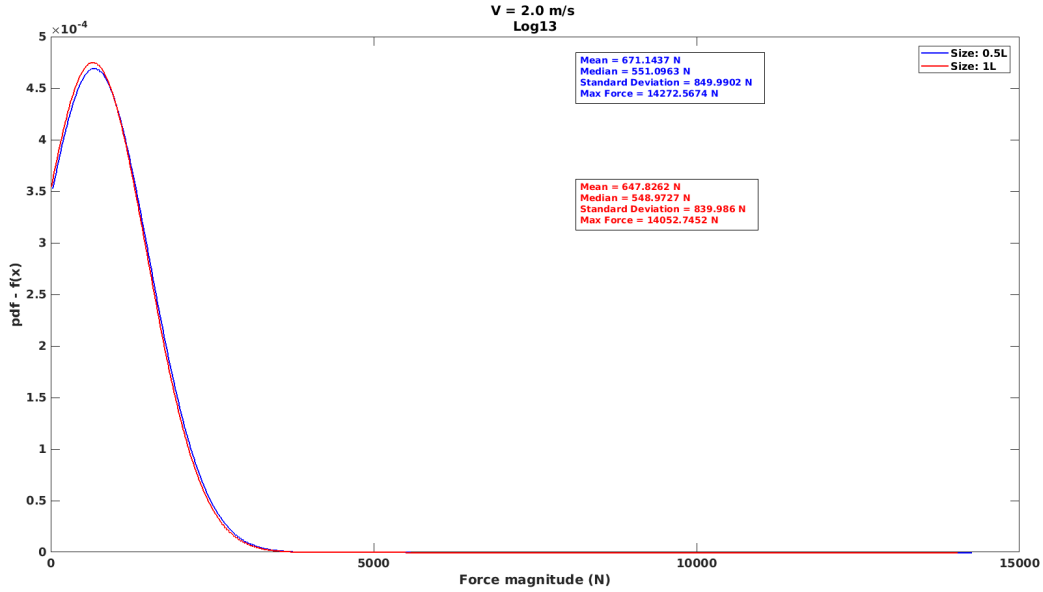

Figure A.135: Comparison the of PDFs of the forces on Log13 at V = 2.0 m/s.

Log13 force magnitude for different log sizes. Mean force decreases with log size. Median force shows inconsistent variation. Maximum force remains fairly constant.

Figures A.139 and A.140 show the comparison of the PDFs of Log13 force magnitude for the two log sizes at different flow velocities. As the velocity increases, the probability of higher forces on log increases. The momentum of logs increases with velocities and therefore so does the impact force.

Figures A.141, A.142, and A.143 show the variation of mean, median, and maximum of Log13 force magnitude for different flow velocities. Both mean and maximum force show an increasing trend with velocity. The variation is quadratic. median force shows inconsistent behavior.

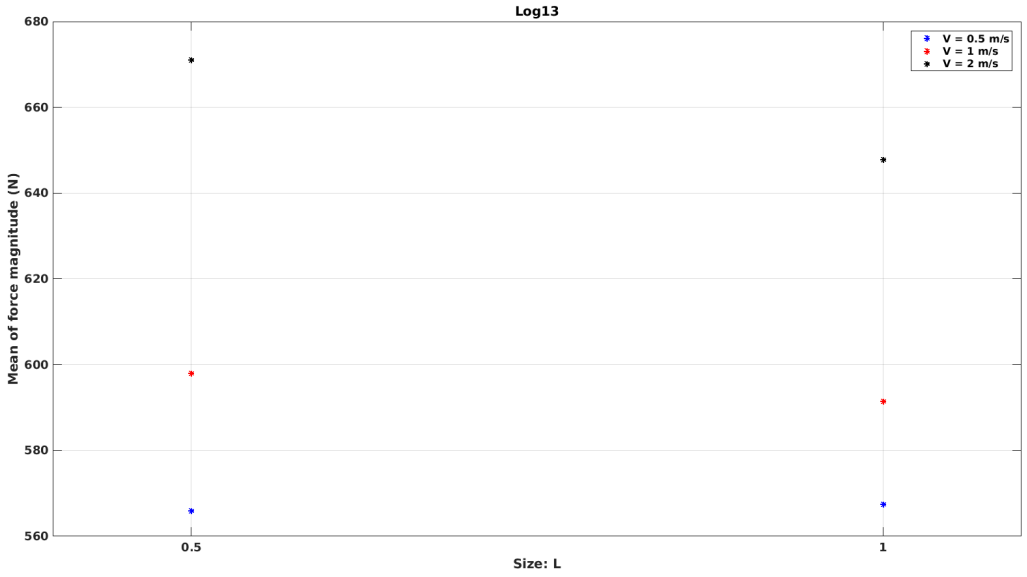

Figure A.136: Variation of mean force magnitude with log size for Log13.

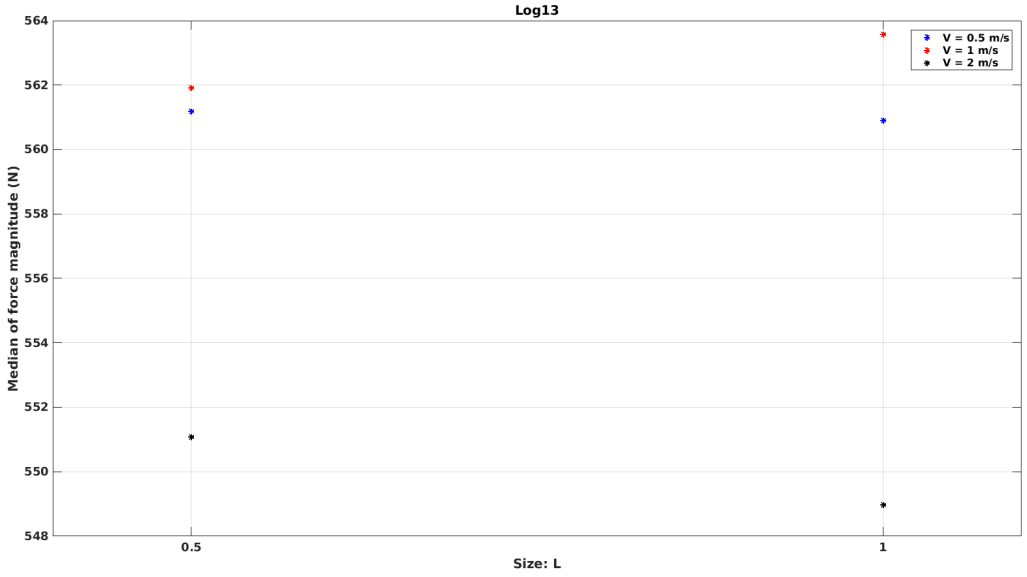

Figure A.137: Variation of median force magnitude with log size for Log13.

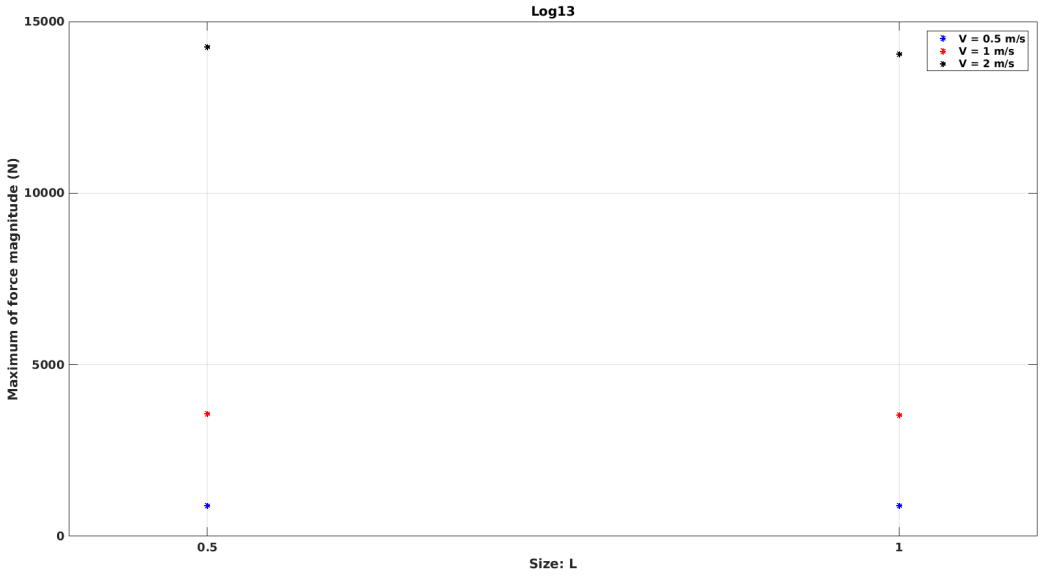

Figure A.138: Variation of maximum force magnitude with log size for Log13.

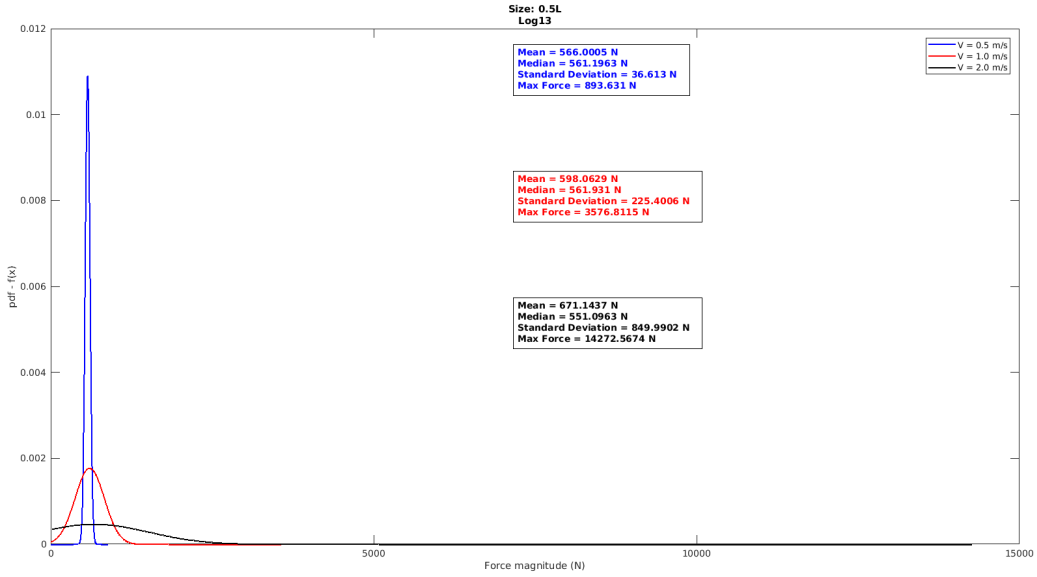

Figure A.139: Comparison of the PDFs of the forces on Log13 of size 0.5L.

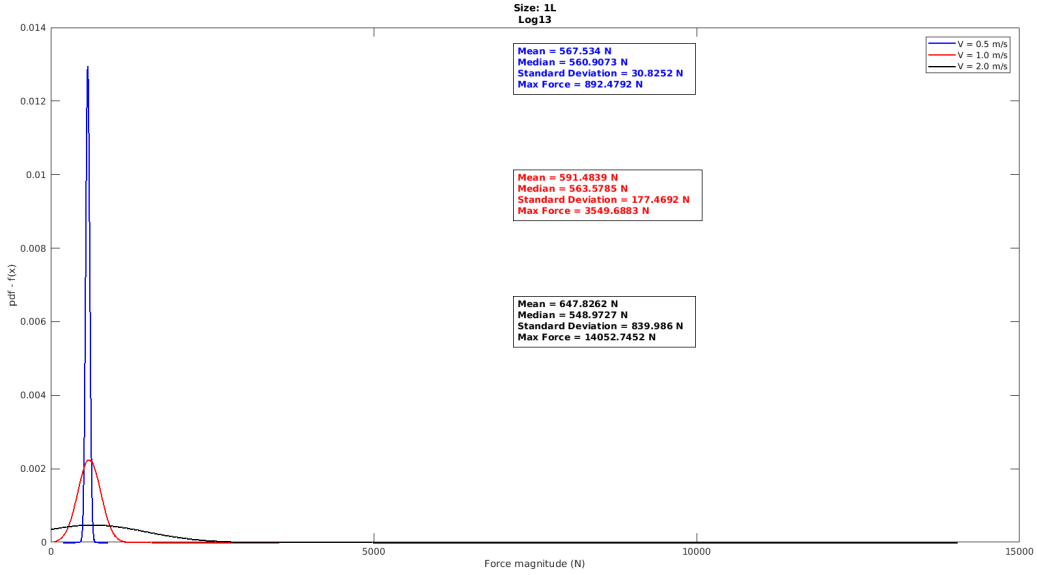

Figure A.140: Comparison of the PDFs of the forces on Log13 of size 1L.

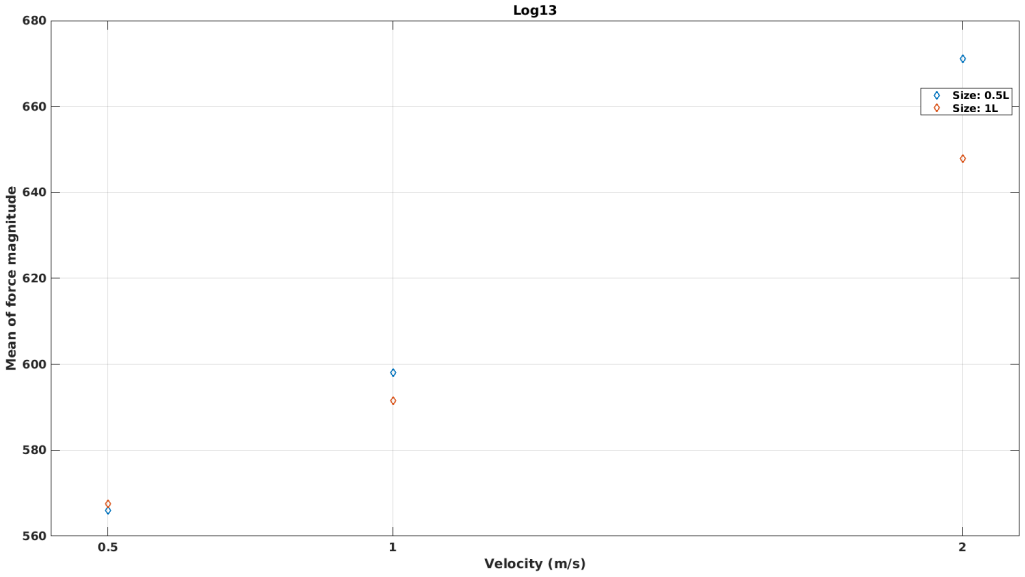

Figure A.141: Variation of mean force magnitude with flow velocity for Log13.

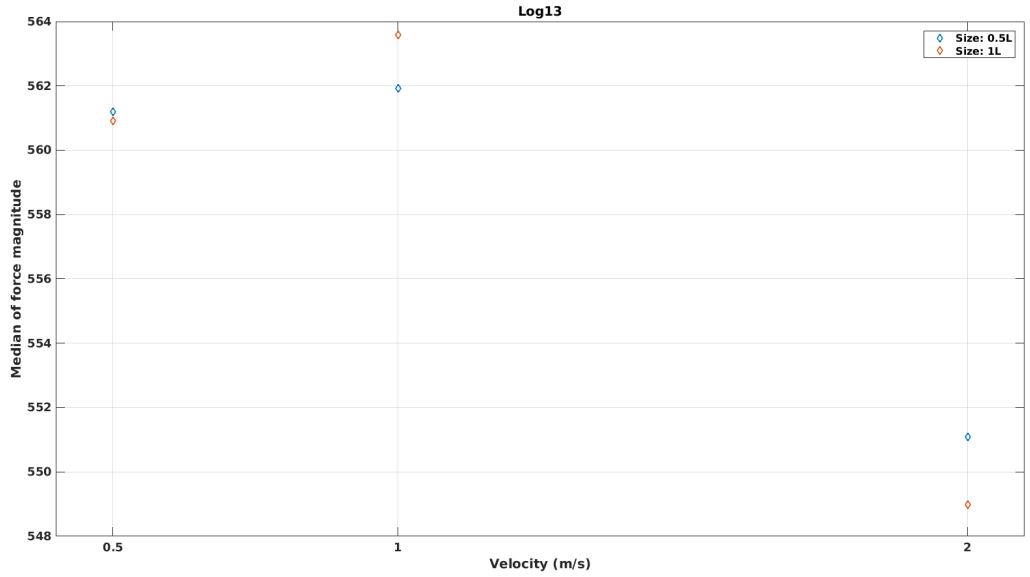

Figure A.142: Variation of median force magnitude with flow velocity for Log13.

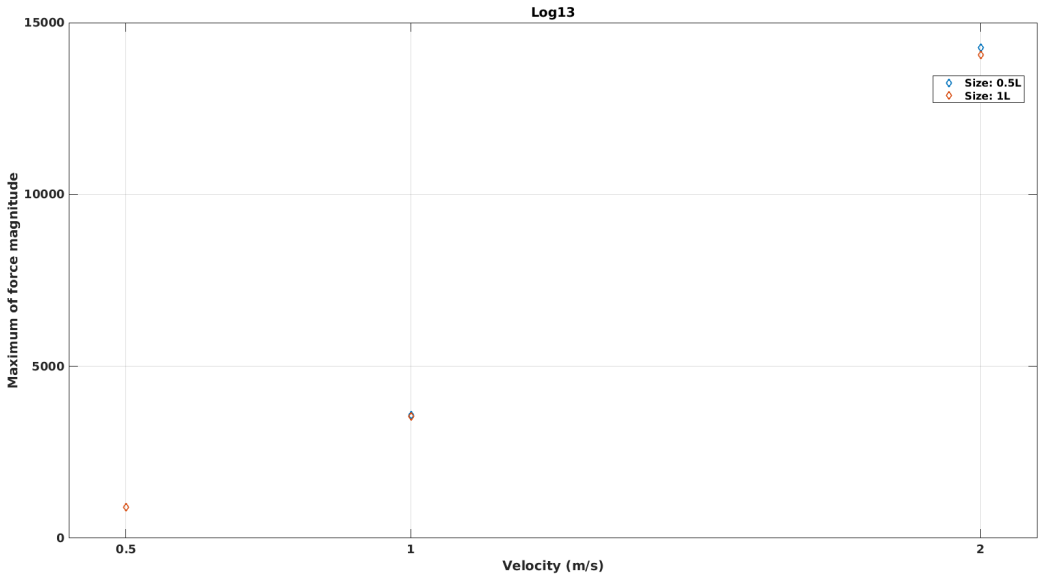

Figure A.143: Variation of maximum force magnitude with flow velocity for Log13.

Log14

This is the log that is injected from location 14 as shown in Figure 4.12. It is injected at the same time as logs 13 and 15. Log14 impacts head on with RDDP and imparts the maximum force on RDDP.

Figure A.144 shows the comparison of the PDFs of Log14 force magnitude for different log sizes at V = 0.5 m/s. Log14 of size 1L has higher probability of forces being around the mean than that for size 0.5L. Log of size 0.5L has higher probability of forces being large and small as well.

Figure A.145 shows the comparison of the PDFs of Log14 force magnitude for different log sizes at V = 1.0 m/s. Log14 of size 1L has higher probability of force being around the mean than that of size 0.5L. Log14 of size 0.5L has higher probability of large and small forces.

Figure A.146 shows the comparison of the PDFs of Log14 force magnitude for different log sizes at V = 2.0 m/s. Log14 of size 0.5L has higher probability of force being around the mean.

Figures A.147, A.148, and A.149 show the variation of mean, median, and maximum of Log14 force magnitude for different log sizes. Mean, median and maximum forces fairly remains constant for V = 0.5 m/s and V = 1 m/s but increases with size for V = 2.0 m/s. This behavior is due high momentum of the log for V = 2.0 m/s.

Figures A.150 and A.151 show the comparison of the PDFs of Log14 force magnitude for the two log sizes at different flow velocities. For log of size 0.5L, probability of force being around the mean is high for V = 0.5 m/s. PDFs for V = 1 m/s and V = 2 m/s are similar but range of forces for V = 1 m/s is large. For log of size 1L, the variation is more consistent with that observed for other logs. As the velocity increases, the probability of high forces increases.

Figures A.152, A.153, and A.154 show the variation of mean, median, and maximum of Log14 force magnitude for different flow velocities. Mean force increases with velocity for log of size 1L, while it remains fairly constant for log of size 0.5L. A similar behavior is observed

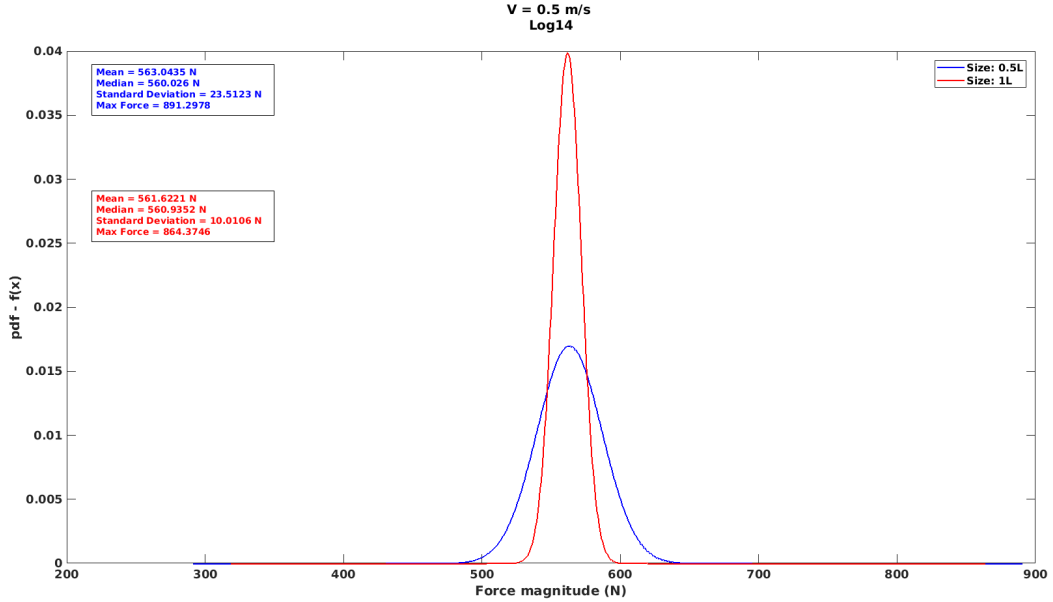

Figure A.144: Comparison of the PDFs of the forces on Log14 at V = 0.5 m/s.

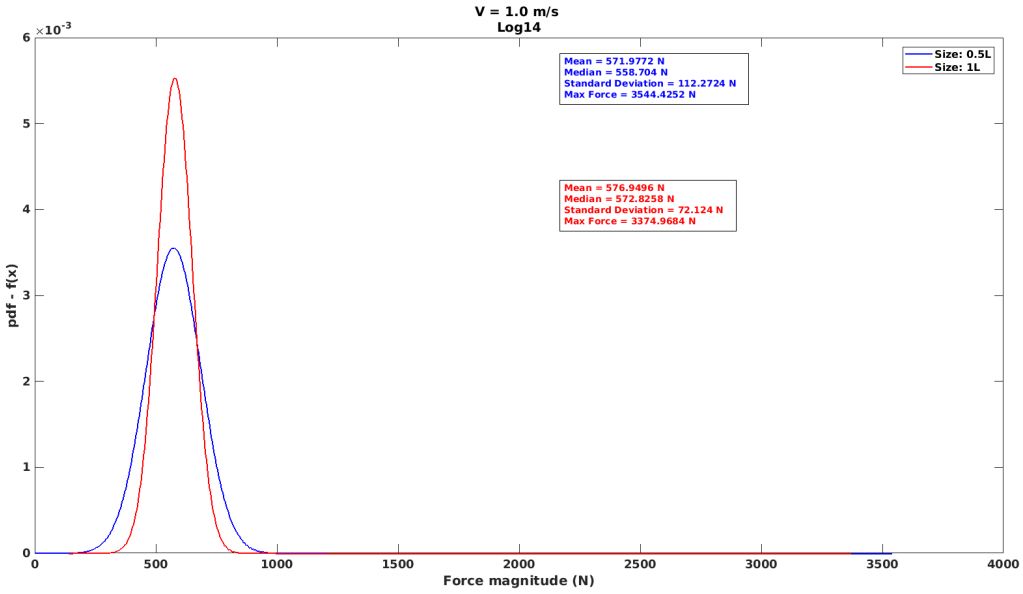

Figure A.145: Comparison of the PDFs of the forces on Log14 at V = 1.0 m/s.

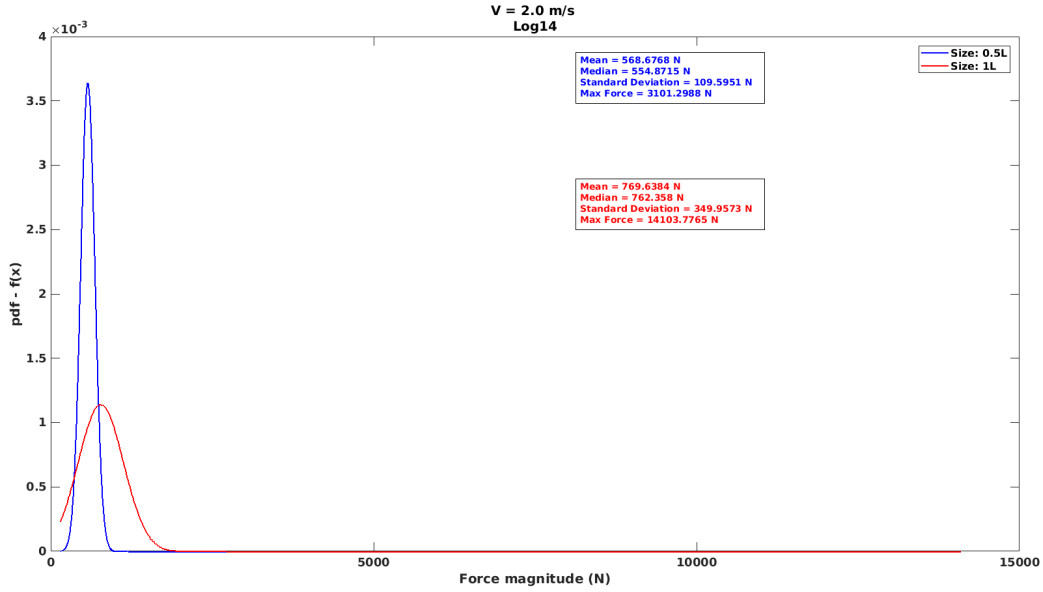

Figure A.146: Comparison of the PDFs of the forces on Log14 at V = 2.0 m/s.

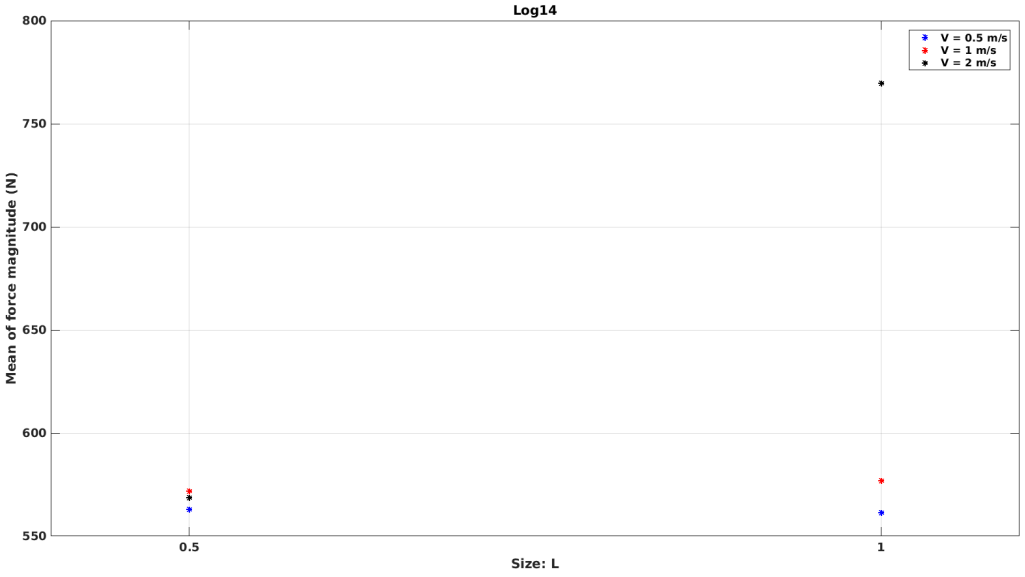

Figure A.147: Variation of mean force magnitude with log size for Log14.

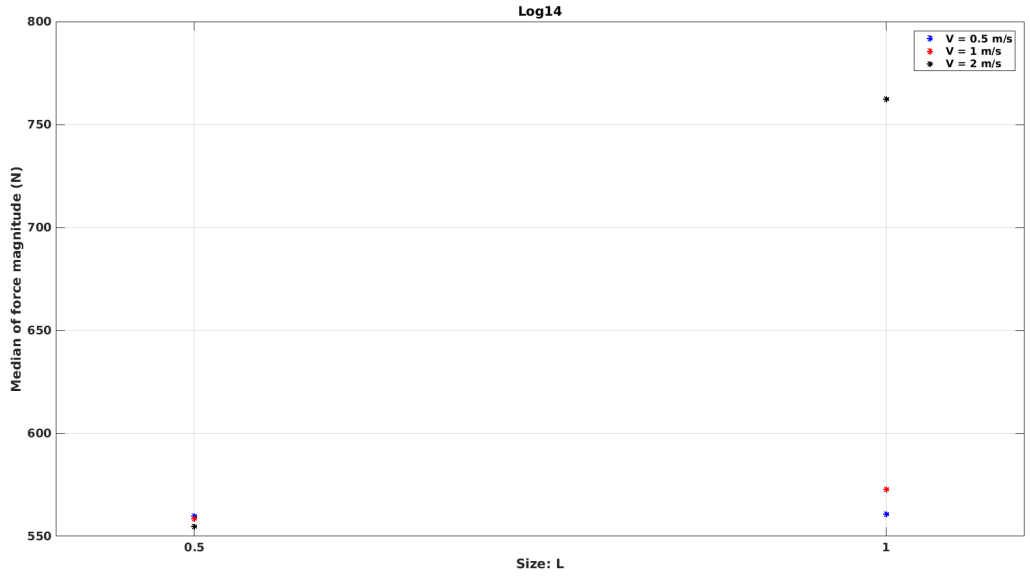

Figure A.148: Variation of median force magnitude with log size for Log14.

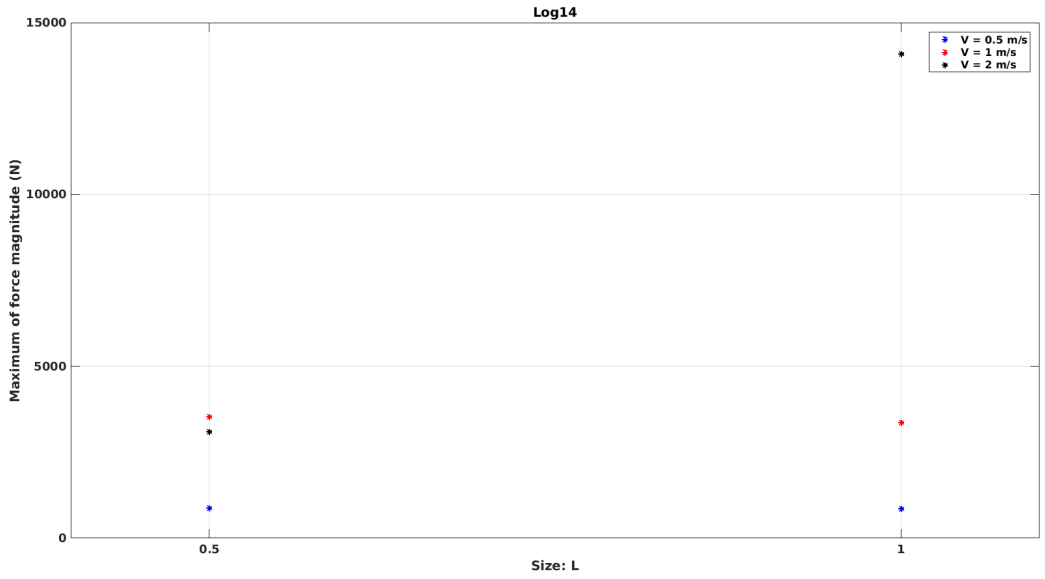

Figure A.149: Variation of maximum force magnitude with log size for Log14.

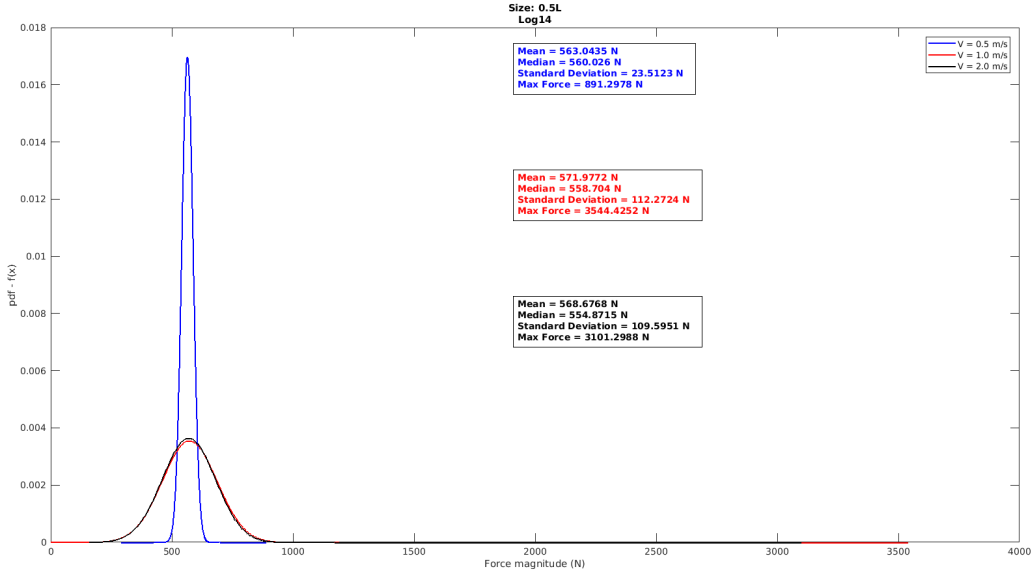

Figure A.150: Comparison of PDFs of forces on Log14 of size 0.5L.

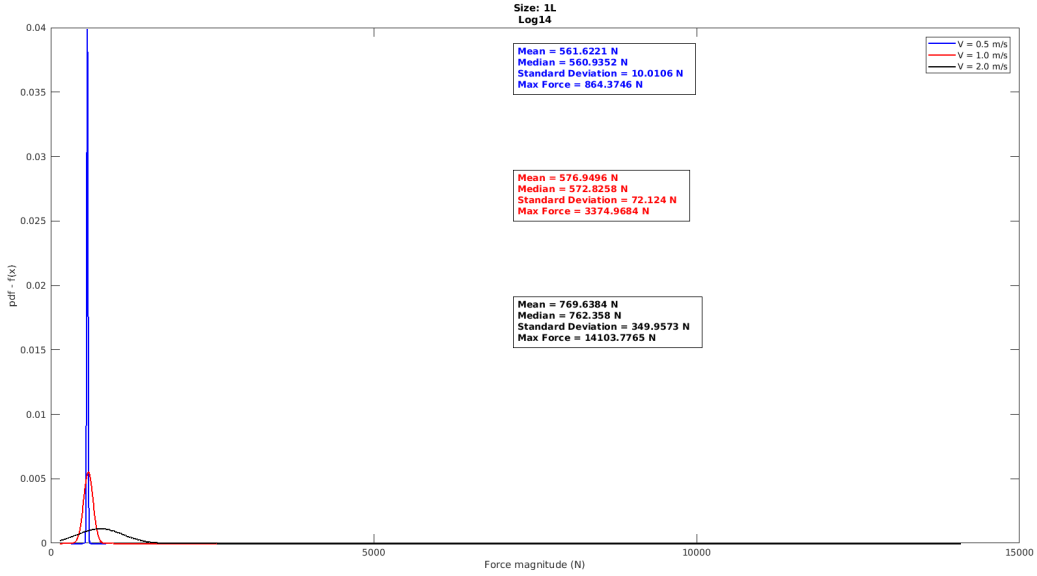

Figure A.151: Comparison of PDFs of forces on Log14 of size 1L.

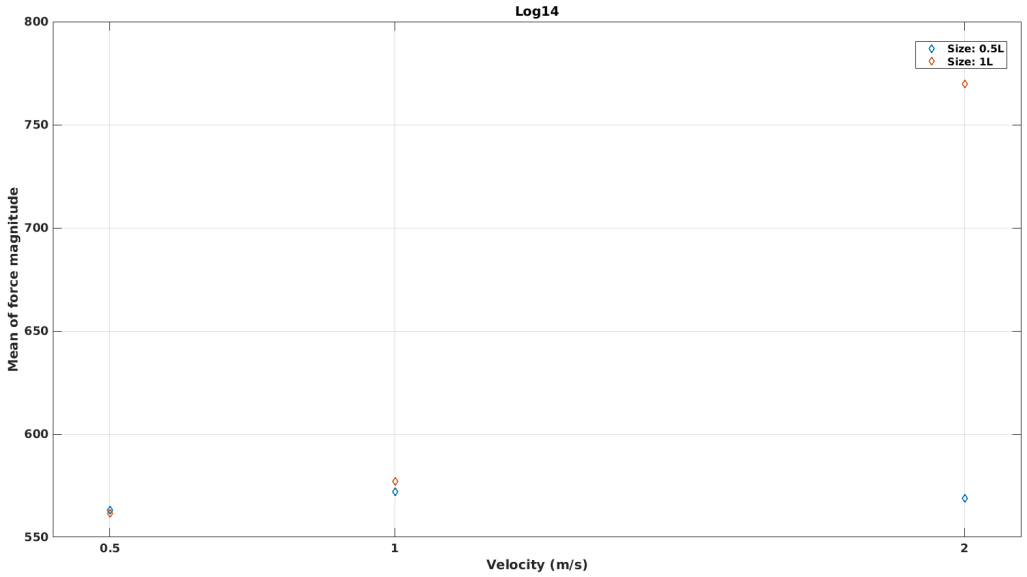

Figure A.152: Variation of mean force magnitude with flow velocity for Log14.

for median force as well. Maximum force increases with velocity for log of size 1L, while it increases at first for log of size 0.5L and then decreases. This is again due to the amount of area that is in contact with RDDP during the impact.

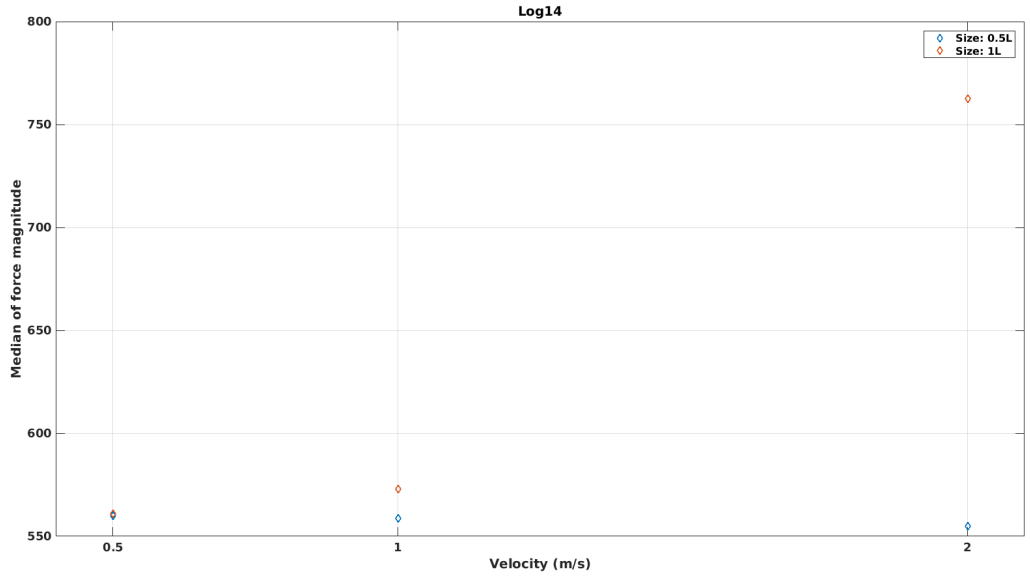

Figure A.153: Variation of median force magnitude with flow velocity for Log14.

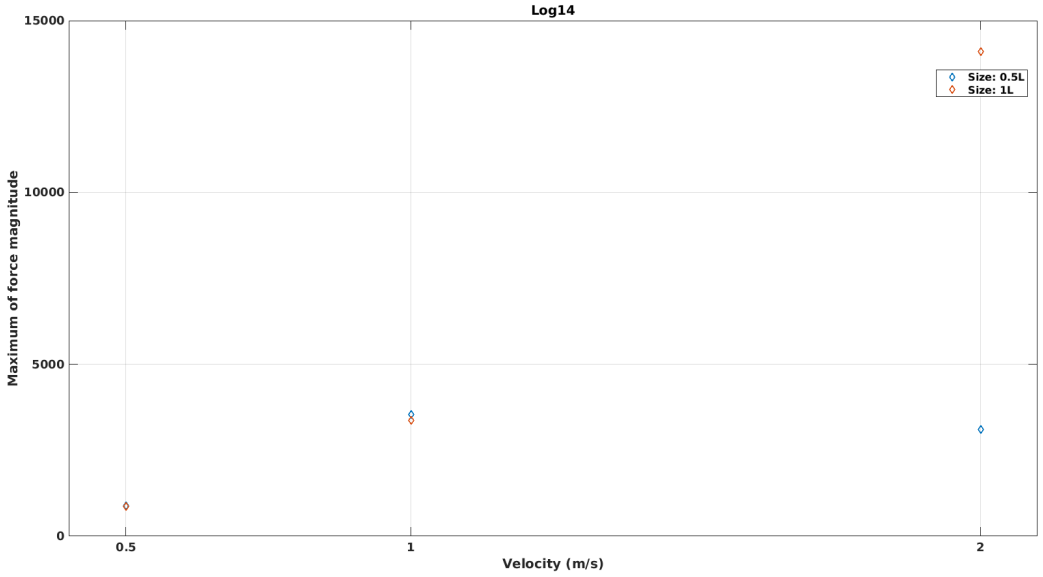

Figure A.154: Variation of maximum force magnitude with flow velocity for Log14.

Log15

This is the log that is injected from location 15 as shown in Figure 4.12. It is injected at the same time as logs 13 and 14. Log15 impacts head on with RDDP and imparts the maximum force on RDDP.

Figure A.155 shows the comparison of the PDFs of Log15 force magnitude for different log sizes at V = 0.5 m/s. Log15 of size 1L has higher probability of forces being around the mean than that for size 0.5L. Log of size 0.5L has higher probability of forces being large and small as well.

Figure A.156 shows the comparison of the PDFs of Log15 force magnitude for different log sizes at V = 1.0 m/s. Log15 of size 0.5L has higher probability of force being around the mean than that of size 1L. Log15 of size 1L has higher probability of large forces.

Figure A.157 shows comparison of the PDFs of Log15 force magnitude for different log sizes at V = 2.0 m/s. Log15 of size 0.5L has higher probability of force being around the mean while size 1L has high probability of large forces.

Figures A.158, A.159, and A.160 show the variation of mean, median, and maximum of Log15 force magnitude for different log sizes. All three increase with log size.

Figures A.161 and A.162 show the comparison of the PDFs of the force magnitude on Log15 of two sizes at different flow velocities. As the velocity increases, the probability of higher forces on log increases. The momentum of logs increases with velocities and therefore so does the impact force.

Figures A.163, A.164, and A.165 show the variation of mean, median, and maximum of Log14 force magnitude for different flow velocities. Mean and maximum force increase with flow velocity. Median force increases with flow velocity for log size 1L, while it increases with size at first for log of size 0.5L and then decreases.

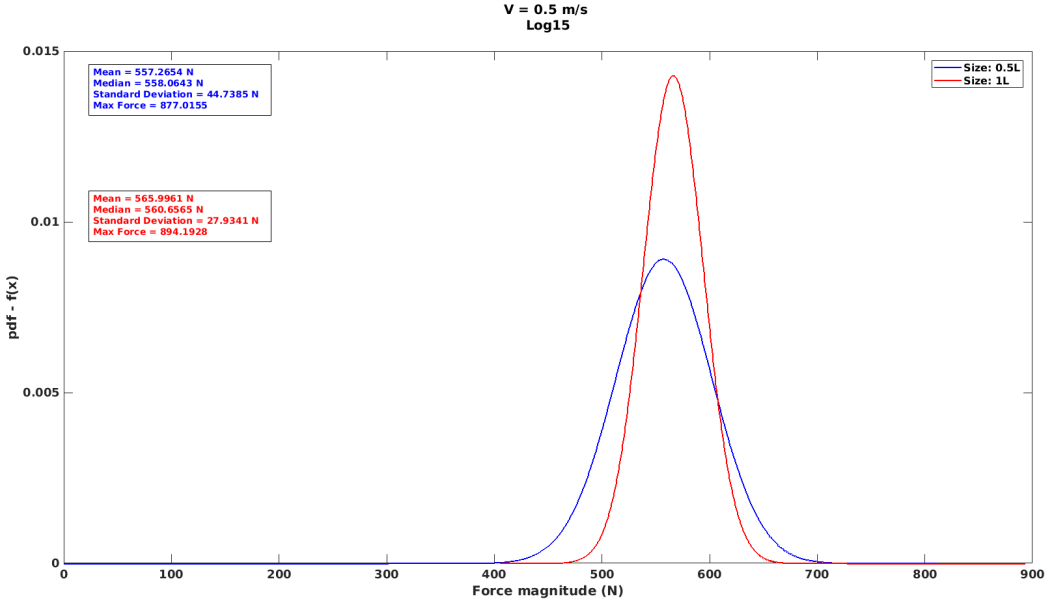

Figure A.155: Comparison of PDFs of forces on Log15 at V = 0.5 m/s.

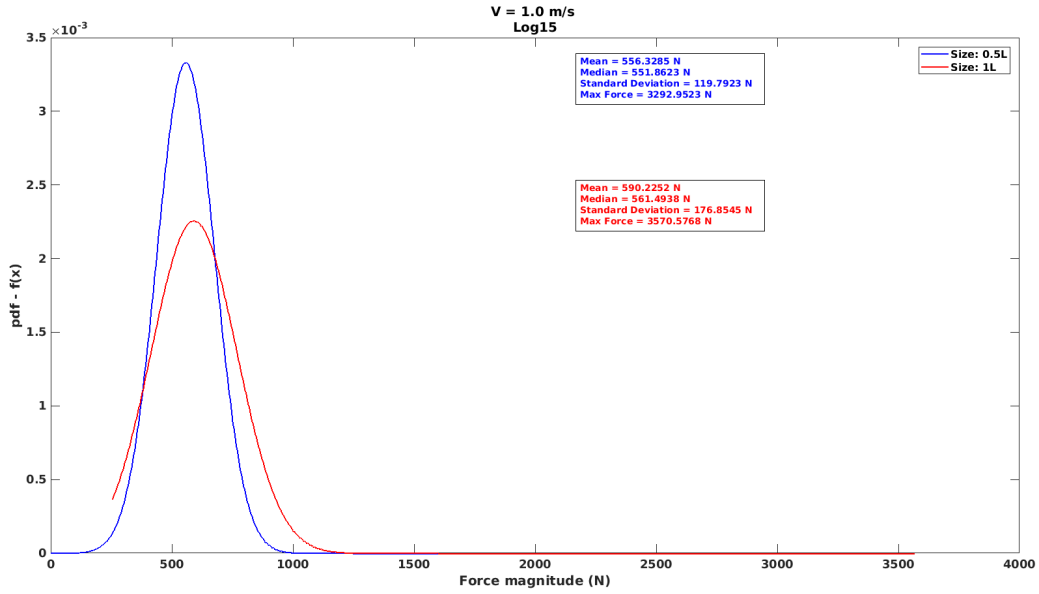

Figure A.156: Comparison of the PDFs of the forces on Log15 at V = 1.0 m/s.

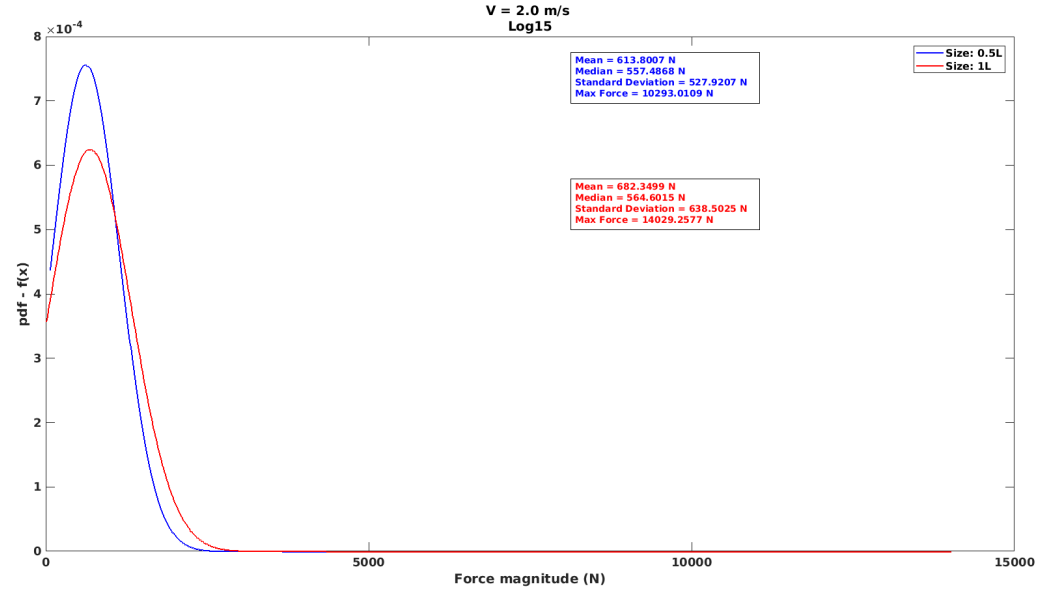

Figure A.157: Comparison of the PDFs of the forces on Log15 at V = 2.0 m/s.

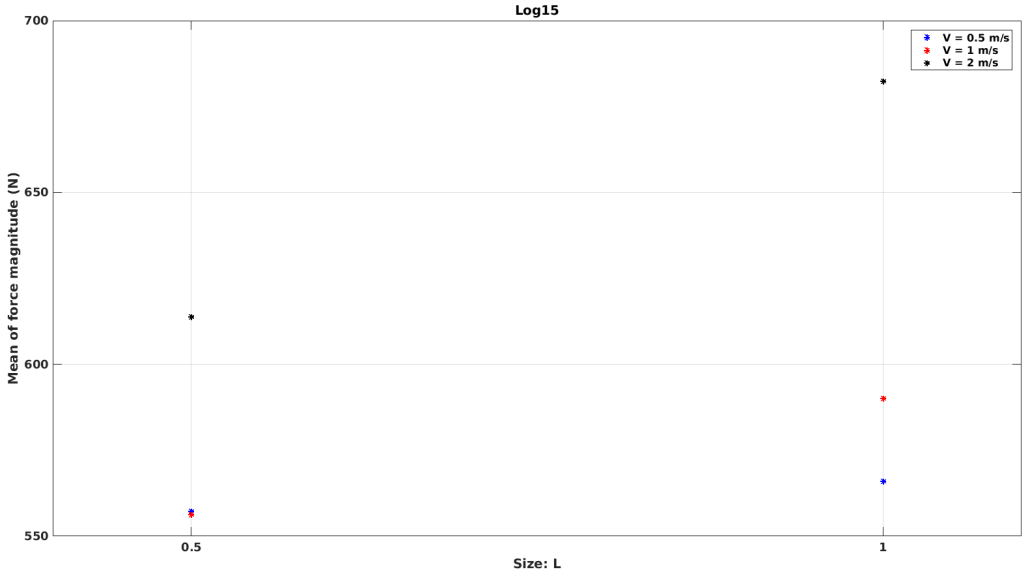

Figure A.158: Variation of mean force magnitude with log size for Log15.

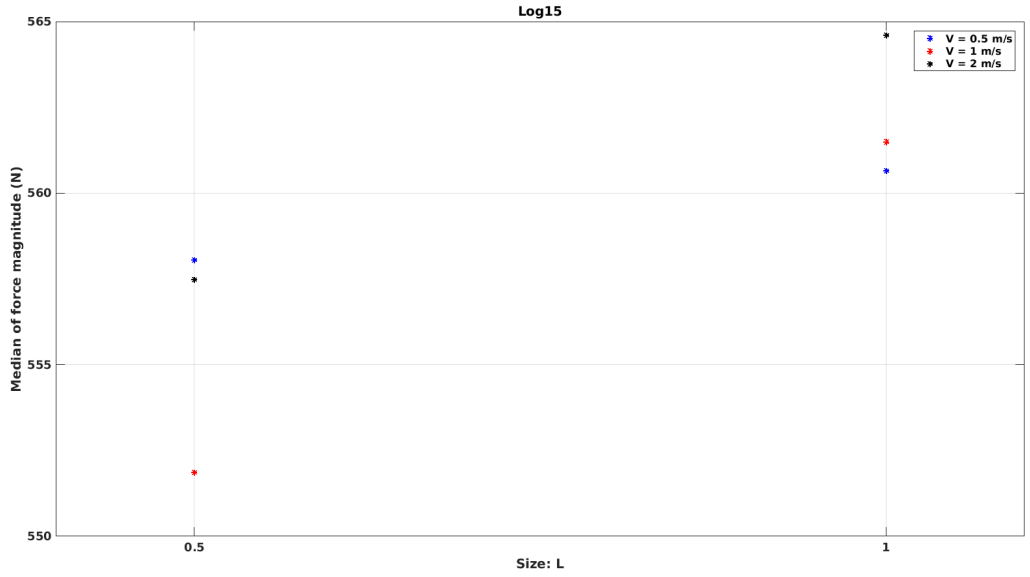

Figure A.159: Variation of median force magnitude with log size for Log15.

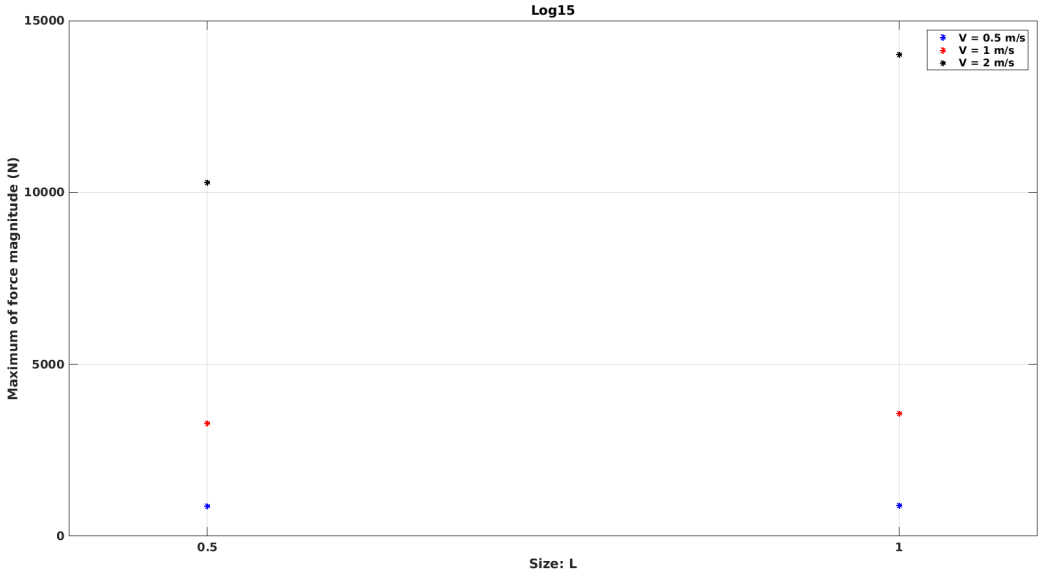

Figure A.160: Variation of maximum force magnitude with log size for Log15.

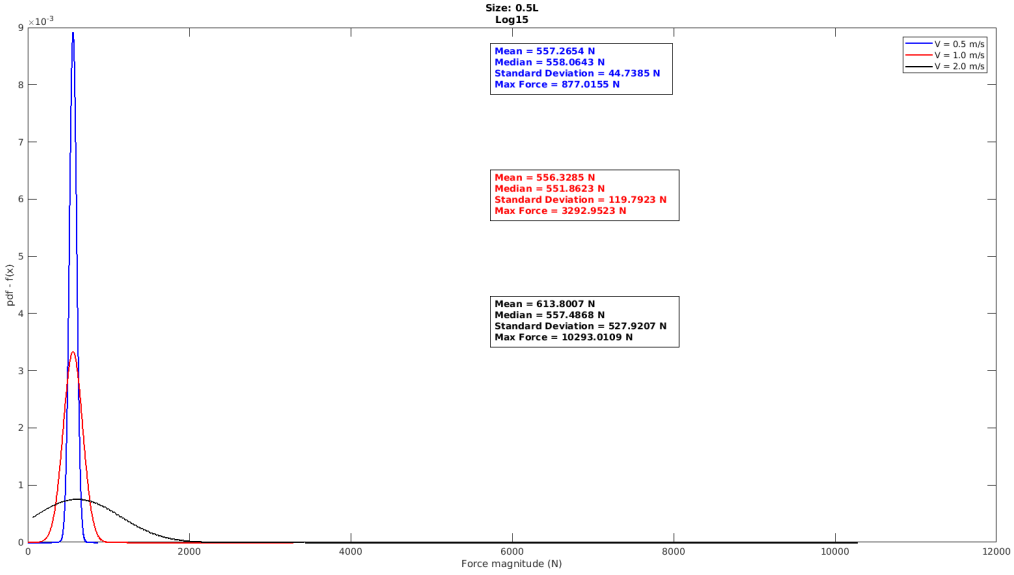

Figure A.161: Comparison of the PDFs of the forces on Log14 of size 0.5L.

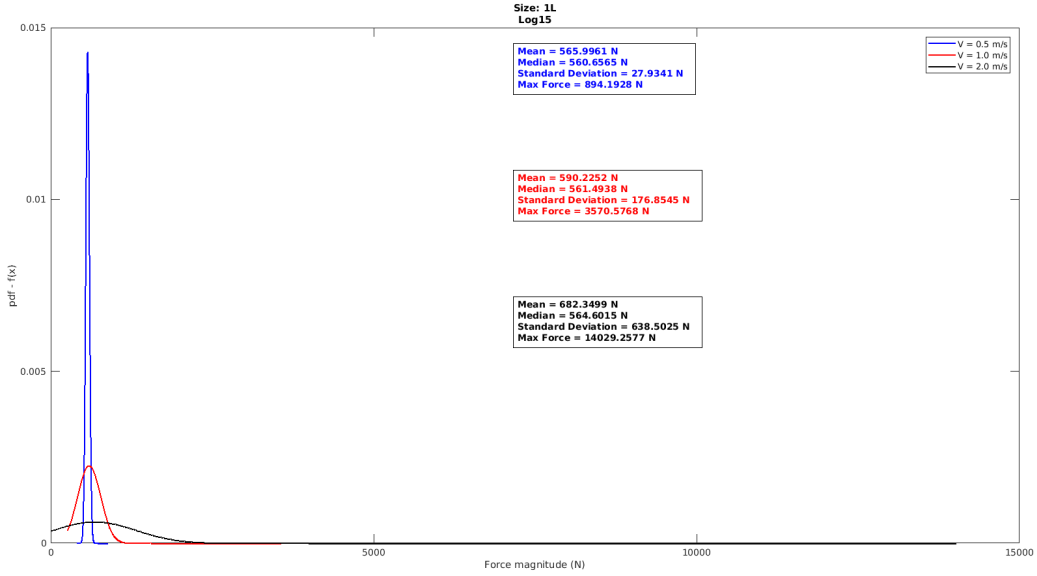

Figure A.162: Comparison of the PDFs of the forces on Log15 of size 1L.

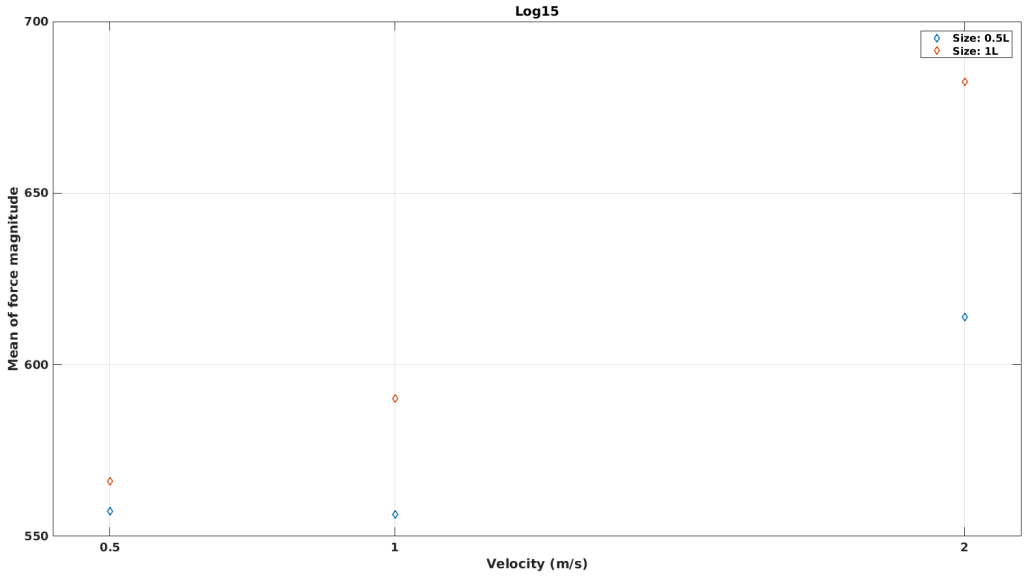

Figure A.163: Variation of mean force magnitude with flow velocity for Log15.

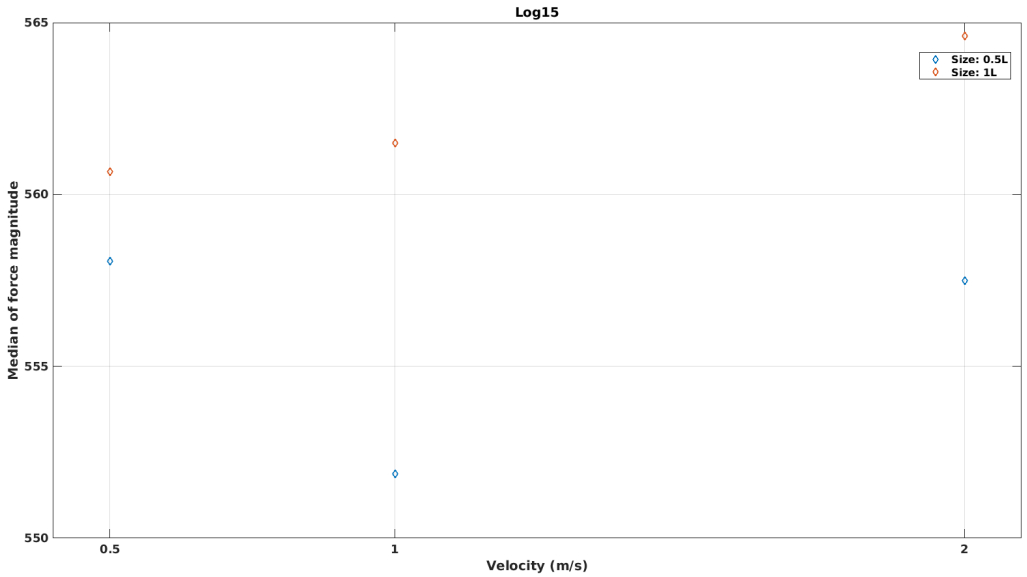

Figure A.164: Variation of median force magnitude with flow velocity for Log15.

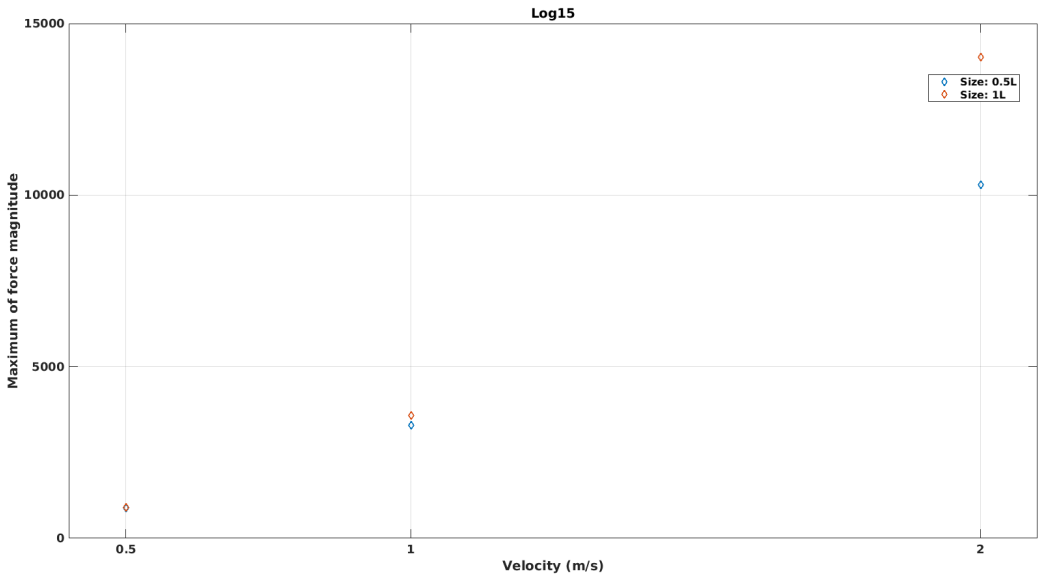

Figure A.165: Variation of maximum force magnitude with flow velocity for Log15.